A FEASIBILITY STUDY ON THE FATIGUE PERFORMANCE OF LASER BEAM WELDS AND HYBRID-LASER ARC WELDS USED IN AN INNOVATIVE MODULAR STEEL SANDWICH PANEL BRIDGE DECK SYSTEM

Garrett J. Passarelli

Thesis submitted to the faculty of the Virginia Polytechnic Institute and State University

in partial fulfillment of the requirements for the degree of

MASTER OF SCIENCE

in

CIVIL ENGINEERING

William J. Wright, Chair

Cristopher D. Moen

Thomas E. Cousins

September 28, 2011

Blacksburg, Virginia

Keywords: Bridge Decks, Sandwich Panel, Laser Weld, LBW, HLAW, Finite Element Analysis, Fatigue Resistance

A FEASIBILITY STUDY ON THE FATIGUE PERFORMANCE OF LASER BEAM WELDS AND HYBRID-LASER ARC WELDS USED IN AN INNOVATIVE MODULAR STEEL SANDWICH PANEL BRIDGE DECK SYSTEM

Garrett J. Passarelli

This research investigation explores the feasibility of implementing a laser welded sandwich steel panel bridge deck system as a viable alternative to standardized reinforced concrete bridge decks. Generally used in naval ship building applications, steel sandwich panels possess attractive characteristics towards the integration with bridge infrastructure such as service life in excess of 100 plus years, dead load reduction, rapid construction, decreased closure time, and automated mass production. The lack of fatigue data for the laser "stake" welds used to create the enclosed sandwich panel geometry raised concerns with respect to fatigue life. The primary focus of this study was to determine whether or not infinite fatigue life was possible. Two different laser welding technologies were investigated, Laser Beam Welding (LBW) and Hybrid-Laser Arc Welding (HLAW). Test specimens were fabricated and tested in order to examine fatigue resistance based on a localized load effect between adjacent core stiffeners. Finite element models were used to obtain the stress range for each individual test due to complex geometry and partially restrained boundary conditions. In order to assess the fatigue performance of the overall deck system, additional finite element models were created to study the local and global behavior of different sandwich panel configurations. As a whole the investigation yielded promising results. Infinite fatigue life is achievable due to outstanding fatigue performance. The HLAW stake welds demonstrated superior fatigue resistance in comparison to the LBW process. Localized load effects can be minimized through the modification of different panel parameters. Pushing forward, full scale testing is essential to the future employment of this innovative bridge deck system.

ACKNOWLEDGEMENTS

Overall this journey has tested me both intellectually and emotionally on numerous levels. There are many people I must thank that have aided me during this venture, but more importantly those whom motivated me to pursue this degree. First and foremost, I would like to thank my sister Dayna. She is always at my side whether it is to provide a listening ear or offer advice that seconds none. Gratitude is fully extended to my parents, Glenn and Laurie for acting as my life support during this two year endeavor. Their encouragement, guidance, and everlasting love have transformed me into the man I am today. They have provided me with life morals that I hold close to my heart and a strong work ethic that is the reason for my success in the world of academia. I would also like to extend a great deal of thanks to my maternal grandparents, Nicholas and Rosalie Russo whose unconditional love and wisdom aided me during this journey. My grandfather Nicholas, better known as "POP-POP" is one of the biggest role models in my life. His vast knowledge and skills in the construction industry, as well as his propensity to be a jack of all trades, sparked my initial interest in engineering. Without his influence I would not be where I am today. I owe a special thanks to Dr. William J. Wright for providing me the opportunity to work on this innovative project under his advisement. Thanks to Dr. Cristopher D. Moen and Dr. Thomas E. Cousins for serving on my thesis committee. Gratitude to my fellow graduate students, Hao Yuan for the assistance he provided me throughout the experimental testing program and Andrew Hardyniec for his guidance on various modeling methodologies. Being a part of the SEM family at Virginia Tech over the past two years is something that I thoroughly enjoyed and am truly going to miss. Lastly, I would like to thank Ethiopian ancestors from the 13th century for the discovery of the coffee bean; I do not know what I would have done without it.

TABLE OF CONTENTS

LIST OF FIGURES

LIST OF TABLES

CHAPTER 1: INTRODUCTION

1.1 BACKGROUND

Since the economic recession of 2008 America's deteriorating infrastructure has been pushed aside while the nation scrambles to deal with issues concerning Wall Street, housing and health care. In 2009, the American Society of Civil Engineers (ASCE) assessed transportation bridges with a grade "C" in their report card for America's infrastructure. Of the 600,905 bridges in service as of December 2008, 161,892 were categorized as structurally deficient or functionally obsolete according to the United States Department of Transportation (USDOT). The American Association of State Highway and Transportation Officials (AASHTO) at the time estimated that it would cost roughly $140 billion to repair every ailing bridge in the country. Past studies have shown that deck deterioration is the leading cause of inadequate bridge systems across the US. For this reason a cost effective deck alternative that is corrosion resistant, lightweight, and restricts invasive construction is sorely needed.(Engineers, 2009)

Over the past decade there has been a significant effort throughout the US to develop modular bridge deck systems that possess these necessary characteristics. The majority of decks developed have been comprised of costly alternative building materials, such as Aluminum and fiber-reinforced polymers (FRP). The ALUMADECK, SPS, and Strongwell deck systems are some examples that were field implemented, as demonstrations to determine structural feasibility, as well as develop long term durability data. Even though the life cycle cost projections of these systems have been promising, the high initial investment in comparison to traditional reinforced concrete decks impeded their use. A deck system that can be competitive on a first-cost basis is therefore needed for the widespread adoption into

highway bridge systems.

Steel orthotropic decks have been used throughout the globe since the 1970's. Though performance data has been debated due to premature design guidelines and specifications, orthotropic steel decks, if designed properly could last in upwards of 100 years with minimal maintenance. Predominately used in the rehabilitation of long spans exceeding 1000 ft due to their weight saving ability, traditional orthotropic bridge decks are considered to be an option of "last resort" due to high fabrication and construction costs associated with conventional welding practices. Consequently, a deck system comprised of steel, targeting a broader spectrum of span lengths that minimizes fabrication costs and complex detailing, has the potential to revolutionize bridge deck standards.

1.2 SANDWICH PANELS

Structurally efficient, biological shapes and forms present themselves throughout nature, as the result of an eternity of evolution. Sir D'arcy Wentworth Thompson, a mathematical biologist, describes evolution as the fundamental determinant of the form and structure of living organisms in his book, "*On Growth and Form*." Through simple mathematical transformations, Thompson explains structuralism as the process of forming biological structural architecture. Structural systems used in various applications throughout the globe resemble these biological forms. Two cases of primary focus are honeycombs and cellular walls, both of which developed over millions of years that depict sandwich panel structures.

Generally comprised of core stiffening elements bounded by two face sheets, sandwich panels permit an equivalent net section with improved performance. The reduction of raw material needed generally results in a lightweight, cost effective structural system that has an

extremely high stiffness to weight ratio. Until recently, sandwich panel applications have been limited to materials that could be extruded or joined through adhesives, such as papers and plastics. Corrugated cardboard boxes used since the late nineteenth century, employ the sandwich panel concept to deliver an economic solution that has never been rivaled. Unfortunately, the geometric profiles of metallic structures have been limited in the past to stiffened plates, such as orthotropic decks, due to fabrication and conventional welding methods. Developed in the late 1970's, laser welding is a versatile metallic joining technique that has recently enabled enclosed metallic sandwich panel structures through their ability to perform "stake" welds. The weld geometry is developed when a high intensity laser beam generates a keyhole of liquefied base metal through overlapped components, fusing them together with a V-shape profile or "stake" when rapidly cooled.

The LASCOR system, developed in the 1980's by the United States Navy was the first metallic sandwich panel assembled through laser welding. Numerous research efforts verified their performance and in 1994 were implemented in naval shipbuilding applications. One of the major limitations to the laser welding process is the laser output power that correlates to the achieved weld penetration non-linearly. Earlier laser technology restricted the component thickness, as LASCOR panels were comprised of face sheets and corrugated cores 0.125 inches and 0.090 inches in thickness respectively. As a result this process leaves them susceptible to localized loading scenarios, limiting their use to specific applications.

In recent years, the progression of laser welding technology has broadened its use by allowing for deeper weld penetrations. In 2004, a conceptual laser welded steel sandwich panel bridge deck was fabricated and studied at Bristol University in the United Kingdom. The sandwich panel was comprised of hot-rolled I-section longitudinal rib stiffeners, joined to a 12-

14 mm top plate and an 8 mm bottom plate through autogenous laser "stake" welds. The research focused on the fatigue resistance of laser welded connections due to a lack of data, which performed with promising results. However, the concept requires extremely powerful lasers that are not available to industry, preventing this system to be streamlined anytime in the near future.

More recently in 2007, Applied Thermal Sciences, Inc. (ATI) in Maine has been working with the MaineDOT and the University of Maine to develop and demonstrate a steel sandwich panel bridge deck system for re-decking a truss bridge. Their panel consists of a 0.625 inch deck plate and 0.25 inch bottom plate, joined to trapezoidal hat section core stiffeners in the longitudinal direction. The panel was designed to meet all current limit states in the AASHTO specifications, in addition to being supported on all four edges by a floor beam and stringer system. The proposed deck system is extremely efficient due to the truss like core, but is very costly due to customized core elements.

1.3 CONCEPTUAL REASONING

The goal of this study is to generate a generic bridge deck system that can be incorporated into conventional girder-type steel bridge superstructures. The conceptualized deck system analyzed in this investigation encompasses beneficial features from similar deck systems; while minimizing the likelihood of stress concentrations, complex construction detailing, and costly fabrication. In comparison to conventional orthotropic decks, the sandwich panel's enclosed structural profile shifts the neutral axis towards mid-depth, allowing for a more efficient section with nearly isotropic behavior. The amalgamation of prior deck systems is believed to result in the highest probability to develop a new deck that is structurally sufficient and competitive on a

first cost basis with reinforced concrete bridge decks.

1.3.1 SANDWICH PANEL DIMENSIONS

Modular construction is an important feature driving the design of the sandwich panel system in order to accelerate deck installation time. Prefabricated deck modules manufactured offsite with minimal field connections required would allow for mass production and decreased field work that can greatly reduce the overall cost of the initial investment. The sandwich panel bridge deck system proposed in this study will be comprised of deck modules that are 7 to 10 ft wide and span the full width of the bridge. Deck segments can therefore be placed and configured in the field with ease using a boom crane, as shown in Figure 1–1.

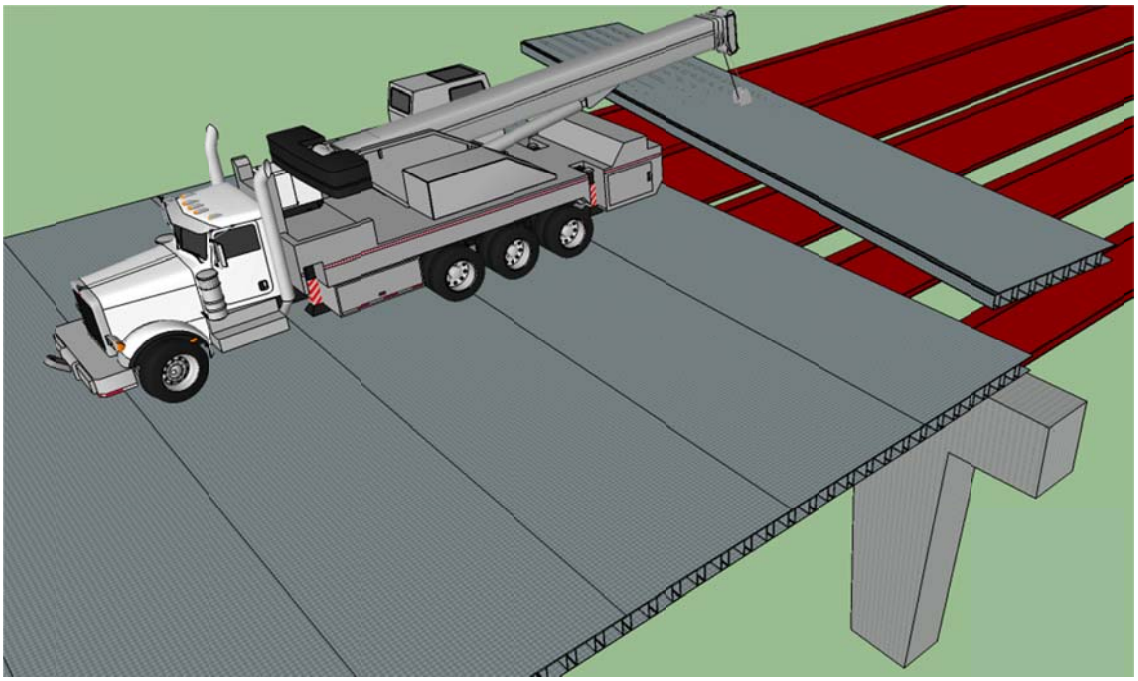

Figure 1–1: Segmental Construction using the Proposed Modular Steel Panel Bridge Deck System

Full width deck segments are extremely advantageous in comparison to other module configurations. A full bridge width deck module eliminates the need for complex and problematic connections at mid-width, as displayed in similar sandwich panel systems. ATI's

deck system is made up of half width modules, where two modules are set in the field to form a roadway crown. This orientation requires a connection at mid-width, which increases installation time and susceptibility to corrosion from de-icing salts.

1.3.2 DECK PLATE THICKNESS

Directly correlated to deck flexibility, surface deterioration is one of the predominant malfunctions in orthotropic bridge decks. Surface cracking and de-bonding has been presented in many cases to follow patterns along longitudinal rib stiffeners due to composite action with the deck plate. Even though thicker wearing surfaces can greatly reduce flexural stresses in the deck plate, decreasing self-weight; they are more problematic due to increased stresses and strains in the surfacing material that accelerate deterioration. Numerous studies have shown that thicker deck plates with thinner wearing surfaces are much less susceptible to cracking and de-bonding. Maintenance and repair of specialized wearing surfaces used in these applications can be very costly, potentially disregarding the deck system to be an economic alternative to concrete. In addition, a minimum deck plate thickness of $^{9}/_{16}$ of an inch is specified by AASHTO 9.8.3.7.1 ((AAHSTO), 2010) for orthotropic deck systems to minimize secondary distortionally induced fatigue. Therefore a range from $^{9}/_{16}$ to 1.25 inches was considered for the deck plate thickness in this study.

1.3.3 INTERNAL STIFFENED RIB DIRECTION

Internal stiffening ribs run in the longitudinal direction, parallel to traffic in orthotropic decks and many other bridge deck systems. This is to support large longitudinal bending moments, as a result of deck integration or composite action with

support girders. Provided that orthotropic decks are mainly used in long span bridge applications exceeding 1000 ft, this orientation is logical. On the other hand, there are many potential benefits to positioning stiffening ribs in the transverse direction, perpendicular to traffic even though the section modulus of the composite bridge girder would be reduced.

A typical two lane bridge with a shoulder assuming a 40 ft bridge width, transverse ribs and deck segments would extend 20 ft eliminating the need for rib splices to provide continuity. Orienting stiffeners perpendicular to traffic would also greatly increase the deck's transverse stiffness resulting in reduced susceptibility to localized truck loads, limited deck distortion, and allow for the eradication of fatigue prone floor beams. Past studies have proven that the structural detailing of floor beams is the biggest concern and probable design flaw that has led to fatigue cracking in orthotropic deck systems. Therefore, their exclusion is extremely beneficial. Lastly, transverse ribs aid in supporting bending moments at deck overhangs caused by crash barriers. This orientation increases the probability of acceptance and widespread use of the deck system, by allowing for a wider spectrum of approved crash barrier systems to be integrated in the design.

1.3.4 INTERNAL RIB STIFFENERS

Though the hat sections used in ATI's deck concept for the MaineDOT project are structurally efficient, promoting isotropic behavior through a truss like core; each rib has to be individually formed increasing overall production time and cost. Another problem with these specialized sections is that the majority of bridge fabricators are unable to produce them to desired lengths; thus requiring spliced connections dismissing an

advantage of the transverse core direction.

To accelerate production time and reduce fabrication costs, prefabricated hot rolled sections were selected, as previously used in the deck concept developed in the United Kingdom. Hot rolled sections are available in wide array of shapes and sizes to bridge fabricators throughout country, promoting deck optimization. In addition, each section is manufactured to specific ASTM guidelines and tolerances, decreasing the need for quality and control measures. Instead of using I-sections, rectangular HSS sections were selected as core stiffeners for a number of reasons that include increased torsional rigidity, highly resistant to shear loading, and less susceptible to fatigue from Vierendeel web bending.

1.3.5 FACE PLATE CONNECTIVITY

As stated previously, conventional welding practices do not allow for closed section geometry of sandwich panels, which is why laser welding is required. Both top and bottom face plates were joined via laser welding processes in previously developed steel sandwich panel bridge deck systems. The panel concept employing prefabricated I-section cores required deep weld penetrations that hindered its ability to perform as economic alternative. In addition, laser welding into the deck plate with a prefabricated core only allowed for open sections. The 12 to 14 mm thick deck plate used was too thick to penetrate, therefore requiring the cores to be welded on the underside of the deck. ATI's deck concept employed specialized hat sections with a ¼ in. thickness that inflated fabrication costs. These sections provided a closed rib core solution, connected through laser stake welds on the underside of the deck with a small lip.

In order to evade high costs stemming from rib assembly to the deck plate, the

developed deck system combines both conventional and laser welding methods to form a hybrid deck assembly. Combining both welding processes shall increase the likelihood to develop a cost effective deck system. Rectangular HSS rib sections are to be connected through continuous flare bevel GMAW welds to the deck plate. The stiffened deck plate shall then turned, and joined to the bottom plate through continuous laser stake weld geometry that is to be determined.

1.3.6 BOTTOM PLATE THICKNESS

The bottom plate thickness was limited by weld penetration attained from current output power of industrial grade lasers. Unlike the study in the United Kingdom, the conceptual deck system was developed to be competitive on a first-cost basis in the near future. For this reason, a range from $^{3}/_{16}$" to $^{5}/_{16}$" was considered for the bottom plate thickness in this study.

1.3.7 OTHER DESIGN CONSIDERATIONS

To allow for proper drainage, it is proposed that the sandwich panels are fabricated with an imposed radius of curvature in the transverse direction to simulate a 2% roadway crown. To produce this geometry, the stiffened deck plate with GMAW flare bevel welded transverse stiffeners could be placed on a set of rollers, on top of the welding table used to perform the LBW/HLAW stake welds, creating a simply supported span in the transverse direction. The rollers could then be adjusted accordingly to allow the stiffened plate to sag from self-weight to create the desired radius of curvature. The bottom plate would then be properly aligned on top of the stiffened deck plate conforming to the implemented curvature due to its flexible nature. The series of laser stake welds would then be

performed starting at the outside ribs, working inward to prevent thermal distortion.

Connection detailing is not a part of this study, but concepts have been proposed to provide integration to support girders and deck continuity. In order to integrate the sandwich panel modules into support girders to achieve composite action, the grouted connection shown in Figure 1–2 has been hypothesized. For this connection, hot-rolled angles are shop welded to the modular sandwich panels according to bridge geometry and as well as bolted to existing girders. Both sets of angles are to be fabricated with slotted holes to ease field fit-up. Once the panel is lowered by the boom crane and fit into the desired location, the connection will be made using an ASTM 325 bolt that spans the width of components. For re-decking applications, residual shear studs can be reused to provide for additional interface shear reinforcement. The entire connection shall then be grouted. It should be noted that this connection is purely conceptual and should by no means be considered structurally sound.

The splice connection shown in Figure 1–3 has been conceptualized to provide for sandwich panel continuity in the longitudinal direction. Using the AASHTO Bridge Welding Code, a prequalified full penetration single V groove weld was selected to join the deck plates of adjacent deck modules in the conceptualized splice connection.(AWS, 2010) To provide longitudinal continuity in the bottom plate of sandwich panel units, powder actuated fasteners were selected to ease field installation methods. Once again, it should be noted that this connection is purely conceptual and should by no means be considered structurally sound.

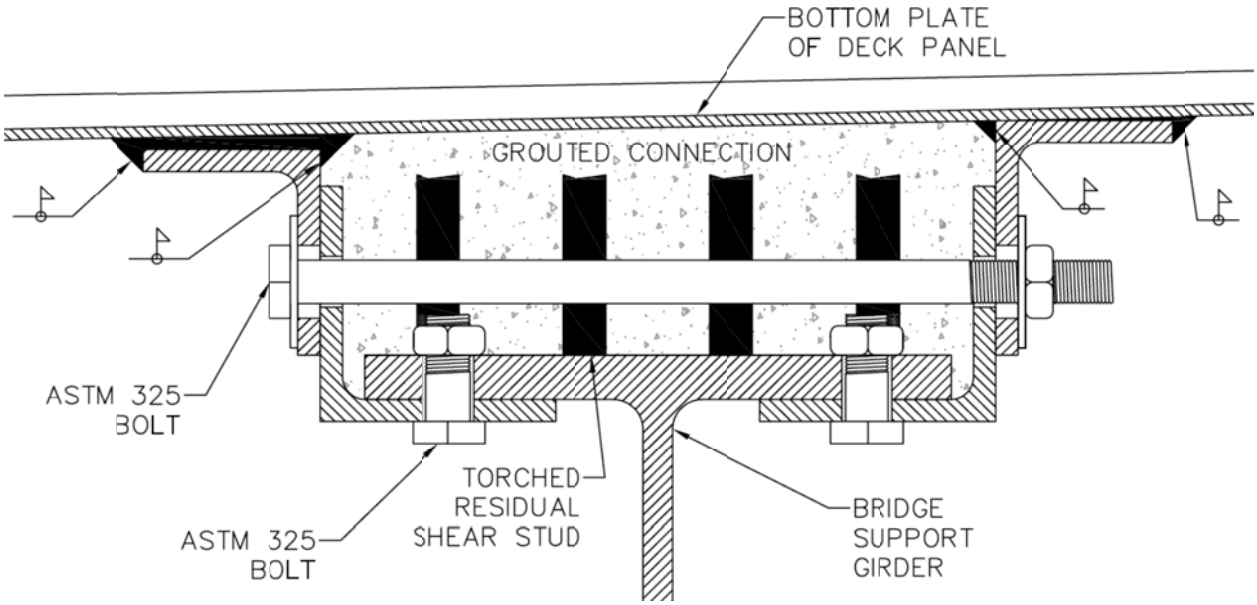

Figure 1–2: Proposed Sandwich Panel Deck Integration Connection

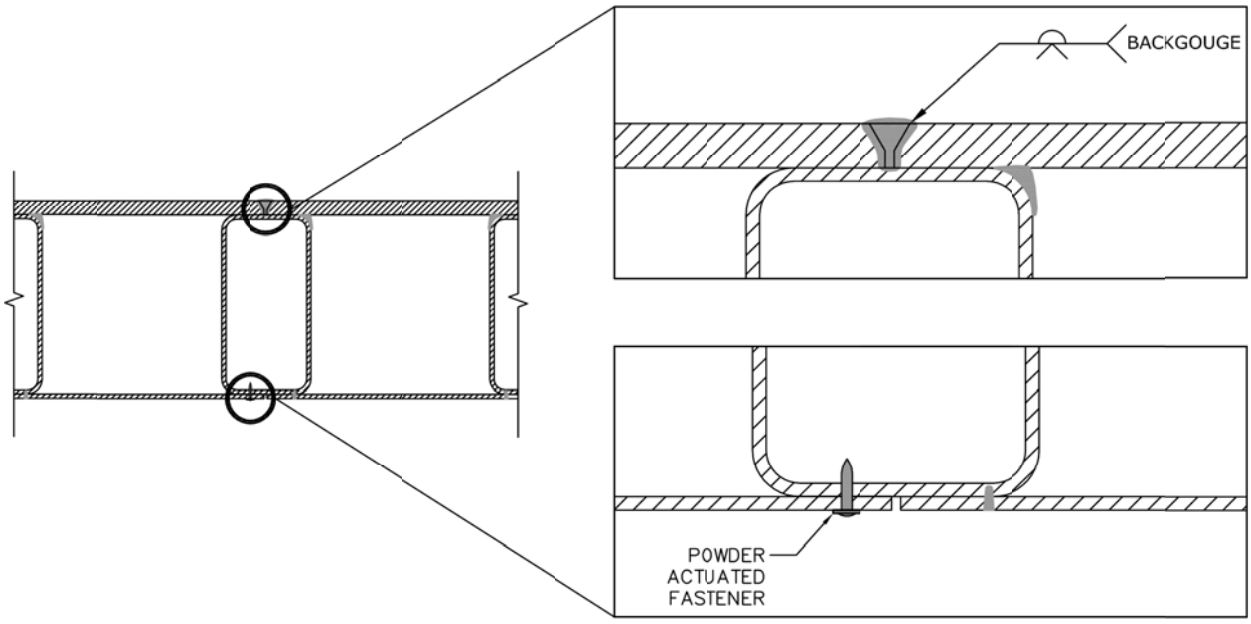

Figure 1–3: Proposed Sandwich Panel Deck Continuity Connection

1.4 PRELIMINARY INVESTIGATION

A simplified structural study of the various panel components and design parameters discussed in the previous section was conducted in order to develop an experimental sandwich panel design. The goal of the investigation was eliminate to strength as main concern for the panel to be used in the experimental study. As a starting point to this analysis, a bridge width of 40ft (3ft overhangs and 8.5ft on center girder spacing) was assumed to depict a typical two lane bridge with a shoulder. Initially, the investigation called for full scale sandwich panel testing. As a cost savings measure to reduce the quantity of steel, a half width sandwich panel was to be continually supported with two 8ft spans and a 4ft overhang. The preliminary investigation was performed using these boundary conditions though the sandwich panel testing fell through.

Provided that strength was the primary concern for this simplified study, the Strength I limit state described in AASHTO 3.4.1 was used for analysis.((AAHSTO), 2010) The sandwich panel was evaluated using a hybrid strip method, further described in the sample calculations provided in Appendix A. The AASHTO LRFD Bridge Design Specifications ((AAHSTO), 2010) and the American Institute of Steel Construction (ASIC) Manual (AISC, 2005) were used to assess the flexure, shear, local instability of the HSS internal stiffening ribs, interface shear in the welded connection between the deck plate and internal stiffening ribs, and local buckling in the bottom plate between rib stiffeners. As a result of the preliminary investigation a $^{5}/_{8}$" deck plate, an HSS 4" X 8" X $^{3}/_{16}$" transverse internal stiffening rib, 12 inch on center rib spacing, and $^{3}/_{16}$" bottom plate were selected. Please refer to Appendix A for all assumptions and sample calculations used in the preliminary investigation of sandwich panel parameters.

1.5 PROJECT OVERVIEW

The following investigation is a baseline study to determine the feasibility of the proposed innovative modular steel sandwich panel bridge deck system. The study is focused on the fatigue performance of the laser stake welded connection between the bottom plate and internal HSS stiffening ribs due to a lack of data and complex detail geometry. Previous studies have shown much promise in the fatigue performance of similar connections to longitudinal core stiffeners. The potential for an infinite fatigue life system was therefore deemed plausible. In the past, localized stress concentrations have been shown lead to the demise of other steel bridge deck alternatives such as orthotropic decks. With this reasoning, the fatigue performance of the conceptualized modular steel sandwich panel bridge deck system was based on a localized wheel load causing a complete stress reversal in the bottom plate similar to that of a Vierendeel Truss.

This localized Vierendeel load effect can be observed by concentrating on a particular HSS internal stiffening rib within the sandwich panel deck system as a truck passes in the longitudinal direction. The critical load case occurs when a truck wheel is directly centered over an internal HSS rib causing positive flexure in the bottom plate and two inflection points located between adjacent internal stiffening ribs. As the truck passes and the wheel relocates to the center of an adjacent HSS stiffening rib, the bottom plate experiences a reversal in flexure to negative bending between inflection points as shown in Figure 1–4.

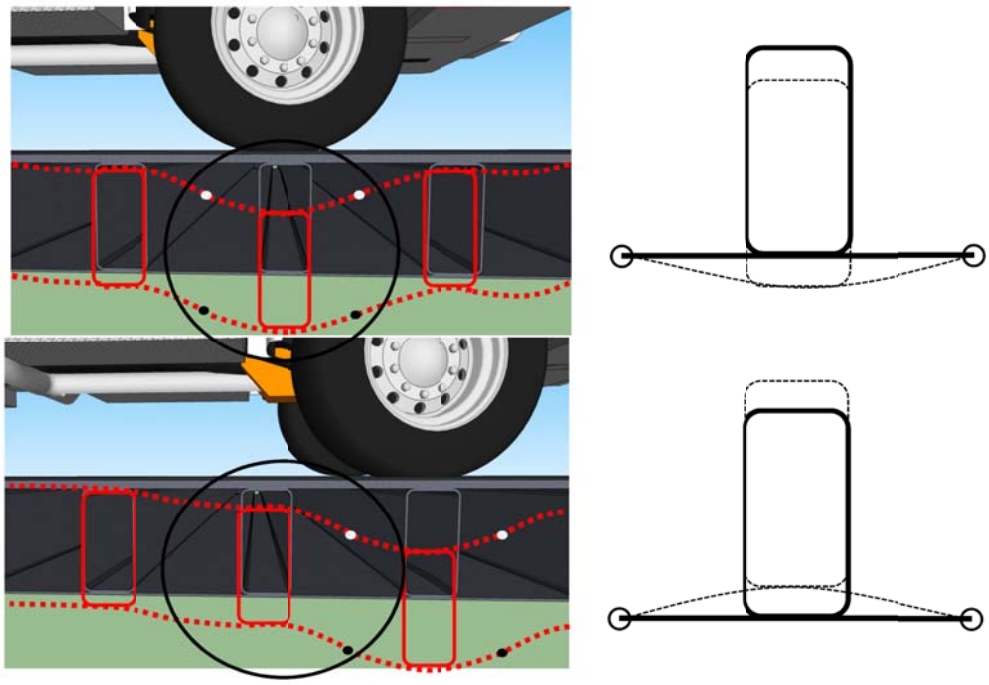

Figure 1–4: Conceptual Localized Vierendeel Load Effect

To fully investigate this localized effect and assess the fatigue performance of the innovative modular steel sandwich panel bridge deck system the following work plan was implemented:

1) Perform a series of fatigue tests on localized steel specimens to evaluate different laser welding processes and perform a fatigue life cycle analysis.
2) Perform static elastic finite element analyses on localized steel test specimens to measure stress concentrations at the laser welded connection.
3) Perform elastic load tests on localized steel specimens to confirm finite element analysis findings.
4) Perform a finite element parametric study on steel sandwich panel modules to investigate fatigue susceptibility and overall structural behavior.

2.1 FIELD IMPLEMENTED SANDWICH PANEL CONCEPTS

2.1.1 LIGHTWEIGHT LASER WELDED CORRUGATED (LASCOR) PANELS

Lightweight LASer welded CORrugated (LASCOR) panels were developed by the United States Navy in the mid 1980's in order to reduce weight of naval structural components, including but not limited to decks, hatch covers, bulkheads, double hull structures, as well as, elevator and hangar bay doors. LASCOR panels are comprised of a metallic corrugated core and face sheets that are joined in a lap configuration by the laser welding process, as shown in Figure 2–1.

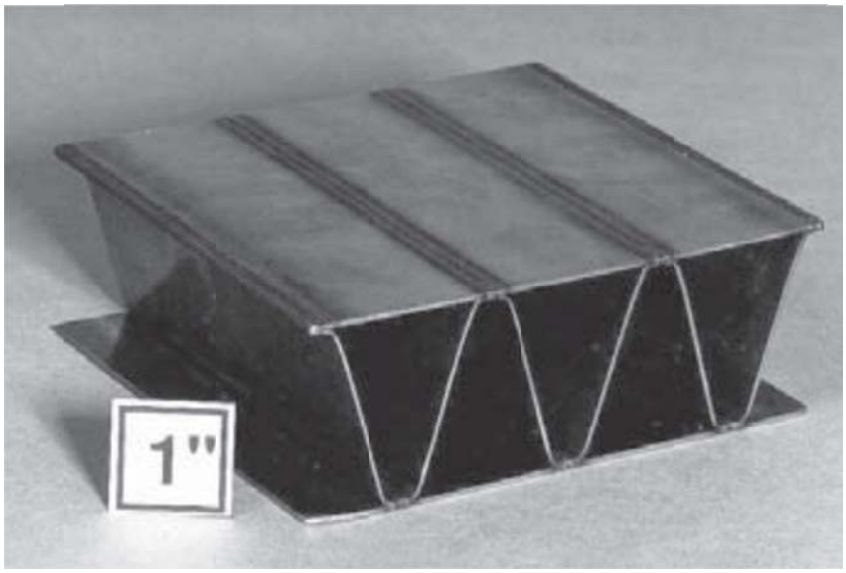

Figure 2–1: Section of Completed LASCOR Panel(Reutzel, 2001)

These panels have demonstrated a 40% weight reduction compared to panels of equal strength and are extremely stiff, not requiring additional reinforcement. Used on the upper decks of naval ships, LASCOR panels have the potential to lower the vessel's vertical center of gravity, increasing the overall ship stability in high seas. In 1994, 2100 sqft of LASCOR panels were

used as antenna platforms on the USS Mt. Whitney resulting in a weight savings of 20,000 lbs. Up until 2001, 30,000 sqft of LASCOR panels have been produced and used in various naval shipbuilding applications.(Reutzel, 2001)

2.1.2 I-CORE SANDWICH PANELS USED IN DREDGING SHIPS

Lower production costs, shorter product delivery times, improved ship performance due to lower structural weight, improved fatigue performance, and enhanced corrosion characteristics are all probable benefits of implementing sandwich panel technology in the design and building of dredging ships. Motivated by these potential advantages, IHC Dredgers launched numerous feasibility studies for the application of using sandwich panels in the structure of dredging ships. These studies showed that total production costs could be reduced in the upwards of 57%, averaging a 25% decrease, instead of using conventional stiffened plates. The reason is due to the high costs of manual fabrication in the shipyard that can be shifted to automated production offsite. Additionally, the research indicated that the structural weight of dredging ships could be lessened by 39%. The only significant disadvantage of utilizing sandwich panels in this application is their low resistance of impact and local concentrated loads.(Kortenoeven, 2008)

As a result of the numerous studies conducted, IHB Dredgers decided to incorporate steel I-Core sandwich panels in the structure of a switch board room in the engine room of a 6000 cubic meter trailing suction hopper dredger. The I-Core panels used were comprised of 2 mm steel face sheets with 4 mm steel plate cores, which were supplied and analyzed by Meyer Werft. (Figure 2–2). In comparison to equivalent conventional stiffened plates, the sandwich panels displayed a moment of inertia that was three times higher, they were 15% less

expensive, but unfortunately were 29% heavier due to design restrictions. A total cost reduction of 34% was attained due to rapid production time. In addition, the number of fatigue sensitive parts, such as cut outs and brackets was reduced by roughly 50%. Given that this was the first attempt to incorporate sandwich panels into the design of dredging ships, IHC Dredgers was convinced about the promising advantages they offered to future ship building applications.(Kortenoeven, 2008)

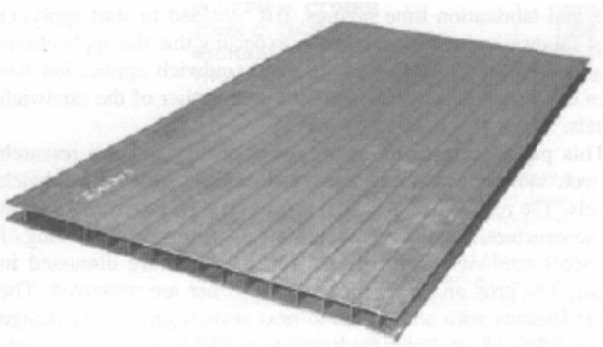

Figure 2–2: I-Core Sandwich Panel(Kortenoeven, 2008)

2.1.3 ALUMINUM BRIDGE DECK PANEL (ALUMADECK) SYSTEM

A proprietary aluminum bridge deck system, known as ALUMADECK was developed in 1997 by the Reynolds Metals Company in Richmond, VA in order to provide a viable alternative to reinforced concrete decks, improving the overall performance of bridge infrastructure. The ALUMADECK panels are comprised of two-voided aluminum extrusions, welded together at top and bottom flanges, as shown in Figure 2–3. These lightweight panels exhibit nearly isotropic behavior, providing excellent load distribution, in addition to possessing superb corrosion resistance. Installed with extrusions parallel to bridge support girders and the flow of traffic, panels act compositely to resist longitudinal bending, as well as, support stresses from panel bending and top deck flange bending between stiffeners resulting from transverse bending between bridge girders.(Dobmeier, 2001)

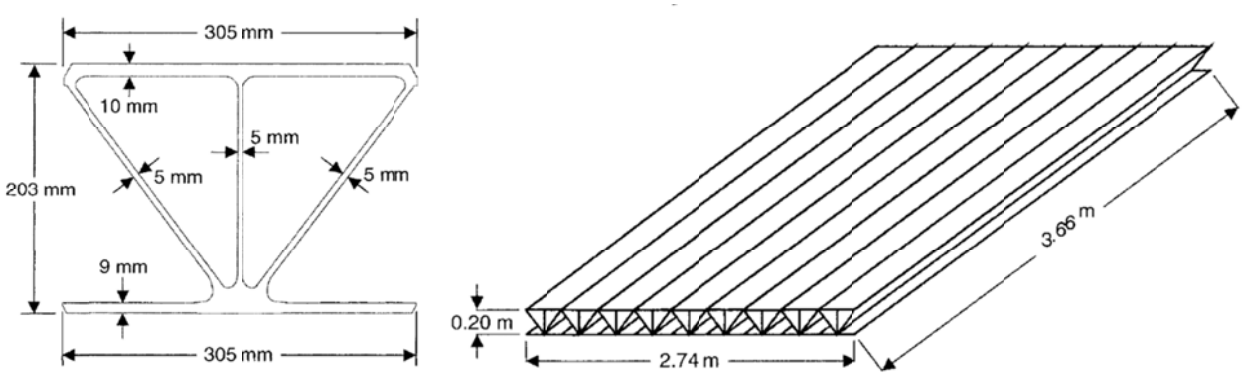

Figure 2–3: Aluminum Extrusion Cross Section and Fabricated Deck Panel(Dobmeier, 2001)

On account of the ALUMADECK's promising characteristics towards extending bridge surface life, dead load reduction, corrosion resistance, and rapid installation; in 1998 VDOT decided to implement this technology in the rehabilitation of a simple span, structurally deficient bridge on U.S. Route 58 in southern Virginia. Prior to the bridge retrofit a study was conducted in order to evaluate the structural response of the aluminum deck panels. Testing was performed at the Turner Fairbank Structural Laboratory on a 9 X 12 ft test panel in two phases. Phase I consisted of elastic static tests to determine the static response. Phase II analyzed the panels when subjected to service-loads and ultimate-load. The testing program established that finite models developed represented the structural response and failure mechanisms accurately.(Dobmeier, 2001)

2.1.4 SANDWICH PLATE SYSTEM (SPS)

Developed by Intelligent Engineering Limited (IE) in collaboration with Elastogran GmbH, the Sandwich Plate System (SPS) consists of steel face plates bonded to a rigid polyurethane core, as shown in Figure 2–4. The steel face plates are designed to resist in-plane flexural and lateral loads; while the less stiff, fully bonded polyurethane core withstands transverse shear loads. These panels are lightweight, exhibiting the potential for dead load

reduction due to their strength in comparison with solutions of equivalent weight. On account of SPS characteristics, they have been implemented as a bridge deck alternative.(Harris, Cousins, Murray and Sotelino, 2008)

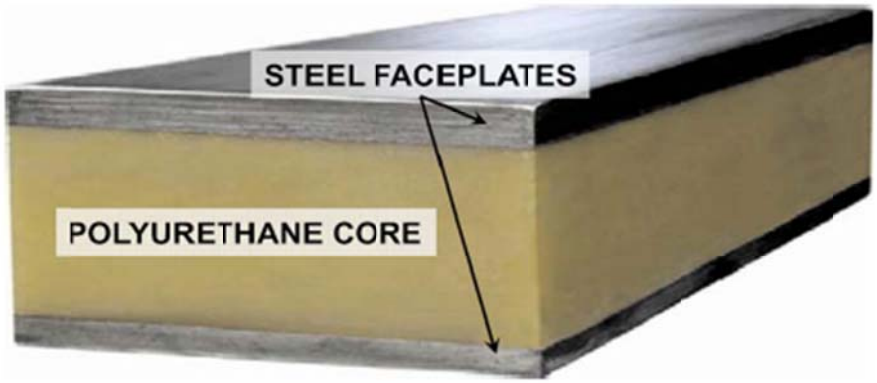

Figure 2–4: Sandwich Plate System (SPS) Configuration(Harris, Cousins, Murray and Sotelino, 2008)

An SPS bridge deck system reduces the overall installation time and consists of a series of panels connected transversely along the span, acting compositely with bridge support girders. In comparison to other bridge panel alternatives, the elimination of local buckling in the deck under direct wheel loads is major beneficial feature of SPS. Other alternatives, such as orthotropic bridge decks, exhibit secondary distortion as a result of an un-braced deck plate, which is not the case with a continuously bonded core used in SPS. The first bridge application of SPS in North America was on the Shenley Bridge in Saint-Martin, Quebec in November 2003. As a result of limited research, a live-load test was conducted to examine lateral load distribution and dynamic load allowance in order to determine if in-service behavior could be estimated by AASHTO or CHBDC design practices. In general, design specifications provided conservative predictions for lateral load distribution and un-conservative estimates of dynamic load allowance. Results obtained from finite element models yielded more accurate estimates of both design parameters.(Harris, Cousins, Murray and Sotelino, 2008)

2.1.5 FIBER-REINFORCED POLYMER COMPOSITE CELLULAR DECK SYSTEMS

Recently, high performance fiber-reinforced polymer (FRP) composite materials have been identified as a new cost effective and durable technology for bridge repair. This was mainly in part due to promising FRP characteristics that include rapid installation, high strength to weight ratio, impressive fatigue performance, and excellent corrosion resistance. In the United States alone, 83 vehicular bridges have implemented FRP bridge decks in new construction or rehabilitation since 1996.(Liu, 2008)

2.1.5.1 Strongwell Tube-and-Deck System

The Strongwell Corporation Tube-and Deck System has been implemented in a variety of bridge applications to date. The deck system is comprised of square glass/polyester pultruded components that are mechanically fastened and bonded together. Tubes sections are ran in the transverse direction, perpendicular to the flow of traffic, which are fixed to face plates with an epoxy adhesive. (Figure 2–5) Generally, FRP decks are fabricated in modular panels optimized for practical transport. Panels are spliced in the field to create a seamless riding surface through a variety of connections and are then installed through the deck plate with mechanical connections to bridge support girders. These systems have proven to be up to 90% lighter than traditional reinforced concrete decks, making them excellent candidates for extending the live load capacity of existing bridges.(Liu, 2008)

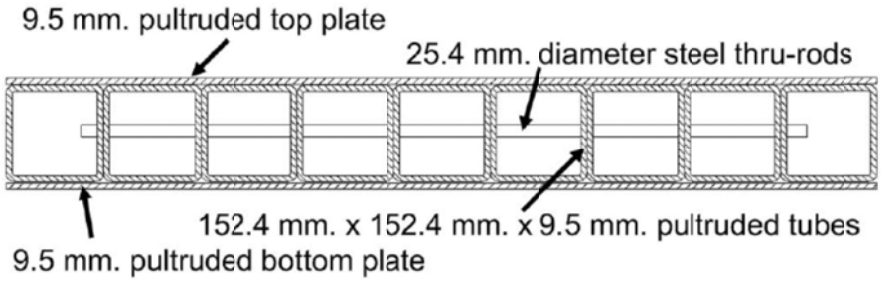

Figure 2–5: Typical Cross Section of the Strongwell Deck System (Liu, 2008)

In order to determine the feasibility of utilizing this system in real world bridge applications, an investigation at Virginia Tech was conducted through static and fatigue tests of a prototype deck section. The testing program studied the flexural strength and stiffness, fatigue resistance, and failure modes of the prototype deck subjected to a simulated wheel load. Results confirmed that the deck section met necessary strength performance, but would be restricted to serviceability limits when compared to pertinent design criteria. Finite element models were in agreement with test results and the decks exhibited linear behavior after 3,000,000 cycles of fatigue testing. (Hayes, 2000)

Further testing of this system was conducted to develop suitable panel to panel connections in order to efficiently transfer bending moments and shear forces throughout deck panels. Connections evolved through four stages of research conducted over 5 years. The fourth stage was conducted in order to implement the Strongwell deck system in the rehabilitation of the historical Hawthorne St. Bridge in Convington, VA. The study analyzed a 33 ft by 22 ft FRP deck, supported by a two-bay mockup of the historical bridge. The experimental testing program investigated connection behavior under service loads, flexural strength and failure modes, fatigue performance of connections, and installation procedures. It was determined that adhesive joints could resist design service loads without cracking and strength was founded to be approximately five times higher than required service loads. In

addition, there were no significant changes in stiffness or strength following fatigue testing.(Liu, 2008)

2.1.5.2 Zellcomp, Inc. FRP Deck System

The Zellcomp, Inc. deck system is comprised of uniquely pultruded glass/fiber shapes that are mechanically connected in the field. As shown in Figure 2–6, bottom plate/T sections are produced using a unique pultrusion dye, that are fastened together at a 2 inch lap joint using stainless steel screws. The assembly is then closed, by joining a ½ inch top plate standard pultruded section via stainless steel screws. A variety of design challenges presented by the severe weather conditions in the Chesapeake Bay, led to the selection of using the Zellcomp deck system on a 55 ft single span bridge on Tangier Island, VA. Limited data on the behavior of this system led to an investigation to study connection performance subjected to service loads, flexural strength and failure mode of connections, fatigue resistance during wheel loading, and viability of transition connection.(Cousins, 2009)

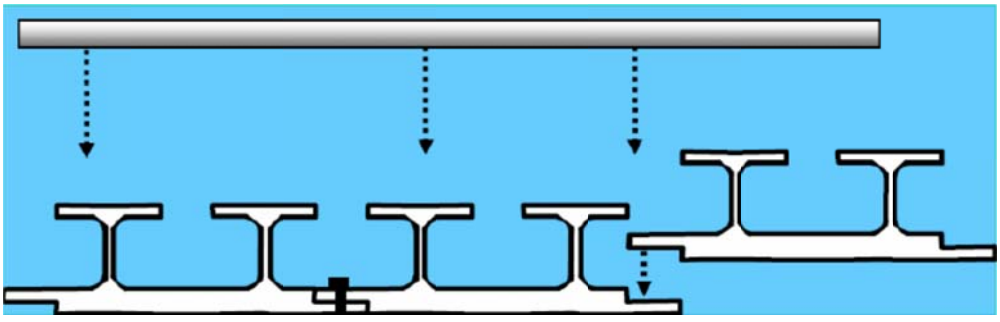

Figure 2–6: Cross Section of the Zellcomp, Inc. FRP Deck (Cousins, 2009)

Testing was performed in two configurations that simulated vital bridge geometry. The first consisted of a one bay mock-up of a 11 X 9 ft flat Zellcomp deck panel to investigate service load, strength, and fatigue limit states. The second test configuration modeled a two bay section of the bridge with a 8 X 17 ft sloped Zellcomp deck panels with a transition connection.

This orientation was aimed at evaluating the construability of the sloped transition joint and the effect of permanent strain in the top plate on the performance of the connection. The test results indicated that the flat deck orientation performed well during the fatigue test, but there was some indication of deterioration of the lap joint after 1 million cycles and loss of stiffness in the system after 2.5 million cycles. On the other hand, the sloped deck geometry was proven to be problematic. The bent lap joint connection was difficult to construct and a permanent gap between the T-sections and top plate existed due to construction tolerances. In addition, numerous screws loosened with several cracking in the sloped deck system during the first 600,000 cycles of load in fatigue testing. Damage in the deck worsened further after the next 400,000 cycles. The study concluded that sloped transitions of the Zellcomp deck system should not exist in the field and that the close inspection of all screw connections be made on a regular basis. It was concluded that the Zellcomp, Inc. deck system was adequate for this particular application due to light traffic it would be subjected to on Tangier Island.(Cousins, 2009)

2.2 ORTHOTROPIC BRIDGE DECKS

Orthotropic bridge decks consist of flat, thick steel plates stiffened by closely spaced longitudinal ribs made up of numerous shapes. Typically longitudinal stiffening ribs are comprised of open (torsionally soft) or closed (torsionally stiff) structural sections. The rigidity of orthogonal floor beams and stiffening ribs are generally unequal, resulting in different elastic behavior in each direction. This orthogonal-anisotropic behavior is reason they are named orthotropic bridge decks.(M.S. Troitsky, 1994) Figure 2–7 illustrates the general components of a standard closed rib orthotropic bridge deck system.

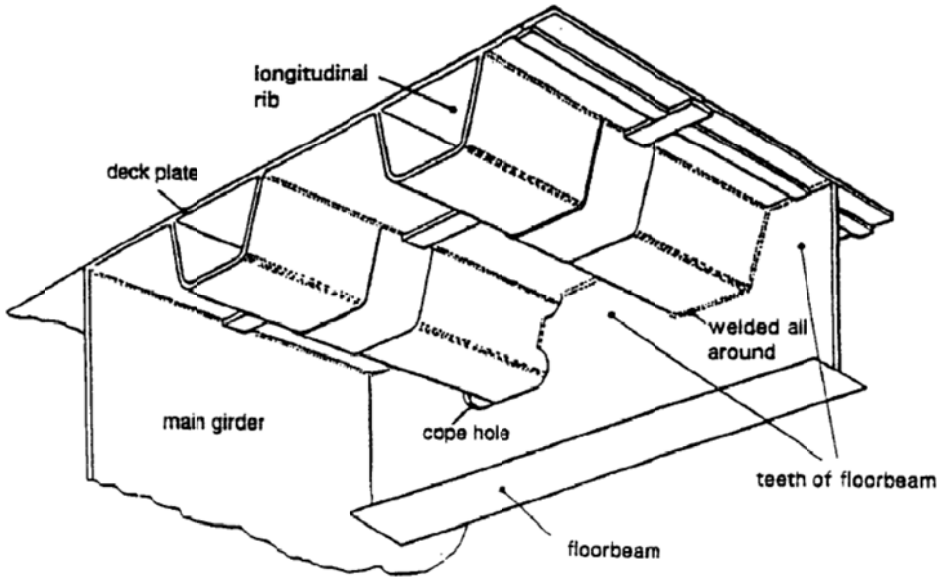

Figure 2–7: Schematic of Orthotropic Deck Components(Wolchuk, 1999)

These decks act as the roadway and behave structurally as the top flange of bridge girders in composite action. For this reason, stiffening ribs are placed longitudinally to support large bending moments in the direction of traffic. Floor beams are normally comprised of steel plates welded together in the shape of an inverted T section as shown in Figure 2–7 and spaced from 4 to 15 feet on center. They are joined to floor beams and supporting girders via welds or high strength bolts.(M.S. Troitsky, 1994)

Typically, decks with closed ribs are preferred for highway bridge applications and decks with open ribs are chosen for railway uses. This is mainly in part due to the closed rib's ability to distribute loads in the transverse direction, resulting in a more efficient and robust structural system. In addition, closed rib decks are lighter, warrant less protective epoxy coating, and require approximately half the overall weld length than an equivalent open rib deck design. However, closed rib decks are much more susceptible to fatigue due to complex detailing and local secondary deformations that are not problematic in open rib deck. Other advantageous characteristics of open rib orthotropic decks are their low

construction depth and absence of unmaintainable closed spaces for water and dirt to accumulate, causing corrosion concerns.(Wolchuk, 1999)

The complexity and overabundance of design considerations for orthotropic bridge decks has led to theoretical design rules and empirical design guides that have been developed over past five decades, with continuing research to improve current specifications. A proper design of orthotropic bridge decks requires great attention to detail, practiced and experienced engineers, research, and testing.(Wolchuk, 2001)

2.2.1 FATIGUE PERFORMANCE OF ORTHOTROPIC BRIDGE DECKS

2.2.1.1 Fatigue Prone Structural Details

Closed rib orthotropic bridge decks are subject to second order and local stress concentrations that make them exposed to fatigue induced failures. Specific problematic structural details have been identified throughout the development of these deck systems. These include the deck plate/rib junction, deck plate at rib intersection with floor beams, deck plate splices, rib splices, and rib floor beam intersections.(Wolchuk, 1999)

The junction where the deck plate meets the rib wall is subject to out of plane bending, making it prone to fatigue. It is classified as a distortion induced fatigue by AASHTO and identified as fatigue categories D and E. Research has shown that this particular detail is highly sensitive to the gap between the deck plate and rib wall prior to welding, lack of penetration, welding method, and weld quality. The nominal stress is taken at the rib wall near the weld toe, but due to a plethora of variables, is not subject a numerical analysis. Instead, fatigue exposure is limited through details to minimize the out of plane bending moment.(Wolchuk, 1999)

The deck plate at rib intersection with floor beams is another area subject to severe stress concentrations and fatigue concerns. The transition where the deck plate meets closed rib, encounters a void that is not supported by the floor T-beam, resulting in localized bending in the deck plate under overhead wheel loads. Initially, this detail was not identified as fatigue prone in the design parameters of closed rib orthotropic decks. It was not recognized until severe deck cracking was discovered in 1997 on a bascule bridge in the Netherlands requiring replacement after only 7 years of service. Thicker deck plates and surfacing have been implemented to alleviate this issue, in addition to placing an internal diaphragm inside closed rib sections.(Wolchuk, 1999)

Deck plate and rib splices are also structural details of concern. Single or double groove butt welds with ceramic backing bars have been accepted for transverse deck plate splices. It has been permitted for longitudinal deck plate splices to be comprised of single groove butt welds with permanent steel backing. Rib splices throughout North America have been traditionally shop welded and field bolted, requiring access holes in the ribs. Whereas, welded field splices are predominantly used in Europe and Asia.(Wolchuk, 1999)

Closed rib and floor beam intersections have been the structural detail most problematic in design, due to complex stress geometry in the floor beam webs and rib walls. The floor beam web is subjected to in-plane axial and shear stress from floor beam teeth, as well as, out-of-plane flexural stresses, due to local distortions, caused by longitudinal rib rotation, resulting from unsymmetrical loading. The rib walls encounter in-plane axial stresses, due to composite action with bridge girders to resist longitudinal flexure, while simultaneously exposed to out-of-plane local flexural stresses caused by

shear deformations of the floor beam teeth. Three viable solutions have been proposed in the past that include continuous ribs passing through floor beam cutouts with coped holes, continuous ribs passing through floor beam cutouts welded around the rib perimeter, and discontinuous ribs fitted between floor beams.(Wolchuk, 1999)

2.2.1.2 Full Scale Laboratory Testing for Fatigue Performance of Steel Orthotropic Decks

The concrete slab roadways of the Williamsburg and Bronx-Whitestone bridges in New York City were replaced with steel orthotropic bridge deck systems. Prior to the final design and production of replacement panels, full scale fatigue tests were conducted to analyze the structural integrity, fatigue performance, and validate finite element models used for design. Testing was conducted at Lehigh University by Paul A. Tsakopoulos and John W. Fisher in a series of two testing programs that targeted the replacement deck design of the Williamsburg and Whitestone bridges conducted from 1995 to 1998 and 2001 to 2002 respectively.(Tsakopoulos, 2005)

The first testing program analyzed a section modeled after the two lane cantilevered roadway of the Williamsburg Bridge that consisted of 3 spans with an overall length of 18.9 m, width of 6.4 m, supported by four floor beams spaced at 6.1 m. The testing was carried out in two phases. Phase I consisted of static and dynamic testing with the equivalent loading of two HS20 design trucks with 15% impact. Phase II involved a detailed study to analyze the fatigue resistance of two different welding schemes for the rib to floor beam connections, a detail that has been previously identified to be prone to fatigue cracking. The loading scheme described in Phase I was first applied, following was a more extreme load case with the equivalent of three HS20 design trucks to induce

cracking and determine the effectiveness of crack repair methods.(Tsakopoulos, 2005)

A test deck modeled after a half width section of the Bronx Whitestone Bridge consisting of two spans with an overall length of 14.5 m, width of 10.4 m; supported by three floor beams spaced at 6 m was investigated in the second testing program. This testing was also performed in two phases. Refined designs of floor beam to rib connections from information gathered from the first testing program were analyzed in this study, which involved internal stiffeners and complete penetration welds with back to back fillet weld reinforcement. The first phase of testing used floor actuators to simulate loads from surfacing that was not included in test specimens, and the equvalient loading of three HS15 fatigue trucks with 15% impact. Phase II was aimed at increasing the potential for fatigue cracking. Thus, an extreme load case of the equivalent of four HS15 fatigue trucks with 15% impact was applied.(Tsakopoulos, 2005)

Previously unknown, poorly defined, or missing knowledge of crucial design parameters for steel orthotropic decks were discovered through these research programs. In addition, valuable information on fatigue performance of these systems was in agreement with preliminary finite element analyses. Critical floor beam to rib connections were determined to be dominated by the in-plane stress component for the stress cycle to develop cracking. It was determined by increasing the thickness of floor beam webs by only 5 mm that the in-plane stresses would be greatly reduced, alleviating the concern for fatigue. Rib and deck plates were identified as areas with low stress concentrations not conducive to fatigue, even with some out-of-plane distortion. Rib and deck plate splices were also proven to have small stress concentrations not problematic for fatigue, even at transverse weld details identified in AASHTO as fatigue category E. Rib and deck plate

connections were considered adequate connections for deck replacement, even though 30 % of welds did not meet the 80% penetration specified.(Tsakopoulos, 2005)

2.2.2 SURFACING OF ORTHOTROPIC DECKS

The choice of wearing surface is a primary concern in the design of orthotropic bridge decks. Not only is the surfacing integral to bridge serviceability, but has been proven to substantially reduce the flexural stresses in the deck plate due to composite action. The overall design and selection of the surfacing material has been problematic since it is one of the main contributors to detrimental malfunctions of orthotropic bridge deck systems, surface cracking and de-bonding. This is due to the composite action with the thin flexible deck plate and surfacing that cause stresses and strains in the surfacing material. These negative outcomes adversely affect bridge serviceability, increase maintenance costs, and reduce the ability for these decks to perform as a viable cost effective alternative.(Wolchuk, 1999)

Surface cracking and de-bonding have been shown to follow the pattern of rib stiffeners, indicating that surface wear and rib flexibility are related. Differential rib deflection and local bending moments from directly imposed wheel loads have therefore been targeted as leading causes of surface deterioration. An approach to limit these effects has been suggested by the German Federal Ministry of Transport to simply increase the deck plate thickness, but is undesirable due to the increase in dead load. Surfacing thickness is another contributor to wearing surface performance. Thicker wearing surfaces have been proven to reduce flexural stresses up to 95%, but unfortunately the stress is redistributed to the surfacing material making it susceptible to

deterioration. For this reason thin elastic pavements are preferred to extend the surfacing life and reduce the probability of cracking.(Wolchuk, 1999)

Wearing surfaces used with orthotropic bridge decks has commonly been asphalt concrete and asphalt mastic for their performance and ability to meet critical design criteria. (M.S. Troitsky, 1994) Other surfacing materials that have shown promise include polyurethane and epoxy polymers. In 1992 the Poplar Street Bridge in St. Louis, Missouri was resurfaced with a thin epoxy polymer surfacing developed at the University of Missouri that has performed very well under heavy traffic.(Wolchuk, 1999)

2.2.3 HIGHWAY BRIDGE APPLICATIONS AND USAGE

Generally speaking, orthotropic bridge decks are not a viable economic alternative due to the high costs of required fabrication and welding. Under special circumstances, such as the re-decking of an existing bridge under traffic with modular deck units, long spans approaching or greater than 1000 feet, or continuous low level river crossings in metropolitan areas; orthotropic bridge decks have been used cost-effectively due to their dead load reduction and rapid construction characteristics. Another design scenario that orthotropic bridge decks prevail is when structural depth is limited. Box girders used to support orthotropic bridge decks can allow for spans up to twice those achieved with a traditional reinforced concrete deck.(M.S. Troitsky, 1994)

In real world applications, closed rib orthotropic bridge deck systems have been used successfully in the design of record breaking bridge spans throughout the globe. Some of which include the Akashi-Kaikyo suspension bridge in Japan spanning 1991 m, the Great Belt East suspension bridge in Denmark with a 1624 m span, Tatara cable stayed bridge in

Japan spanning 890 m, and the cable stayed Normandy Bridge in France spanning 856 m.(Wolchuk, 1999)

2.2.3.1 Re-decking of Bridges

Failed bridge decks account for two thirds of bridge deficiencies. Bridge deck replacement is deemed necessary when yearly maintenance costs outweigh yearly life cycle costs of a new deck. A suitable bridge deck replacement should possess the following characteristics, strength and rigidity, lightweight, deck resisting longitudinal flexure in composite action, limited joints, rapid installation, durability, and long term economy. Steel orthotropic bridge decks are strong candidates for bridge deck replacement, especially in cable supported long spans, since they satisfy all necessary requirements.(Wolchuk, 2001)

In addition to the Williamsburg Bridge and Bronx-Whitestone Bridge in New York mentioned previously, completed re-decking projects in North America from 1975 to 1993 include the following bridges; Lions Gate, George Washington, Golden Gate, Throgs Neck Viaduct, Benjamin Franklin, and Champlain. They have exhibited dead load reduction ranging from 24 to 46 psf with deck weights ranging from 61 to 89 psf, coming in at costs from $41 to $110 per sqft of roadway. Early re-decking projects of orthotropic bridge decks did not attempt to take advantage of using the decks as a participating member of main bridge girders. Thus, all existing expansion joints were retained that led to fatigue problems, required seismic retrofitting, and surface deterioration at joints. The re-decking projects that used shear connectors for interaction forces between the new deck and main bridge girders eliminated all deck joints. The continuous orthotropic decks increased the

overall structural rigidity of the bridges and enhanced their seismic performance. Thus, AASHTO LRFD specifications specifically advise against the use of orthotropic bridge decks not acting compositely with the supporting framing. The erection method is another important aspect of re-decking that can greatly influence the overall cost of the project. Less intrusive erection methods that minimize lane closure can result in a more cost effective solution.(Wolchuk, 2001)

2.3 LASER WELDING

2.3.1 A BRIEF HISTORY AND INTRODUCTION TO MODERN LASERS

In 1917 Albert Einstein developed theories exploring the concept of stimulated emission which served as the benchmark for the development of the laser, an acronym for Light Amplification by Stimulated Emission of Radiation. It was not until 1960 until the first laser was built and demonstrated using a ruby crystal by Theodore Maiman, based upon a publication in 1958 by Arthur Schawlow and Charles Townes.(Olsen, 2009)

The Carbon Dioxide (CO_2) laser exhibited in 1964 by C.K.N. Patel, the Neodymium-Doped Yttrium Aluminium Garnet (Nd:YAG) laser described in 1964 by J.E. Geusic, H.M. Marcos, and L.G. Van Uitert, and the fiber laser demonstrated by Elias Snitzer in 1961 form the three modern lasers used today.(Olsen, 2009) A laser beam is monochromatic light that radiates with a characteristic wavelength dependent on the beam source; CO_2, Nd:YAG, and fiber laser characteristic wavelengths are 10.6 μm, 1,064 nm, and 1070 nm respectively. Depending on the beam source, the laser can radiate steadily to provide a continuous wave (CW) or emit very short pulses. The light beam is delivered without loss through a mirror-and-lens system or light cables depending upon the

wavelength of the beam. Absorption and reflection characteristics of the beam are contingent on the material itself and beam wavelength. (Schwartz, 2011)

Other than output power, delivery method, and beam quality there are few discrepancies between each laser technology. Undoubtedly the most powerful is the CO_2 laser, available to industry with output power up to 20 kW, with research facilities systems capable of 150 kW. However, due its longer characteristic wavelength, far into infrared the region, the beam has to be transmitted with hard optics mirror-lens systems, which are complex and require high levels of maintenance. On the other hand, Nd:YAG lasers are commercially available with output power up to 8 kW and can be transmitted through fiber optics due to their shorter wavelengths, which require much less maintenance and ease integration into mechanized automated systems. Technological advancement in recent years has made fiber lasers available at output powers up to 10 kW commercially and 50 kW in research facilities. These lasers can also be delivered through fiber optic cable, but due to poor beam quality, power per unit area is typically decreased. (Olsen, 2009)

2.3.2 LASER BEAM WELDING (LBW)

Autogenous laser beam welding is typically classified into two modes, conduction and keyhole mode welding. Conduction mode welding is the process in which the heat provided by the laser beam is controlled only to allow melting, while limiting evaporation with the beam out of focus at low irradiance. More commonly, keyhole mode welding is performed at high irradiance which breaks the bonds between atoms causing vaporization. This high temperature vapor and plasma expands, resulting in a recoil force that pushes

the molten metal to form a cavity or keyhole.(Olsen, 2009)

2.3.2.1 Process

In order to perform high quality laser welds a variety of components and considerations are required on a consistent basis, which can be broken down into two categories; (1) laser, beam, and optics, and (2) process gases and auxiliary process equipment.(Olsen, 2009)

As mentioned previously there are three types of lasers used predominantly for welding; CO_2, Nd:YAG, and fiber. CO_2 lasers operate far-infrared requiring a complex mirror-lens system for transmission and are absorbed more readily by welding plasma resulting in the need for shield gases and special nozzles for plasma suppression. Nd:YAG and fiber lasers operate near infrared wavelengths allowing them to be delivered through fiber optics and are less absorbed in metals. All lasers can be operated in a CW or pulsed mode allowing further control of weld parameters. Optics required for laser transmission to the focusing optics, whether it is a complex mirror-lens system for CO_2 lasers or fiber optic cable for Nd:YAG and fiber lasers, greatly influences the ability to produce a small spot to reach the required irradiance of 10^6 W cm^{-2}. Once the beam is delivered to the weld location, focusing optics are used to collimate and focus the beam to the desired shape and size. This equipment is usually very expensive and tailored to the specific weld application. In order to increase the efficiency of the focal optic, a coating of anti-reflective material is typically applied. To prevent damage to this expensive focal equipment from spatter or fumes, it is customary that a protective cover lens is placed between the welding area and focus optics.(Olsen, 2009)

In order to alleviate potential problems in the laser welding process, various gases are utilized in different ways. Since the CO_2 laser beam is strongly absorbed from plasma emission, high ionization potential gases such as Helium are fed at high velocities to deter plasma from the beam path. High brightness lasers are prone to spatter and additional gas may be used to serve as focal lens protection. Lastly, dependent on material, shielding gas such as Argon is used to prevent oxidation of the welding surface at high temperatures.

2.3.2.2 Optimization

The travel speed and power are selected to achieve the desired weld penetration, but are affected by many of the process variables and material properties of the work piece. Therefore, there are no definitive travel speed and power parameters that relate to weld penetration and quality. Instead these input selections are very specific to the weld application at hand. Clever manipulation of pulse parameters can help reduce formation of porosity and reduce capital costs to weld deeper and faster than CW lasers operating at the same power.(Olsen, 2009) Beam quality of a laser affects four crucial parameters associated with weld optimization that include focus diameter, depth of focus, working distance, and raw beam diameter. Smaller focus spot diameter allows for a higher power density applied on a work piece to facilitate deeper weld penetration. Greater working distance between processing optics and the work piece allows for remote welding and versatility with weld components. Small optics diameter enables a more compact design of processing optics, aiding in the flexibility for integrated robot-aided manufacturing processes. Finding the optimum focus spot is specific to each individual application, but is vital to obtaining a high quality weld.(Schwartz, 2011)

2.3.2.3 Advantages

There are many potential advantages that LBW offers in comparison to conventional arc welding technologies. LBW results in deep and slim zones of fusion with a smaller heat affected zone (HAZ), welding versatility for joint and material combinations, reduction of micro cracks, decreased chemical changes, and fine-grained joints with better mechanical properties are all beneficial material characteristics of LBW. In addition, small thermal distortion, accurately reproducible welds, higher welding speeds, higher degree of automation, higher reliability, larger flexibility, short warm-up and cooling times, and real time quality control are the construction and manufacturing advantages of LBW.(Schwartz, 2011)

2.3.2.4 Disadvantages

The major disadvantage to LBW in comparison to conventional arc welding is the considerably higher initial capital investment. Joint fit up is extremely is critical and the root gap must be limited to ensure sufficient weld quality. Fast cooling rates with high speed welding can lead to an increase in micro pores and result in centerline cracking. In addition, there are safety issues making it nearly impossible to use this technology in portable or manual operations. (Olsen, 2009)

2.3.3 HYBRID LASER ARC WELDING (HLAW)

The combination of laser welding with any other welding technology is called a hybrid welding process.(Schwartz, 2011) Originally conceptualized and experimented with in the 1970's by Steen and Ebbo, the combination of laser light and arc welding harnesses the benefits of laser welding, while compensating for the weaknesses with

increased stability due to the addition of an traditional welding arc. As a result of the first group of HLAW welds performed using a 2 kW CO_2 laser and TIG arc in 1979, there were many promising effects that sparked further development from many other researchers and welding engineers to bring HLAW where it is today. The blend of the HLAW process allows for deeper penetration with higher welding speeds, wider gap tolerances, better weld surface aesthetics, and reduced weld defects.(Olsen, 2009)

2.3.3.1 Process

The HLAW welding process consists of at least one primary heat source (laser type) and one secondary heat source (electric arc) that can be combined in variety of geometrical patterns. The primary heat source allows for deep penetration, whereas the secondary heat source serves many functions to improve the stability, reliability, and efficiency of the welding process. Other than output power and beam quality, the main criterion for the selection of the laser to act as the primary heat source is based upon the characteristic wavelength, which can restrict the choice of shielding gas to be used. The secondary heat source is typically selected based upon the welding problem at hand, either arcs with consumable electrodes (MIG) or arcs with non-consumable electrodes (TIG) can be utilized. Consumable electrodes are typically chosen if the welding configuration requires filler material to fill gaps between weld components, otherwise it is common that arcs with non-consumable electrodes are selected.(Olsen, 2009)

In a small area surrounding the weld location during the HLAW process, all states of matter coexists and coalesce, complicating the interaction between the laser and welding arc. A keyhole is formed in the molten pool of base metal with the laser beam of high

power density, while simultaneously a plume (light emission), vapors, ultrafine particles or fume, and spatters are formed. Additional plasma and droplets from the welding arc coincide above the molten pool of metal. For a better understanding please refer to Figure 2–8 for a basic visualization of the HLAW process.(Olsen, 2009)

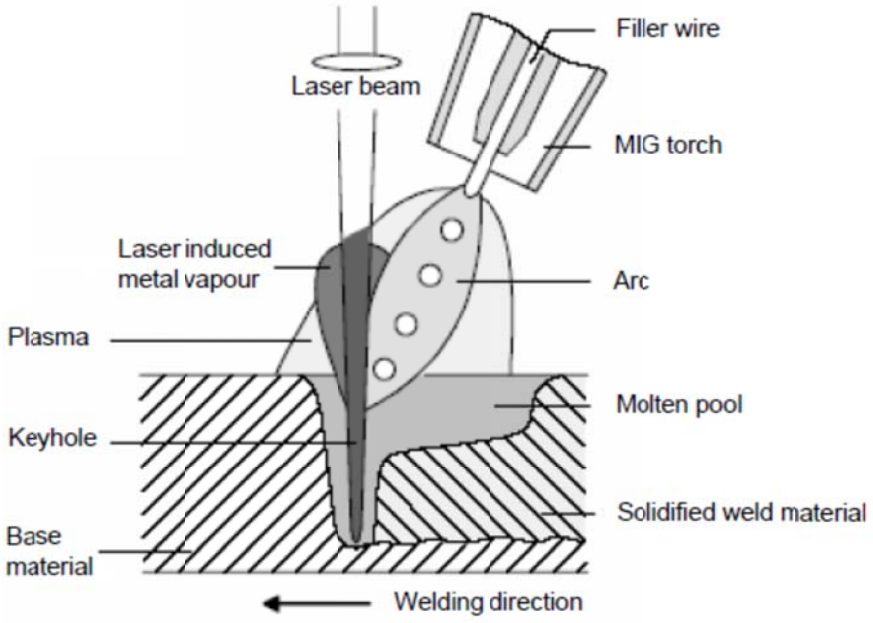

Figure 2–8: A Simple Schematic of the Hybrid Laser Arc Welding Process ((DNV), 2006)

2.3.3.2 Optimization

This interaction between the laser beam and electrode arc is highly dependent on the type of laser, electrode arc, shielding gas, distance from the electrode to work piece, distance from the laser irradiation spot and electrode, and electrode inclination. Specification of process combinations and parameters is regarded as an extremely convoluted task that is highly dependent on the welding challenge at hand.(Olsen, 2009) In April 2006, Det Norske and Veritas published guidelines for the "Qualifications and Approval of Hybrid Laser Arc Welding in Shipbuilding," which identifies key parameters, tolerance windows, test requirements, monitoring specifications, and safety procedures for

the HLAW process.

Unlike the guidelines for LBW, no special restrictions with regards to chemical composition and material properties are required for the HLAW process. Approved steel thickness for HLAW are 4 mm minimum and 30 mm maximum for butt welds, and 4 mm minimum and 15 mm maximum for fillet welds. It must be demonstrated prior to welding approval that a stable and repeatable welding process is developed with well documented welding parameters. Non-destructive testing should be carried out during the HLAW process that includes visual, radiographic or ultrasonic, and surface crack detection testing. Destructive testing should also be conducted which include tensile, bend, Charpy V-notch, macro section, and hardness testing. As surface preparation, the primer should be removed from weld specimens prior to the welding process to avoid pores or spatters that cause the process to become unstable. Some welding configurations require tack welds that are commonly performed with LBW to tack so small that it does not disturb the HLAW process.((DNV), 2006)

It is important that all welding equipment is in good condition for acceptable weld quality. Thus, continuous checks of mechanical parts and conventional equipment related to the HLAW process are essential. Characteristic laser beam parameters should also be measured periodically to ensure that they are kept within defined limits. All welding parameters should be stored in a data base and transferred automatically to the machine control. This allows for weld defects to be traced back to the welding parameter used and optimized in future weld configurations.((DNV), 2006)

2.3.3.3 Advantages

In comparison to conventional arc welding, the HLAW process possesses all the advantages of LBW and more. High root opening bridging ability in the case of a gap existing for a short period, wider and deeper penetration, a broader range of applications, lower investment costs by reduced laser power requirements, and increased toughness are all benefits the hybrid laser welding process offers that autogenous laser welding does not. In addition, the combination of a laser beam and welding arc forms a larger molten pool of metal, which allows for components with larger root openings to be welded. Also, higher welding speeds, process stabilization due to laser and arc interaction, slower cooling rates due to heat via the welding arc reduces hardness peaks, and neutralization of tolerances are all beneficial components of the HLAW welding process.(Schwartz, 2011)

2.3.3.4 Disadvantages

The biggest disadvantage to HLAW process is the selection of welding parameters. It requires a well trained professional to optimize these constraints in order to obtain a weld of suitable quality for the application at hand. Heat sources, shielding gas, and welding speed are only a few parameters that greatly influence the performance of the weld.

2.3.4 BENEFICIAL PRE-STRESS IN AUTOGENOUS LASER WELDS

Laser welding has been proven to reduce residual stresses induced upon the material, as well as provide a beneficial pre-stress to aid in fatigue resistance and prevent other failure modes. In 2006, a paper was published by Stephen Copley, Peter Vigna, and Eduard Ventsel that confirmed the development of beneficial pre-stress by reporting thermally induced strains at various steps of the autogenous laser welding process.(Copley,

2006)

During the development of LASCELL, a lightweight, stiff, strong, metallic, square cellular sandwich panel to act as a new watertight door for surface ships, the beneficial pre-stress from laser welding was recognized. LASCELL sandwich panel doors are comprised of orthogonal notched stiffeners, mechanically interlocked that are attached to face sheets by laser stake welds. It was observed that panels tested in four-point bending failed by local buckling in face sheets at 5,500 lbs, about 60% above the theoretically predicted load of 3,470 lbs. This was attributed to the thermally induced residual stresses developed during the laser welding of face sheets to stiffeners.(Copley, 2006)

Thermally induced residual strains and stresses are a result of the fast speed of the laser welding process. The LASCELL doors were welded at 150 inches per minute which limits heat flow to the surrounding region. Thus, the solid that forms from melt is surrounded by material much cooler that shrinks less that the just-solidified melt. This generates tension stresses perpendicular to the welding direction, parallel to the plane of face sheets. In order to further document and study these effects strain gages were placed on the exterior surface of the face sheets to monitor strains during the laser welding process. The results of strain measurements from this study confirmed the development of beneficial pre-stress in autogenous laser welds, but further investigation was suggested to refine strain measurement techniques.(Copley, 2006)

2.3.5 LASER WELDING IN STEEL SANDWICH PANEL BRIDGE DECKS

Until recently the majority of laser welding technology and development has been associated with shipbuilding throughout the globe.(Abbott, 2007) Modern developments

over the past decade enabled laser welding to be employed in the commercial sector, capable of penetrating steel thicknesses associated with bridge deck components. The emergence of this equipment allows for the potential of steel sandwich panel bridge decks to mass produced and act as an economic alternative.

There are many projected advantages laser welding offers to bridge deck fabrication and sustainability. Laser welding provides an extremely robust and environmentally resistant method to connect steel plates to the stiffened core components. Unlike other proprietary panel bridge deck systems that rely on fastening methods, laser welding provides continuous connections resulting in a redundant structural system. In addition welds can be performed at speeds up to 10 times that of conventional welding, resulting in less manufacturing time. Another benefit is the push for the ability of these welds to be automated using computer aided drawing and manufacturer software that enables process control and quality assurance. (Abbott, 2007)

2.4 RELEVANT RESEARCH

"Fatigue Performance of Laser-Welded Steel Bridge Decks" (Bright and Smith, 2004)

Due to the emergence of laser welding technology capable of penetrating steel plate thicknesses suitable for bridge deck use, Bright and Smith investigated a laser welded sandwich steel panel concept to challenge orthotropic and concrete steel grid bridge decks. Their panel was comprised of a 12 to 14mm (9/16 to 15/32 in.) top plate and a 8mm (5/16 in.) bottom plate, laser welded via autogenous stake welds to an IPE 240 (W10x15 –W10X22) I-section core running parallel to traffic.

A stress analysis of the deck using three-dimensional finite elements, assuming that the

top and bottom plates were fully bonded to the I-beam core flanges yielded two cases that were of concern to cause fatigue cracking. The panel was subjected to a double tire wheel load directly over the web of an I-beam, which identified the first concern for fatigue at the largest stress concentration founded where the top plate met the core I-beam flange. Secondly a stress reversal was recognized in web bending of the I-beam that occurred from the double tire wheel load applied to an adjacent I-beam. Two experimental fatigue tests were conducted to model these loading scenarios, which were called the "deck bending" and "joggle" tests respectively.

Fatigue test specimens were comprised of three different laser weld configurations for the plate I-beam flange connections, which consisted of two linear stake welds per flange, four linear stake welds per flange, and a sinusoidal stake weld per flange. Test specimens were extracted from 900mm (35-7/16 in.) long welded "beams." Weld quality at the beam's ends was poor due to "run-on" and "run-off" of the laser. Therefore a 45mm (1-3/4 in.) length was removed from each end of the beam resulting in a total length of 810mm (31-7/8 in.), which was divided into three 270mm (10-5/8 in.) equal sections. Each of the three sections was then cut along mid depth of the I-section generating a total of six specimens from each fabricated "beam."

The "deck bending" test simulated bending in the top plate and upper flange of the I-beam from a critical load case to study fatigue performance of the connection. The test specimens were inverted and supported by a pair of cylindrical supports 180mm on center so that 90mm separated either roller from the I-beam web centerline. Each specimen was then loaded axially through I-beam web sinusoidally from a lower compressive load of 10kN (2,250 lbs) to stabilize the specimen, to a maximum compressive load of 163kN (36,643 lbs). The stress distribution used to generate the S-N curve was derived from a localized finite element model of

the test specimen that simulated contact in order to provide conservative fatigue data. The first bending test was subjected to blocks of cyclic loading with varying amplitude until there was visible failure, which initiated at the edge of the laser weld at the top plate and flange interface and propagated at a 45° angle from the horizontal into the stake weld. Failure for all bending tests was defined as when fatigue cracks first appeared at both ends of any individual laser weld. It was observed that test specimens were inclined to failure across the weld interface. Test data was then compared to that published in BS 54001 for all weld configurations, but none of the fitted curves were parallel to the BS 5400 curves which was possible due to insufficient data.

The "joggle" test was intended to simulate bending forces at the top and bottom of each web to determine their effect on stake weld fatigue. The bending stresses in the web are subject to stress reversal based on the location of the truck wheel, which causes an "S-shape" deformation with an inflection point approximately a mid-height of the web. The test was created by considering the web of each test specimen as short cantilever loaded by horizontal shear force. A unique testing frame was created that secured each test specimen vertically by a line of bolts that offset the specimen 4mm (5/32 in.) from the frame via shims so that they were not in contact initially. The specimen was then loaded by a hydraulic ram connecting rod bolted through the I-beam web allowing free rotation. The connecting rod was strain gauged to act a load cell and detect excessive deformation to determine failure. Unlike the specimens in the "deck bending" test, these test specimen lengths varied from 135mm (5-5/16 in.) to 190mm (7-1/2 in.) to reduce alternating load from the actuator. The "joggle" tests resulted in four possible locations of fatigue failure, demonstrating the complexity of this failure and unknown stake weld fatigue in this mode. The first test was carried out in blocks of increasing load until failure occurred at the highest stress concentration in the web root fillet. The majority of failures

occurred in the parent metal of the I-beam web and the simple stress range parameter was not appropriate as it would be for welds. The equivalent stress parameter was therefore calculated as the tensile stress range plus 60 % of the compressive stress range, resulting in 80% of the actual stress range conducted at zero mean stress. Overall these tests provided no data fatigue performance of the welds and no conclusions could be drawn on weld survival.

The overall fatigue performance of the conceptual sandwich panel proposed in this paper was proven to be very good, satisfying the overall objective of the study to minimize probability fatigue failures. The "deck bending" test determined that the best weld configuration was that with two linear welds per flange, whereas the sinusoidal weld and four linear welds per flange configurations were inferior. The "joggle" test configuration identified the robustness of the sandwich panel in that the fatigue occurred in the plain metal of the web at the root fillet. In addition there are also many other beneficial factors in comparison to orthotropic bridge decks that make this concept a suitable bridge deck alternative.

"A New Design for Steel Bridge Decks Using Laser Fabrication" (Bright, 2007)

As a follow up to their previous study on the fatigue performance of laser welded bridge decks in 2004, Bright and Smith provide an in depth comparison of laser welded fabricated bridge decks to conventional orthotropic bridge decks. The study identifies orthotropic bridge decks as an 'option of last resort' due to the manufacturing and operational problems associated with their use. The capital cost of an orthotropic bridge deck system is generally four times greater than an equivalent reinforced concrete deck due to high fabrication costs. In addition, many associated structural details are prone to fatigue cracking that can require difficult and

expensive in situ repairs. Another area of concern in orthotropic decks is surface deterioration that has been directly related to deck flexibility.

An ideal bridge deck would be exhibit nearly isotropic behavior to distribute wheel loads in both longitudinal and transverse directions, decreasing the probability of stress concentrations. Current state of the art steel bridge decks accepted by governing bodies are limited to specific geometric profiles due to restrictions of conventional welding practices. Also, current technology makes it uneconomical and impractical to fabricate panels with equivalent stiffness in orthogonal directions. Adding a continuous plate along the underside of typical steel bridge decks, enclosing the deck section, which is can be referred to as a "sandwich panel," provides the deck with amplified uniform load distribution and torsional stiffness. The overall structural performance would be improved by the downward shift of the neutral axis, enhancing longitudinal bending efficiency and transverse load distribution.

Incorporating laser welding in steel deck fabrication allows for the enclosed panel profile. Stiffening core elements are required to support heavy localized loads and minimize cost. For these reason hot rolled sections are preferred, especially I-sections to meet fit up tolerance necessary for suitable laser welding quality. Preliminary fatigue testing indicates considerable fatigue durability in comparison to similar joints used in conventional orthotropic bridge decks. Sandwich panel steel bridge decks are an attractive proposition for mass production, leading to economic viability. Fast welding speeds demonstrated in the fabrication of prototype deck panels was also promising to a cost effective alternative. A significant downside to the fabrication of the prototype panels was the required output power of the laser used. In order to obtain sufficient weld penetration, a 20 kW CO2 laser was needed. Unfortunately, industrial lasers operate at 10% efficiency, thus requiring a 200 kW laser that is not available outside

research facilities. Another noteworthy benefit of employing sandwich panels is the potential to eliminate cross girders, better known as floor beams that can contribute up to 35% of the deck system weight. Structural connections and the incorporation with bridge support girders offered by the sandwich design are potentially much simpler and cheaper than conventional orthotropic bridge deck systems. Also the tensile stress range in the wearing surface would be reduced as a result of superior transverse load distribution from the enclosed section.

"Automated Laser Welded High Performance Steel Sandwich Bridge Deck Development" (Abbott, 2007)

This research effort was aimed at developing a thorough investigation of the potential use of steel sandwich panel bridge decks through numerical analysis, structural connection detail development, laboratory testing, and field demonstration in order to identify problems faced by a state transportation agency and the potential benefits to the highway bridge program. This paper also characterizes the surplus of advantages that HLAW welding offers to bridge component fabrication and how they can be implemented to result in a cost effective steel sandwich panel. A comprehensive study of the fatigue performance of pertinent HLAW welded details demonstrated that laser welding fatigue life can be equal or better than that of conventional welding. Through numerous papers they distinguished that the overall fatigue performance of laser welds was promising, but sensitive to the geometry and initial fit up of members prior to welding.

In part of the rehabilitation of the historic Gardiner Maine New Mills Bridge, the Maine Department of Transportation integrated a new steel sandwich panel deck system developed by

PLSystems that was indicative of a double-plate orthotropic bridge deck. The bridge was a single span riveted Warren thru-truss erected in 1908 with a length of 126 ft and width of 24 ft. The existing steel grid deck was supported by longitudinal steel stringers spaced at 5 ft on center and transverse steel floor beams spaced at approximately 15 ft on center. The new deck system to be implemented was to be supported only by the transverse steel beams with stiffening core ribs running longitudinal to traffic. Through static and fatigue finite element analysis the ideal depth and weight of the sandwich panel was calculated to be 7.25 inches and 48 lbs/ft^2 respectively in order to meet all AASHTO specifications for a steel orthotropic bridge deck with a 15 ft span. An iterative finite element method was used to determine the required thickness of 0.25 in. for core and bottom plate elements by using an AASHTO HS25 truck tire central load with simple supports along the strong axis. A 12% Chromium 'stainless' steel was selected for the innovative sandwich panel in order to eliminate corrosion concerns with the hollow cores.

Overall it was concluded that steel sandwich panels are feasible bridge deck alternatives. Not only do they possess a great deal of potential due to their ability reduce weight and be rapidly deployed as a modular system, but are structurally more efficient and robust than traditional systems. With the capability of automated fabrication with reduced production time and improved weld quality and assurance, this technology can possibly change the future of bridge structures as we know it.

3.1 FATIGUE TEST SPECIMEN FABRICATION

The Vierendeel loading effect of internal stiffening ribs described earlier was believed to govern the fatigue life of the modular bridge deck units. Therefore, test specimens were designed to perform cyclic load tests in order to generate S-N curves for laser stake welded configurations used to join the HSS internal stiffening ribs to the bottom plate of the proposed sandwich panel. Based upon the preliminary investigation discussed previously, it was decided to produce test specimens comprised of HSS8"X4"x3/16" and 3/16" plate steel. To begin the fabrication of the fatigue test specimens, a A500 Grade C HSS8"X4"X3/16" carbon steel tube and A572 3/16" steel plate were precisely cut into (6) 48" and (6) 14"X48" sections respectively at the Thomas Murray Structures and Research Laboratory at Virginia Tech as shown in Figure 3–1: Steel Components of Fatigue Test Specimens.

The 12 steel components were then shipped to the Applied Research Laboratory (ARL) at Penn State to be laser welded at their facility. Due to limited familiarity with laser welding, various joint configurations were conceptualized initially, but were later refined into four arrangements through discussions with laser welding experts from the ARL at Penn State. The four weld configurations included two linear stake welds and two linear stake welds with a variable gap each performed with the LBW and HLAW welding processes as depicted in Figure 3–2. These testing configurations were devised to analyze the fatigue life of LBW and HLAW welds used in the proposed sandwich panel bridge deck system, as well as investigate gap tolerance between weld components in the event of improper fit up prior to welding.

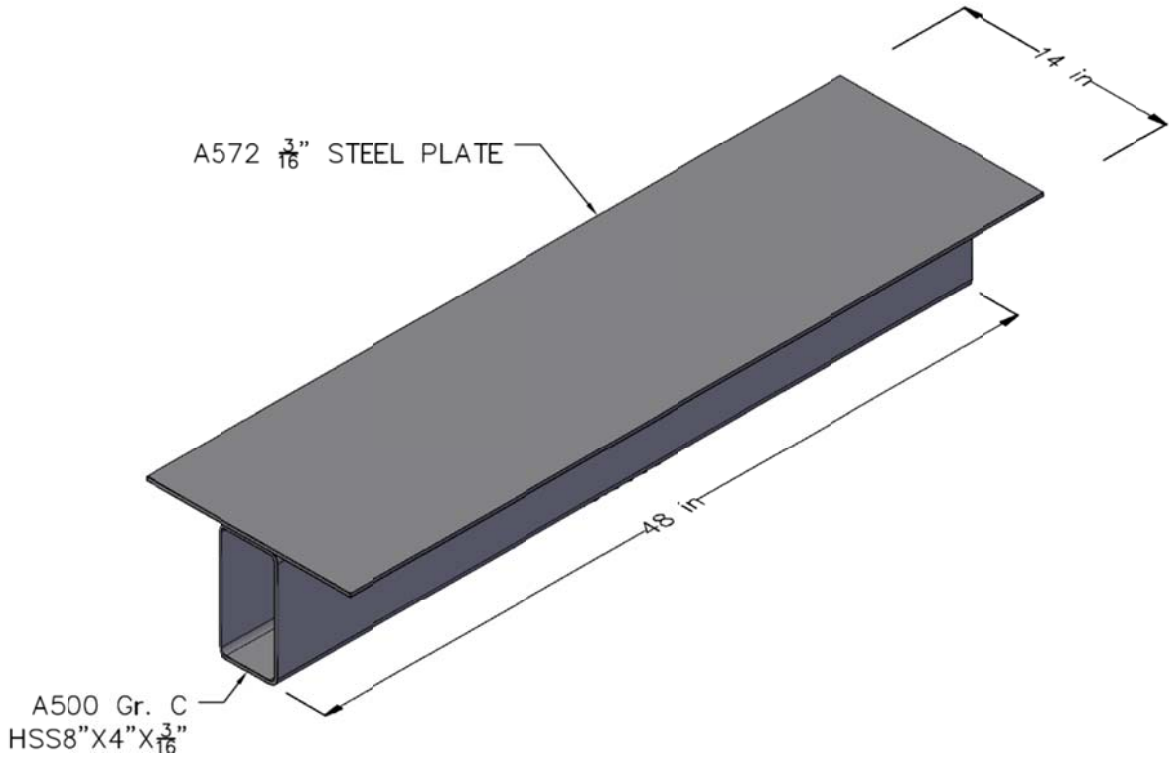

Figure 3–1: Steel Components of Fatigue Test Specimens

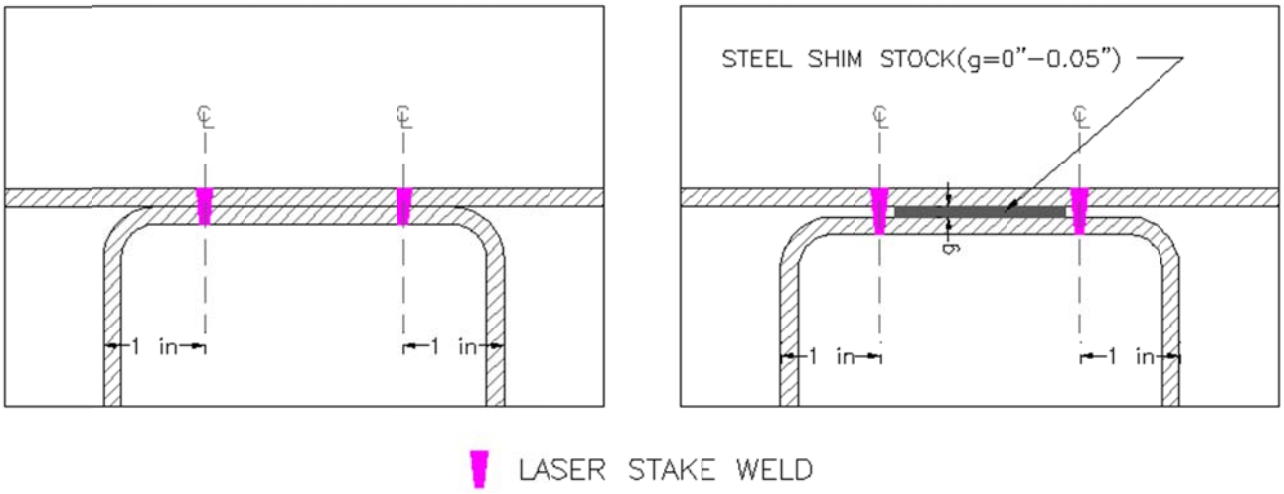

Figure 3–2: HLAW and LBW Welding Configurations

Eight of the steel components shipped to the facility at the ARL were used to fabricate

the four weld configurations that made up the fatigue test specimens, whereas the other four components were used to optimize laser welding parameters for both the LBW and HLAW processes. As mentioned previously, laser welding optimization is convoluted task specific to the problem at hand and requires a great deal of experience. Through various practice trials using the additional components provided, technicians from the ARL at Penn state determined laser power, travel speed, gas flow rate, focusing optics, focus head standoff, wire feed speed, MIG weld type, trim and wave control to be used in the welding processes. The laser welding parameters used to fabricate the four different types of fatigue test specimens are summarized in Table 3-1.

Table 3-1: Laser Welding Parameters Used to Fabricate Fatigue Test Specimens

Fatigue Test Specimen	Laser Power	Travel Speed	Gas Flow Rate	Focusing Optics	Focus Head Standoff	Wire Feed Speed	MIG Weld Type	Trim	Wave Control
	(kW)	(in./min)	(ft^3/hr)	(mm focus)	(mm)	(in./min)			
Two, Linear LBW Stake Welds	9	35	70	500	487	***	***	***	***
Two Linear LBW Stake Welds With Variable Gap	9	35	70	500	487	***	***	***	***
Two, Linear HLAW Stake Welds	8	60	95	200	196	360	PULSED	1.5	OFF
Two, Linear HLAW Stake Welds With Variable Gap	8	60	95	200	196	360	PULSED	1.5	OFF

*** Not Applicable to LBW Fatigue Test Specimens

NOTES:

1. All laser welding was performed using an IPG 12 kW CW fiber laser with a 1070 nm wavelength.
2. The shielding gas used was Argon.
3. There was no preheating.
4. HLAW welds were executed using a Lincoln Powerwave 455M/STT MIG Power Supply
5. HLAW welds were tacked prior to welding via LBW, laser power= 6 kW, travel speed = 40 in./min

In order to generate the LBW and HLAW laser weld configuration with a linearly varying gap, technicians from the ARL at Penn State used steel shim stock at various

thicknesses up to 0.050 in. placed along the centerline of top flange of the HSS section. The curvature of the HSS top flange from the tube forming process with the shim stock created a gap between weld components that varied from 0 in. to 0.035 in. along the length of the welded beam as shown in Figure 3–3. To later distinguish the actual gap between components of individual test specimens, ARL technicians marked the top plate designating the gap dimension along the length prior to welding.

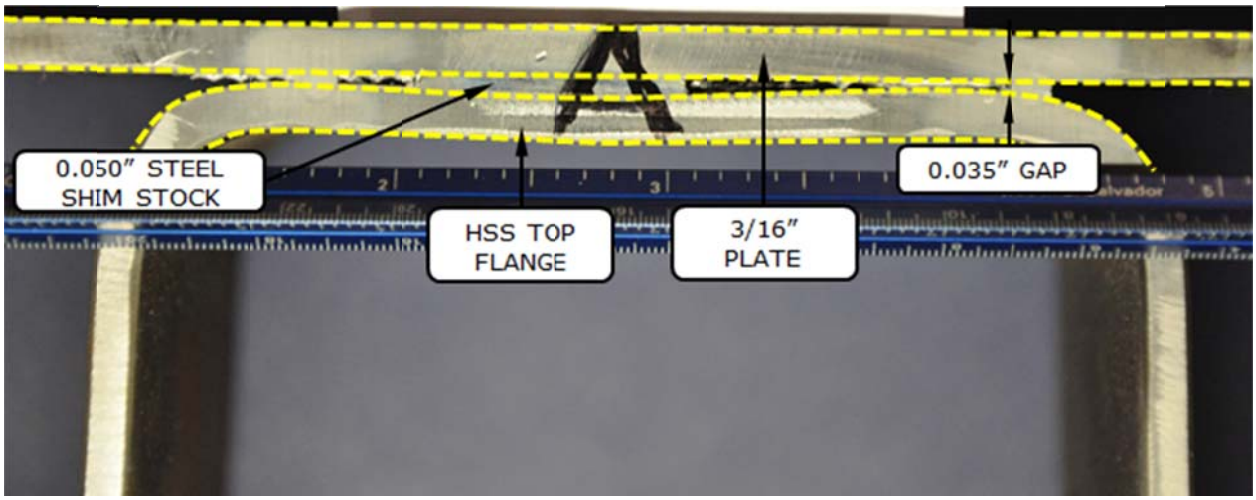

Figure 3–3: Cross Section of LBW Variable Gap Fatigue Test Specimen

The (4) 48 in. laser welded "beams" returned to the Thomas Murray Structures and Research Laboratory at Virginia Tech in order to fabricate the individual fatigue test specimens. Weld quality at the ends of each "beam" was poor due to damage from laser "run-on" and "run-off", as was the case in the study conducted at Bristol University in 2004.(Bright and Smith, 2004) These areas were visually identified and disregarded from the welded "beams", which typically extended from 0.5 in. to 2 in. from either end. The remaining portion of the (4) welded "beams" were then precisely cut into 4.25 in. sections to form 10 to 11 specimens from each welded "beam" depending on the "run-on" and "run-off" area identified, Figure 3–4.

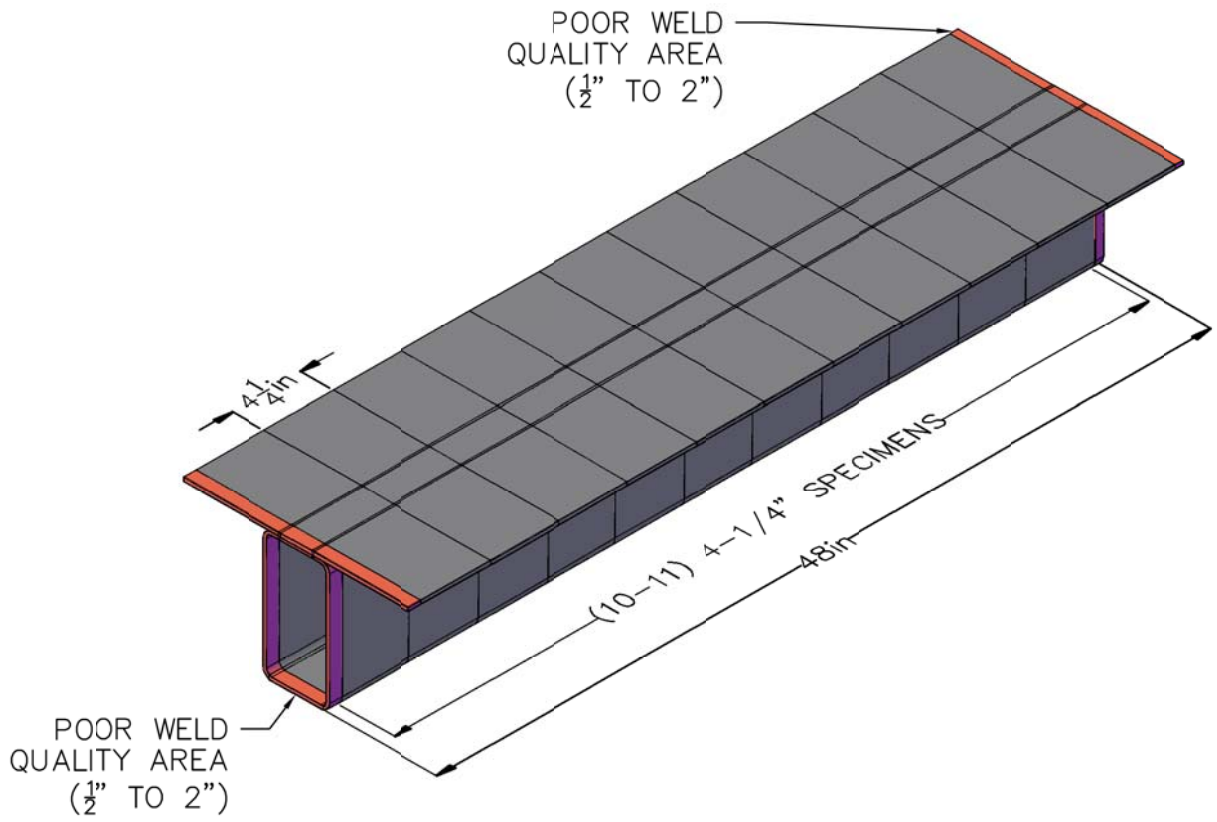

Figure 3–4: Welded "Beam" Sectioning Schematic

Each of the LBW and HLAW variable gap specimens were then engraved with the gap range according to the notes recorded on the top plate from ARL technicians. The gaps closest to the edges of each specimen were chosen. The 4.25 in. specimens were then shipped to a machine shop to be finalized, where they were milled to a width of exactly 4 in and had a 1 in. hole drilled through the center of the HSS bottom flange, as shown in Figure 3–5. Altogether the laser welded "beams" yielded a total of 43 fatigue test specimens, which are summarized in Table 3-2.

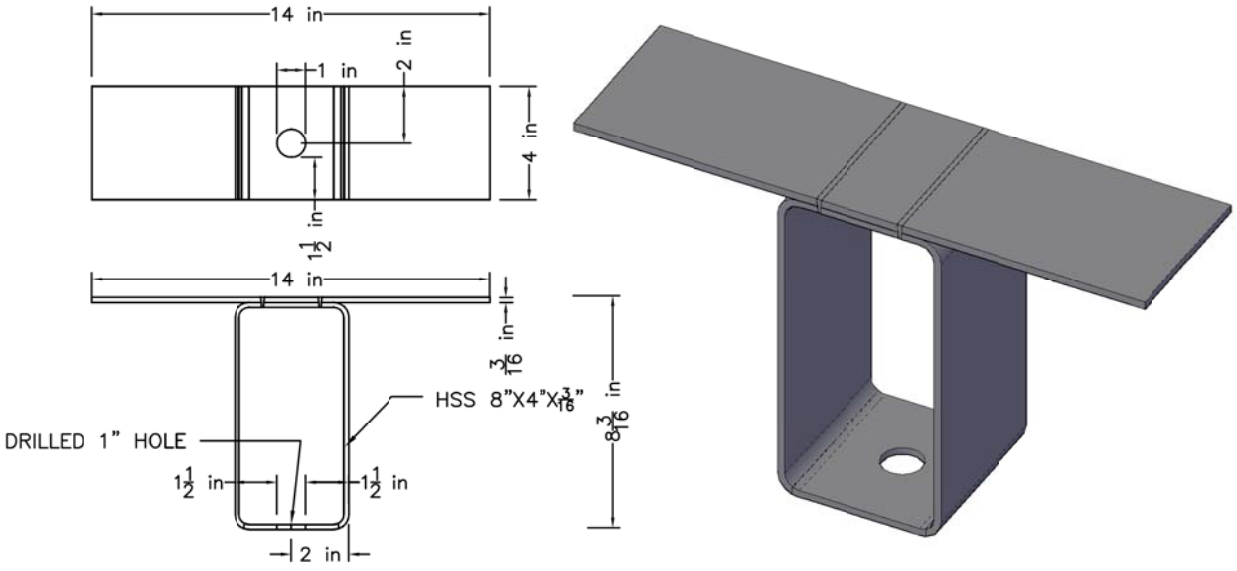

Figure 3–5: Fatigue Test Specimen Finalized Dimensions

Table 3-2: Fatigue Test Specimens Yielded from Welded "Beams"

Two, Linear LBW Stake Welds	Two Linear LBW Stake Welds With Variable Gap	Two, Linear HLAW Stake Welds	Two, Linear HLAW Stake Welds With Variable Gap
Specimen Name	Specimen Name (Gap)	Specimen Name	Specimen Name
FAT-LBW-01	FAT-LBWG-01 (0.000 - 0.000)	FAT-HLAW-01	FAT-HLAWG-01 (0.000 - 0.000)
FAT-LBW-02	FAT-LBWG-02 (0.000 - 0.003)	FAT-HLAW-02	FAT-HLAWG-02 (0.000 - 0.000)
FAT-LBW-03	FAT-LBWG-03 (0.003 - 0.006)	FAT-HLAW-03	FAT-HLAWG-03 (0.000 - 0.004)
FAT-LBW-04	FAT-LBWG-04 (0.006 - 0.010)	FAT-HLAW-04	FAT-HLAWG-04 (0.004 - 0.006)
FAT-LBW-05	FAT-LBWG-05 (0.010 - 0.012)	FAT-HLAW-05	FAT-HLAWG-05 (0.006 - 0.009)
FAT-LBW-06	FAT-LBWG-06 (0.012 - 0.016)	FAT-HLAW-06	FAT-HLAWG-06 (0.009-0.010)
FAT-LBW-07	FAT-LBWG-07 (0.016 - 0.018)	FAT-HLAW-07	FAT-HLAWG-07 (0.010 - 0.014)
FAT-LBW-08	FAT-LBWG-08 (0.018 - 0.022)	FAT-HLAW-08	FAT-HLAWG-08 (0.014 - 0.019)
FAT-LBW-09	FAT-LBWG-09 (0.022 - 0.032)	FAT-HLAW-09	FAT-HLAWG-09 (0.020 - 0.025)
FAT-LBW-10	FAT-LBWG-10 (0.032 - 0.035)	FAT-HLAW-10	FAT-HLAWG-10 (0.025 - 0.035)
FAT-LBW-11	FAT-LBWG-11 (0.035 - 0.035)	***	FAT-HLAWG-11 (0.035 - 0.035)

3.2 FATIGUE TEST SPECIMEN DIMENSIONS

Prior to the commencement of cyclic fatigue testing, two fatigue test specimens from each of the four different groups were chosen at random to be dimensioned. Important measurements shown in Figure 3–6 were scrupulously collected using a pair of calipers. A summary of these dimensions is provided in Table 3-3. For all measurements refer to Appendix B.

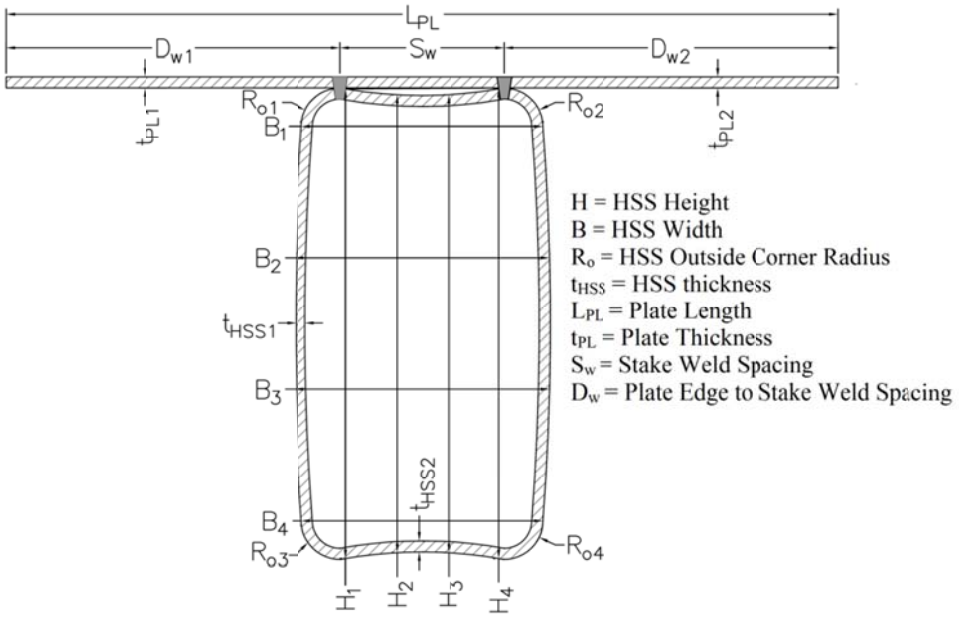

Figure 3–6: Fatigue Test Specimen Recorded Dimensions Legend

Table 3-3: Fatigue Test Specimen Dimension Summary

DIMENSION	LBW	LBWG	HLAW	HLAWG
H (in)	8.0019	8.0009	8.0003	7.9984
B (in)	3.9857	3.9929	3.9921	3.9855
R_o *(in)*	0.7053	0.6835	0.6794	0.6818
t_{HSS} *(in)*	0.1761	0.1766	0.1751	0.1773
L_{PL} *(in)*	13.9914	13.9878	14.0080	14.7415
S_w *(in)*	2.5919	2.5864	2.5785	3.3510
D_w *(in)*	5.6998	5.7007	5.7148	5.6953
t_{PL} *(in)*	0.1888	0.1864	0.1891	0.1914

NOTES:

1.) The table above summarizes the dimension means.

2.) Dimension H denotes the height of the HSS section, which was averaged from measurements H_1 and H_4.

3.) Dimension B denotes the width of the HSS section, which was averaged from measurements B_1 and B_4.

4.) Dimension L_{PL} denotes the width of the plate, which was achieved through the summation of D_{w1}, D_{w2}, and S_w.

More importantly in addition to the overall measurements recorded, laser weld profiles were identified and dimensioned for each fatigue test specimen with the exception of FAT-LBW-07 due to a mishap. In order to identify each weld profile, the surrounding surface was polished and etched according to the procedure outlined in section 3.2.1. The etched weld surfaces were then maliciously photographed according to the procedures in 3.2.2 and select photographs were imported into AutoCAD Civil3D to be dimensioned according to section 3.2.3. Please refer to Table 3-4 for a summary of all laser weld dimensions. For detailed reports of each individual fatigue test specimen's interpolated weld profiles and dimensions refer to Appendix C.

Table 3-4: Fatigue Test Specimen Laser Weld Profile Dimension Summary

LBW LEGEND

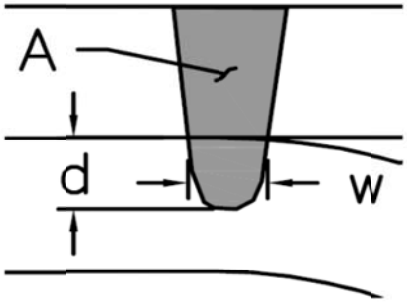

HLAW LEGEND

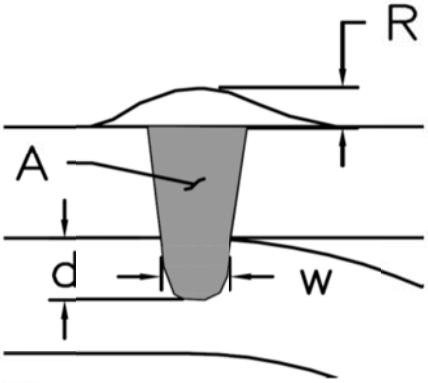

Two, Linear LBW Stake Welds				
	A (in.^{2})	w (in.)	d (in.)	R (in.)
Mean	0.0280	0.0941	0.1006	***
σ_v	0.0055	0.0154	0.0219	***
Range	0.0332	0.0750	0.0967	***
Two, Linear LBW Stake Welds With Variable Gap				
	A (in.^{2})	w (in.)	d (in.)	R (in.)
Mean	0.0292	0.0973	0.0835	***
σ_v	0.0042	0.0182	0.0199	***
Range	0.0156	0.0660	0.0457	***
Two, Linear HLAW Stake Welds				
	A (in.^{2})	w (in.)	d (in.)	R (in.)
Mean	0.0219	0.0679	0.0901	*0.0586*
σ_v	0.0032	0.0097	0.0175	*0.0061*
Range	0.0153	0.0462	0.0760	*0.0230*
Two, Linear HLAW Stake Welds With Variable Gap				
	A (in.^{2})	w (in.)	d (in.)	R (in.)
Mean	0.0273	0.0842	0.1000	*0.0511*
σ_v	0.0033	0.0105	0.0248	*0.0157*
Range	0.0131	0.0481	0.1156	*0.0736*

NOTES:
1. *** Not Applicable
2. A = Laser Stake Weld Area
3. w = Laser Stake Weld Interface Width
4. d = Laser Stake Weld Penetration Depth
5. R = Laser Stake Weld Reinforcement Height

3.2.1 ETCHING LASER WELD PROFILES FOR FATIGUE TEST SPECIMENS

1) A fabricated and machined fatigue test specimen was attained.
2) Each face of the fatigue test specimen was observed at the HSS/Plate interface in order to approximately identify 1 in. boundaries around each laser weld. Please refer to Figure 3–7.

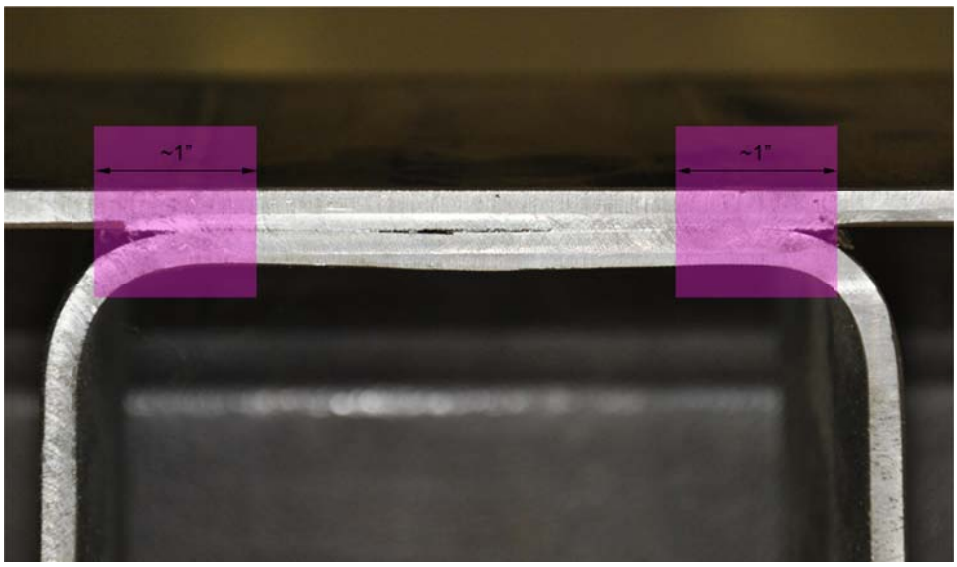

Figure 3–7: Laser Weld Regions on Fatigue Test Specimen Face

3) Using a pneumatic driven hand operated 1 in. belt sander, the four boundaries identified previously were polished with 320 grit all-purpose sandpaper. Given that each specimen was machined to strict dimensions to reduce variability in size, the utmost attention was allotted during this process to minimize abrasion. Each surface was sanded until the residual circular patterns from milling were alleviated. In addition, the specimens were handled with caution as they were turned to prevent scratching on the newly polished surfaces. Please refer to Figure 3–8 and Figure 3–9 for reference to the belt sander utilized and the finished polished surface.

Figure 3–8: Sanding Laser Weld Profile with Belt Sander

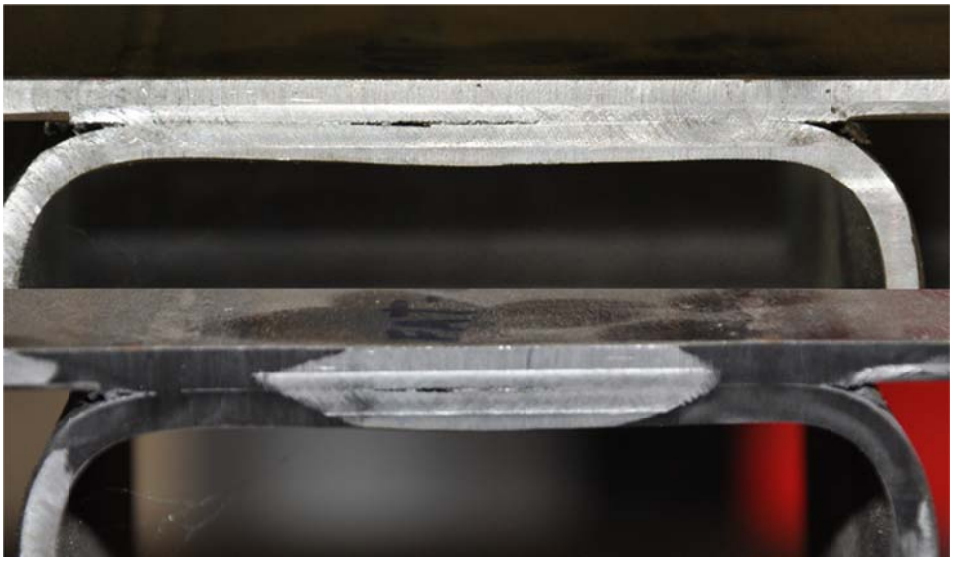

Figure 3–9: Fatigue Test Specimen Finished Polished Surface

4) Four layers of shop towels were laid on the floor and the polished fatigue test specimen carefully placed on top to prevent scratching.

5) Using a plastic graduated 3 mL transfer pipet, two drops of Hydrochloric Acid (HCL), 38% concentrated by volume were applied to each weld face as shown in Figure 3–10.

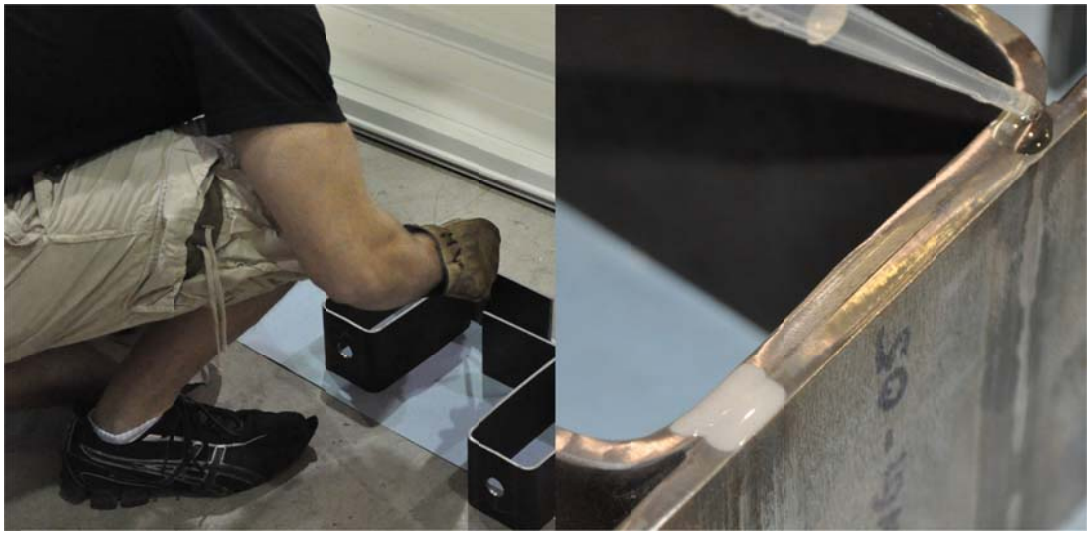

Figure 3–10: Applying HCL to Polished Fatigue Test Specimen Face

6) Approximately five minutes was allotted in order for the chemical reaction to take place and the acid to neutralize. This was determined by one of following two observations. Either the acid completely evaporated from the weld face or turned yellowish in color and stopped fizzing. Once the acid was neutralized, the laser weld face was wiped clean and another two drops of HCL were applied to each weld profile. This process was repeated approximately five to ten times until the laser weld profile was clearly evident as shown in Figure 3–11.

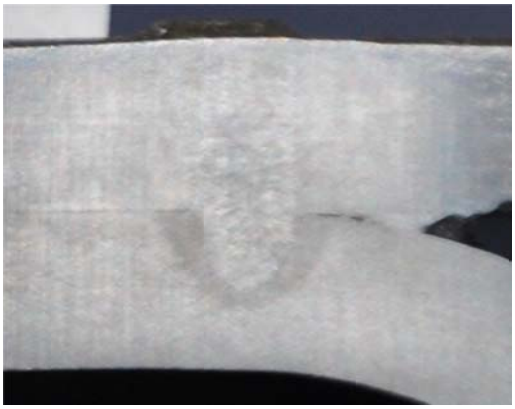

Figure 3–11: Etched Laser Weld Profile

7) Given that the chemical reaction rapidly accelerates the development of rust, the laser

weld profiles were immediately photographed following this process according to the photography procedures outlined in section 3.2.2.

8) The test specimen was then flipped over after being photographed to the opposite side and steps 4 through 7 were repeated.

3.2.2 FATIGUE TEST SPECIMEN PHOTOGRAPHY

1) To begin, the camera tripod was placed with two legs parallel to the surface being photographed, approximately 12 inches away from the center of the mounting bracket.
2) The tripod legs were then adjusted to an appropriate height and leveled using the integrated target level as shown in Figure 3–12.

Figure 3–12: Leveled Camera Tripod

Figure 3–13: Leveled Pan-Tilt Head

3) Once the tripod base was leveled, a Nikon Digital SLR camera was mounted to the tripod.
4) The tripod pan-tilt head was then leveled using the integrated bar level as shown in , rotated 90 degrees and re-leveled to assure that the camera was on a perfectly level plane in order to attain the highest level of accuracy.
5) The tripod pan-tilt head was then rotated so that the camera lens was parallel to the edge of the mounting table for specimen being photographed.
6) Using the camera's smallest focus area in conjunction with the optical viewfinder, the tripod was raised so that the focus area matched exact height of the desired region on the specimen to be photographed.
7) The specimen was then labeled, fixed with a leveled engineering scale parallel to the

surface being photographed, and prepped with a constant color background as shown in Figure 3–14.

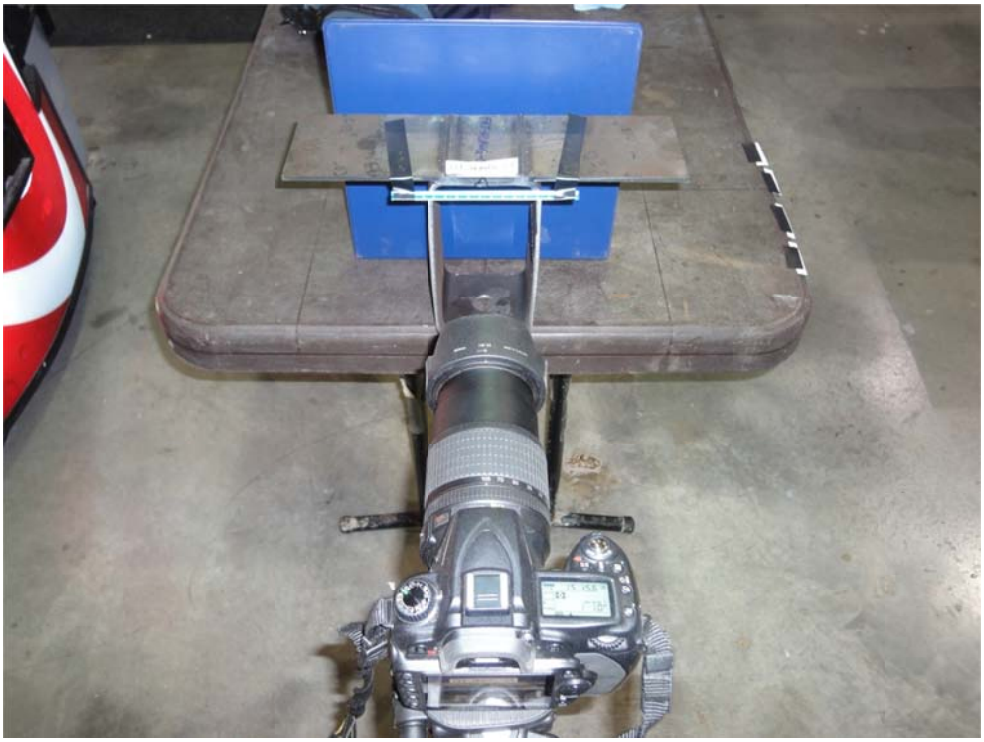

Figure 3–14: Fatigue Test Specimen Prepped to Be Photographed

8) The specimen was then moved so that the desired region on the surface to be photographed was centered on the camera's optical viewfinder as shown in Figure 3–15. It was extremely important to assure that while centering the specimen, the surface being photographed remained parallel to the camera lens to minimize topographical errors.

Figure 3–15: Centered Specimen in Camera's Optical Viewfinder

9) The tripod's integrated levels were checked and if necessary re-leveled.

10) The specimen was then photographed with and without additional light, using four different settings on the camera's dial denoted by a flower symbol, AUTO, and letters "S" and "P" as shown in Figure 3–16.

Figure 3–16: Nikon Digital SLR Camera Dial Settings

11) The eight photographs were then viewed and the best suited was selected.

3.2.3 LASER WELD DIMENSIONS WITH AUTOCAD CIVIL 3D 2011 IMPERIAL

1) Enter model space in AutoCAD Civil3D 2011 Imperial
2) Using the DIMSTYLE command in AutoCAD Civil3D 2011 Imperial under the Primary Units; modify the precision of the linear and angular units to the nearest ten thousandth in the current dimension style as shown in Figure 3–17: AutoCAD DIMSTYLE Precision Modifications.

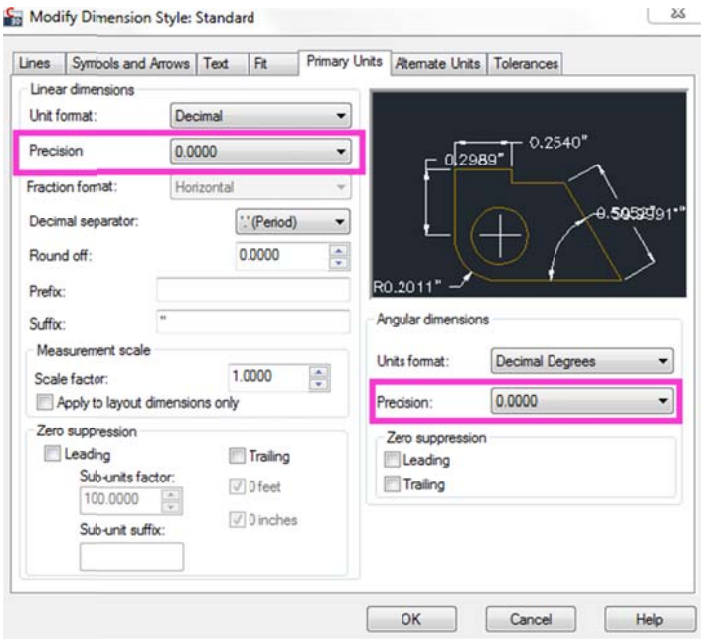

Figure 3–17: AutoCAD DIMSTYLE Precision Modifications

3) Using the INSERT/ATTACH command in AutoCAD Civil3D 2011 Imperial; import the photograph of fatigue test specimen profile with engineering scale 1:10
4) Using the LINE command in AutoCAD Civil3D 2011 Imperial; draw a line on edge of the scale tick marks that connects tick marks 2 and 3 as shown in Figure 3–18.

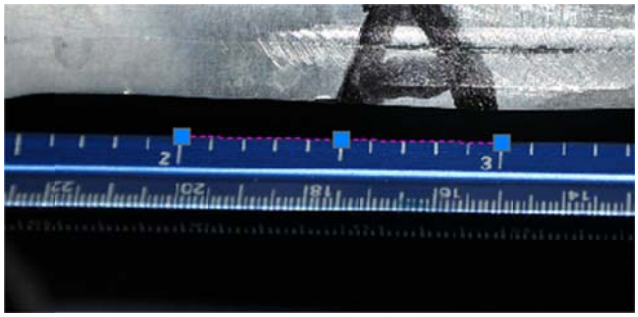

Figure 3–18: AutoCAD Line to Scale Photographs

5) Using the DIMENSION/ALIGN command in AutoCAD Civil 3D 2011 Imperial; determine the aligned distance between points drawn in the previous step.

6) Using the SCALE command in AutoCAD Civil 3D 2011 Imperial; scale the photograph by a calculated value of one divided by the aligned distance determined in the previous step. The aligned dimension should read a value of one. If not, the photograph should be re-scaled accordingly.

7) Using the LINE command in AutoCAD Civil3D 2011 Imperial; draw a line along the top edge of the plate as shown in Figure 3–19.

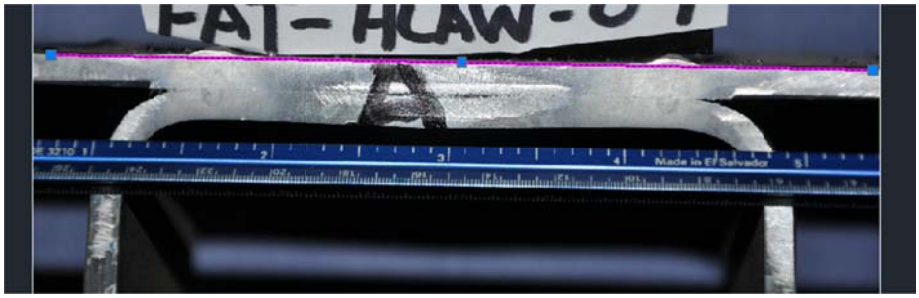

Figure 3–19: AutoCAD Line to Rotate Photograph Horizontally

8) Using the LINE command with object snap and the ORTHO mode turned on in AutoCAD Civil3D 2011 Imperial; draw a line that starts at the beginning of the line drawn in the previous step. End the line outside the photograph so that the line runs parallel to the X-axis at zero degrees as shown in Figure 3–20.

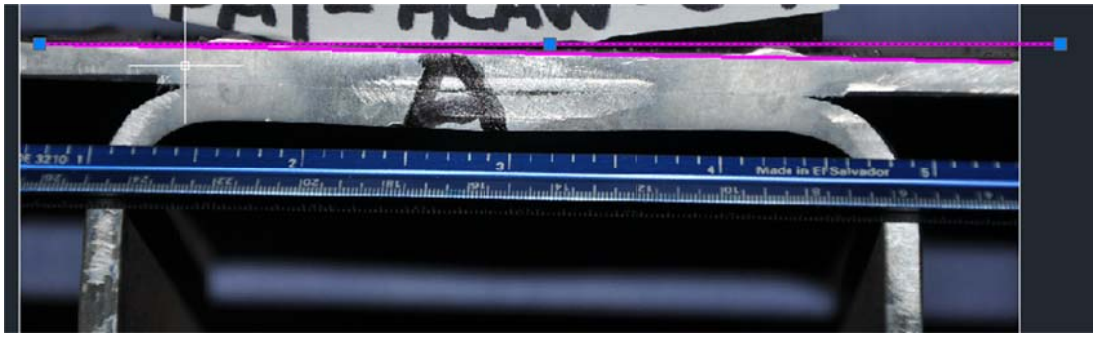

Figure 3–20: AutoCAD Line Used for Horizontal Datum to Photographs

9) Using the DIMENSION/ANGULAR command in AutoCAD Civil3D 2011 Imperial; determine the angle draw between the lines drawn in the previous two steps.

10) Using the ROTATE command in AutoCAD Civil3D 2011 Imperial; rotate the photograph by the angle measured in the previous step so that the line drawn along the top edge of the plate is parallel to the X-axis.

11) Using the ERASE command in AutoCAD Civil3D 2011 Imperial; delete all lines and dimensions drawn in previous steps except for the line that runs along the top edge of the plate.

12) Using the PLINE command in AutoCAD Civil3D 2011 Imperial; draw a continuous line around each of the two laser welds excluding the Heat Affected Zone (HAZ). Due to the faint nature of the laser weld profiles, all boundaries should be interpolated in the same manner to reduce errors. On average each polyline boundary should be comprised of approximately 12 nodes, 4 of which must depict the width of the laser weld at the top of the plate surface and at the HSS/plate interface. Please refer to Figure 3–21.

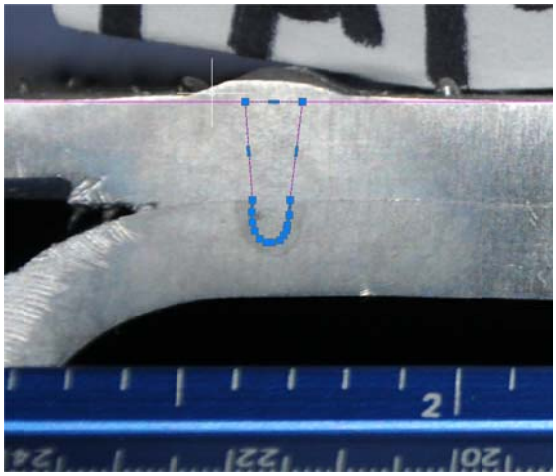

Figure 3–21: AutoCAD PLINE Perimeter of Laser Stake Weld

(For HLAW and HLAWG fatigue specimens only)

Using the LINE command with object snap and the ORTHO mode turned on in AutoCAD Civil3D 2011 Imperial; draw a line that starts at the zenith of the raised portion of the laser weld and ends at a point on the line along the top surface of the plate drawn previously parallel to the X-axis to form a right angle. Please refer to Figure 3–22.

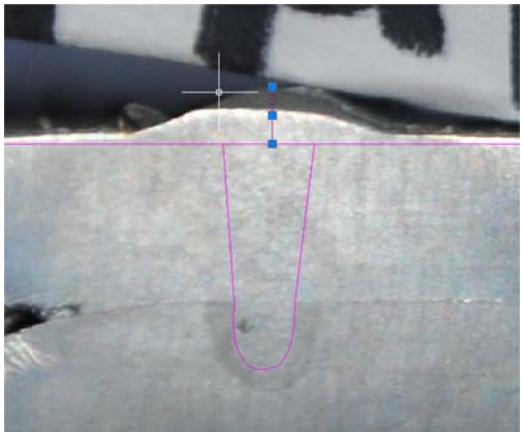

Figure 3–22: AutoCAD LINE Used to Dimension Height of the Hybrid Laser Stake Weld Reinforcement

13) Using the ERASE command in AutoCAD Civil3D 2011 Imperial; delete the line that runs along the top edge of the plate.

14) Using the DIMENSION/HORIZONTAL command in AutoCAD Civil3D 2011 Imperial;

determine the width of each laser weld at the HSS/plate interface via two interpolated nodes of each laser weld boundary drawn in the previously. Please refer to Figure 3–23.

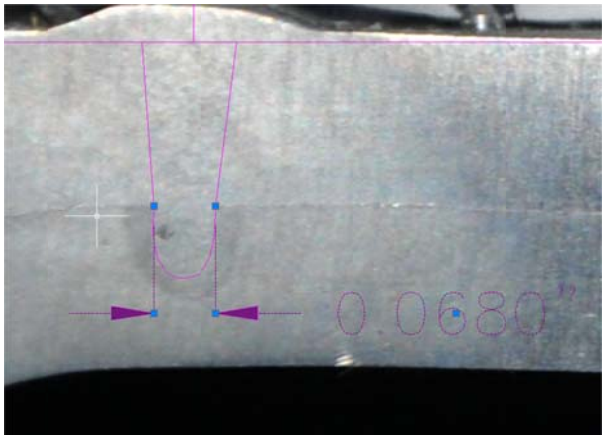

Figure 3–23: AutoCAD Dimension for Weld Interface Width

15) Using the DIMENSION/VERTICAL command in AutoCAD Civil3D 2011 Imperial; determine the HSS penetration depth of each laser weld via two interpolated nodes of each laser weld boundary drawn previously. Please refer to Figure 3–24.

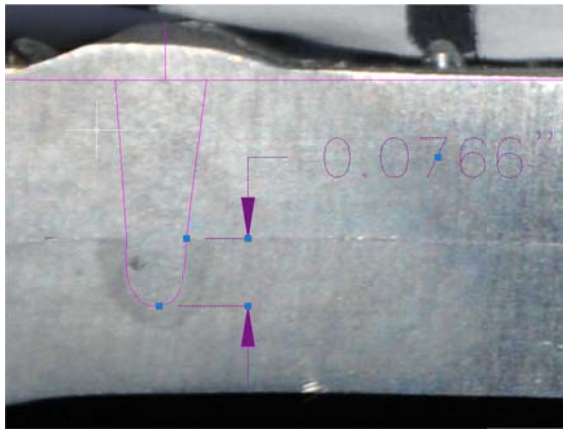

Figure 3–24: AutoCAD Dimension for Weld Penetration Depth

(For HLAW and HLAWG fatigue specimens only)

Using the DIMENSION/VERTICAL command in AutoCAD Civil3D 2011 Imperial; determine the HLAW surplus height for each laser weld via lines drawn previously. Please refer to Figure 3–25.

Figure 3–25: AutoCAD Dimension for Weld Reinforcement Height

16) Using the REGION command in AutoCAD Civil3D 2011 Imperial; create two regions from the polyline laser weld boundaries drawn previously.

17) Using the MASSPROP command in AutoCAD Civil3D 2011 Imperial; calculate the laser weld surface area from the regions created in the previous step.

18) Repeat for all laser weld profiles.

3.3 MATERIAL PROPERTIES

3.3.1 TENSILE COUPON TESTING

Tensile coupon testing was performed in accordance with ASTM E8/EM-08 Standard Test Methods for Tension Testing of Metallic Materials ((ASTM), 2008), to acquire material properties of the steel plate and HSS carbon steel tube utilized to fabricate all fatigue test specimens. Due to limited dimensions, the subsize rectangular tensile specimen was required. Two fatigue test specimens from each of the four different groups were chosen at random to extract tensile coupons from. Coupons were removed from each fatigue test specimen following cyclic fatigue testing from the steel plate and HSS carbon steel tube as shown in Figure 3–26. The tensile coupon extraction area for the HSS tube was selected based upon the side without the seam weld, whereas the plate lateral location was taken at random.

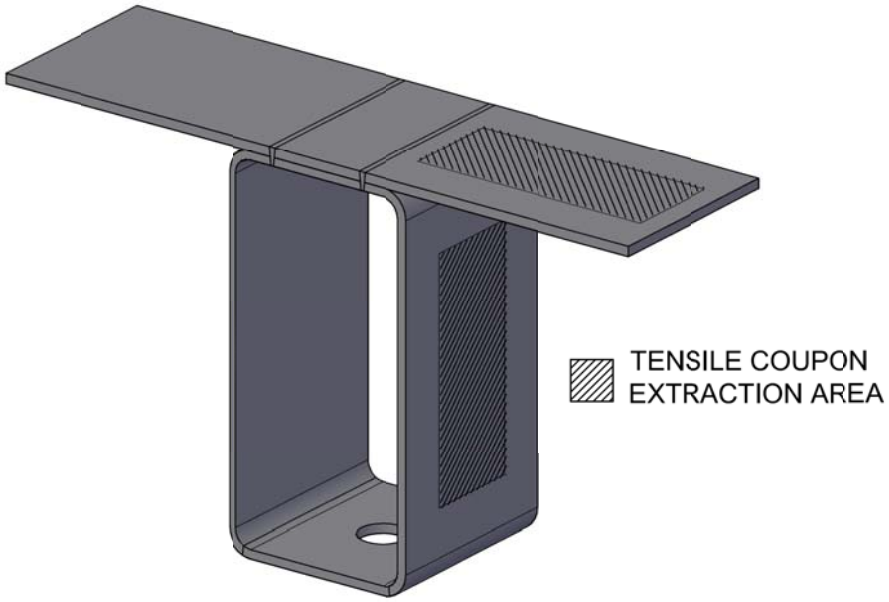

Figure 3–26: Fatigue Test Specimen Tensile Coupon Extraction Areas

3.4 EXPERIMENTAL TESTING

All testing was conducted at the Thomas Murray Structures Laboratory in Blacksburg, Virginia using the MTS Landmark Servohydraulic Test System operated by MTS Hydraulic Power Unit (HPU), Flextest Controller and MTS 793 software as shown in Figure 3–27. The following sections provide detail descriptions of the tests performed over the course of this investigation.

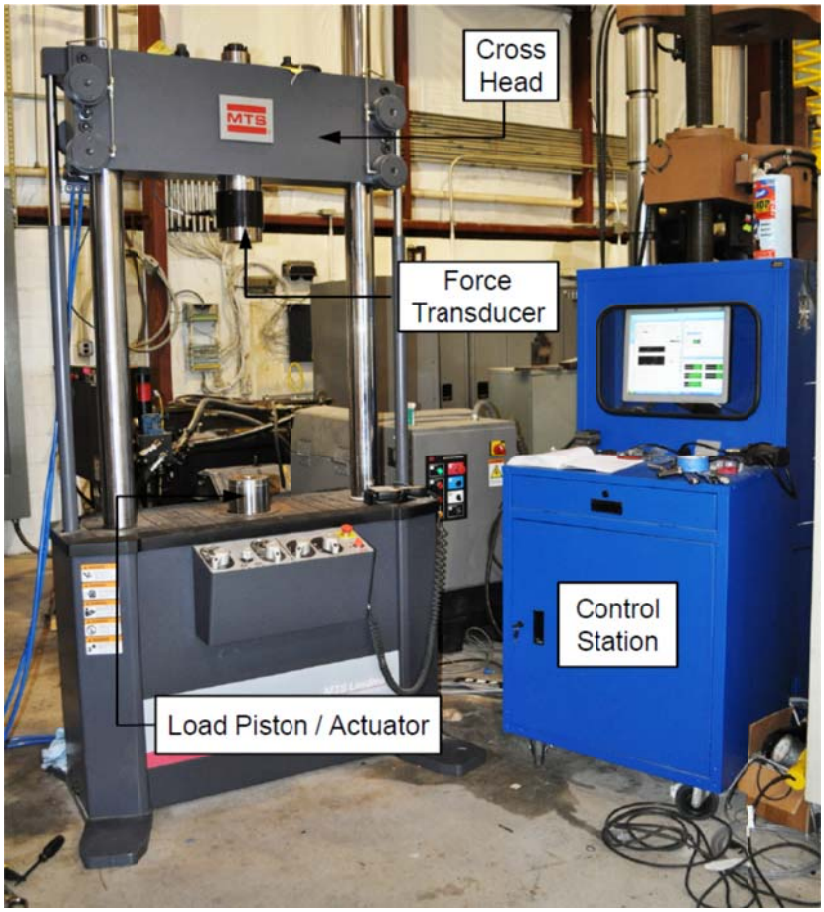

Figure 3–27: MTS Servohydraulic Landmark Test System

3.4.1 FATIGUE TESTING

To assess the potential use of LBW and HLAW stake welds in the proposed modular steel sandwich panel bridge deck system, a series of fatigue testing was performed on the 43 test specimens fabricated. The purpose of this testing program was to generate preliminary stress-life (S-N) curves for the specialized laser welded connection and determine the effect gaps between weld components from improper fit-up prior to welding have on fatigue performance for both laser welding processes.

3.4.1.1 Methodology

In order to investigate the Vierendeel load effect on adjacent HSS internal stiffening ribs, a test was designed around the loading configuration illustrated in Figure 3–28. Test specimens were simply supported with rollers at a span of 12-$^{1}/_{4}$", cyclically loaded through the bolt hole located at the center of the HSS flange with a load ratio, R_P = -1 at rate ranging from 5 to 7 Hz. Given that the loaded HSS flange would actually be restrained by the top plate of the sandwich panel, possessing a possible thickness ranging from $^{9}/_{16}$" to ¾", localized bending between the outside bend radiuses of the HSS was restricted through the use of a 2 $^{5}/_{8}$" X 5" X 1" steel bearing plate as shown in Figure 3–28 and Figure 3–31. The addition of the bearing plate also allowed for larger cyclic frequencies during testing by reducing the lag in load response of each specimen.

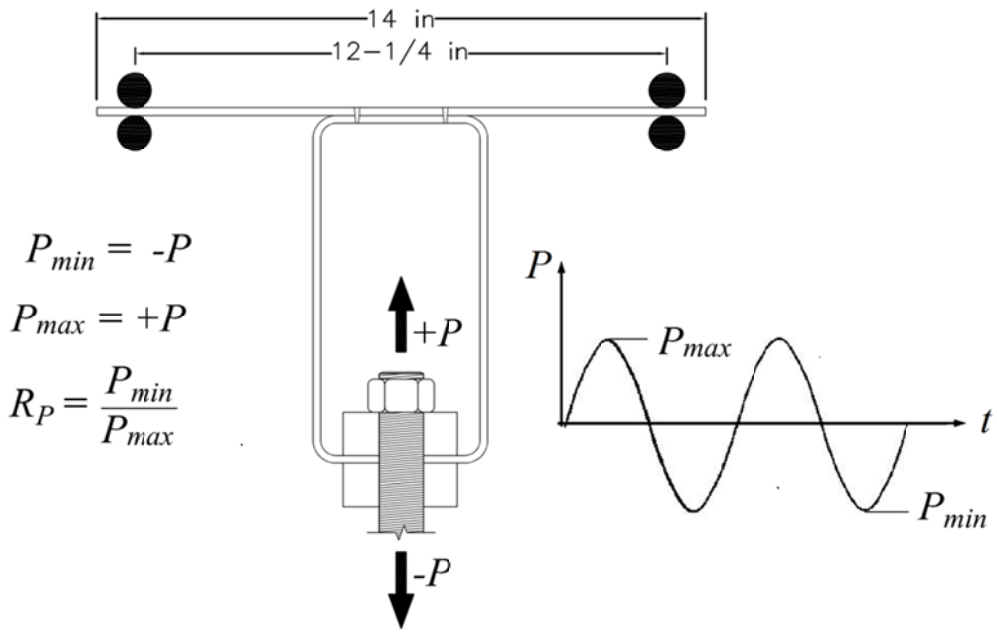

Figure 3–28: Fatigue Testing Configuration

Due to the complex geometry of the test specimens, nominal stress driven cyclic loading was not feasible. Contact between the HSS flange and plate caused variable system stiffness dependent on load direction, as well as a discontinuity in stress at the laser welded lap joint that required a finite element analysis. To provide a general understanding of the stress distribution throughout each test specimen, a model was created using beam elements and analyzed with the direct stiffness method to produce the moment diagrams and deflected shape diagrams shown in Figure 3–29 and Figure 3–30 respectively. For this simplified analysis it was assumed that the components were fully integrated between stake welds acting as one beam element. In addition, the nodes along the bottom flange of the HSS were constrained to only allow vertical translation in order to simulate the presence of the bearing plate.

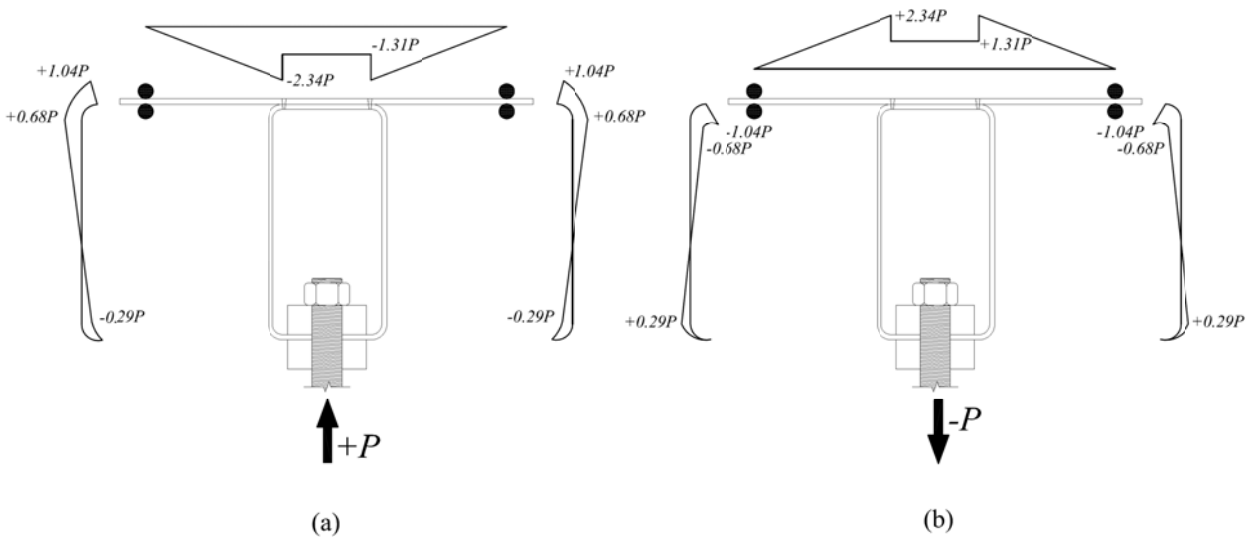

Figure 3–29: (a) Fatigue Test Specimen Moment Diagram Subjected to Positive Loading (b) Fatigue Test Specimen Moment Diagram Subjected to Negative Loading

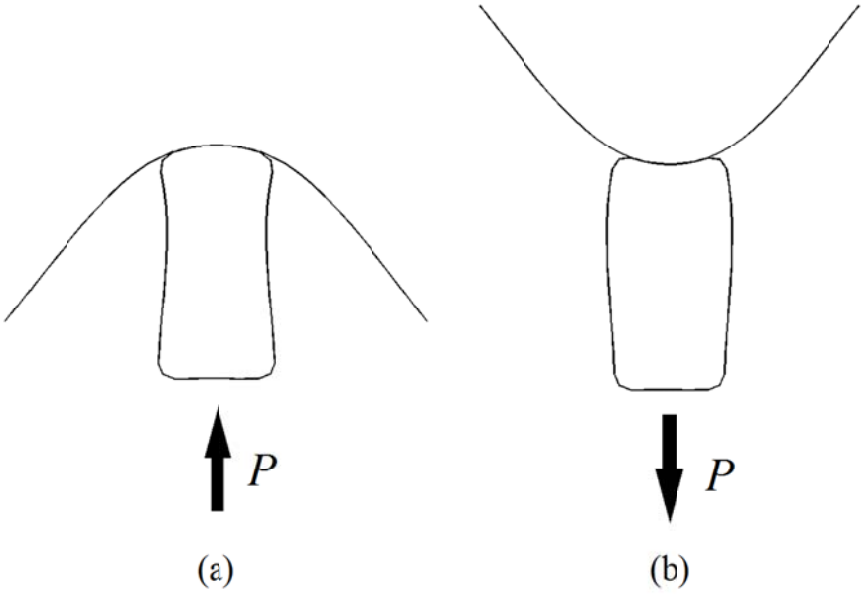

Figure 3–30: (a) Fatigue Test Specimen Deflected Shape Subjected to Positive Loading at a 5000x Scale (b) Fatigue Test Specimen Deflected Shape Subjected to Negative Loading at a 5000 Scale

3.4.1.2 Setup

Each specimen was installed onto the threaded rod incorporated into Landmark actuator through the 1" fabricated hole in the free HSS flange with a bolted connection. To simulate the conditions of the modular bridge deck unit, the HSS flange was sandwiched between bearing plates that rested on two 4" X 5" X 1" steel plate spacers and tapered leveling rings as shown in Figure 3–31. To replicate the simply supported boundary conditions shown in Figure 3–28, each specimen was tested using the loading fixture depicted in Figure 3–32 and Figure 3–33. This fixture was connected in series with a110 kip force transducer to the cross head of the MTS Servohydraulic Landmark Test System. To provide a stable connection between the three, an initial compressive force of 500 lbs was applied prior to securing the bolted connection shown in Figure 3–34. The predominant variables measured in each fatigue test were load and vertical displacement. Test loads were measured through the force transducer fixed between the Landmark cross head and load fixture. Whereas, test displacements were measured using the integrated Linear Variable Differential Transformer (LVDT) in the Landmark actuator.

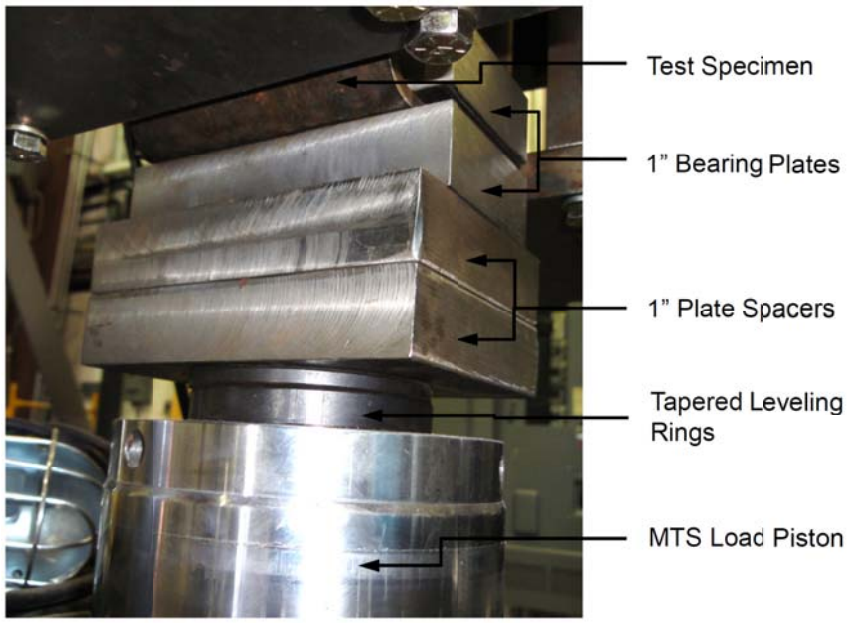

Figure 3–31: Test Specimen Connection to the MTS Load Piston

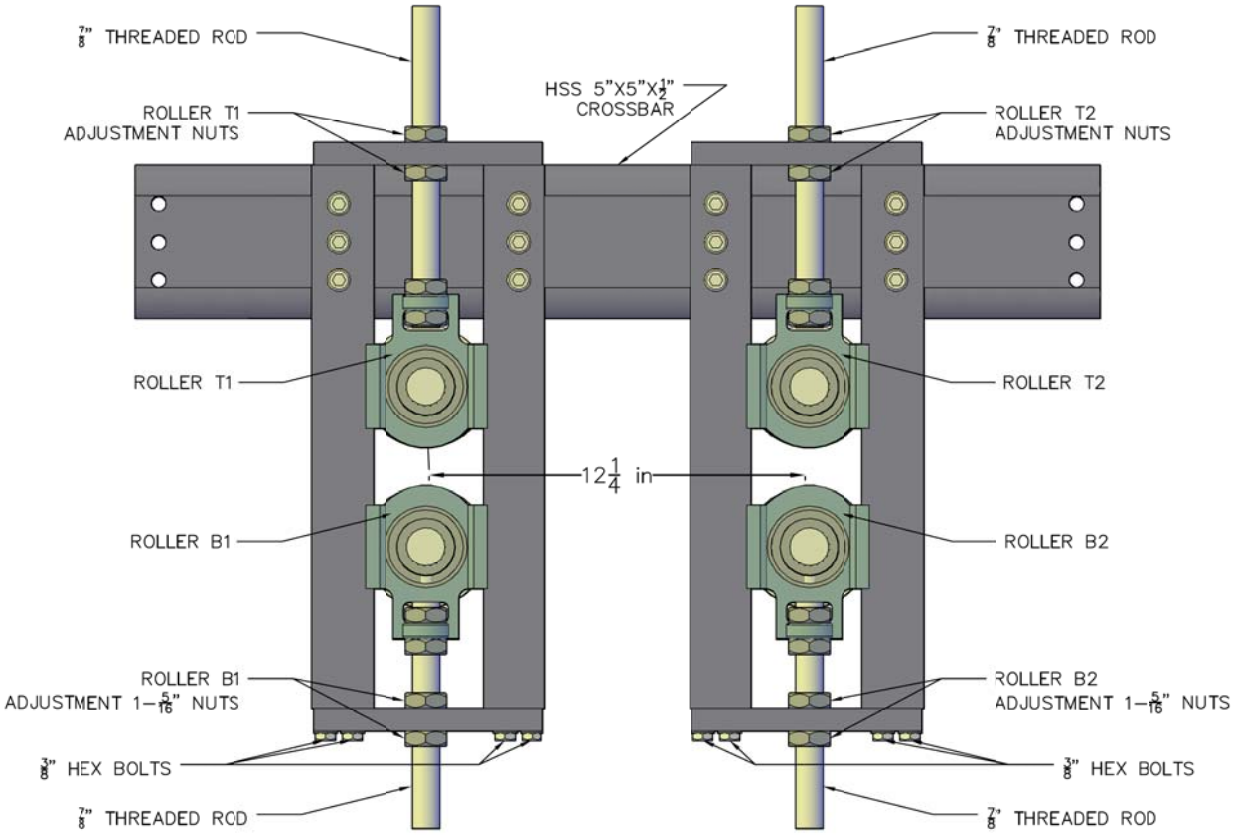

Figure 3–32: Side Fatigue Testing Load Fixture

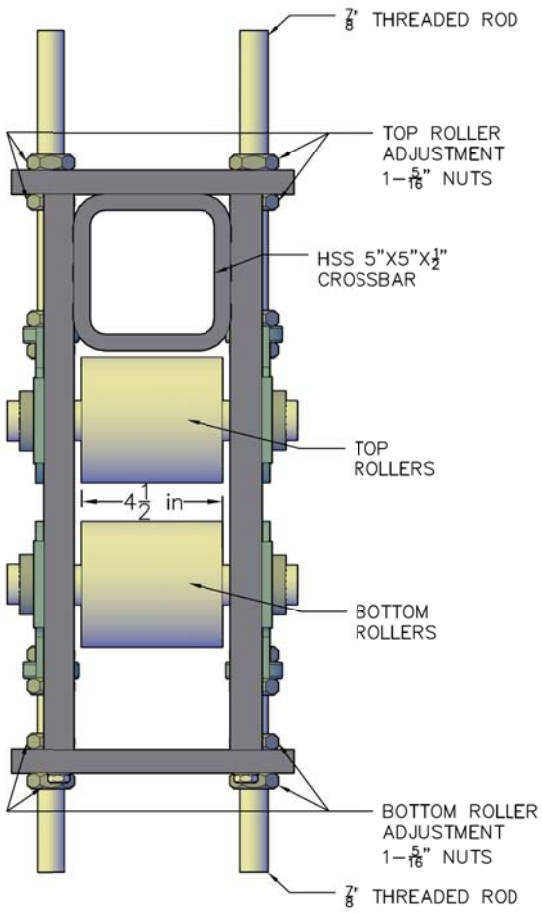

Figure 3–33: Front View of the Fatigue Testing Load Fixture

Figure 3–34: Load Fixture Connection to the MTS Servohydraulic Landmark Test System

The setup of each specimen prior to testing required a set of meticulous procedures to minimize experimental error and maintain test precision that are discussed in section 3.4.1.3.1. Maintaining a level specimen throughout the setup was extremely important to prevent an asymmetric loading scenario that would lead to an uneven stress distribution to the laser welds in question. The specimen was initially leveled during the connection to Landmark actuator through the use of a target level and tapered leveling rings. Securing 1½" hex bolt with the one third turn method occasionally caused the specimen to fall out of the leveled alignment due to friction with the upper bearing plate. Thus it was important to constantly reassure that the specimen remained level prior to being set into the load fixture. To reduce friction and ease installation, a lubricant was applied to the upper bearing plate frequently.

To allow for imperfections and fabrication tolerances, the load fixture enabled the vertical adjustment of each roller on a set of two threaded rods through the 1 $^{5}/_{16}$" adjustment nuts. Ideally test specimens were set into the load fixture with an equal clamping force in each of the four rollers, evenly distributed over the contact area. Maintaining equivalent clamping force in all rollers with uniform contact during setup was essential to prevent the asymmetric loading scenario discussed. A combination of differential clamping forces could easily pre-load the specimen prior to testing without being detected as shown in Figure 3–35 and greatly alter the outcome of each test. Though the vertical force is balanced in the scenario depicted in Figure 3–35, producing a load reading of zero, the initial moment would alleviate stress in one weld and increase it in the other. Therefore, a great deal of attention was allocated to maintaining identical clamping force to each roller. Non-uniform contact between rollers and the $^{3}/_{16}$"

specimen plate could also taint the conclusions drawn from each test by inducing torsion in the test specimen as shown in Figure 3–36, possibly resulting in a premature failure. To prevent this undesired load case, the rollers were visually inspected with a close eye during the application of roller clamping force. In addition, prior to using a wrench, the $1^{5}/_{16}$" adjustment nuts were simultaneously turned by hand to ensure uniform contact.

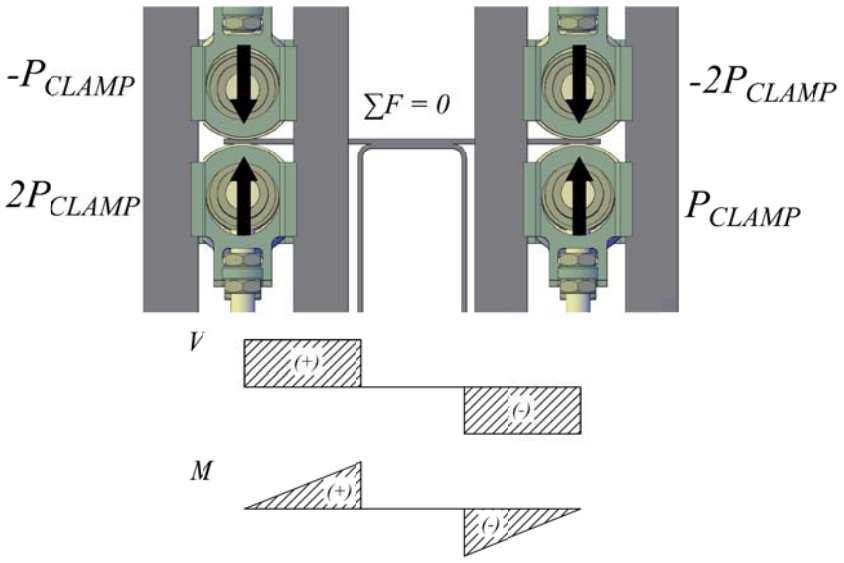

Figure 3–35: Induced Shear and Moment from Differential Clamping Force

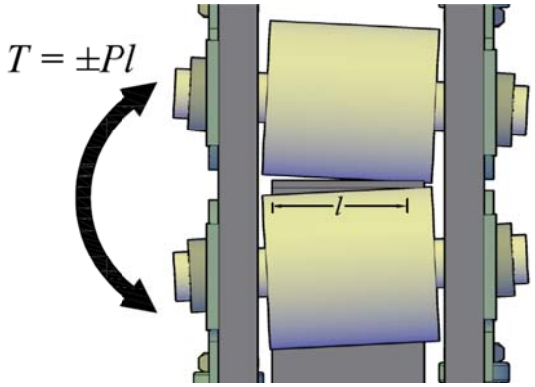

Figure 3–36: Torsion from Non-Uniform Contact between Rollers and Test Specimen

The rigidity of the load fixture in comparison to the flexible $^{3}/_{16}$" plate presented many problems in addition to the potential errors highlighted above. Towards the end of the study, it was founded through experimental measures that the clamping force applied through rollers to the specimens was not received as reaction force to the force transducer. Initially, it was believed that the adjustment bolts bearing on the load fixture would create a reaction force equivalent to the clamping force from the rollers. Unfortunately the test specimen's flexibility did not permit this reaction due to a lack of stiffness. Therefore, the first upward clamping force applied through the rollers induced strains in the specimen plate and the downward clamping force from the upper rollers relieved them. The clamping forces were not entirely received by the force transducer until the rollers were essentially pushing against one another. This caused the majority of the fatigue test specimens to be installed with a clamping force much higher than that which was perceived. The large clamping forces led to many issues with the overall investigation, especially with the boundary conditions for each fatigue test that were later resolved through additional testing discussed in sections to follow.

It was important to maintain vertical alignment between both bottom rollers during the application of the initial upward clamping force to avoid a discrepancy in position. A difference in the vertical location between of each set of rollers as shown in Figure 3–37, would prompt stresses in the test specimen similar to those seen with differential clamping force, but likely with more severity. Unlike the potential problem dealing with differential clamping force, the vertical alignment of rollers is much harder to follow and identify during the specimen setup due to the flexibility in $^{3}/_{16}$" plate. As stated previously the reaction force is not received by the force transducer due to a lack of

stiffness the specimen plate. Thus, this misalignment is not represented through the measured load making it very difficult to notice. Unfortunately this problem was encountered during the setup of test specimen FAT-LBW-06. The difference in vertical alignment between each set of rollers produced large strains, locked in prior to testing that resulted in premature failure, excluding it from the finalized S-N curve. For this reason a very small initial clamping force of 5 lbs was applied to limit strain in the $^{3}/_{16}$" and avoid another mishap.

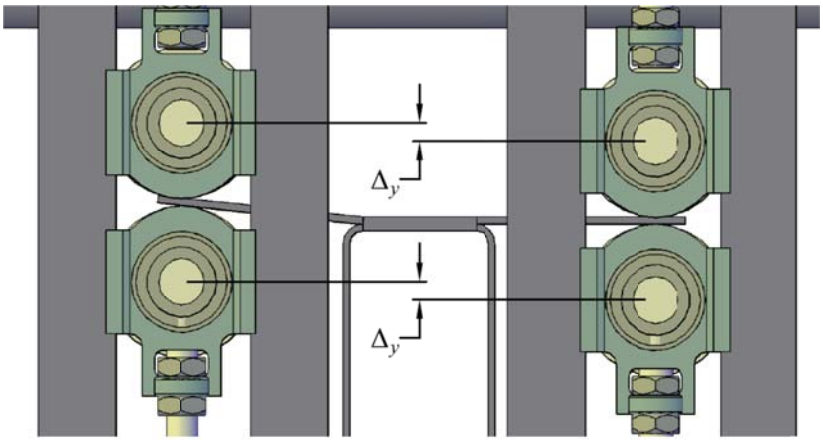

Figure 3–37: Differential Vertical Alignment of Rollers

3.4.1.3 Procedures

To maintain precision throughout each individual fatigue test, uniform testing procedures were designed to minimize all experimental errors, while maximizing accuracy with efficiency. Standardized procedures were designed for specimen setup and automated control during testing. The physical setup of each specimen was an arduous undertaking, as discussed in the previous section due to a plethora of possible experimental blunders. Thus, the sequence of rigorous procedures outlined in section 3.4.1.3.1 were developed and evolved over the course of the study that was closely

adhered to for the placement of each specimen into the test setup. Prolonged test durations and unpredicted failure outcomes due to an absence of data made test automation essential. Using the associated MTS 793 software, a generalized procedure was programmed to control and monitor each fatigue test with appropriate data acquisition, allowing for full automation. This procedure is described in section 3.4.1.3.2.

3.4.1.3.1 Physical Setup of Each Fatigue Test Specimen

1) To begin, the rollers were adjusted using the 1-5/16" bolts so that the top and bottom rollers were separated by approximately one inch, while maintaining an even horizontal plane between each set of rollers as shown in Figure 3–38. Rollers were properly aligned when there was clear sight distance looking through the 1 inch gap between top and bottom rollers from the side of the load frame.

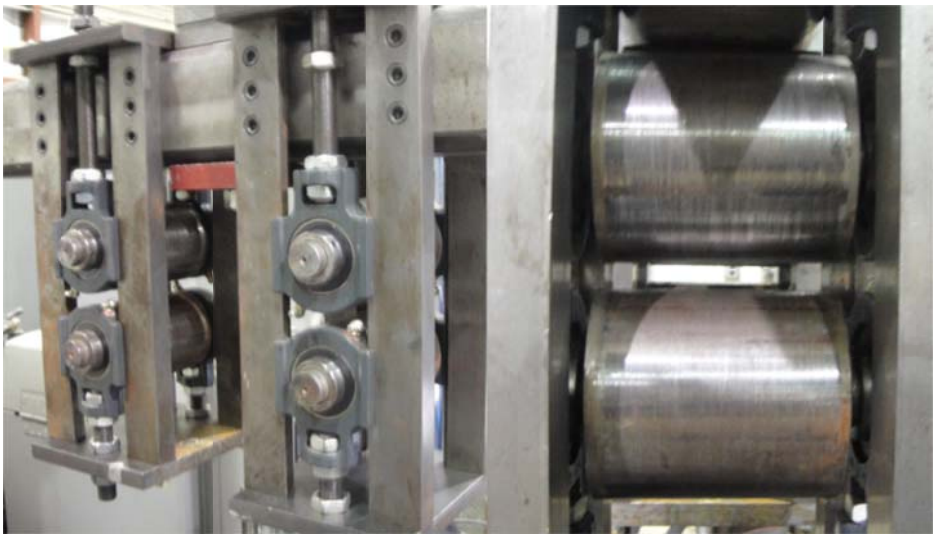

Figure 3–38: Initial Roller Alignment

2) The bottom plate supporting roller B2 was removed from the load frame by unscrewing the (8) 3/8" hex bolts that secured it in place as shown in Figure 3–39.

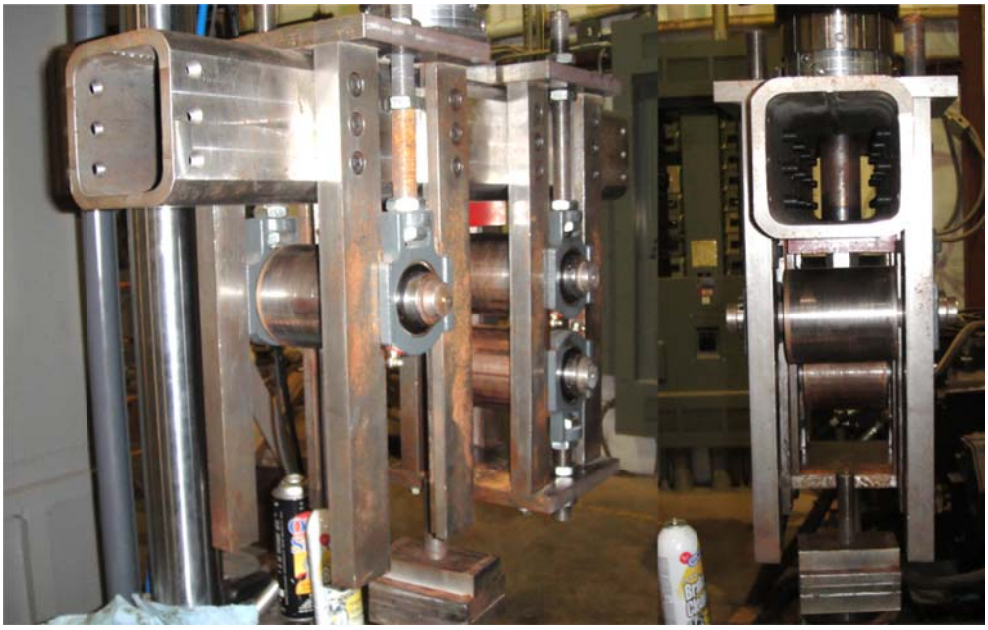

Figure 3–39: Roller B2 Removed from Load Frame

3) Using the station manager from the MPT of the MTS 793 software integrated with the MTS Landmark Servohydraulic Test System, the hydraulic pump was turned on and hydraulic flow was initiated to the loading piston.

4) The station manager was then switched to manual control in displacement mode and the load piston was raised/lowered to the approximate median of its travel distance.

5) The MTS Landmark Servohydraulic Test System's cross head was then raised to allow access to the load piston bolt for the fatigue test specimen. The test specimen was then placed into the 1 inch gap between rollers T1 and B1, while being orientated so that load piston's 1 inch threaded rod was partially inserted into the hole on the bottom flange of the specimen as shown in Figure 3–40.

Figure 3–40: Placing the Fatigue Test Specimen in the Load Frame Using the Crosshead

6) The crosshead was then lowered, while the fatigue test specimen was simultaneously guided the along the threaded rod of the load piston until it rested on the bottom bearing plate without contacting rollers T1 or B1 as shown in Figure 3–41.

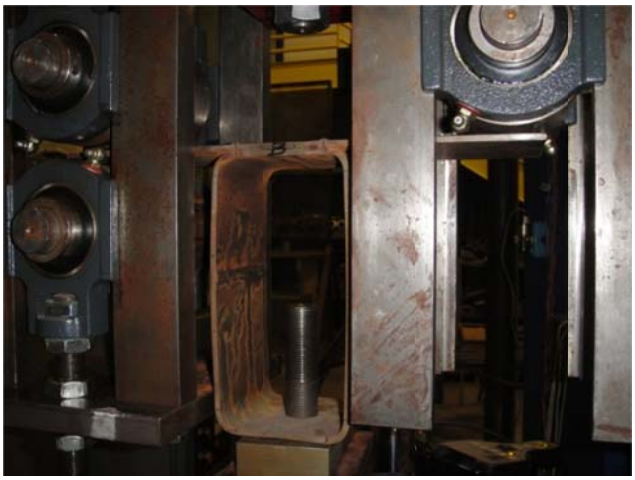

Figure 3–41: Fatigue Test Specimen Placement into the Load Frame

7) The top bearing plate was inserted onto the load piston's threaded rod, sandwiching the bottom HSS flange of the fatigue test specimen between bearing plates. The 1-1/2" hex nut was then screwed into position loosely over the top bearing plate. It was important to make sure that the both the top and bottom bearing plates were parallel with one another, in addition to the bottom of the HSS section. Please refer to Figure 3–42.

Figure 3–42: Fatigue Test Specimen Alignment with Bearing Plates

8) The fatigue test specimen was then leveled using a target bubble level placed on top of the specimen's plate. It was important that target level rested flush on the plate's surface. For this reason the target level was usually placed outside the weld area closer to the roller to avoid an uneven surface from any laser weld spatter, Figure 3–43.

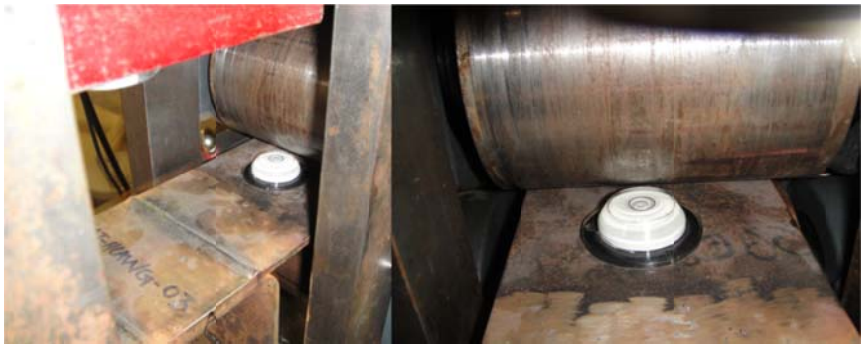

Figure 3–43: Leveling the Fatigue Test Specimen on the Load Piston

9) The 1-1/2" hex nut was then tightened to provide a secure connection to the load piston and engage full contact between bearing plates. The target level was re-checked to assure that the specimen remained level. If for any reason the specimen was not level after tightening, steps 8 and 9 were repeated.

10) The bottom plate supporting roller B2 removed previously was re-fastened to the load frame via the (8) 3/8" hex bolts.

11) Using the 1-5/16” adjustment bolts, all four rollers were positioned as close as possible to the surface of the test specimen without any contact.

12) In the station manager a mean/amplitude force meter was created to provide a live reading of the force in the 110 kip MTS force transducer. The force was then offset to zero and the auto offset option was locked. This meter type was selected since the live force reading was ±5 lbs, which was a problem due to the relatively small forces needed to set the test specimen in place.

13) In order to achieve a load rate during cyclic fatigue testing from 5 Hz to 7 Hz, an evenly distributed clamping force of approximately 30 lbs along the centerlines of each set of the rollers, 60 lbs total was required. The procedure of applying equivalent clamping force to each roller was extremely convoluted and difficult task, due to the very flexible test specimen in relation to the load frame and the precision of the 110 kip MTS force transducer. Through numerous trials, the following procedure was discovered to be the best approach to apply 60 lbs of clamping force through the rollers to the test specimen. It should be noted that this procedure was frequently repeated due to the difficulty of aligning the rollers in perfect manner that was required. Also, in most cases due to a slight unbalance of rollers during the adjustment process and the precision of the associated MTS force transducer, the clamping force varied ± 15lbs. This was later discovered to present a problem in determining the stress range that is discussed in sections 3.4.3 and 4.1.1.4.

    a) Roller B2 was raised by hand using both of the interior 1-5/16” adjustment bolts simultaneously, while maintaining a leveled roller to provide even contact with the specimen plate until the force meter mean readout read 5 lbs ± 0.5 lbs.

Roller B1 was raised by hand in the same manner until the force meter mean read 10 lbs ± 1 lbs.

b) Rollers T1 and T2 were then released from all 1-5/16" adjustment bolts and lowered slowly to rest on top of the specimen, sandwiching the plate between rollers. The force meter mean was then recorded, which typically read around 8 lbs.

c) Roller T1 was lowered using the interior 1-5/16" adjustment bolts by hand until the force meter mean read half of the previously recorded value. Roller T2 was then lowered in the same manner until the force meter mean read zero. At this time 10 lbs of clamping force, 5 lbs per roller, was achieved.

d) Roller B2 was raised using a wrench to turn both interior 1-5/16" adjustment bolts equally, to raising the roller in a level fashion, until the force meter mean read 10 lbs ± 0.5 lbs. Roller B1 was then raised in the same manner until the force meter mean read 20 lbs ± 1 lbs.

e) Roller T1 was lowered using a wrench to turn both the interior 1-5/16" adjustment bolts equally, lowering the roller in a level fashion, until the force meter mean read 10 lbs± 0.5lbs. Roller T2 was then lowered in the same manner until the force meter mean read 0 lbs± 0.5lbs. At this time 30 lbs of clamping force, 15 lbs per roller, was achieved.

f) Roller B2 was raised once again, using a wrench to turn both interior 1-5/16" adjustment bolts equally, to raising the roller in a level fashion, until the force meter mean read 15 lbs ± 0.5 lbs. Roller B1 was then raised in the same manner until the force meter mean read 30 lbs ± 1 lbs.

g) Roller T1 was lowered again using a wrench to turn both the interior 1-5/16" adjustment bolts equally, lowering the roller in a level fashion, until the force meter mean read 15 lbs± 0.5lbs. Roller T2 was then lowered again in the same manner until the force meter mean read 0 lbs± 0.5lbs. At this time the final clamping force of 60 lb was achieved, 30 lbs per roller.

h) All 8 exterior 1-5/16" adjustment bolts were then tightened to secure the clamping force adjustment during cyclic fatigue test. First all the exterior 1-5/16" adjustment bolts were hand tightened, and then further tightened using a wrench for an additional half revolution. Fine adjustments were then made until the force meter mean was at 0 lbs ± 0.5lbs.

14) Once the clamping force was applied correctly; the station manager was used to offset the displacement to zero.

15) The manual control module was then turned off and all external interlocks were alleviated. External interlocks included the stop button and crosshead lock of the MTS Landmark Servohydraulic test system.

16) Using the station manager in the MTS 793 software, a new specimen was created with name of the fatigue test specimen and assigned the corresponding test procedure. The software procedure lock was engaged and the fatigue testing was initiated.

17) Due to the response lag from the fatigue specimen to the command function; there was a difference in amplitude between the force command function and the actual force applied to the specimen. In order to align the amplitudes of the actual force in the specimen to the command force, the P-gain and I-gain were adjusted accordingly. This adjustment was made within the first 1000 cycles.

3.4.1.3.2 Automated Control Procedure

A test procedure was developed using the procedure editor in Multi-Purpose Testware (MPT) of the MTS 793 software. The procedure was programmed to fully automate each fatigue test by providing load control criteria and test interlock parameters for the MTS HPU, as well as data acquisition initiation detectors for the MTS 793 software. The load command developed for this procedure utilized a sine wave loading function with peak/valley values of equal magnitudes, but opposite signs to the corresponding cyclic load as defined in__. The loading frequency and number of cycles to distinguish a test run-out were also defined in the load command. A test run-out was characterized as 10 million cycles and in the case it was reached, an interlock was tripped to end the test. A load rate ranging from 5 to 7 Hz was specified, dependent on load magnitude and specimen response lag.

The procedure was programmed to detect crack initiation and failure through the use of two data limit detectors in the MPT. The peak/valley change detector in the MPT was implemented to monitor the relative difference in displacement between the peak/valley of consecutive load cycles. In essence crack initiation was perceived as a rapid change in displacement. This limit varied between individual fatigue tests, dependent on the magnitude of cyclic load, P, but if tripped would halt the test in progress. The other data limit detector utilized to monitor each fatigue test was a peak/valley displacement detector. Through this command an upper and lower limit for vertical displacement was set to prevent damage to the test system, as well as provide an additional fail safe to end the test.

To provide detailed log and quantitative understanding of each fatigue test, three data acquisition commands were added to the MPT procedure. Any given test was stopped and resumed within the first couple thousand cycles to determine the loading frequency based upon the ability to tune the proportional and inverse gain to compensate for specimen lag, as well as noise the load signal. The ability to tune the actual force received by the force transducer to the force command generally relied on clamping force and cyclic load magnitude. For maximum productivity the highest cyclic load rate was desired, but was limited to that which was achievable. Therefore, the force in the specimen was not stabilized until approximately 1,000 to 2000 cycles after the test was initiated. This data was important in that it typically provided a wide array of data points that allowed the elastic relationship for the stiffness of the overall system prior to fatigue cracking. Later this relationship was proven to be crucial to the overall stress range prediction that is discussed later sections.

In order to document this data, a data acquisition command was implemented to the procedure to record the first 2000 cycles of peak/valley load and displacement after each instance the test was initiated. To provide a comparison of the system stiffness before and after crack initiation, another command for data acquisition was employed into the MPT procedure that recorded the last 2000 cycles of peak/valley load and displacement after each instance the test was stopped. Both sets of data provided quantitative documentation for all tests to demonstrate the structural response of each specimen during the regulation of the cyclic load command and cycles right before failure. Lastly, a third data acquisition command was added to MPT procedure to document the progress of each test by recording the peak/valley load and displacement every 30 minutes.

3.4.1.4 Failure Criterion

Defining the failure criteria was not a simple task given that the crack initiation site was invisible to the naked eye. Depicted in Figure 3–44, the highest stress concentration analyzed was on the underside of the $^{3}/_{16}$" plate, perpendicular to the laser stake weld, located at the center of the interface sandwiched between the HSS plate. It was believed that the crack began at this location and propagated outwards in a circular pattern through the plate. Though the procedure described previously accounted for crack initiation, the set limit for the peak/valley change detector was subjectively determined and did not possess the precision needed to define failure throughout each test. Therefore, test failure was defined at point during the test that the load command was no longer achievable.

Since the fatigue test durations extended in the upwards of week, it was impossible to maintain a constant watch over the entire test. Thus, the peak/valley change detector limit was set with a relatively low to stop the test in any event of a change in stiffness. With regular inspections, engaging this detector was anticipated. At this point the specimen was visually examined for cracks and in the event none were identified, the test was resumed. The remainder of the fatigue test was then monitored closely until failure was observed from the live display of force command and force measured. Occasionally, failure would occur rapidly, which was recognized by the peak/valley displacement.

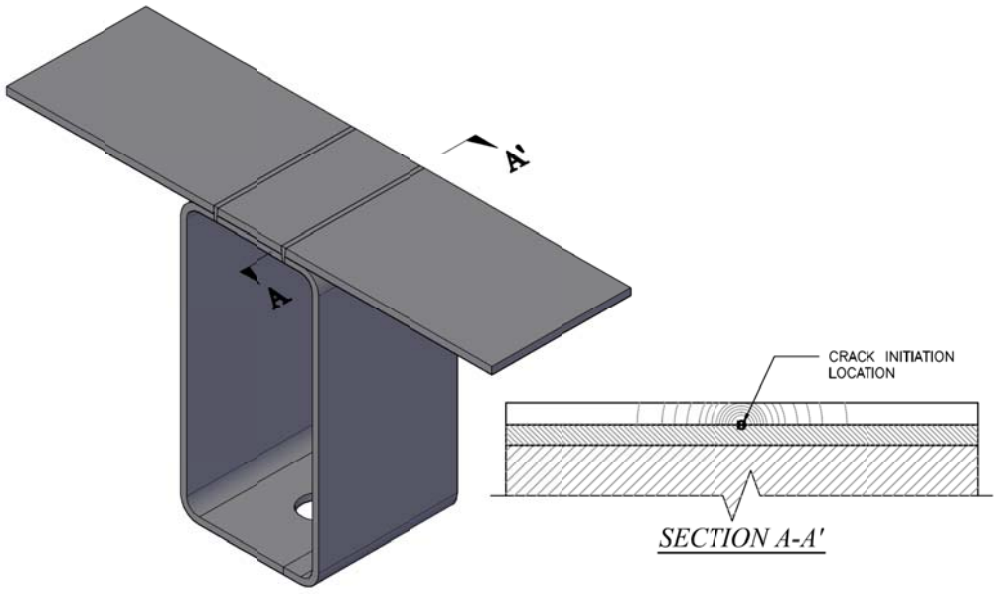

Figure 3–44: Hypothesized Fatigue Crack Initiation Location

3.4.1.5 Failure Documentation

As a baseline investigation, it was important to provide well detailed documentation of each failure. The direction for any unfamiliar research endeavor constantly evolves with new discoveries and the realization of unknown parameters. Additionally, in the event this research is continued; the documentation can possibly provide insight to support other themes found in future studies. Given this reasoning, the failure characteristics of all fatigue test specimens were methodically logged, with the exception of test run-outs. Each set of failure surfaces and two sets of failure profiles were photographed for each specimen following the same precautions outlined in section 3.2.2 and scaled according to the procedures described in 3.2.3. The photographs were then cataloged with the test setup, failure type, cyclic load magnitude, loading frequency, number of cycles to failure, and runtime. All failure documentation can be found in Appendix F.

3.4.1.6 Testing Program

The testing matrix displayed below in Table 3-5 summarizes the tests performed in the fatigue testing program.

Table 3-5: Fatigue Testing Matrix

Cyclic Load $R_P = -1$ $P_{min,max}$ *(lbs)*	**Weld Process** (*Weld Component Gap Range*)																			
	LBW *(0 .000)"*	**HLAW** *(0 .000)"*	**LBW** *(0.000 - 0.003)"*	**HLAW** *(0.000 - 0.004)"*	**LBW** *(0.003 - 0.006)"*	**HLAW** *(0.004 - 0.006)"*	**LBW** *(0.006 - 0.010)"*	**HLAW** *(0.006 - 0.009)"*	**LBW** *(0.010 - 0.012)"*	**HLAW** *(0.009 - 0.010)"*	**LBW** *(0.012 - 0.016)"*	**HLAW** *(0.010 - 0.014)"*	**LBW** *(0.016 - 0.018)"*	**HLAW** *(0.014 - 0.019)"*	**LBW** *(0.018 - 0.022)"*	**HLAW** *(0.020 - 0.025)"*	**LBW** *(0.022 - 0.032)"*	**HLAW** *(0.025 - 0.035)"*	**LBW** *(0.032 - 0.035)"*	**HLAW** *(0.035)"*	**LBW** *(0.035)"*
425		1		1				1				1				1				1	
400	3	3			1	1			1	1			1	1			1	1			1
375		3																			
350		2	1				1				1				1				1		
300	3																				
250	2	1																			
200	1																				

3.4.1.7 Fractography

To the naked eye, the failure surfaces from initial fatigue tests did not exhibit any characteristics of typical fatigue failure such as beach marks.(Dowling, 2007) Alternatively, peculiar rounded protrusions and depressions on each failure surface were observed and raised question to the classification as a fatigue driven failure. Consequently, in order properly classify the failure mechanism of each test, fractographic methods were needed. Through the use of the FEI Quanta 600 FEG Environmental Scanning Electron Microscope (SEM) located in the ICTAS Nanoscale Characterization and Fabrication Laboratory (NCFL) at Virginia Tech, the failure surfaces were studied on microscopic level to identify known failure characteristics such as ductile dimples, brittle cleavage, and striations from crack propagation.

3.4.2 ELASTIC LOAD TEST

An elastic static strain test was performed to provide insight to the structural behavior of fatigue test specimens in relation to the analytical model created. A fatigue test specimen was instrumented with various strain gages to monitor bending induced strains in targeted areas during an elastic load test. The same test was simulated using the finite element analysis described in section 4.1, allowing for direct comparison of the results, as well as verification to the modeling methodology.

3.4.2.1 Setup

Test specimen FAT-LBW-02 was instrumented with a total of 6 strain gages according to the installation scheme depicted in Figure 3–45. Micro-Measurements (MM) linear pattern, general all-purpose strain gages with a gage length $^{1}/_{8}$", 350 Ω resistance, and a gage factor of 2.105 were used. Proper installation procedures recommended by the manufacturer were methodically followed to initiate the highest level accuracy during testing. The instrumented FAT-LBW-02 specimen was then set onto the MTS actuator and into the load fixture used throughout the fatigue testing according to the same set of meticulous procedures outlined in section 3.4.1.3.1. The only difference between the physical setup with this particular test was an elevation in precision. Typically, roller adjustment was a convoluted task due to the difference in relative stiffness between the $^{3}/_{16}$" plate and the load fixture. The live display of measured strain in the six locations of the $^{3}/_{16}$" plate greatly simplified the roller adjustment and reassured zero initial strain.

Provided that the MTS control station was unable to suffice as a data acquisition system for the strain gages during the elastic load test, a Vishay System 5000 was utilized in conjunction with the MTS control station during testing. In order to correlate the measured strains recorded by the System 5000, to the data outputted by the MTS force transducer and actuator LVDT; a standalone Trans-Tek LVDT with 0.310 inches of travel was installed along the centerline of the $^{3}/_{16}$" plate as shown in Figure 3–46.

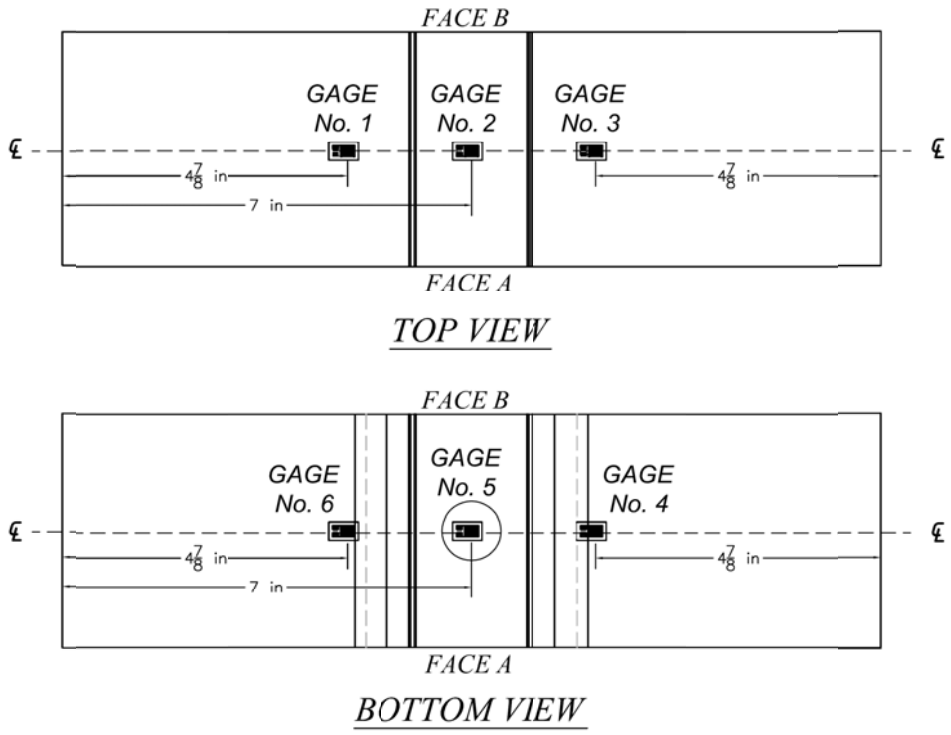

Figure 3–45: FAT-LBW-02 Strain Gage Installation Locations and Numbering Scheme

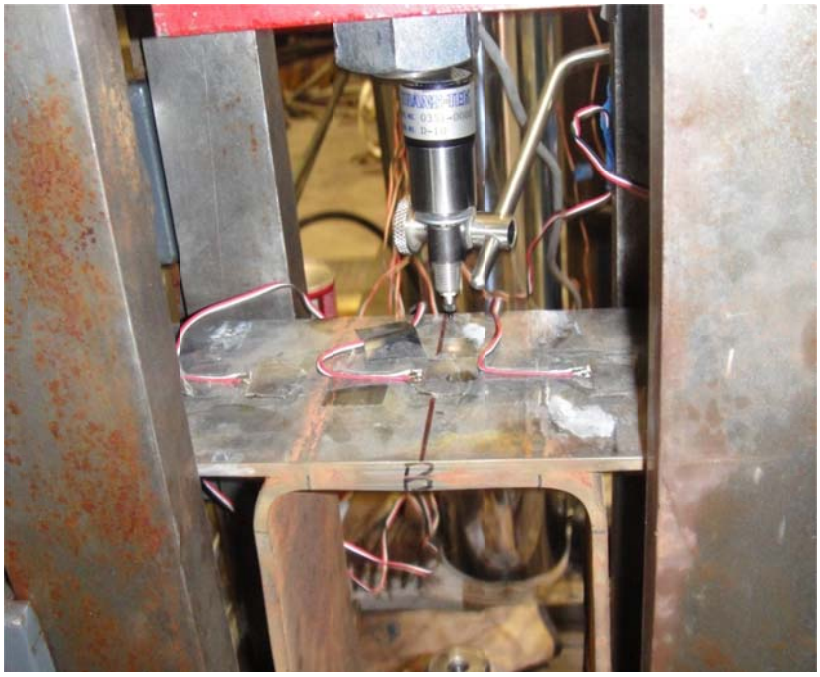

Figure 3–46: Standalone LVDT for Strain Data Correlation

3.4.2.2 Procedures

Using the incorporated strain smart software to the System 5000, a continuous test session with a sample rate of 10 Hz was created to record the measured strain in each of the 6 gages and vertical displacement measured by the LVDT simultaneously. Another procedure was created using the procedure editor in MPT of the MTS 793 software to perform a displacement controlled elastic load test on the instrumented test specimen. A displacement command using a segmental ramp function with upper and lower bounds of ±0.05 inches was specified at a frequency of $^{1}/_{80}$ Hz for duration of 20 cycles. The bounds for the ramped displacement function were determined at 50% yield from the initial analytical model assuming roller-roller boundary conditions. A data limit detector was added to the procedure as a precaution to limit the load magnitude to 500 lbs in either direction. In the event this limit was reached, the test would terminate to prevent the possibility of yielding. Lastly, a timed data acquisition command with a sample rate

of 20 Hz was implemented into the procedure to record time, running time, displacement command, measured displacement in the MTS actuator LVDT, and measured load in the MTS force transducer.

To allow for the correlation between both sets data outputted from the MTS and Vishay System 5000, the test session created in the strain smart software was initiated approximately 10 seconds prior to the commencement of the procedure created in MPT of the MTS 793 software. After testing, both sets of data were then synchronized according to the initiation of a change in vertical deflection recorded by the standalone LVDT. Using the find command in Matlab, the surplus of MTS data was refined to coincide with the strain data recorded in the test specimen.

3.4.3 PARTIAL RESTRAINT VERIFICATION TESTING

Following the elastic static strain test of fatigue test specimen FAT-LBW-02 it was founded that the boundary conditions of the test setup were not definitive. Test specimens fell between a roller-roller and fixed-fixed condition, which with this investigation was determined to be highly dependent on clamping force. Unfortunately this measure was nearly impossible to quantify during the setup of each fatigue test, due to the specimen's thin nature and extreme flexibility relative to the loading frame as discussed. In addition, using the accompanying 110 kip MTS load cell to gage forces smaller than 50 lbs only further complicated this problem. After the termination of nearly every fatigue test, a strip approximately an eighth of an inch in width along the plate was observed to be scratched as a result of contact with testing rollers, Figure 3–47. An idea was than formulated to model the partially restrained conditions with grounded springs along the nodes that fell within this contact region, in addition to the roller-roller boundary conditions already in place. Please refer to section 4.1.1.4. In order to justify this analysis method, the following test was performed to demonstrate the influence of clamping force on system stiffness for both LBW and HLAW test specimens.

Figure 3–47: Residual Scratches from Roller Contact during Fatigue Testing

3.4.3.1 Methodology

To demonstrate the clamping force influence on the overall structural behavior of each fatigue test, elastic load tests were performed at five varying increments of clamping force. As discussed previously, the clamping force was impossible to gage through MTS force transducer due to the flexibility in the $^{3}/_{16}$" plate. Therefore, independent load cells were installed to gage the clamping force in each set of rollers. It was hypothesized that single degree of freedom stiffness of the overall system would possess a mutual relationship with clamping force, bounded by roller-roller and fixed-fixed boundary conditions.

3.4.3.2 Setup

Test specimens FAT-LBW-09 and FAT-HLAW-06 were instrumented with 8 strain gages according to the instrumentation scheme displayed in Figure 3–48. The two additional strain gages in comparison to the elastic load test were installed to study plate behavior near the roller contact area. The identical strain gages were used and installed taking the same precautions as in the elastic load test. The standalone Trans-Tek LVDT was installed along the centerline of the $^{3}/_{16}$" plate, as displayed in Figure 3–46. The standalone LVDT deflections were used to correlate the MTS data to the strain and load recorded by the System 5000 in the same manner used for the elastic load test.

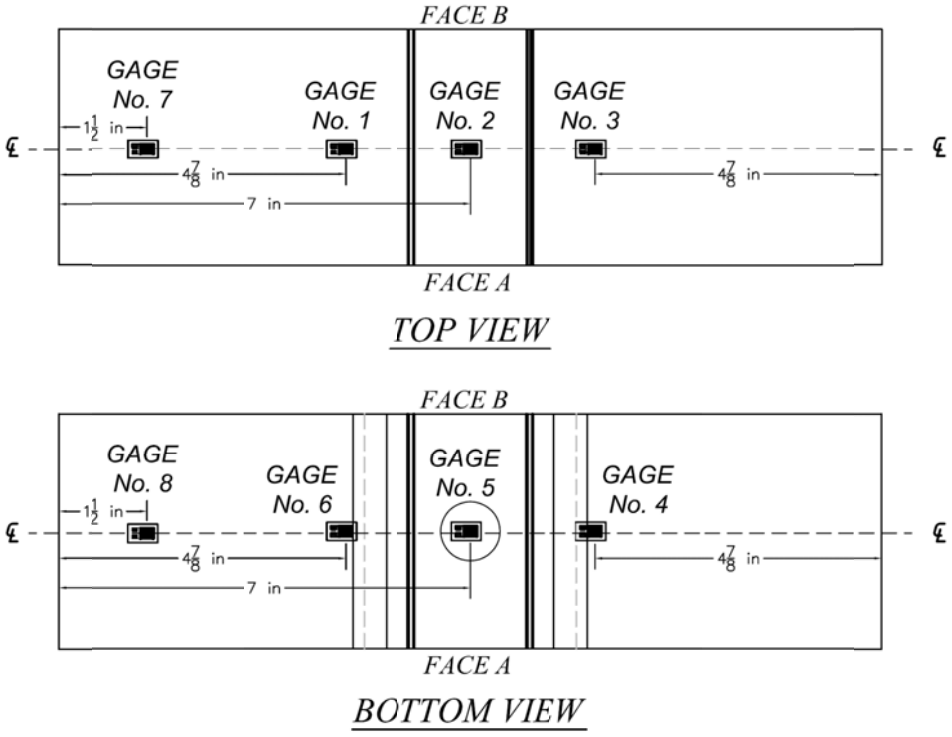

Figure 3–48: FAT-LBW-09 & FAT-HLAW-06 Strain Gage Installation Locations and Numbering Scheme

The load fixture depicted in Figure 3–32 and Figure 3–33 used throughout the fatigue testing and elastic load test was modified to allow for the measurement of clamping force through independent loads. The four threaded rods and accompanying adjustment nuts connected to bottom rollers were removed, causing them to rest on the fixture plate as shown in Figure 3–49. Each set of threaded rods were replaced with two 10 kip load cells along their previous centerline, each sandwiched between two $2^1/_2$"x$2^1/_2$"x$^3/_8$" steel plates illustrated in Figure 3–50. A direct measurement of clamping force in each roller was then obtained through the sum of the reaction forces gaged by both load cells for each roller illustrated by Figure 3–51. To prevent the experimental errors discussed in section 3.4.1.2, an amended set of detailed procedures were developed and precisely followed to set each specimen onto the MTS actuator and modified load fixture that are described in section 3.4.3.3.1.

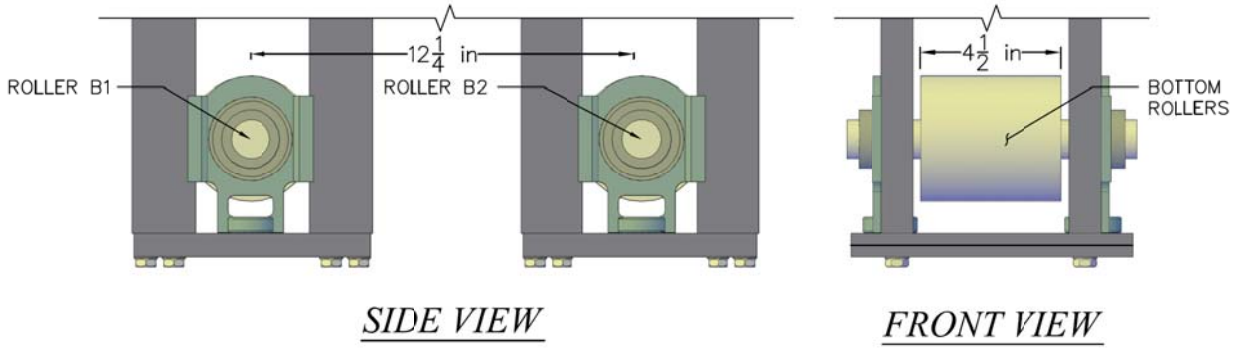

Figure 3–49: Modifications to the Load Fixture for Partial Restraint Verification Testing

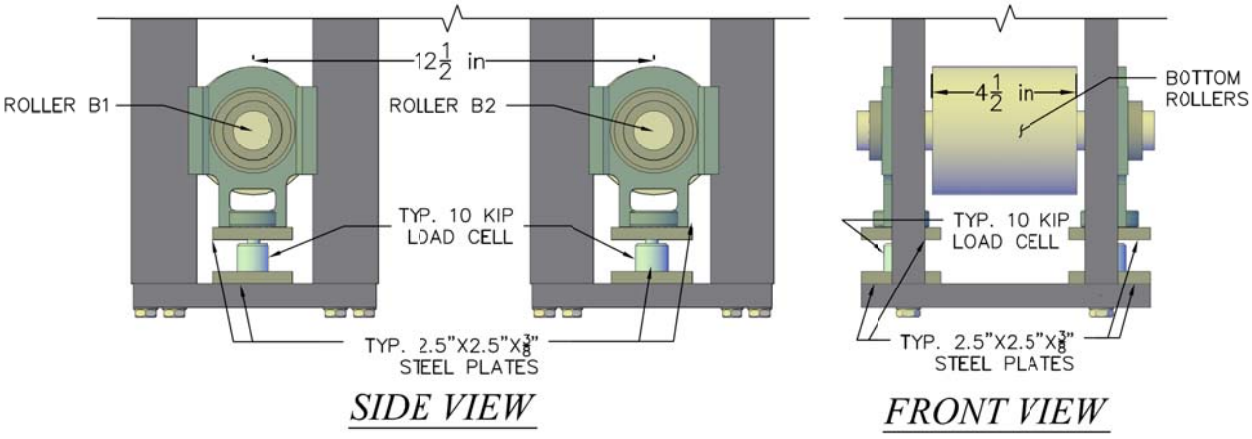

Figure 3–50: Independent Load Cell Placement Incorporated into the Load Fixture

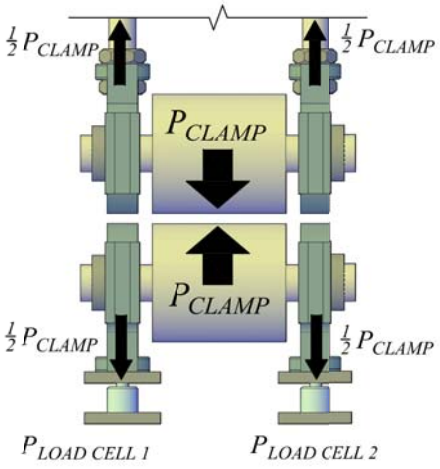

$$P_{CLAMP} = \Sigma P_{LOAD\ CELL}$$

Figure 3–51: Clamping Force Load Path

3.4.3.3 Procedures

The amended set of procedures devised for the physical setup of FAT-LBW-09 and FAT-HLAW-06 onto the MTS actuator and into the modified load fixture is described in section 3.4.3.3.1 They were developed to minimize experimental error, while applying an accurate clamping force to each test specimen in a precise manner. To generate a displacement controlled elastic load test for each increment of clamping force, the procedure developed in the MPT of the MTS 793 software described in section 3.4.2.2 was used. A data session was created in the strain smart software associated with Vishay System 5000 for each increment of clamping force to record force in the four load cells, strain from the eight strain gages, and displacement from the standalone LVDT continuously at sample rate of 10 Hz.

A total of five displacement controlled elastic load tests were carried out for each test specimen to observe the variance in structural behavior between 40, 200, 600, 1200, and 2400 lbs of clamping force per roller. Prior to the physical setup of each test, the corresponding data session in the strain smart software was armed to provide a live display of measured strain and force. This ensured zero strain prior to the commencement of the displacement controlled elastic load test and accurate application of the desired clamping force in each roller. Once the test specimen was properly set onto the MTS actuator and into the modified load fixture, the armed data session was engaged into the record mode. The procedure for the displacement controlled elastic load test was then finally initiated. After all testing was completed; the two corresponding data sets from the MTS and System 5000 were refined using the same method described in section 3.4.2.2.

3.4.3.3.1 Physical Setup into the Modified Load Fixture

To begin, each specimen was fixed to the MTS actuator according to steps 2 through 10 previously defined in section 3.4.1.3.1. The following process was then followed to apply the desired clamping force per roller to the test specimen.

1) The bottom roller B2 was raised and two 10 kip load cells, each sandwiched between two 2.5"X2.5"X$^{3}/_{8}$" steel plates were placed at the centerline of previously existing 1" threaded rods used for the vertical adjustment of each roller. Please refer to Figure 3–52.

Figure 3–52: Placement of Independent 10 k Load Cells

2) The data session created in the strain smart software associated with the System 5000 was armed and online displays were created to provide live readouts of measured load in the four 10 kip load cells, as well as strain in the eight instrumented areas.
3) Using the manual displacement control in the MPT of the MTS 793 software, the specimen fixed to the MTS actuator was lowered initiating contact with the bottom rollers connected in series to the four load cells. The specimen was lowered until the maximum live strain readout from strain gages 1, 3, 4, and 6 was approximately 60 με.

4) As a result of imperfections and fabrication tolerances of the $^{3}/_{16}$" plate, the current configuration caused non-uniform contact between the $^{3}/_{16}$" plate and the bottom rollers. To prevent torsion from non-uniform contact illustrated in Figure 3–36, cutouts from a thin gauge cold form steel sheet were wedged underneath the bottom 2.5"X2.5"X$^{3}/_{8}$" plates supporting each load cell accordingly to create uniform contact as shown in Figure 3–53. This painstaking process required numerous iterations until an even strain distribution was observed in strain gages 1 through 6. Typically at this point in time, the measured force in each load cell was approximately 20 lbs, equating to 40 lbs of clamping force per roller.

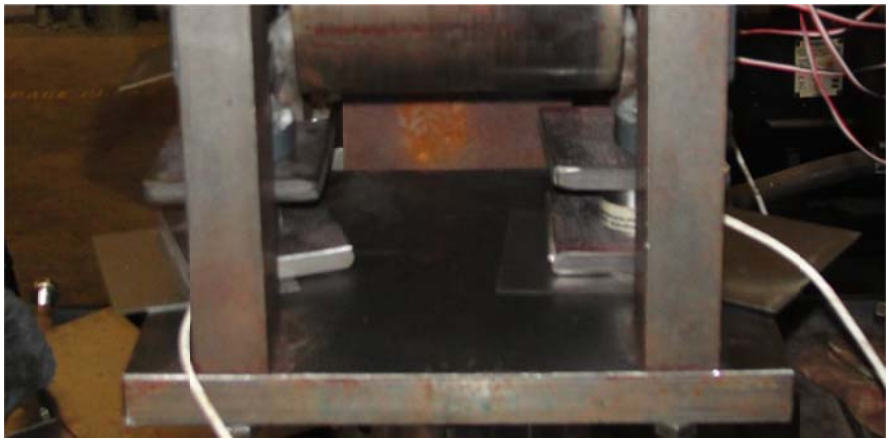

Figure 3–53: Cold Form Steel Sheets used to Adjust for Uniform Contact

5) Rollers T1 and T2 were then released from all 1-$^{5}/_{16}$" adjustment bolts and lowered slowly to rest on top of the specimen, sandwiching the plate between rollers. The two 1$^{5}/_{16}$" adjustment bolts for each roller were tightened equally, until the measured load in each of the two corresponding load cells read one half the desired clamping force per roller with a range of ±5 lbs.
6) To reassure an even strain distribution in the $^{3}/_{16}$" plate, strain gages 1 through 6 were checked once again. Generally, the strain initially induced in $^{3}/_{16}$" plate

from lowering the specimen was still present, but with lower magnitudes due to some relief from the applied clamping force. It was crucial to the accuracy of the test that the strain was evenly distributed throughout the plate at this point time. Thus, in the event the strain was not evenly distributed, the clamping force was removed and reapplied using the same process.

7) To alleviate the residual strain in the $^{3}/_{16}$" plate, the actuator was raised at 0.0005 inch increments until the live display read ±2 με in strain gages 1 through 6.
8) The measured force in the load cells was rechecked to assure that desired clamping force was maintained. Occasionally, a slight reduction of load occurred and the upper rollers were readjusted, equally tightening 1-$^{5}/_{16}$" adjustment bolts to achieve the desired clamping force. With this occurrence, the actuator was lowered at 0.0005 inch increments until the live display once again read ±2 με in strain gages 1 through 6.
9) In the station manager a mean/amplitude force meter was created to provide a live reading of the force in the 110 kip MTS force transducer. The force was then offset to zero and the auto offset option was locked.
10) The station manager was used to offset the displacement to zero.
11) The manual control module was then turned off and all external interlocks were alleviated. External interlocks included the stop button and crosshead lock of the MTS Landmark Servohydraulic test system.
12) The associated data session in the strain smart software incorporated with the Vishay System 5000 was turned to record mode.
13) Using the station manager in the MTS 793 software, a new specimen was created

with name of the test specimen and applied clamping force, as well as assigned to the displacement controlled elastic load test procedure. The software procedure lock was engaged and the test was initiated.

3.4.4 FATIGUE CONFIRMATION TESTING

Unfortunately, a nominal stress range was not applicable to the laser welded connection in question, as a result of the non-definitive boundary condition problem and the localized stress concentration in the plate at the laser weld. Therefore, a customized analysis method, described in section 4.1.2.2 , was implemented to predict the stress range in each fatigue test. Provided that the analysis method was believed to obtain a stress value extremely close to the true stress in the $^{3}/_{16}$" plate, the results were comparable to AASHTO detail category A. In order to confirm the findings from the fatigue tests described in section 3.4.1, tensile fatigue tests were performed with a known nominal stress range to allow for the comparison with other AASHTO weld categories.

3.4.4.1 Methodology

To confirm the findings from the testing program described in section 3.4.1, a tensile fatigue test was designed around the loading configuration shown in Figure 3–54. Test specimens were set into a pair of hydraulic grips and cyclically loaded in pure tension with a stress ratio, R= 0 at a frequency ranging from 10 to 15 Hz. Unlike the previous fatigue testing program, these fatigue tests were regulated with a known nominal stress range. Nominal stress ranges of 35 ksi and 30 ksi were selected for the LBW and HLAW fatigue test specimens respectively. Through an initial comparison with AASHTO fatigue categories, the laser welded connection between the bottom plate and HSS internal stiffening rib was considered to resemble either a welded cover plate connection, detail category E' or a full penetration groove welded butt splice, LBW detail category B and HLAW detail category C.

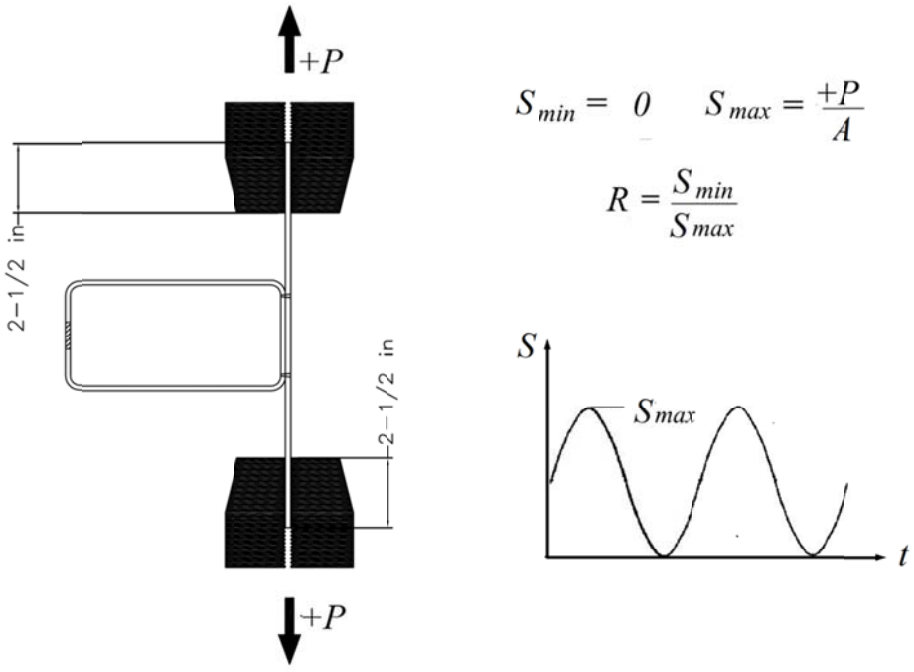

Figure 3–54: Fatigue Test Confirmation Testing Configuration

3.4.4.2 Setup

Each specimen was placed into the MTS 647 Hydraulic Wedge Grip assembly incorporated into the cross head and actuator of the MTS Servohydraulic Landmark test system as shown in Figure 3–55: MTS 647 Hydraulic Wedge Grip. The upper grip assembly was connected in series with the 110 kip force transducer to the cross head in order to provide a measurement for load. While the lower grip assembly was joined directly into the load piston, taking advantage of the integrated LVDT to measure displacement. To provide a suitable connection between the hydraulic grip assemblies and the Landmark test system during fatigue testing, as well as align the pair of hydraulic grips to prevent torsion in test specimens; a 4”X10”X$^3/_8$” steel bar was used to preload the assembly with 50 kips.

Figure 3–55: MTS 647 Hydraulic Wedge Grip Assembly

As was the case with the initial fatigue testing program, a set of procedures were meticulously followed during the test setup to minimize experimental error and maintain testing precision that are outlined in section 3.4.4.3.1. Ensuring that each test specimen remained plumb throughout the test setup was important to maintain a uniform tensile stress distribution throughout the specimen's $^{3}/_{16}$" plate during testing. Therefore, special attention was allotted to each test specimen during the vertical alignment and placement of into the hydraulic grip assemblies. Assuming a discontinuity at the laser weld, essentially two plates were tested in series as shown in Figure 3–56. To prevent a difference in displacement in each of the two plate sections, additional measures were taken to ensure that equivalent lengths of the $^{3}/_{16}$" plate were fixed into the upper and lower hydraulic grip assemblies. Even though in theory the stress and strain in each of the two plate sections should be equal, this precaution was taken as a preventative measure.

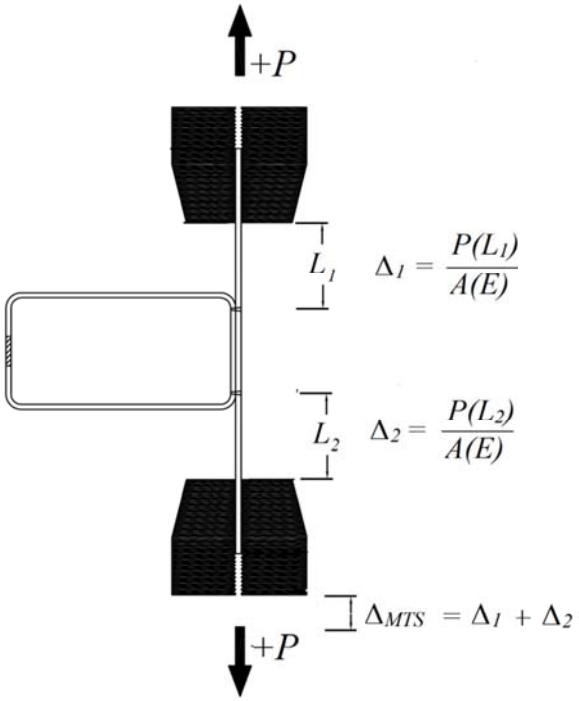

Figure 3–56: Tensile Fatigue Test Displacement

3.4.4.3 Procedures

The tensile fatigue confirmation tests were conducted in nearly the same manner as the initial fatigue testing program. Regimented procedures were implemented for specimen setup and automated control during testing. Setup procedures outlined in section 3.4.4.3.1, were followed to properly fix each specimen into the hydraulic grip assembly. The automated procedure developed for initial series of fatigue tests in the MPT of the MTS 793 software was slightly modified to accommodate for a stress ratio of $R = 0$ and the maximum testing tensile stress, otherwise remained identical to the procedure described in section 3.4.1.3.2. In order to determine the maximum tensile load to achieve the desired testing stress, a set of calipers was used to gage the cross sectional area by measuring thickness of the $^{3}/_{16}$" plate in four locations around the laser welds to develop an accurate and precise mean plate thickness.

3.4.4.3.1 Physical Setup into the MTS 647 Hydraulic Grip Assembly

1) To begin, it was important that 2 ½" of either end of the $^{3}/_{16}$" plate was set into both hydraulic grip assemblies. This would not only provide ample clamping force to prevent slip , but also ensure that equal lengths were fixed in the upper and lower hydraulic grips to prevent a difference in displacement in each of the two plate sections separated by the laser stake welds. Therefore, 2 ½" offset lines from either end of the $^{3}/_{16}$" plate were created. First, a set of calipers was used to mark three points 2 ½" from either end of the $^{3}/_{16}$" plate using a pencil. A permanent marker was then used to connect the marks using a straight edge to create the 2 ½" offset line referenced during the test setup. Please refer to Figure 3–57.

Figure 3–57: Creation of Tensile Fatigue Test Specimen Offset Lines

2) Using the station manager from the MPT of the MTS 793 software integrated with the MTS Landmark Servohydraulic Test System, the hydraulic pump was turned on and hydraulic flow was initiated to the loading piston.
3) In the station manager a mean/amplitude force meter was created to provide a live reading of the force in the 110 kip MTS force transducer. The force was then offset to zero and the auto offset option was locked.
4) The station manager was then switched to manual control in displacement mode and the load piston was raised/lowered to the approximate median of its travel distance.
5) The manual control was then switched to force mode and set to a value of zero.
6) The MTS Landmark Servohydraulic Test System's cross head was then raised to allow clearance for the fatigue test specimen.
7) The lower and upper hydraulic grips were then fully opened.
8) The fatigue test specimen was placed into the open hydraulic grip assembles so that side A faced outward and the joined HSS pointed away from the control station. The specimen was then held in position so that it remained in contact with the associated guides that were initially adjusted to maintain a plumb setup. Simultaneously the specimen's vertical position was adjusted so that 2 ½" offset line was aligned with the edge of the set lower hydraulic grip wedges. The lower set of hydraulic grips was then closed with 4,000 psi of clamping pressure, securing the specimen into the lower hydraulic grip assembly. Please refer to Figure 3–58.

Figure 3–58: Specimen Placement into the Lower Hydraulic Grip Assembly

9) To confirm that the specimen remained plumb while securing it into the lower hydraulic grip assembly, a bubble level was used as shown in Figure 3–59. In the event that the specimen was not plumb, it was removed and reinstalled into the lower hydraulic grip assembly.

Figure 3–59: Check to Ensure Test Specimen Remained Plumb

10) The cross head was lowered until the other 2 ½" offset line was aligned with the edge of the upper hydraulic grip wedges, as depicted in Figure 3–60. The upper set of hydraulic grips was then closed with 4,000 psi of clamping pressure, securing the specimen into the upper hydraulic grip assembly.

Figure 3–60: Test Specimen Alignment into the Upper Hydraulic Grip Assembly

11) The manual control was then switched to force mode and set to a value of zero to alleviate the vertical force locked into the specimen from securing into both hydraulic grip assembles.

12) The manual control module was then turned off and all external interlocks were alleviated. External interlocks included the stop button and crosshead lock of the MTS Landmark Servohydraulic test system.

13) The station manager was then used to offset the displacement to zero.

14) A new specimen was created using the station manager with name of the fatigue test specimen and assigned to the corresponding test procedure. The software procedure lock was engaged and the fatigue testing was initiated.

3.4.4.4 Failure Criterion

Defining the failure criteria was much simpler than the initial fatigue testing program. Provided that the tests were conducted at far higher loads, the failure was abrupt, leaving no room for interpretation. Detectors set in the automated procedure captured failure, generally from the limit set on maximum displacement, provided that all but one specimen completely separated at the laser weld interface.

3.4.4.5 Failure Documentation

The failure characteristics of all tensile fatigue test specimens were methodically logged in the same manner as the initial testing program described in section 3.4.1.5. Please refer to Appendix F for all failure documentation.

3.4.4.6 Testing Program

The testing matrix displayed below in Table 3-6 summarizes the tests performed in the tensile fatigue confirmation testing program.

Table 3-6: Fatigue Confirmation Testing Matrix

Cyclic Stress S_{max} *(ksi)* $R = 0$	**Weld Process** (*Weld Component Gap Range*)	
	LBW *(0 .000)*"	**HLAW** *(0 .000)*"
30		2
35	3	

4.1 FATIGUE TEST SPECIMEN FINITE ELEMENT ANALYSIS

A finite element analysis was required to determine the reported stress range for each experimental fatigue test. The ideal approach for this problem was to model each individual specimen with tailored dimensions to achieve the highest level of accuracy. Using this logic, an adaptable program was created in Matlab to generate input files for each individual fatigue test specimen to be analyzed in ABAQUS v6.9. Unfortunately, this approach was not feasible due to the partially restrained boundary conditions and component sensitivity discussed later in section 4.1.1.6.2. Thus, the developed Matlab program was used to model a generalized fatigue test specimen with customized boundary conditions to each experimental fatigue test.

4.1.1 MODELING METHODOLOGY

4.1.1.1 Input Parameters

The unit convention used throughout the modeling scheme for length and force was inches and pounds respectively. Input parameters used to model the generalized fatigue test specimen are defined below. Please refer to Figure 4–1 and Figure 4–2.

E_{SIZE} = desired S8R5 element size (in.)

W = width of the fatigue test specimen plate (in.)

L = length of the fatigue test specimen (in.)

t_{PL} = fatigue test specimen plate thickness (in.)

l_w = laser weld interface width (in.)

l_{OFFSET} = laser weld offset location from the point of tangency of the HSS corner bend radius (in.)

H = HSS height (in.)

B = HSS width (in.)

R = centerline HSS corner bend radius (in.)

t_{HSS} = HSS wall thickness (in.)

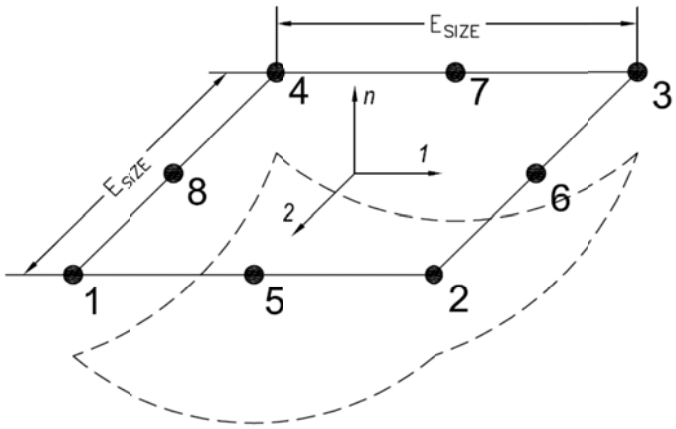

Figure 4–1: ABAQUS S8R5 Thin Shell Element

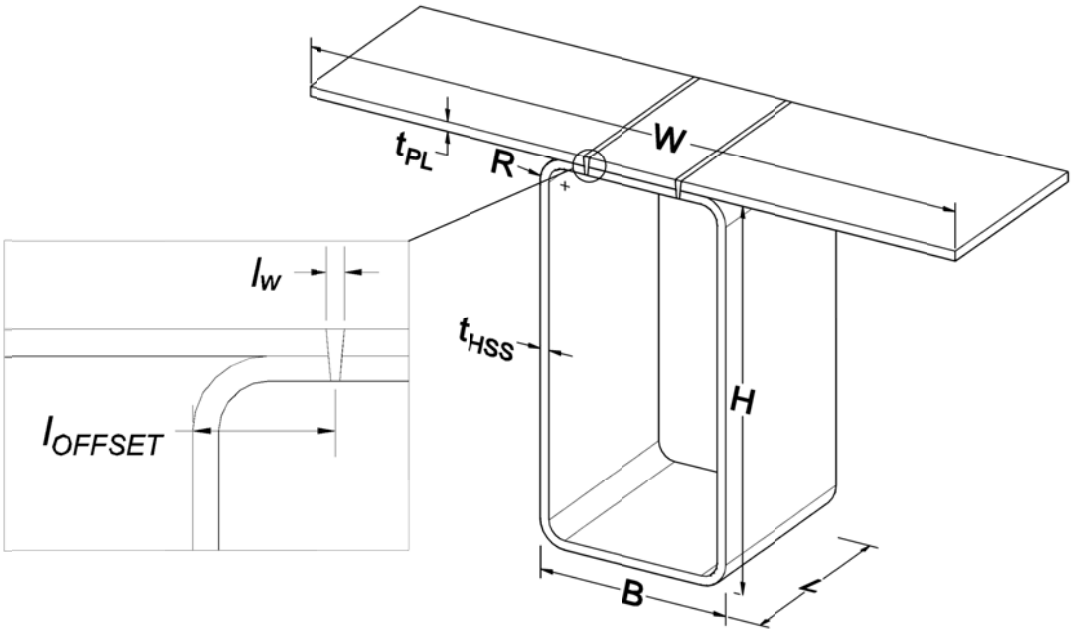

Figure 4–2: Modeling Parameters for a Typical Fatigue Test Specimen

4.1.1.2 Component Discretization

The generalized model for the fatigue test specimens was comprised of three parts that included a plate, HSS section, and laser weld, which were all instanced and constrained to interact with one another. Each component was modeled along its centerline as a homogenous shell using S8R5 elements in ABAQUS version 6.9. S8R5 elements are eight node conventional thin shell elements that assume a quadrilateral shape function and satisfy Kirchhoff plate theory by assuming negligible transverse shear flexibility making the shell normal orthogonal to the shell reference surface.(Simulia, 2010) For all homogeneous shells, the ABAQUS documentation recommends that the thickness is less than about $^{1}/_{15}$ of the characteristic length on the surface of the shell, which all shell components used in this application satisfied.

4.1.1.2.1 HSS Section

All of the fatigue test specimens were fabricated from a single HSS8"X4"X$^{3}/_{16}$" carbon steel tube, machined to a length, L of 4 inches as described in section 3.1. The HSS section was discretized based on a both design and measured dimensions. The design dimensions for height, H and width, B defined by the AISC manual for an HSS8"X4"X$^{3}/_{16}$" were used. However, the average measured HSS wall thickness, t_{HSS} of 0.1763 inches was used, supplanting the AISC design thickness of 0.174 inches. The cross section of the HSS internal stiffening rib was divided into three main regions; HSS.MESH1 for the horizontal portions, HSS.MESH2 for the vertical sections, and HSS.MESH3 for the rounded edges as shown in Figure 4–3. Each region was then discretized in the xy plane with nodes to accommodate the desired element size, E_{SIZE}.

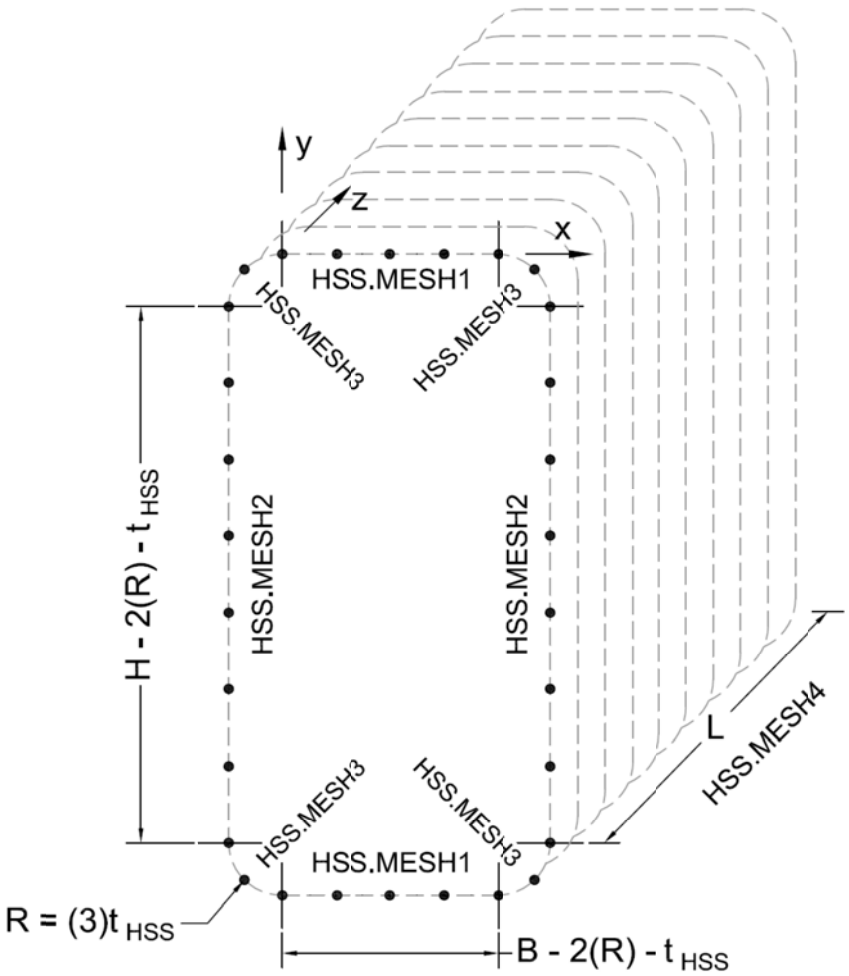

Figure 4–3: HSS Section Part Discretization and Localized Coordinate System

4.1.1.2.2 Plate

An A572 steel plate with an averaged measured thickness, t_{PL} of 0.1889 inches and width, W of 14 inches was used to fabricate all 43 fatigue test specimens as described in section 3.1. The plate was modeled as a single part in ABAQUS v6.9 and the cross section was divided into two main regions that included the area above the horizontal portion of the HSS section and the outside areas to the plate edges. The x-coordinates from HSS.MESH1 were used as a nodal projection to discretize the region in the plate

above the horizontal segment of the HSS section as shown in Figure 4–4. The outside areas to the plate edges were defined with PLATE.MESH1, which were discretized to acquire the chosen element size, E_{SIZE} as shown in Figure 4–4. The cross section of the plate was discretized in this manner to reduce the complexity of simulating the laser weld connectivity as discussed in section 4.1.1.3.1.

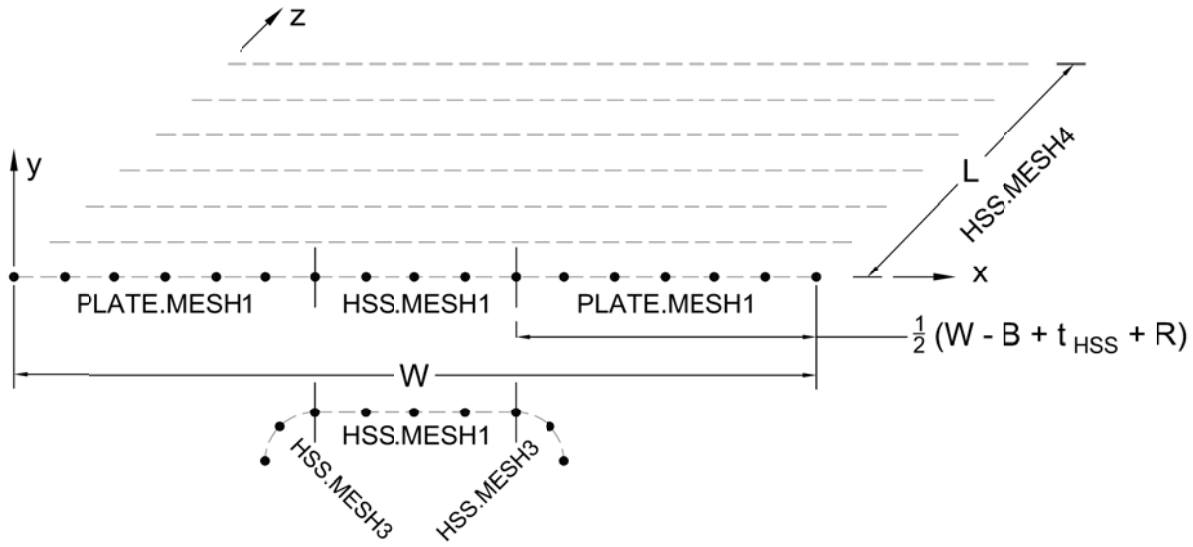

Figure 4–4: Plate Discretization and Local Coordinate System

4.1.1.2.3 Laser Weld

In order to generalize both the LBW and HLAW stake welds into a single part, the weld reinforcement in the HLAW welds was assumed to have no influence on the structural behavior, thus neglecting its presence as shown in Figure 4–5. The laser welds were modeled as a single part in ABAQUS through the centerline of each laser weld, as shown in Figure 4–5(c). A localized node set in the xy plane was created to develop a nodal cross section based upon the plate thickness, t_{PL} and the HSS wall thickness, t_{HSS}. The cross section was categorized with one region, LASER.MESH1 that was discretized to accommodate the desired element size, E_{SIZE} as shown in Figure 4–6.

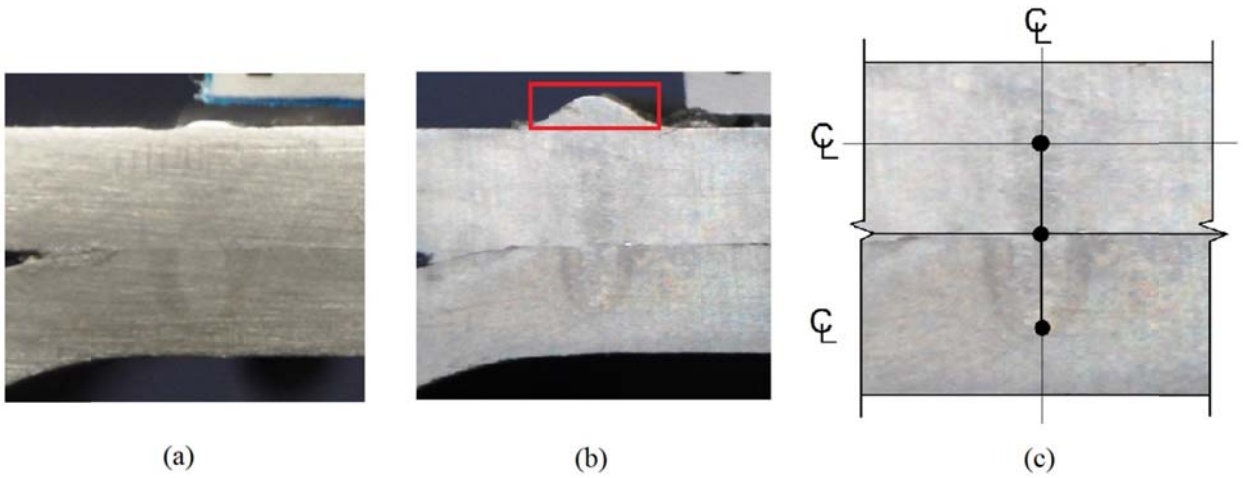

Figure 4–5: a) LBW Stake Weld, b) HLAW Stake Weld with Weld Reinforcement Outlined, c) Generalized Laser Weld Model

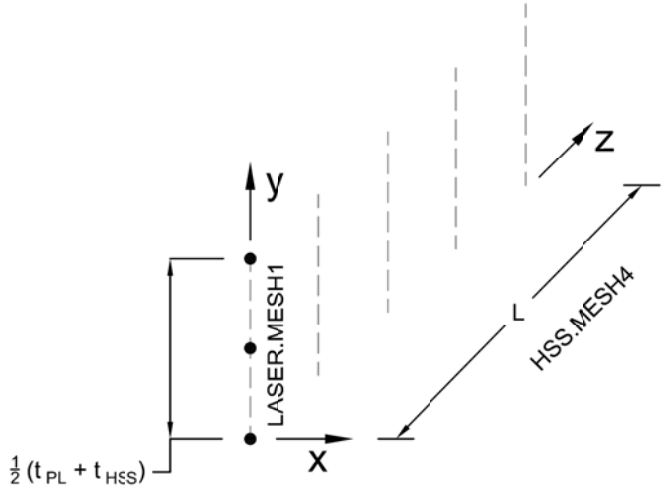

Figure 4–6: Laser Weld Part Discretization and Localized Coordinate System

The discretization scheme outlined in this section to model the laser welds as a separate part did not allow for the measured interface thickness, l_w to be used. The assigned laser weld shell thickness was observed to possess a strong influence on global behavior, thus requiring a sensitivity study that is discussed in section 4.1.1.6.2.

4.1.1.2.4 Nodal Sweep and Section Assignments

Each of the component's xy node set was swept along the desired length, L through the add-on of a z-coordinate according to HSS.MESH4 shown in Figure 4–3, Figure 4–4, and Figure 4–6 to maintain the desired element size, E_{SIZE}. The XYZ node sets were then numbered and used to create an element list according to the ABAQUS S8R5 numbering convention as shown in Figure 4–1. The plate and HSS parts were sectioned with the appropriate thicknesses, whereas the laser weld part was assigned a specialized thickness based on the sensitivity study discussed in section 4.1.1.6.2. Material properties were then assigned all components to mimic those of hot rolled steel that included a mass density of 7.34×10^{-4} lbf·s^2/in^4, Young's modulus of 29,000,000 psi and Poisson's ratio of 0.3.

4.1.1.3 Component Assembly

Each of the components discussed in section 4.1.1.2 were assembled in a global coordinate system using instances according to modeling parameters W, t_{PL}, and t_{HSS} illustrated by Figure 4–7. The following sections describe the modeling methods used to simulate the laser weld connectivity and contact regions of the generalized fatigue test specimen.

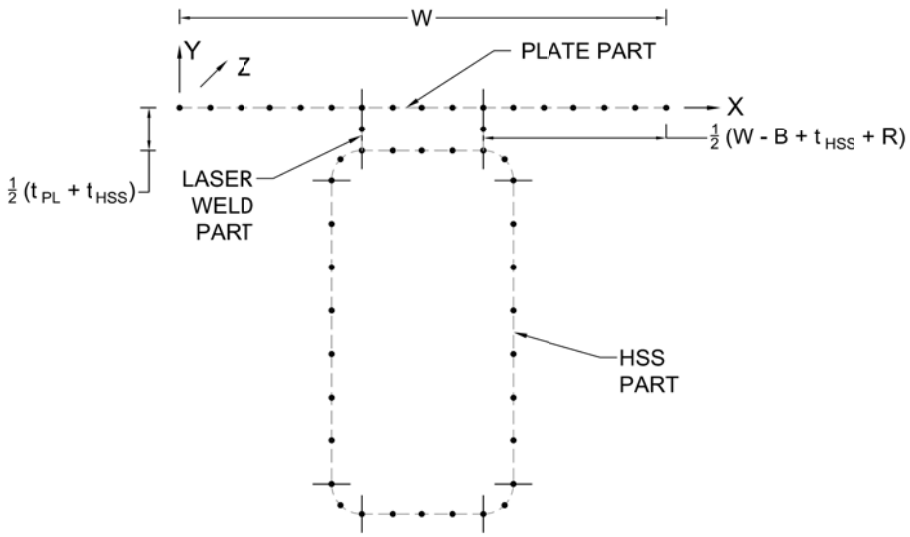

Figure 4–7: Fatigue Test Specimen Finite Model Component Assembly and Global Coordinate System

4.1.1.3.1 Laser Weld Connectivity

Each laser weld component was constrained to corresponding nodes on the plate and top flange of the HSS using TIE type multi-point constraints (MPC) as shown in Figure 4–8. According to the ABAQUS documentation, a TIE type MPC makes the global displacements and rotations as well as all other active degrees of freedom equal at two nodes. If there are different degrees of freedom active at the two nodes, only those in common are constrained.(Simulia, 2010) With regard to the MPCs used to tie the plate to the laser weld component, master nodes were allocated as the nodes in the plate and the slave nodes taken as those along the top edge of the laser weld component. In relation to the MPCs used to connect laser weld components to the HSS section, the nodes along the bottom edge of the laser weld were designated master nodes and the slave nodes were assigned as those in the HSS section.

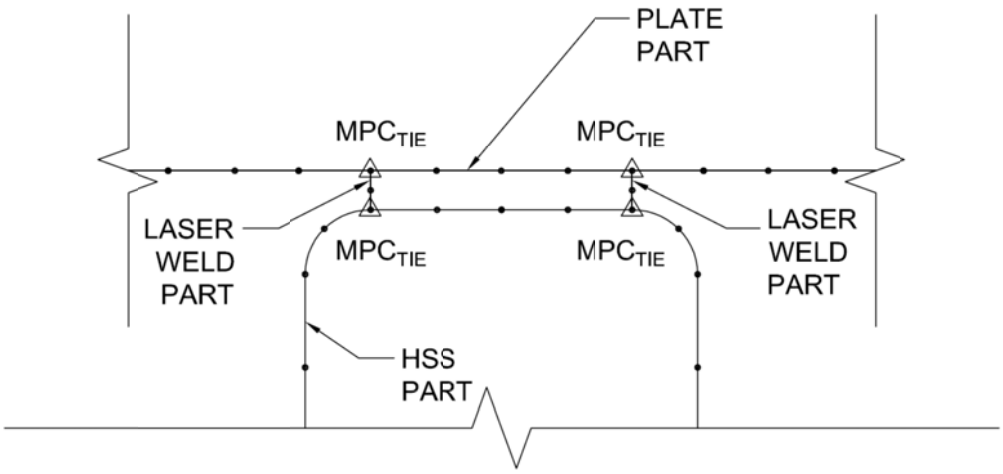

Figure 4–8: Generalized Fatigue Test Specimen Finite Model Laser Weld Connectivity

4.1.1.3.2 Contact

In order to model contact between the plate and horizontal portion of the HSS section, non-linear Spring2 elements defined in the Y-direction were used as shown in Figure 4–9. Spring2 elements were assigned to corresponding nodes of the plate and HSS section within the contact region. The non-linear spring elements were assigned pairs of force-relative displacement values required by ABAQUS to define non-linear stiffness. To simulate contact, a zero tensile stiffness and compressive stiffness that created zero differential displacement between nodes were allocated to the non-linear Spring2 elements. The appropriate compressive stiffness was determined through the sensitivity study described in section 4.1.1.6.3.

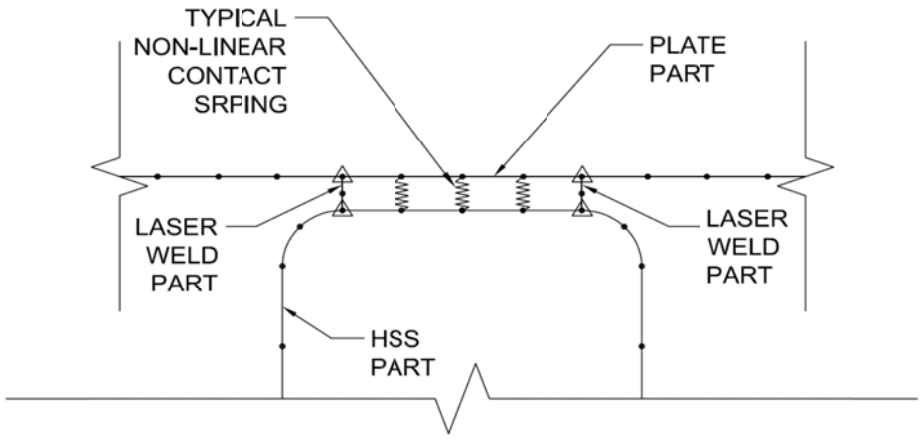

Figure 4–9: Non-Linear Springs used for Contact between the Plate and HSS Section

4.1.1.4 Boundary Conditions

Determining the appropriate boundary conditions for the generalized fatigue test specimen model was single handily the most convoluted and challenging aspect of the entire study. Initially, the boundary conditions were modeled as roller-roller conditions illustrated by Figure 4–10, which was based on the design of the fatigue testing configuration and load fixture discussed in section 3.4.1. Using this assumption, the calculated deflections were founded to be exceptionally high in comparison to those observed in the initial fatigue tests. Therefore, the elastic load test described in section 3.4.2 was conducted to quantify the difference and study the disparity between experimental and analytical strains. The astute observation was confirmed, as the analytical displacements and strains were approximately two orders of magnitude greater than the experimental results. In an attempt to create analytical bounds for the experimental data, another model was analyzed by pinning the nodes that fell within the $^{1}/_{8}$" roller contact area observed from the residual scratches on the $^{3}/_{16}$" plate shown in Figure 3–47. The analysis with the newly modeled *"Fixed-Fixed"* boundary conditions

illustrated in Figure 4–11, joined with the previous analysis effectively bounded the experimental data, verifying partially restrained boundary conditions.

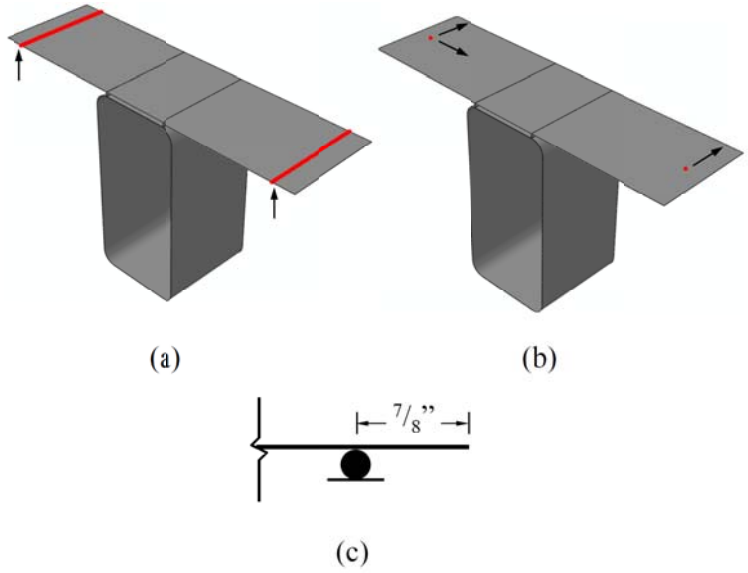

Figure 4–10: Generalized Fatigue Test Specimen Roller-Roller Boundary Conditions (a) Nodes Restrained in the Y Direction to Simulate the Presence of a Roller (b) Nodes Restrained in the X and Z Direction to Prevent Rigid Body Motion (c) Idealized Boundary Condition

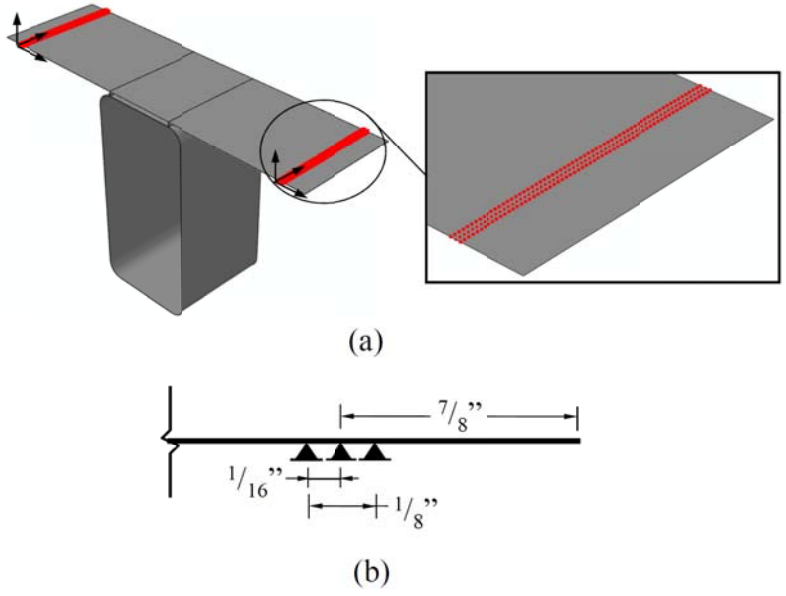

Figure 4–11: Generalized Fatigue Test Specimen *"Fixed-Fixed"* Boundary Conditions (a) Nodes Restrained in the X, Y, and Z Direction to Simulate a Pin (b) Idealized Boundary Conditions

This was exceedingly problematic provided that the reported fatigue stress varied approximately three orders in magnitude between the two bounded conditions. To make matters worse, the non-definitive boundary conditions were variable throughout each fatigue test. Discussed in section 3.4, the application of clamping force was convoluted due to the flexibility of the $^{3}/_{16}$" plate relative to the nearly rigid loading fixture, as well as the precision of the 110 kip force transducer. As a result, the applied clamping force varied between each fatigue test and through additional testing was determined to be much higher than that which was perceived. Therefore, determining a precise and accurate method to model the partial restrained boundary conditions that could be conformed to each fatigue test was imperative to rectify the dilemma at hand.

Provided that the partially restrained condition was bounded, a concept using grounded springs to create an amalgamation of the two known conditions was implemented. The nodal restraints to create the initial roller-roller condition were transitioned to pinned fixities. The pinned nodes from the other analytical bound were replaced with grounded springs, modeled with Spring1 elements in ABAQUS v6.9. Refer to Figure 4–12 for a visual representation. The definition of the grounded spring stiffness parameter, $K_{GSPRING}$ allowed the method used model the non-definitive boundary conditions to be adjusted accordingly. A sensitivity study was performed to develop a relationship between grounded spring stiffness, $K_{GSPRING}$ and the one dimensional system stiffness, K_{SYSTEM} that is discussed in section 4.1.1.6.4.

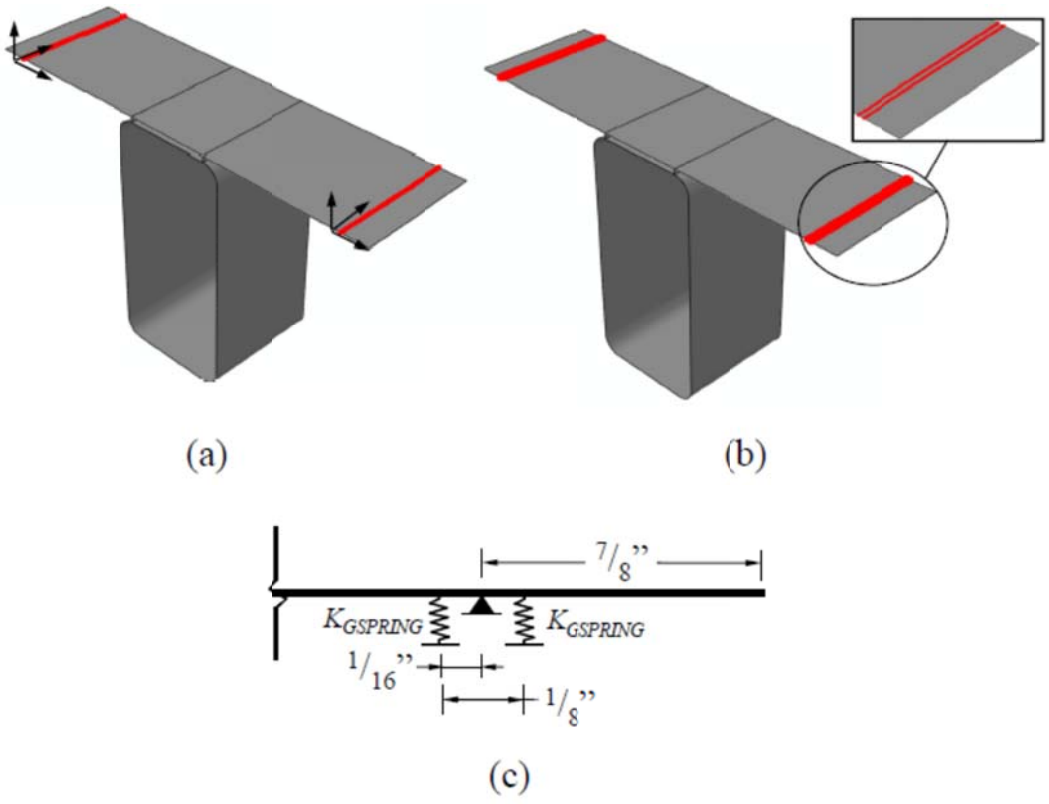

Figure 4–12: Generalized Fatigue Test Specimen Partially Restrained Boundary Conditions (a) Nodes Restrained in the X, Y, and Z Direction to Simulate a Pin (b) Nodes Assigned with Grounded Springs (c) Idealized Model of the Partially Restrained Boundary Conditions

4.1.1.5 Loading

A kinematic coupling constraint was used in ABAQUS v6.9 to model the presence of the steel 2 $^{5}/_{8}$” X 5” X 1” bearing plates described in section 3.4.1.1 and displayed in Figure 3–31. ABAQUS documentation defines this as the option used to impose constraints between degrees of freedom of a node or node set and the rigid body motion defined by a reference node.(Simulia, 2010) In this case the reference node was selected at the center of the HSS bottom flange as shown in Figure 4–13 (a) and the node set was defined with all the nodes that fell within the $2^{5}/_{8}$” width in the HSS bottom flange depicted in Figure 4–13(b). The desired load magnitude and direction was then applied to the reference node using a concentrated load in ABAQUS v6.9.

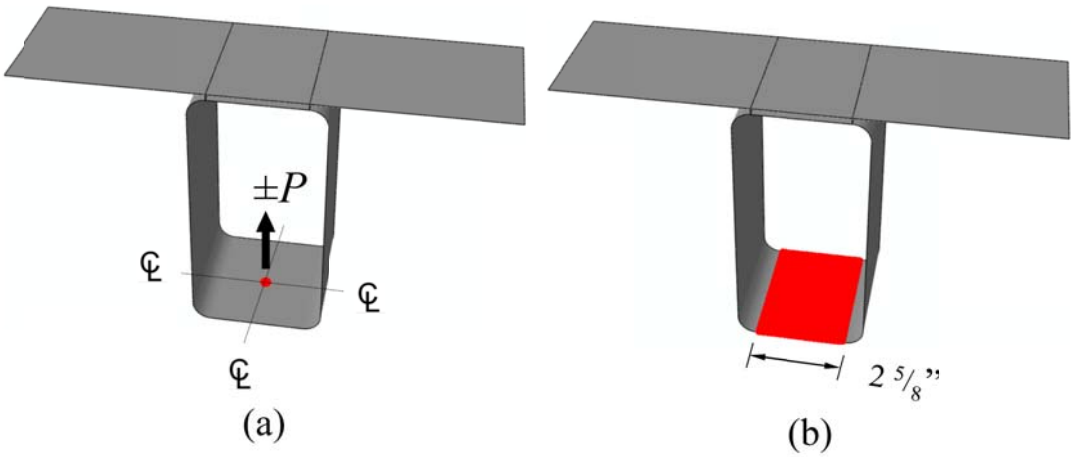

Figure 4–13: Generalized Fatigue Test Specimen Model Loading (a) Loaded Reference Node used in the Kinematic Coupling Constraint (b) Node Set used in the Kinematic Coupling Constraint

4.1.1.6 Model Sensitivity

4.1.1.6.1 Convergence Study

Generally any finite element analysis converges to a solution as the particular model is further discretized. Though an increased density of elements yields a more accurate solution, the computational time grows exponentially. In order to optimize the discretization scheme to generate accurate results in timely fashion, as well as verify the method used to model the generalized fatigue test specimen, a convergence study was performed. The criteria used convergence was the maximum vertical global displacement in the $^{3}/_{16}$" plate at mid span, Δ_y in relation to element size, E_{SIZE}. To simplify the models used for the convergence study, the initial roller-roller boundary conditions illustrated by Figure 4–10 were applied and the non-linear springs used to simulate contact were excluded. Additionally the laser weld offset location, l_{OFFSET} was defined at 0 inches and the laser weld interface width, l_w was assigned as 0.0941 inches

which as later refined in section 4.1.1.6.2 due to its influence on the overall behavior of the model. Eight models were created using the parameters defined above and in section 4.1.1.2, while varying the desired element size, E_{SIZE} from $^1/_8$" to 1" at $^1/_8$" increments. Using the static general step in ABAQUS v6.9, the eight models were subjected to a negative load of 400 lbs in the downward direction according to section 4.1.1.5 and analyzed elastically.

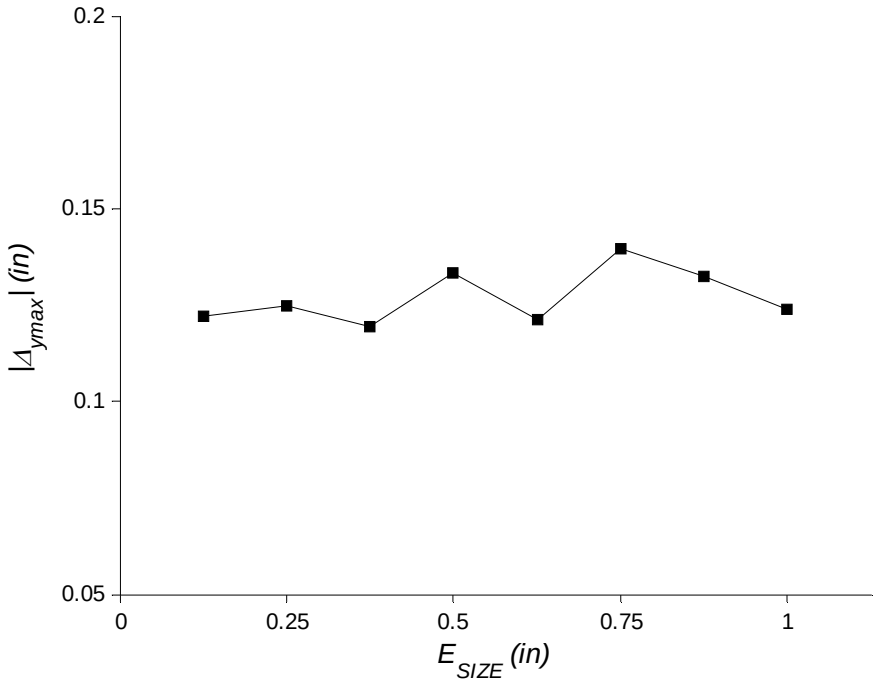

Figure 4–14: Generalized Fatigue Test Specimen Finite Element Model Convergence Study

The results from the convergence study summarized in Figure 4–14 exhibit notable disparities between each of the larger desired element sizes analyzed, but are shown to converge towards constant value as the desired element size was decreased, providing verification to the modeling approach. Given that the computation time was significantly low in all eight convergence models, an element size $^1/_8$" was chosen.

4.1.1.6.2 Laser Weld Shell Thickness Study

The method used to model the laser welds as homogenous shells between welded components made them susceptible to fictitious bending about the Z-axis. Provided that the laser welds were essentially embedded elements within the weld components, it was necessary to assign an elusive value to the shell section thickness to counteract the spurious behavior. The fictional thickness had to be large enough to prevent the localized bending in Z-axis, but with the same regard small enough so that the model was not over stiffened.(Caccese, 2009) In order to determine an appropriate thickness, a sensitivity study was performed to understand the influence of the laser weld thickness or as defined in the modeling parameters, the laser weld interface width, l_w on the behavior of the generalized fatigue test specimen finite model. Numerous models were created and analyzed in the same manner described in the convergence study with a desired element size $^1/_8$", while varying the laser weld shell thickness to its evaluate the effect on the maximum vertical displacement Δ_y.

The results of the laser weld shell thickness study are summarized in Figure 4–15, which the relationship between the absolute maximum vertical displacement Δ_y and non-dimensional laser weld shell thickness l_w/t_{PL} is displayed on a semi-log plot. (Caccese, 2009) The laser weld shell thickness was non-dimensionalized to the specimen plate thickness t_{PL} of 0.1889 inches for easier interpretation of the results. In conclusion, the laser weld interface width, l_w does not influence the behavior of the model when it is defined with a thickness greater than $2.5t_{PL}$. Based upon this study an even value of 0.5 inches was chosen for the laser weld interface width, l_w.

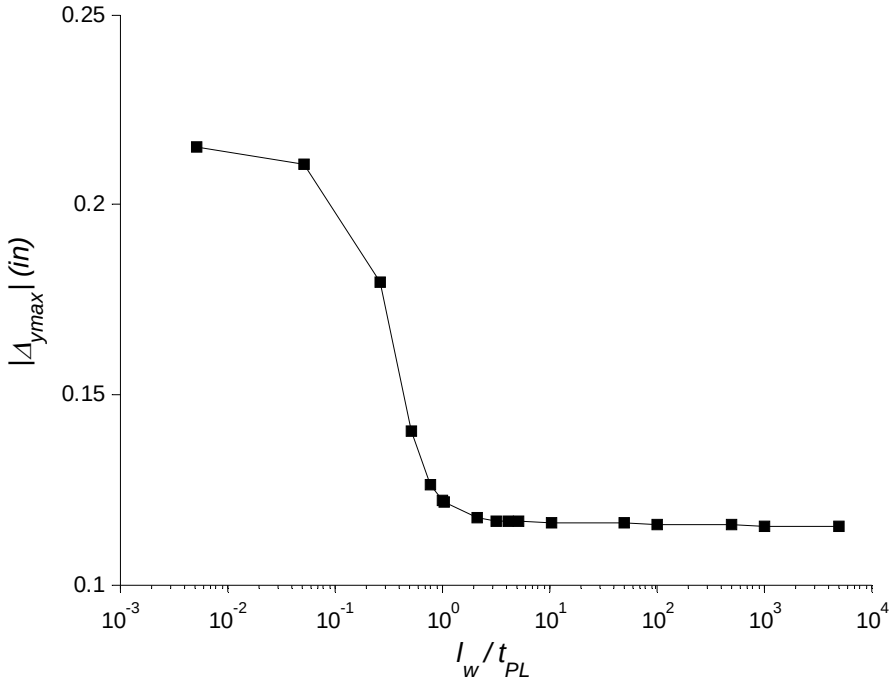

Figure 4–15: Laser Weld Interface Width Influence on the Generalized Fatigue Test Specimen Finite Model

4.1.1.6.3 A Study on the Compressive Stiffness of Non-Linear Springs used for Contact

Theoretically, non-linear springs used to model contact should possess a tensile stiffness of zero and compressive stiffness of infinity. Seeing as an infinite stiffness was not supported in ABAQUS; a sufficient stiffness was required that forced interconnected nodes to move together without differential displacement, while the non-linear spring was engaged in compression. Initially, an extremely large value was assigned for the compressive stiffness, but was founded to cause singularity as the ABAQUS solution diverged and tolerances were not met. For this reason a sensitivity study was performed on the non-linear springs to determine an appropriate compressive stiffness to model contact.

Numerous generalized fatigue test specimen models were created and analyzed in the same manner as the convergence study with the addition of non-linear springs described in section 4.2.1.3.3, a desired element size $^{1}/_{8}$", and laser weld interface width of 0.5 inches, while varying non-linear compressive stiffness from 0 $^{lb}/_{in}$ to 7,000 $^{lb}/_{in}$. Two nodes connected by a non-linear spring to simulate contact between the plate and center of the HSS top flange were analyzed for global vertical displacement illustrated by Figure 4–16 (a). The differential displacement between nodes shown in Figure 4–16(b) was used to determine an appropriate compressive stiffness for the non-linear springs to model contact. Ideally, the differential displacement between nodes should equal zero demonstrating that they move together as discussed previously. The results from the sensitivity study on the compressive stiffness of the non-linear springs between the plate and HSS top flange are summarized in Figure 4–17.

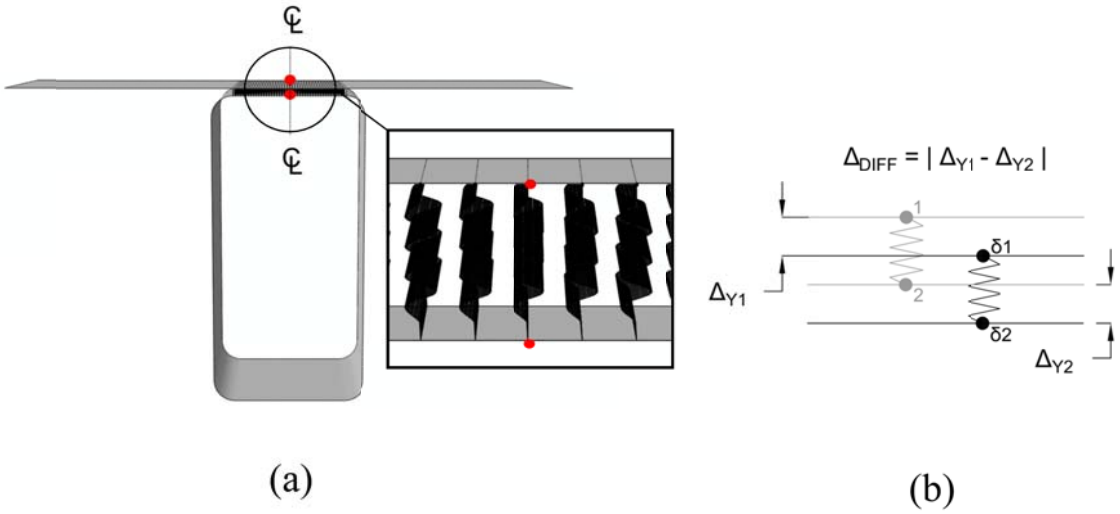

Figure 4–16: Generalized Fatigue Test Specimen Finite Element Model Compressive Stiffness Sensitivity Study Definition (a) Nodes Analyzed in the Finite Element Models Created (b) Differental Displacement between Nodes Connected by a Non-Linear Spring to Model Contact

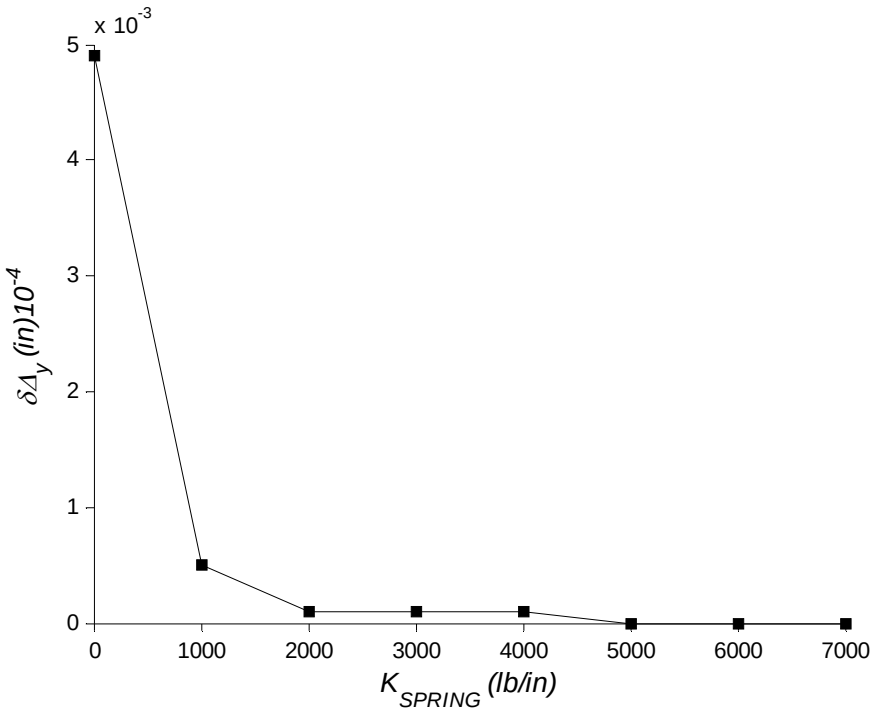

Figure 4–17: Non-Linear Springs used to Simulate Contact in the Generalized Fatigue Test Specimen Finite Element Model Compressive Stiffness Sensitivity Study

The sensitivity study to determine the compressive stiffness of the non-linear springs used to model contact between the plate and HSS top flange was successful in demonstrating the convergence of the differential displacement to zero. Figure 4–17 shows that the differential displacement converged to zero at compressive stiffness of 5000 $^{lb}/_{in}$. Though, a compressive stiffness of 2000 $^{lb}/_{in}$ was analyzed with negligible differential displacement, sufficing without an additional 3000 $^{lb}/_{in}$ of stiffness. As a result of the study, a 2000 $^{lb}/_{in}$ compressive stiffness was chosen for the non-linear springs to simulate contact between the plate and HSS top flange in the generalized fatigue test specimen finite model.

4.1.1.6.4 Grounded Spring Stiffness Study

To properly model the partially restrained boundary conditions in each experimental test involving the load fixture displayed in Figure 3–32 and Figure 3–33, a relationship between the grounded spring stiffness, $K_{GSPRING}$ and the one dimensional vertical stiffness of the generalized fatigue test specimen model, K_{SYSTEM} was mandatory. As a result of the contact between the plate and the HSS top flange, the model's one dimensional vertical stiffness was nonsymmetrical with regards to load direction. The negative load direction inducing positive curvature in the $^{3}/_{16}$" plate, while engaging the non-linear contact springs in compression was chosen to minimize error. In the case of the positive load direction, the unknown and non-measurable potential contact region on the rounded corner of the HSS section could either cause a gap effect or prying action, altering behavior.

To unravel the relationship between $K_{GSPRING}$ and K_{SYSTEM}, twenty-six generalized fatigue test specimen finite element models were analyzed in a parametric study, varying only the grounded spring stiffness, $K_{GSPRING}$ from 0 to 2,250,000 $^{lb}/_{in}$. The refined parameters from each of the other sensitivity studies were included and the partially restrained boundary conditions discussed in section 4.1.1.4 were implemented. Each model was subjected to four different loads of varying magnitude in the downward direction using the method discussed in section 4.1.1.5 that included -100 lbs, - 200 lbs, -300 lbs, and -400 lbs. The four loads were elastically analyzed using a static general step in ABAQUS v6.9. The vertical displacement at the center of the HSS bottom flange shown in Figure 4–18, the same location measured by the integrated LVDT in the MTS actuator, was outputted to the DAT file. The calculated vertical displacements were

collected and used to create load displacement plots for each of the twenty-six finite element models analyzed. A line was fit to each plot and the slope was extracted as the one dimensional vertical stiffness of the generalized fatigue test specimen, K_{SYSTEM}.

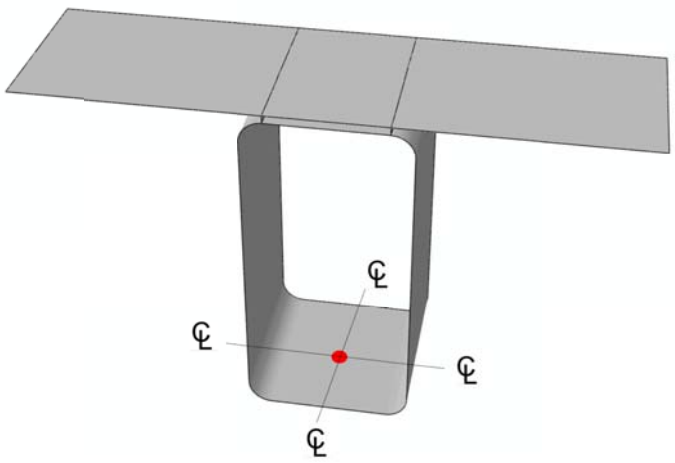

Figure 4–18: Generalized Fatigue Test Specimen Model Vertical Displacment Location

A non-linear least squares regression was performed using a numerical optimization routine in Matlab to fit a curve to the data points in the $K_{GSPRING}$ verses K_{SYSTEM} plot. Using $K_{GSPRING}$ as the dependent variable and the K_{SYSTEM} as the independent variable, many attempts were made to guess the correct form of mathematical relationship, but were unsuccessful. Through an internet search on non-linear regression, the Michaelis-Menten model for enzyme kinetics was discovered, a double reciprocal function. With minor manipulation the function was transformed into the correct form of the mathematical relationship between $K_{GSPRING}$ and K_{SYSTEM} . The optimization scheme fit a curve to the data with a squared sum of residuals equal to one that is represented below by equation (4.1).

$$K_{GSPRING} = \frac{159029 \cdot K_{SYSTEM}}{13843 - K_{SYSTEM}} - 55299 \qquad \textbf{(4.1)}$$

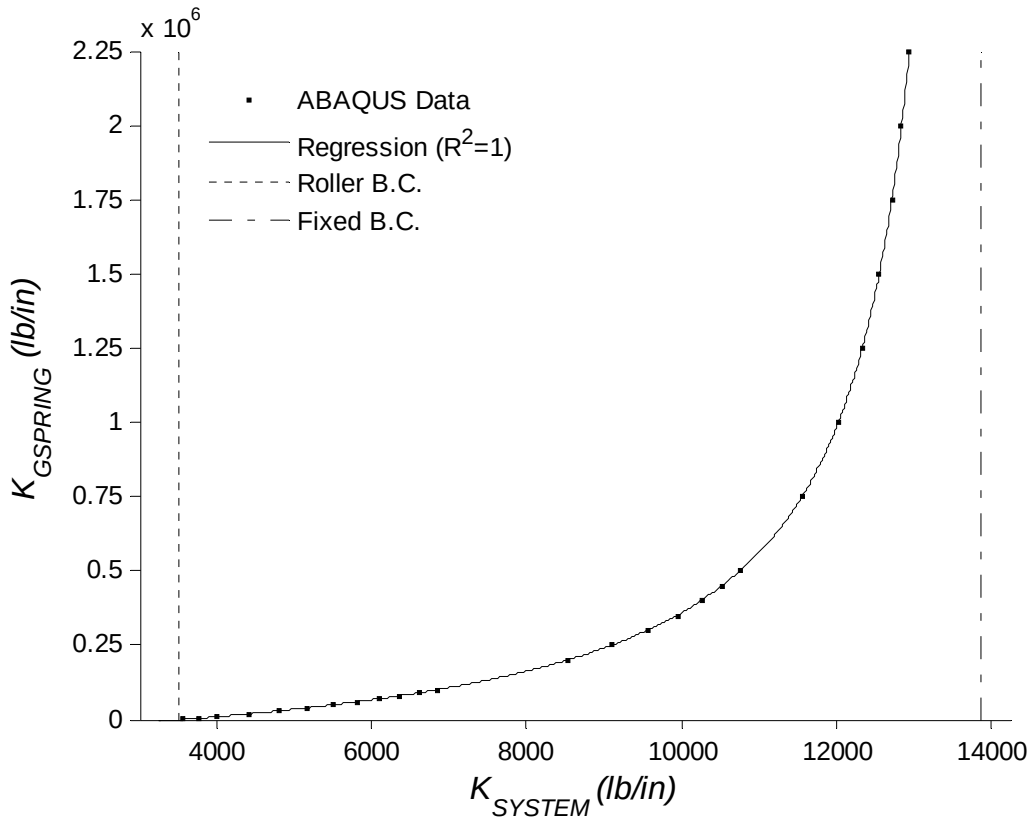

Figure 4–19: Grounded Spring Stiffness vs. System Stiffness

The plot displayed in Figure 4–19 is graphical representation of on the boundary conditions influence on the negative one dimensional vertical stiffness of the generalized fatigue test specimen model. The partially restrained boundary conditions are displayed through the data collected from the twenty-six finite element analyses and the non-linear relationship derived between $K_{GSPRING}$ and K_{SYSTEM}. The relationship is bounded by the roller-roller and fixed-fixed boundary conditions as shown by the vertical lines in Figure 4–19. To provide further understanding of the structural behavior represented by the graph in Figure 4–19, the deformed shapes for each different boundary condition are displayed in Figure 4–20. Figure 4–20 (a) represents the roller-roller boundary condition in which zero moment restrained at the fixities, Figure 4–20b) represents the fixed-fixed boundary condition, and Figure 4–20(c) represents the partially restrained boundary

condition with grounded spring stiffness of 300,000 $^{lb}/_{in}$.

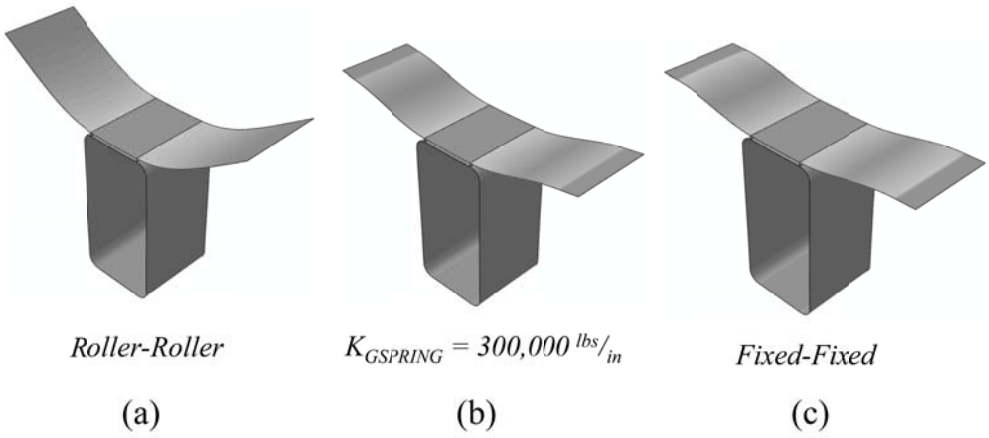

Figure 4–20: Generalized Fatigue Test Specimen Deformed Shape (a) Roller-Roller Boundary Condition 20x Scale (b) Partially Restrained Boundary Condition 20x Scale (c) Fixed-Fixed Boundary Condition 20x Scale

4.1.2 ANALYSIS

All generalized fatigue test specimen finite element models were analyzed elastically, using the static general analysis step in ABAQUS v6.9. Targeted values were written to the DAT file, exported by ABAQUS, through NODEPRINT and ELPRINT commands, and then extracted in an efficient manner using Matlab for all post processing.

4.1.2.1 Determining Grounded Spring Stiffness

The double reciprocal relationship between $K_{GSPRING}$ and K_{SYSTEM} determined in section 4.1.1.6.4 was used to simulate the partially restrained conditions in nearly every test performed throughout the study. For each of the 38 fatigue tests performed, elastic load test, and 10 tests that made up the partial restraint verification testing program; a different value for the grounded spring stiffness, $K_{GSPRING}$ was computed to properly model the experimental partially restrained boundary conditions. Provided that the one

dimensional vertical stiffness of the generalized fatigue test specimen model, K_{SYSTEM} was derived in the negative/downward direction to minimize error; the negative load displacement data was required from each experimental test. Therefore, the associated output data from the 110 kip MTS force transducer and integrated LVDT in the MTS actuator for each test was extracted and organized. A line was fit to the targeted set of negative load displacement data and the calculated slope was taken as the experimental one dimensional vertical stiffness, K_{SYSTEM}. This value was then used in equation (4.1) to calculate the associated value for $K_{GSPRING}$ to properly model the experimental partially restrained boundary conditions.

4.1.2.2 Reported Fatigue Stress

Undoubtedly, the normal stress in the x-direction, σ_x at the laser weld interface due bending about the z-axis was the dominant stress in the $^3/_{16}$" plate most likely to initiate a fatigue crack. Illustrated by Figure 4–21, this location on the bottom of the $^3/_{16}$" plate was initially believed to be a notched detail, but with further examination was proven otherwise. Figure 4–22 represents the contours of σ_x on the underside of the $^3/_{16}$" from a finite element analysis using a $K_{GSPRING}$ of 115,000 lb/in, E_{SIZE} of 1/8 inches, and load magnitude of ±400 lbs. Provided that the stresses are discontinuous between finite elements, a large stress gradient between the Gaussian integration points on either side of the laser weld link was reported at slope approximately 350 ksi/in, demonstrating a significant reduction in the σ_x stress.

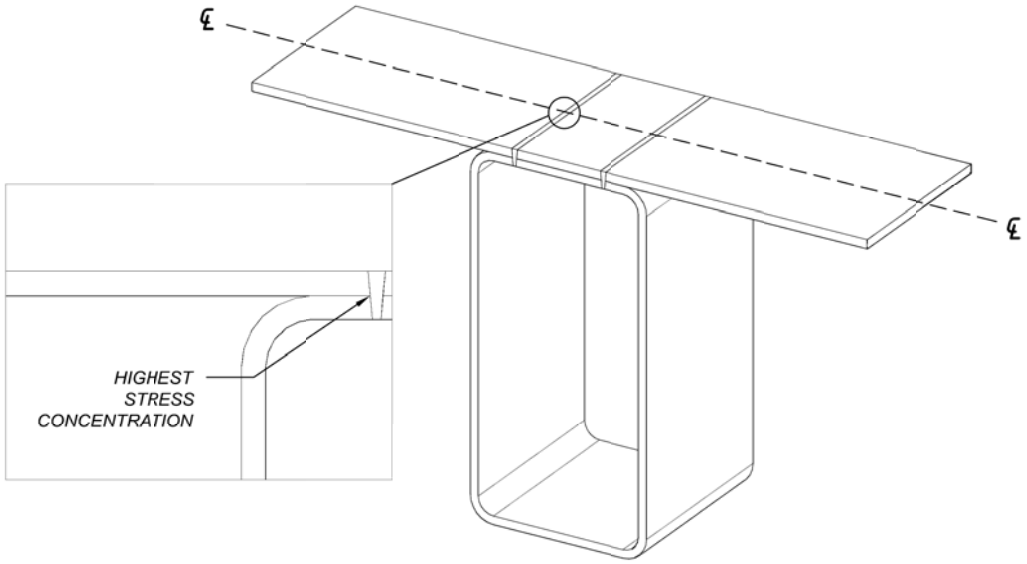

Figure 4–21: Highest Stress Concentration Location

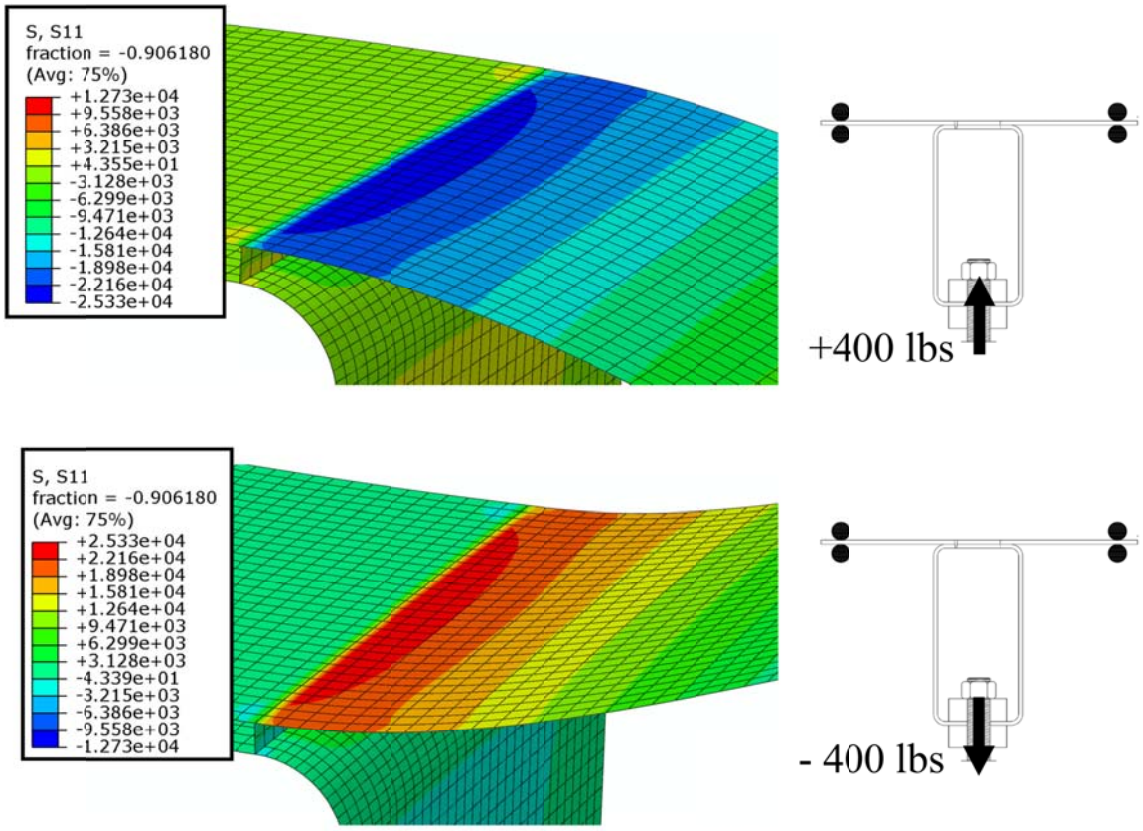

Figure 4–22: Finite Element Analysis Contours Demonstrating the Stress Reduction Gradient

The reduction in stress at the laser weld was understood through the geometry of

the laser welded connection to the HSS section. To begin with, the transition into the laser stake weld doubled the cross sectional thickness, increasing the moment of inertia by 8 orders of magnitude, decreasing the stress in the plate. Secondly, this transition area in the $^{3}/_{16}$" plate was greatly stiffened from the two linear stake welds that essentially altered the boundary conditions to nearly a fixed-fixed condition.

A study was performed to investigate that the stress concentration immediately before the reduction gradient was not sensitive to mesh density, thus indicating a hot spot stress. Models were created using three refined mesh densities with E_{SIZE} equal to $^{1}/_{8}$", $^{1}/_{16}$" and $^{1}/_{32}$". Provided that the grounded springs and non-linear springs would alter the stresses analyzed at the targeted location with varying mesh densities, they were excluded from the models created. To disengage contact between the $^{3}/_{16}$" plate and HSS top flange due to the absence of the non-linear springs, a positive/upward load with a magnitude of 400 lbs was analyzed. The σ_x stress profile along the center of the $^{3}/_{16}$" plate, starting at the plate edge to the first element past the laser weld link was examined. Refer to Figure 4–23. The σ_x stresses were extrapolated to centroid of each element and plotted against their location along the x-axis. The plot shown in Figure 4–24 graphically summarizes the findings from the study.

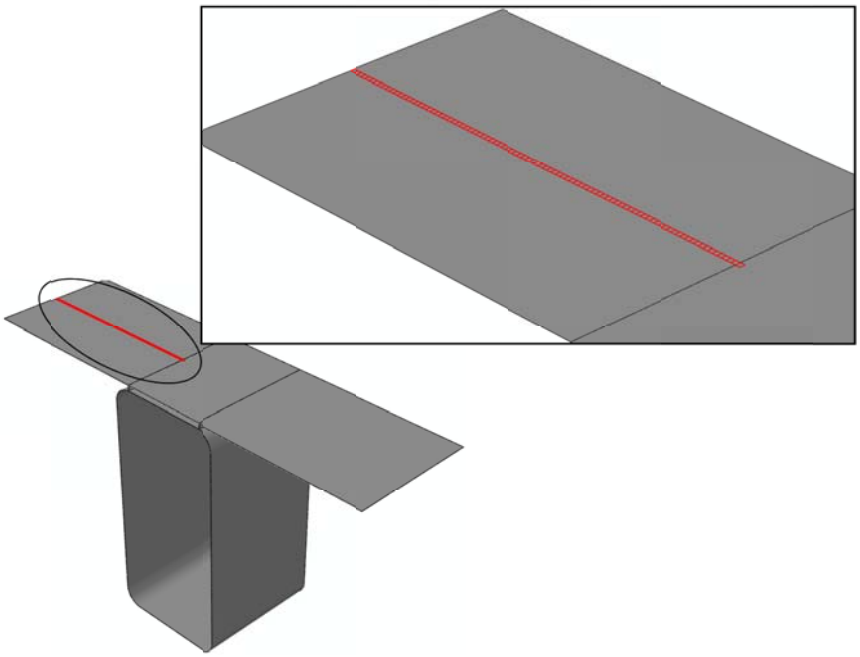

Figure 4–23: Element Set Selected to Generate the Stress Profile for the Mesh Study

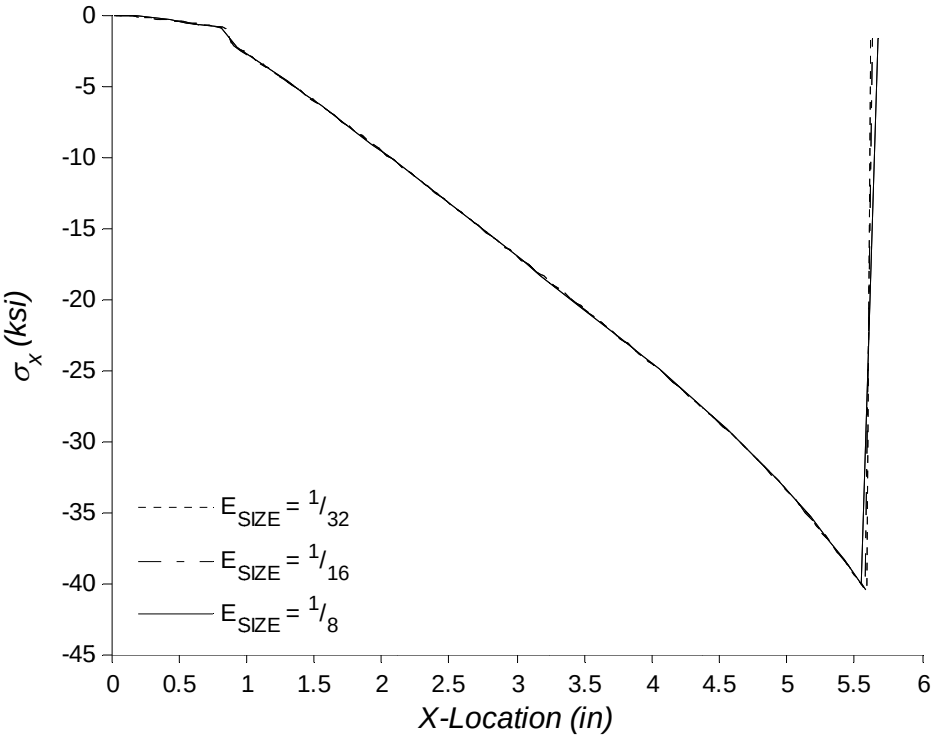

Figure 4–24: σ_x Stress Profile in $^3/_{16}$" Plate at Reduced Mesh Densities

The results from the mesh study demonstrate that a hot spot stress is not issue with the stress concentration in the $^{3}/_{16}$" prior to the reduction gradient as shown in Figure 4–22. Therefore, the reported fatigue stress in the S-N curves was taken at the Gaussian integration point before to the stress reduction gradient as shown in Figure 4–25.

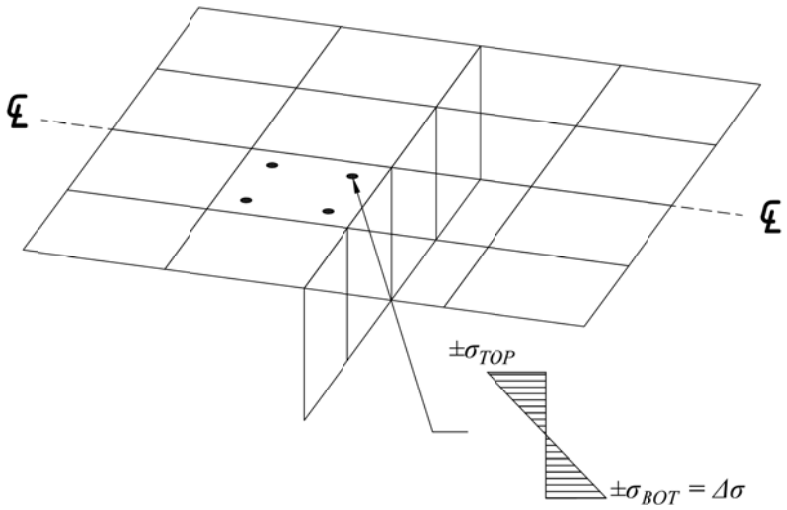

Figure 4–25: Reported Stress Range in S-N Curves

4.1.2.3 Reported Strains

In order to provide an analytical comparison to the experimental strains measured in the elastic load test and partial restraint verification testing program; the following approach was taken. The M-M strain gages used in the experimental tests measure the average linear strain over a bonded area that was measured to be approximately ¼" X ¼". To mimic this measurement in the finite element analysis, element sets were created with four of the $^{1}/_{8}$" X $^{1}/_{8}$" elements in locations in which the strain gages were installed according to Figure 3–45 and Figure 3–48. Figure 4–26 illustrates the element sets created in the finite element model.

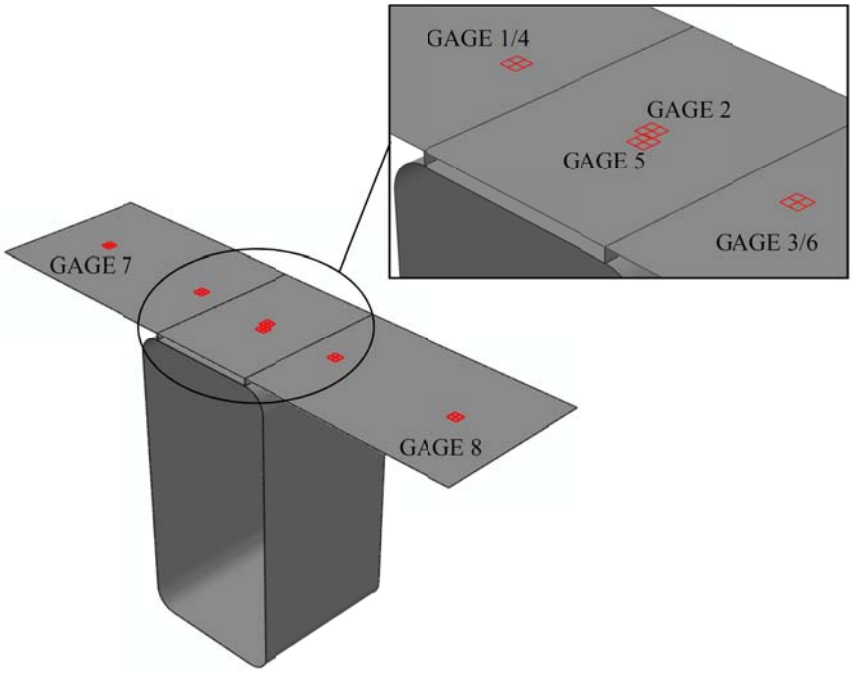

Figure 4–26: Element Sets used for Analytical Strains

The strain in the x direction, ε_x or as reported by ABAQUS, E11 was extrapolated to the center of each of the four elements from the four Gaussian integration points as a result of the reduced integration of an 8-noded isoparametric quadrilateral element. The four extrapolated strains were then averaged at the appropriate through thickness section and reported as analytical strains.

4.1.2.4 Comparison Parameters to Sandwich Panel Module Models

To provide a comparison between the fatigue test specimens and sandwich panel modules, in order to assess the overall fatigue performance; the fatigue stress, maximum vertical differential displacement, maximum slope, and distance between inflection points were computed in both load directions and tabulated for each individual fatigue test model. These values were also computed in the parametric study performed on the sandwich panel modules discussed in section 4.2.2. Ideally, these values shall allow for a

particular sandwich panel configuration to compare to the average of the values of the fatigue test specimens, thus being able to take advantage of the S-N curves generated. Figure 4–27 visually demonstrates the values computed for the fatigue test models to be used in the comparison.

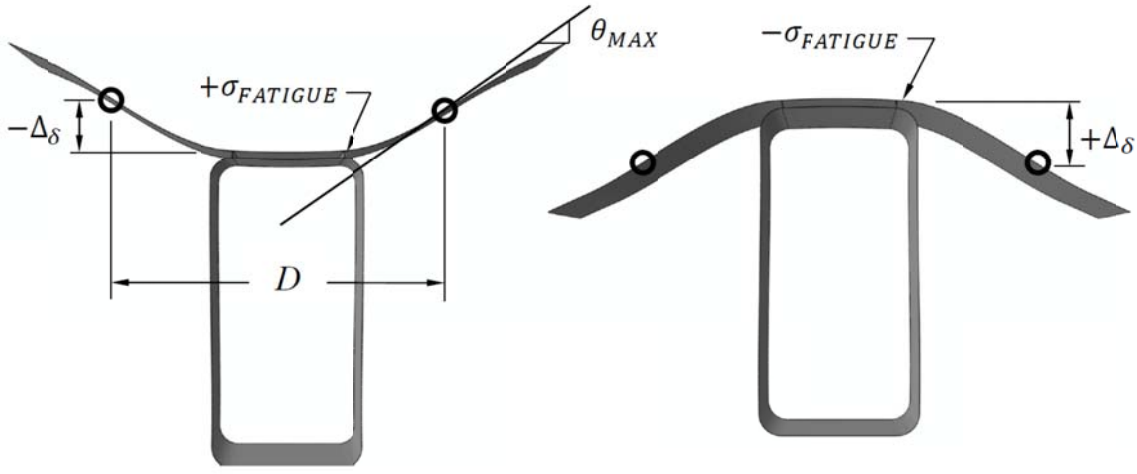

Figure 4–27: Comparison Parameters to the Sandwich Panel Modules

The fatigue stress at the laser welds was calculated in the same manner described previously in section 4.1.2.2. The maximum differential displacement, $\pm\Delta_{DIFF}$ was computed by initially fitting a cubic function to the global vertical displacements at each node in the $^3/_{16}$" plate along the centerline between the pinned nodes and centerline projection of the HSS section verses their location along the x-axis. The function was differentiated twice, set to zero, and solved to determine the point of inflection. The differential displacement was then determined through the difference between the global vertical displacement at the inflection point and centerline projection of the HSS section on the $^3/_{16}$" plate. The maximum slope, θ_{MAX} was then computed at the inflection point using the first derivative of the cubic displacement function. Due to symmetry, the distance between inflection points, D was computed by doubling the horizontal distance

from the inflection point to the centerline of HSS section. The maximum slope and distance between inflection points was only determined for the negative load case. Please refer to Figure 4–28.

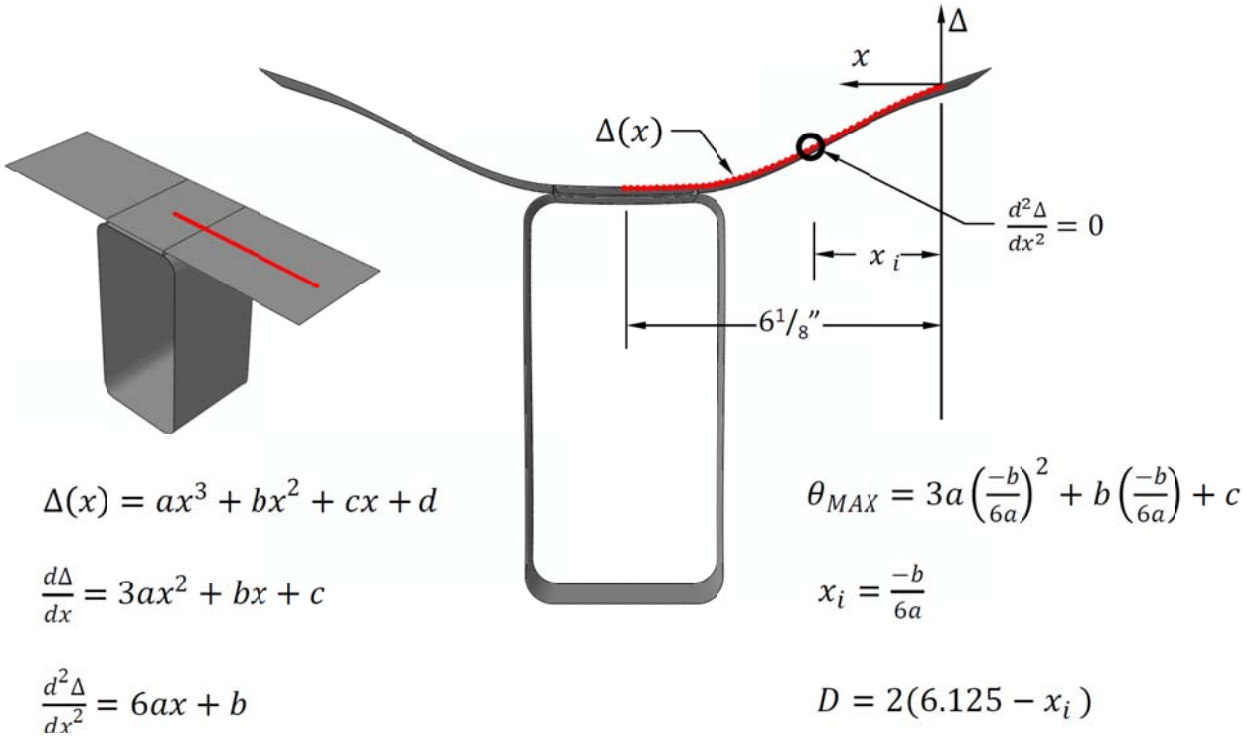

Figure 4–28: Determining Comparison Parameters from Finite Element Analysis Nodal Output

4.2 SANDWICH PANEL FINITE ELEMENT MODELING

Currently at the infancy of development, the problem at hand concerning the proposed modular steel sandwich panel bridge deck system was not only extremely vague, but consisted of endless configurations. Therefore, a versatile modeling approach that eased manipulation with minimal inputs and handled numerous permutations in a timely manner was essential. With this rational, a program was created in MATLAB to generate input files for ABAQUS v6.9 Standard to be analyzed using the supercomputers at Virginia Tech. The Matlab program created was designed around the predominate parameters of the proposed sandwich panel that included panel length (transverse bridge direction), panel width (longitudinal bridge direction), internal rib spacing, top plate thickness, bottom plate thickness, and AISC prefabricated HSS section selection.

Bridge geometry was assumed in section 1.4 with a transverse width of 40ft (3ft overhangs and 8.5ft on center girder spacing) to depict a typical two lane bridge with a shoulder. This configuration was chosen in order to perform a preliminary investigation to evaluate strength and size test specimen components for fabrication. The primary focus of the finite element analysis on the sandwich panel bridge deck system was to determine maximum differential rib deflection and localized stress concentration in the bottom plate. Bridge geometry has a large impact on the overall behavior of the bridge deck. Speculating "typical" longitudinal length and various components, in addition to the transverse dimensions of a two lane bridge with a shoulder was not acceptable. This would have resulted in a restricted study with a subjective interpretation, which was not in the intent for this investigation. The limited number of known variables needed to properly assess the overall deck behavior in a bridge setting resulted in the decision to take a simplified approach. The proposed sandwich panel bridge deck system was

modeled as a simply supported panel with an 8.5 ft span. Provided that the bridge deck would be continuously supported, it was assumed that this analysis method yielded conservative estimates.

4.2.1 MODELING METHODOLOGY

4.2.1.1 Input Parameters

The unit convention used throughout the modeling scheme for length and force was inches and pounds respectively. Important parameters used to model the sandwich panel bridge deck modules are defined below. Please refer to Figure 4–1 and Figure 4–29.

E_{SIZE} = desired S8R5 element size (in.) Refer to Figure 4–1.

S = center to center spacing of HSS internal stiffening ribs (in.)

W = sandwich panel width in the longitudinal direction evenly divisible by chosen internal rib spacing (in.)

L = sandwich panel length in the transverse direction (in.)

t_{TOP} = top plate thickness (in.)

t_{BOTTOM} = bottom plate thickness (in.)

l_w = laser weld interface width (in.)

l_{OFFSET} = laser weld offset location from the point of tangency of the corresponding HSS corner bend radius (in.)

$HSS_{SECTION}$ = one of thirty-seven prefabricated HSS sections correlated to Table 4-1 for cross sectional properties.

H_{HSS} = height of the HSS section selected (in.). Refer to Table 4-1.

B_{HSS} = width of the HSS section selected (in.) Refer to Table 4-1.

t_{HSS} = thickness of the HSS section selected (in.) Refer to Table 4-1.

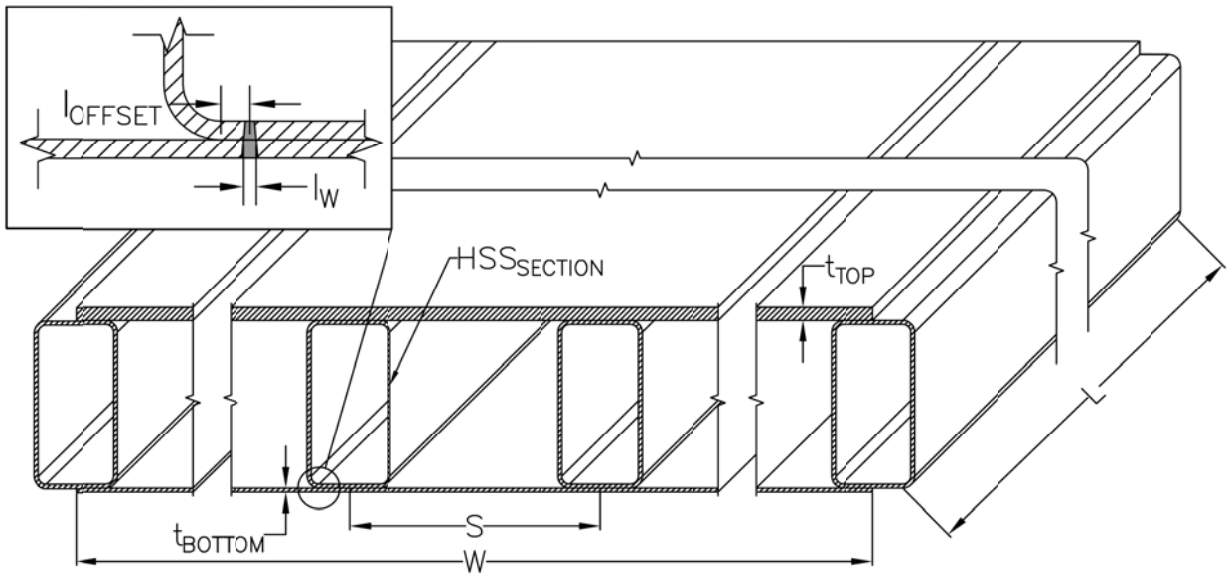

Figure 4–29: Primary Modeling Parameter for the Sandwich Panel Bridge Deck Unit

Table 4-1: AISC HSS Cross Sectional Dimensions

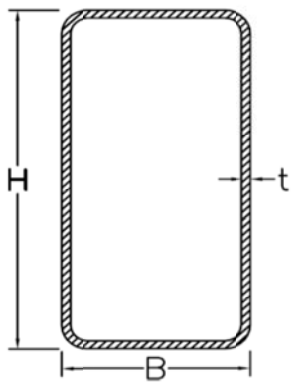

NOTES:

1.) All table values were obtain from the AISC Manual

2.) The design thickness was used for HSS thickness reported in the table

$HSS_{SECTION}$	AISC SECTION	B (in.)	H (in.)	t (in.)	$HSS_{SECTION}$	AISC SECTION	B (in.)	H (in.)	t (in.)
1	HSS10X8X5/8	8	10	0.581	20	HSS8X4X5/8	8	4	0.581
2	HSS10X8X1/2	8	10	0.465	21	HSS8X4X1/2	8	4	0.465
3	HSS10X8X3/8	8	10	0.349	22	HSS8X4X3/8	8	4	0.349
4	HSS10X8X5/16	8	10	0.291	23	HSS8X4X5/16	8	4	0.291
5	HSS10X8X1/4	8	10	0.233	24	HSS8X4X1/4	8	4	0.233
6	HSS10X8X3/16	8	10	0.174	25	HSS8X4X3/16	8	4	0.174
7	HSS8X8X5/8	8	8	0.581	26	HSS8X4X1/8	8	4	0.116
8	HSS8X8X1/2	8	8	0.465	27	HSS8X3X1/2	8	3	0.465
9	HSS8X8X3/8	8	8	0.349	28	HSS8X3X3/8	8	3	0.349
10	HSS8X8X5/16	8	8	0.291	29	HSS8X3X5/16	8	3	0.291
11	HSS8X8X1/4	8	8	-0.767	30	HSS8X3X1/4	8	3	0.233
12	HSS8X8X3/16	8	8	0.174	31	HSS8X3X3/16	8	3	0.174
13	HSS8X8X1/8	8	8	0.116	32	HSS8X3X1/8	8	3	0.116
14	HSS8X6X5/8	8	6	0.581	33	HSS8X2X3/8	8	2	0.349
15	HSS8X6X1/2	8	6	0.465	34	HSS8X2X5/16	8	2	0.291
16	HSS8X6X3/8	8	6	0.349	35	HSS8X2X1/4	8	2	0.233
17	HSS8X6X5/16	8	6	0.291	36	HSS8X2X3/16	8	2	0.174
18	HSS8X6X1/4	8	6	0.233	37	HSS8X2X1/8	8	2	0.116
19	HSS8X6X3/16	8	6	0.174	***	***	***	***	***

4.2.1.2 Component Discretization

Each model was primarily comprised of four parts including the HSS internal rib, top plate, bottom plate, and laser weld that were all instanced and constrained to form the sandwich panel. As was the case in the generalized fatigue test specimen model, each component was modeled along its centerline as a homogenous shell using S8R5 elements in ABAQUS version 6.9. All shell components used to model the sandwich panel satisfied the recommended ratio of 1:15 for thickness to length.

4.2.1.2.1 HSS Internal Stiffening Ribs

Given that all internal stiffening ribs were identical in each model, a single part was created for the $HSS_{SECTION}$ selected. The cross section of the chosen HSS internal stiffening rib was discretized in the exact same scheme used for the fatigue test specimen model as shown in Figure 4–3 according to the dimensions in Table 4-1. Each of the three regions were discretized in the XY-plane with nodes to accommodate the desired element size, E_{SIZE} as in the generalized fatigue test specimen model.

4.2.1.2.2 Top Plate

The top plate was modeled as a part in ABAQUS v6.9. A localized node set in the xy plane was created to develop a nodal cross section based upon panel width, W and internal rib spacing, S. The cross section was divided into two main regions, the area above an HSS internal rib stiffener and the area between the internal rib stiffeners. The nodal projection of HSS.MESH1 and HSS.MESH3 was used to discretize the regions in the top plate above internal rib stiffeners as shown in Figure 4–30. The regions in the top plate at the start and end also used a nodal projection of HSS.MESH1 and HSS.MESH3,

but were discretized using only half the number of nodes as shown in Figure 4–30. The area between stiffeners, TOPPLATE.MESH1 was then discretized to attain the desired element size, E_{SIZE}. The top plate was discretized in this manner to have corresponding mesh to each internal rib stiffener to ease the simulation of the flare bevel weld discussed in section 4.2.1.3.1.

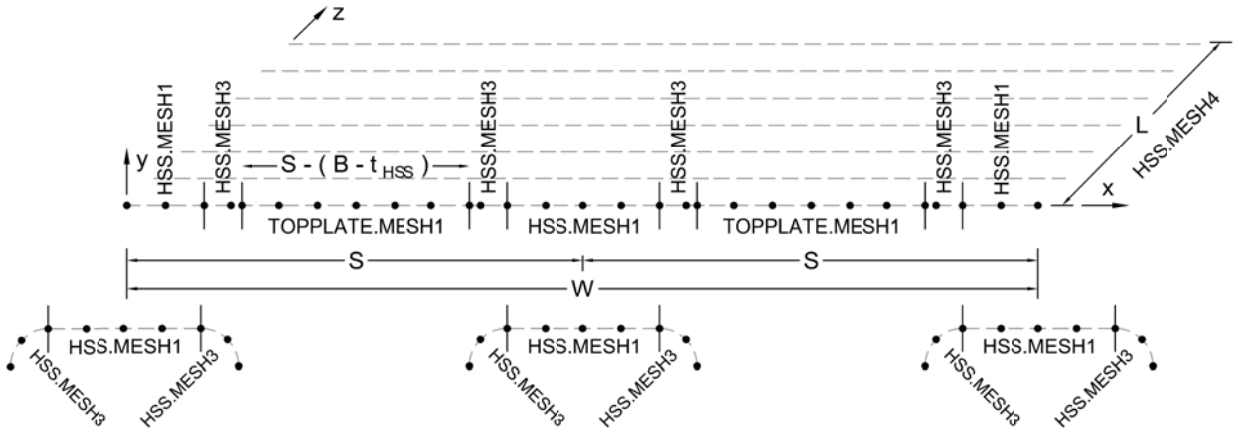

Figure 4–30:Top Plate Part Discretization and Localized Coordinate System

4.2.1.2.3 Bottom Plate

The bottom plate was modeled as a part in ABAQUS v6.9. A localized node set in the xy plane was created to develop a nodal cross section based upon panel width, *W* and internal rib spacing, *S*. The cross section was divided into two main regions, the area below a horizontal region of an HSS internal rib stiffener and the area between the internal rib stiffeners. The nodal projection of HSS.MESH1 was used to discretize the regions in the bottom plate below the horizontal regions of internal rib stiffeners as shown in Figure 4–31. The regions in the bottom plate at the start and end also used a nodal projection of HSS.MESH1, but were discretized using only half the number of

nodes as shown in Figure 4–31. The area between stiffeners, BOTTOMPLATE.MESH1 was then discretized to attain the desired element size, E_{SIZE}. The bottom plate was discretized in this manner to have corresponding mesh to each internal rib stiffener that eased the simulation of the laser weld discussed in section 4.2.1.3.1.

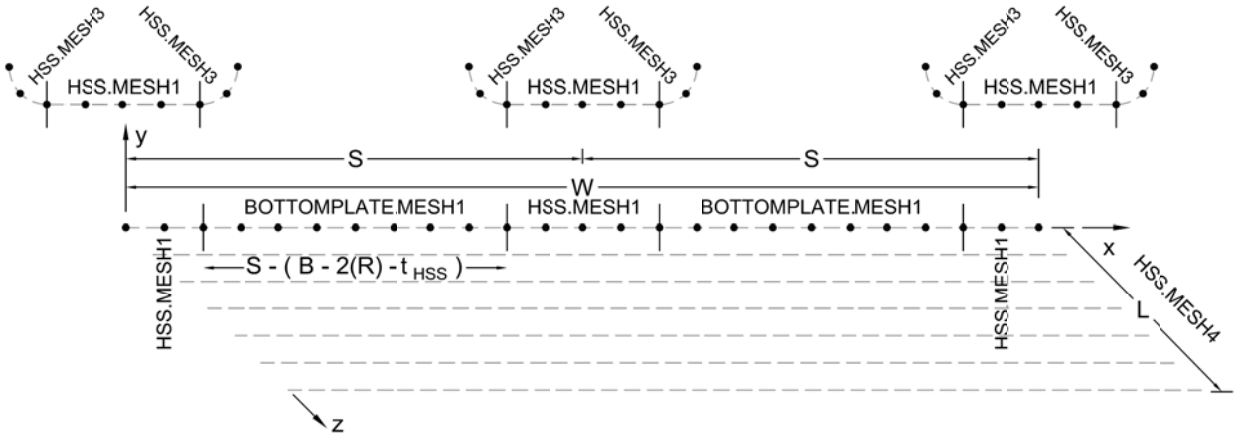

Figure 4–31: Bottom Plate Part Discretization and Localized Coordinate System

4.2.1.2.4 Laser Weld

The laser welds in each sandwich panel model were developed from a single part in the same manner used in the generalized fatigue test specimen model. The localized node set in the xy plane was based upon the top plate thickness, t_{TOP} and the HSS internal rib thickness, t_{HSS}. The laser weld cross section was categorized with one region, as in the fatigue test specimen model, LASER.MESH1 that was discretized to accommodate the desired element size, E_{SIZE} as shown in Figure 4–32.

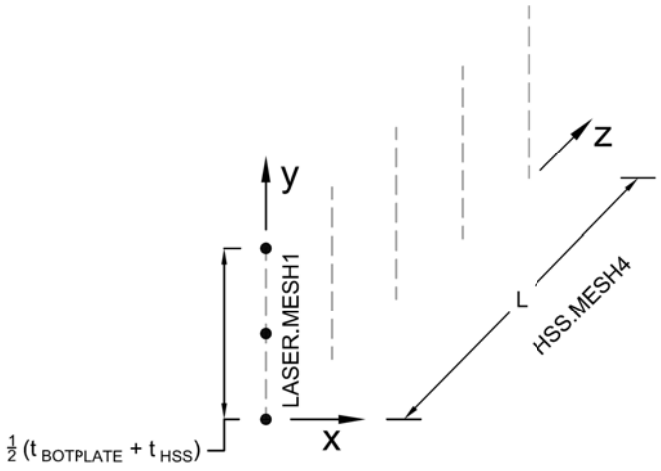

Figure 4–32: Laser Weld Part Discretization and Localized Coordinate System

4.2.1.2.5 Nodal Sweep and Section Assignment

Each of the component's xy node set was swept along the desired length, *L* with the addition of a z-coordinate according to HSS.MESH4 to maintain the desired element size, E_{SIZE}. Please refer to Figure 4–3, Figure 4–30, Figure 4–31, and Figure 4–32. The XYZ node set was numbered and used to create an element list according to the ABAQUS S8R5 numbering convention as shown in Figure 4–1. Each part was then sectioned with the appropriate thickness except that of the laser weld which is discussed in section 4.2.1.6.2. Material properties were then assigned to mimic those of hot rolled steel that included a mass density of 7.34×10^{-4} lbf·s^2/in^4, Young's modulus of 29,000,000 psi and Poisson's ratio of 0.3.

4.2.1.3 Component Assembly

Each of the components discussed in section 4.2.1.2 were assembled in a global coordinate system using instances according to modeling parameters W, S, $t_{TOPPLATE}$, t_{HSS}, and $t_{BOTPLATE}$ as shown in Figure 4–33. The sections to follow describe the modeling methods used to simulate various welds and contact regions of the sandwich panel.

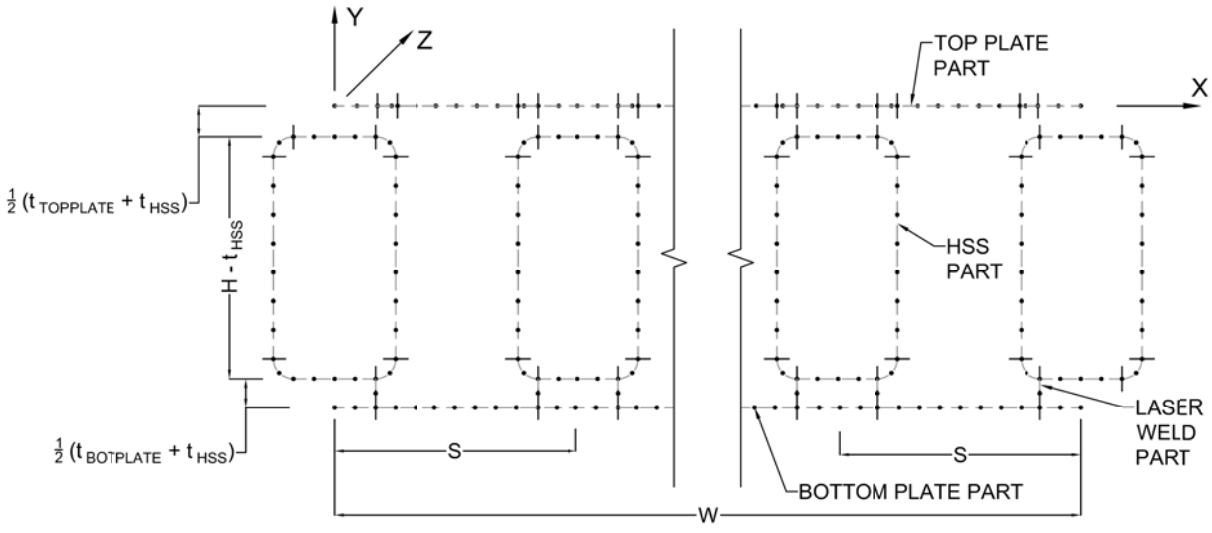

Figure 4–33: Sandwich Panel Finite Model Component Assembly and Global Coordinate

4.2.1.3.1 Flare Bevel Weld Simulation

The top plate was discretized to coincide with each of the HSS internal stiffening ribs to reduce the complexity of modeling the flare bevel weld used to join the top plate to the HSS internal core components. The flare bevel weld was modeled using BEAM type MPCs along the rounded corner of HSS sections that joined nodes of the top plate to HSS cores as shown in Figure 4–34. Nodes along the top plate were assigned as master nodes in the MPCs and nodes in the HSS were designated as slave nodes in the MPCs.

ABAQUS documentation defines a MPC type Beam as rigid beam between two nodes to constrain the displacement and rotation at the first node to the displacement and rotation at the second node, corresponding to the presence of a rigid beam between the two nodes.(Simulia, 2010)

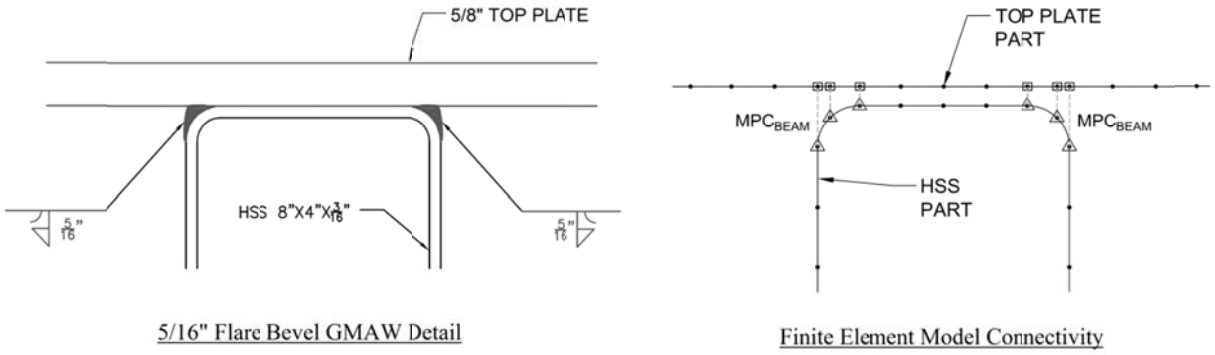

Figure 4–34: Sandwich Panel Finite Element Model Simulation of the Flare Bevel GMAW

4.2.1.3.2 Laser Weld Connectivity

Similarly to the generalized fatigue test specimen finite model, each laser weld component in the sandwich panel model was constrained to the bottom flange of the parallel HSS core and the corresponding location on the bottom plate using TIE type MPCs as shown in Figure 4–35. With regard to the MPCs used to tie the HSS sections to the laser weld component, master nodes were allocated as nodes in the HSS sections and the slave nodes taken as those along the top edge of the laser weld component. In relation to the MPCs used to connect laser weld components to the bottom plate, the nodes along the bottom edge of the laser weld were designated master nodes and the

slave nodes were assigned as those in the bottom plate.

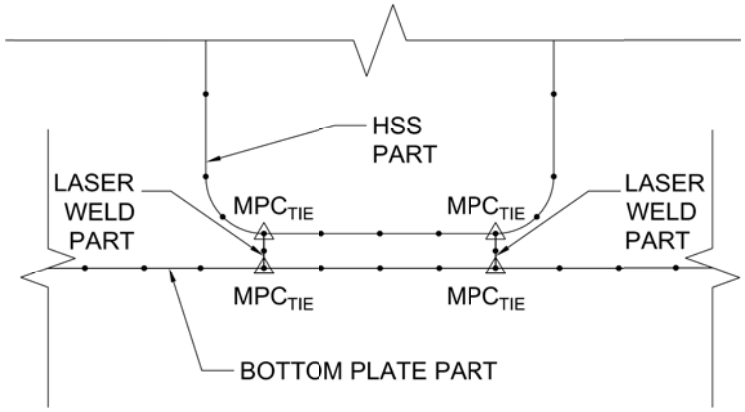

Figure 4–35: Sandwich Panel Finite Element Model Laser Weld Connectivity

4.2.1.3.3 Contact

Contact between the horizontal portions of the HSS internal stiffening ribs and the top and bottom face plates of the sandwich panel, was also modeled using non-linear Spring2 elements as shown in Figure 4–36. The non-linear springs were also assigned a zero tensile stiffness and a compressive stiffness that created no differential displacement between nodes, determined through the sensitivity study described in section 4.2.1.6.3.

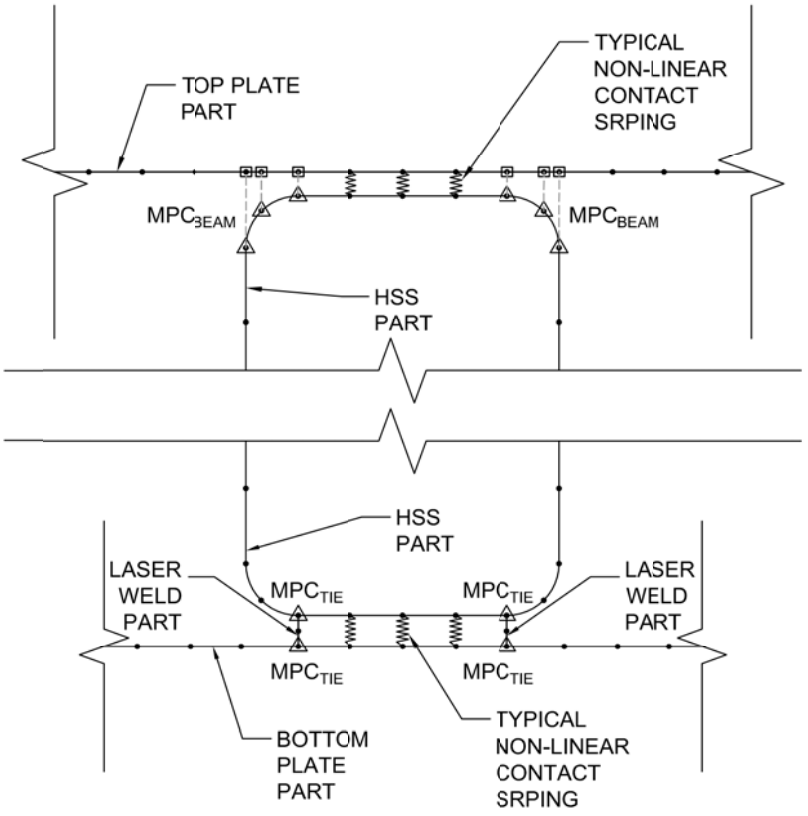

Figure 4–36: Non-Linear Springs used for Contact between HSS Components and Panel Face Plates

4.2.1.4 Boundary Conditions

In order to model the sandwich panel as a simply supported member in the transverse direction with a span length *L* the following approach was taken. Nodes with a Z-coordinate value of 0 (in.) and panel length, *L* (in.) were fixed in the Y direction. This created a theoretical roller at each "*support*" and allowed in-plane and out of plane deformation. A node on the bottom plate with an X-coordinate of half the sandwich panel width, *W*(0.5) and a Z-coordinate of zero was then fixed in the X and Z-direction. Another node on the bottom plate with an X-coordinate of half the sandwich panel width, *W*(0.5) and a Z-coordinate equal to the panel length, *L* (in.) was fixed in the X-direction. These two nodes were restrained to prevent rigid body translation and rotation of the sandwich panel. Please refer to Figure 4–37 for a visual depiction of the restrained nodes

described in this section.

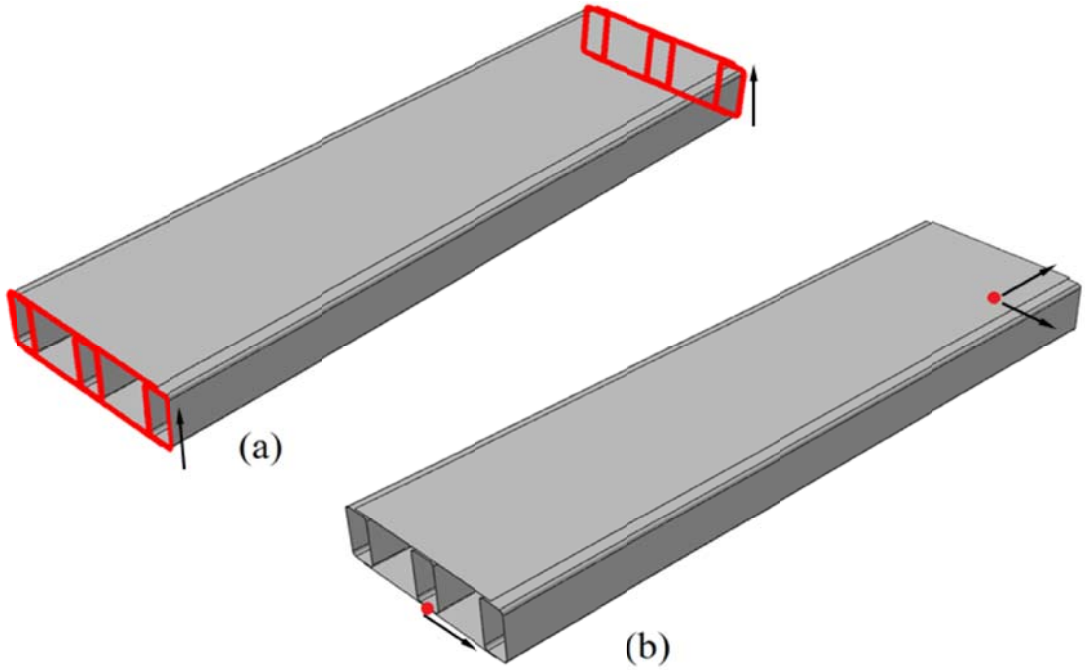

Figure 4–37: Restrained Nodes in a Generic Sandwich Panel Model. (a) Nodes to Restrain Vertical Movement (b) Nodes to Restrain Lateral Translation and Rotation

4.2.1.5 Loading

According to section 3.6.4.1 of the *AASHTO LRFD Bridge Design Specifications*, a 16,000 lbs truck wheel load evenly distributed over a 10"X20" patch was used with a conservative dynamic load allowance, *IM* of 33%. To generate the largest stress in the bottom plate and maximum differential rib deflection the load was placed at mid span, directly over the HSS internal stiffening rib as shown in Figure 4–38. The load was applied in ABAQUS using an evenly distributed downward surface pressure over an element set on the top plate as shown in Figure 4–38.

In addition to the truck wheel patch load, the self-weight of the sandwich panel

was also taken into consideration by turning on gravity in ABAQUS. A gravitational constant of 384.6 in/s^2 was applied in the negative Y-direction. This constant was applied to the mass density in the section properties of each shell defined previously to model the unit weight of steel as 0.284 lb/in^3.

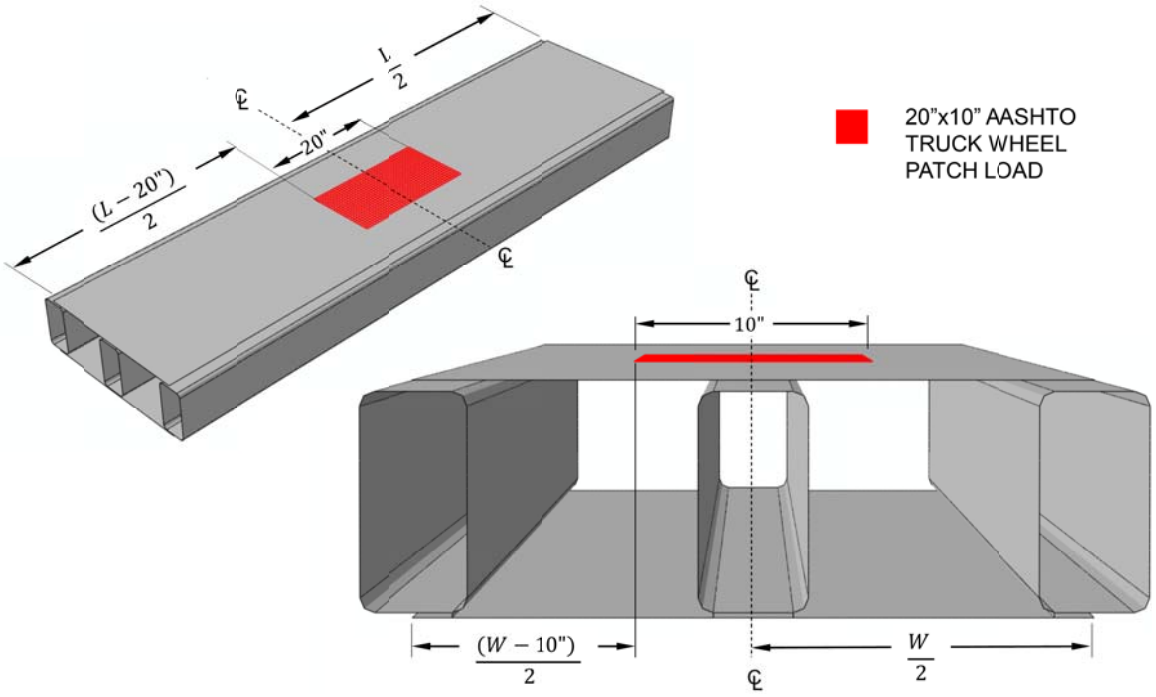

Figure 4–38: Sandwich Panel Truck Wheel Patch Loading

4.2.1.6 Model Sensitivity

4.2.1.6.1 Convergence Study

As in the case with the generalized fatigue test specimen model, a convergence study was also performed on the finite element model of a sandwich panel bridge deck module to verify the modeling methodology and optimize the discretization scheme to generate accurate results in timely fashion. The criteria used convergence was the maximum vertical global displacement at mid span, Δ_y in relation to element size, E_{SIZE}. In order to generalize the model used for convergence, non-linear contact springs were neglected and the following modeling parameters were used:

S = 12 inches

W = 24 inches

L = 102 inches

t_{TOP} = 5/8 inches

t_{BOTTOM} = 3/16 inches

l_W = 0.0860 inches

l_{OFFSET} = 0 inches

$HSS_{SECTION}$ = HSS8”X4”x3/16”

Models were created using the parameters defined above, while varying the desired element size, E_{SIZE} from 0.375” to 1”. In addition to self-weight, the sandwich panels modeled for convergence were subjected to a uniform downward pressure of 3.75 psi distributed over the top plate, and then analyzed elastically using the static general analysis in ABAQUS v6.9.

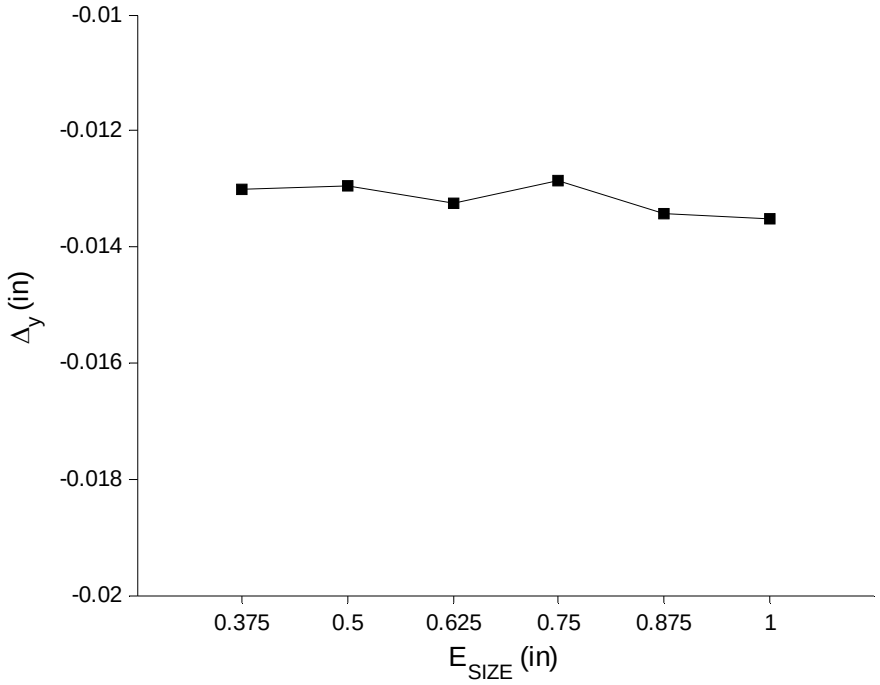

Figure 4–39: Sandwich Panel Finite Element Model Convergence Study

The results from the convergence study summarized in Figure 4–39 exhibits nearly identical behavior for each element size analyzed. This provides verification to the modeling approach, as the discrepancies in the maximum vertical displacement can be attributed to ABAQUS tolerances. Consequently, the selected element size used to discretize each component is completely arbitrary as it does not influence the overall result of the model. In order to minimize element distortion and provide a more suitable comparison to the fatigue testing performed in this investigation, an element size of 0.5 in. was chosen.

4.2.1.6.2 Laser Weld Shell Thickness Study

Provided with the same reasoning described in section 4.1.1.6.2, a study was performed to understand the influence of the laser interface width, l_w on the structural behavior of the sandwich panel module finite element model. Thus, numerous models were created using the modeling parameters described in the convergence study to reduce computational time with an E_{SIZE} of 0.5 inches, while varying the laser weld link thickness to evaluate the effect on the maximum vertical displacement Δ_y in the bottom plate.

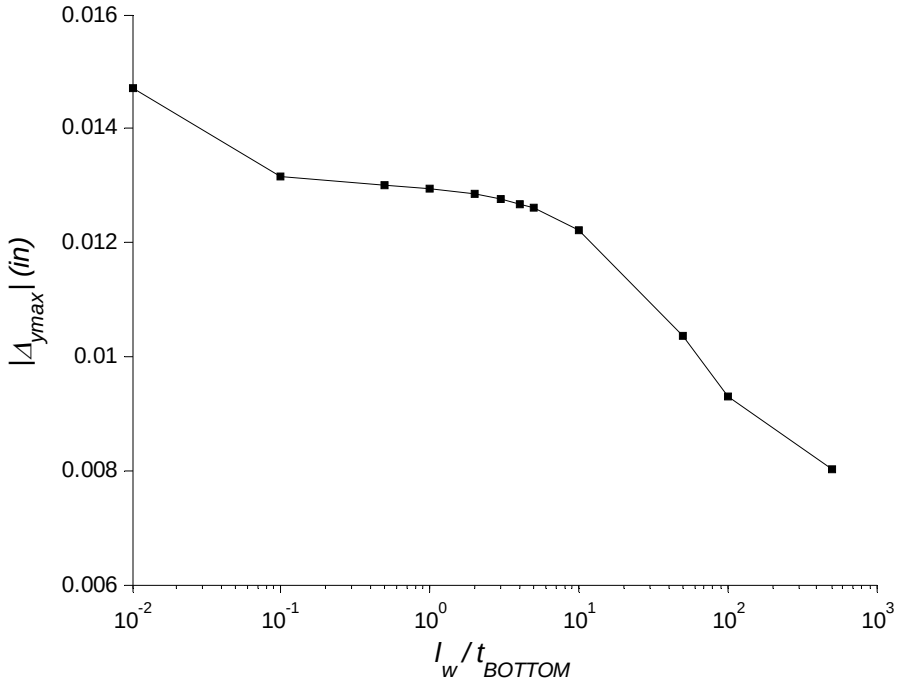

Figure 4–40: Laser Weld Interface Width Influence on the Sandwich Panel Finite Model

The results of the laser weld shell thickness study are summarized in Figure 4–40, which the relationship between the absolute maximum vertical displacement Δ_y and non-dimensional laser weld shell thickness l_w/t_{BOTTOm} is displayed on a semi-log plot.

(Caccese, 2009) The laser weld shell thickness was non-dimensionalized to the bottom plate thickness t_{BOTTOM} of 0.1875 inches, similarly to the study performed for the generalized fatigue test specimen model, for easier interpretation of the results. In conclusion, the laser weld interface width has minimal influence the behavior of the model when it is defined with a thickness between than $0.1t_{BOTTOM}$ and $1t_{BOTTOM}$. Based upon this study, an even value of 0.1 inches was chosen for the laser weld interface width.

4.2.1.6.3 A Study on the Compressive Stiffness of Non-Linear Springs used for Contact

Provided with the same reasoning from the Generalized Fatigue Test Specimen Model, discussed in section 4.1.1.6.3, sensitivity study was performed on the non-linear springs to determine an appropriate stiffness to model contact. Sandwich panel models were created using the modeling parameters for the convergence study to reduce computational time, while varying non-linear compressive stiffness from 0 $^{lb}/_{in}$ to 10,000 $^{lb}/_{in}$. Given that a uniform downward pressure would not engage the non-linear springs connecting the HSS internal stiffening ribs and bottom plate in compression, the loading scheme described in section 4.2.1.5 was applied. Two nodes connected by a non-linear spring to simulate contact between the top plate and center HSS internal stiffening rib at mid span were analyzed for global vertical displacement. Another set of two nodes connected by a non-linear spring to model contact between an outside HSS internal stiffening rib and bottom plate at mid span were also analyzed for global vertical displacement, refer to Figure 4–41. The differential displacement between nodes shown in Figure 4–41 was used to determine an appropriate compressive stiffness for the non-linear springs to model contact. Ideally, the differential displacement between nodes

should equal zero demonstrating that they move together as discussed previously. The results from the sensitivity study on the compressive stiffness of the non-linear springs between the top plate, HSS internal stiffening ribs, and bottom plate are summarized in Figure 4–42 and Figure 4–43.

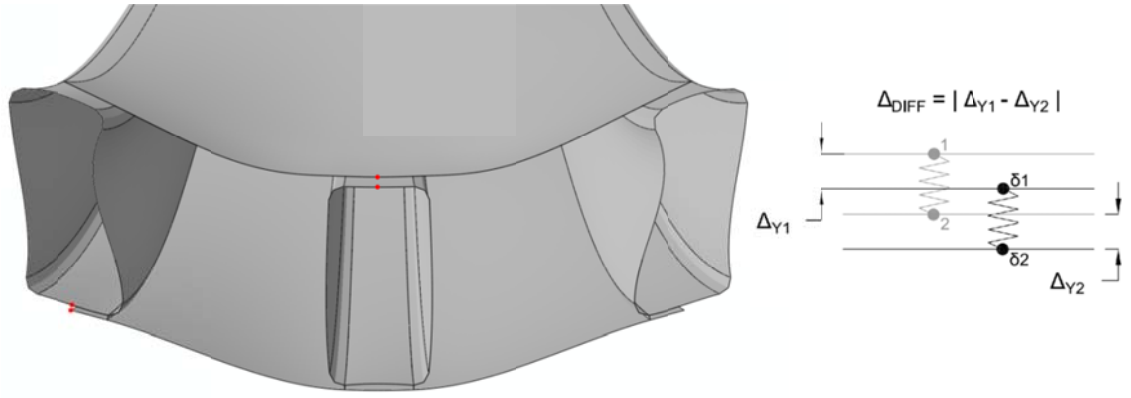

Figure 4–41: Differental Displacement between Nodes Connected by a Non-Linear Spring to Model Contact

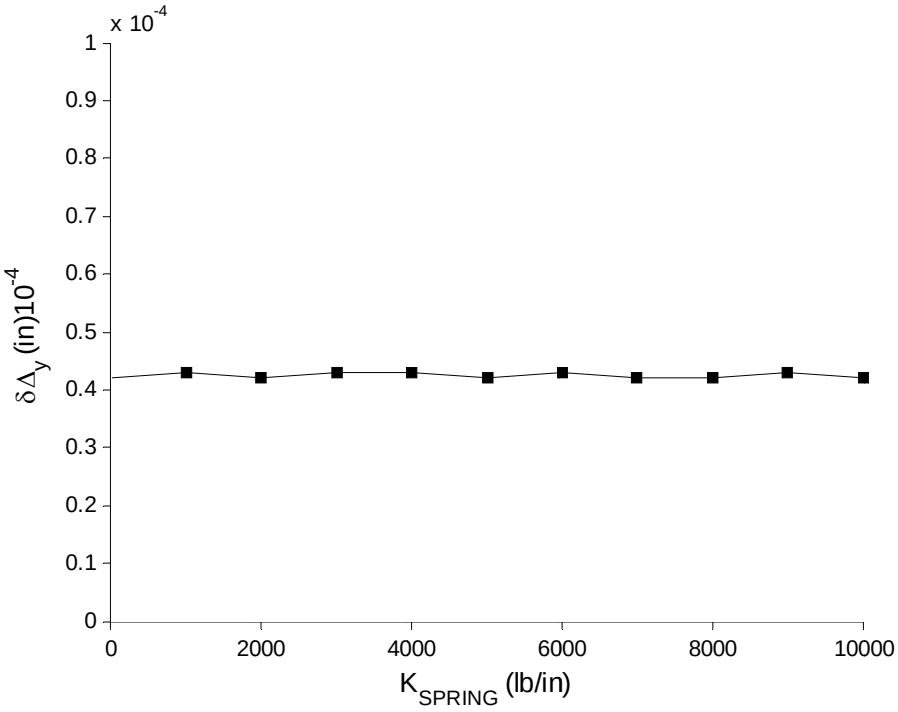

Figure 4–42: Top Plate and HSS Internal Stiffening Rib Non-Linear Springs Stiffness Sensitivity Study

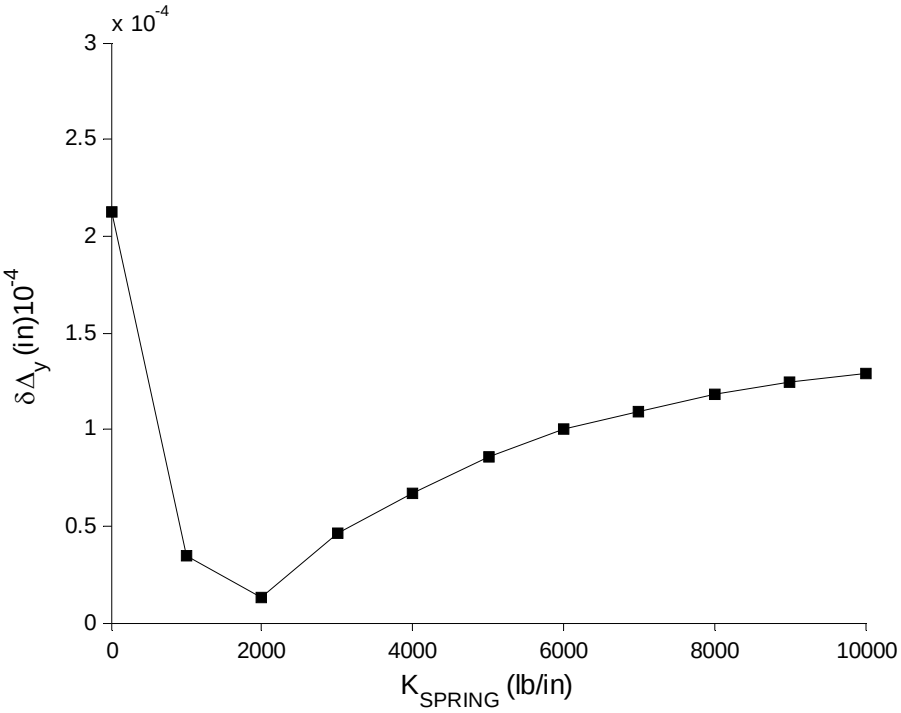

Figure 4–43: HSS Internal Stiffening Ribs and Bottom Plate Non-Linear Springs Stiffness Sensitivity Study

The sensitivity study established that non-linear springs were not necessarily needed for the contact interaction between the top plate and HSS internal stiffening ribs. The differential deflection between nodes remained constant, close to zero, as the compressive stiffness was increased. This demonstrated the negligent influence of contact interaction between the top plate and HSS internal stiffening ribs. This was believed to be the result of the top plate's considerable stiffness in relation to the HSS components. As a result, these non-linear springs between the top plate and HSS internal ribs were removed to reduce computational time.

On the other hand, the sensitivity study to determine the compressive stiffness of the non-linear springs used to model contact between HSS internal stiffening ribs and the bottom plate, presented promising results. The optimal compressive stiffness was founded to be 2000 $^{lb}/_{in}$. The plot shown in Figure 4–43 demonstrates how increased

stiffness can fictitiously alter the behavior of non-linear springs. As a result the compressive stiffness of these non-linear springs used to simulate contact between the HSS internal ribs and bottom plate was taken to be 2000 $^{lb}/_{in}$.

4.2.2 PARAMETRIC STUDY: INTERNAL RIB SPACING AND TOP PLATE THICKNESS

The primary purpose of modeling the global behavior of a sandwich panel was to assess overall the fatigue performance by studying the localized Vierendeel effect of internal HSS stiffening ribs. In order to compare the global behavior of sandwich panel bridge deck modules to the fatigue tests performed in this research endeavor, a parametric study was conducted that focused on the bottom plate behavior between adjacent HSS ribs at mid span. Due to the fluctuating boundary conditions for any given fatigue test, the parametric study concentrated on the center to center spacing of HSS stiffeners, *S*. It was hypothesized that as the boundary conditions for a fatigue test approached a fixed-fixed condition, the correlated global behavior would relate to a sandwich panel with smaller internal rib spacing. In addition, the parametric study also explored top plate thickness, t_{TOP} as its substantial stiffness in relation to the other sandwich panel components indicated that it would govern behavior.

In all, 28 different sandwich panel configurations were investigated that were made up of four different top plate thicknesses ranging from 9/16"to 3/4" and seven different internal rib spacing values ranging from 6" to 18". In order to provide symmetry in both planer directions for each sandwich panel configuration, an odd number of internal stiffening ribs was specified. As a result, the sandwich panel width, *W* ranged from 84 in. to 108 in. according to the rib spacing as shown in Table 4-2. The other modeling parameters were held constant and were defined as follows:

E_{SIZE} = 0.5 inches

L = 102 inches

t_{BOTTOM} = 3/16 inches

l_W = 0.0860 inches

l_{OFFSET} = 0 inches

$HSS_{SECTION}$ = HSS8"X4"x3/16"

Table 4-2: Sandwich Panel Width and Internal Rib Spacing used in the Parametric Study

S (in)	***W (in)***	***HSS Rib Quantity***
6	96	17
8	96	13
10	100	11
12	96	9
14	84	7
16	96	7
18	108	7

Each sandwich panel configuration was bounded and loaded according to sections 4.2.1.4 and 4.2.1.5 respectively. Non-linear springs with a tensile and compressive stiffness of 0 psi and 2000 psi respectively were used to model contact between the HSS stiffening ribs and bottom plate. The models were analyzed elastically using the static general analysis in ABAQUS.

4.2.2.1 Global Behavior

To provide a general understanding of global behavior, the mid span deflection and maximum shear were analyzed along the longitudinal direction of the sandwich panel to determine the influence of internal rib spacing and top plate thickness. Provided the boundary conditions described in section4.2.1.4, the sandwich panel was assumed to

react similar to a one way system depicted by Figure 4–44. To investigate the maximum deflection at mid span, the nodal displacements in the bottom plate at mid span shown in Figure 4–45 were outputted in the vertical direction. The maximum shear region was examined by extracting the shear stress, σ_{xy} on the outside of every web of the internal HSS stiffening ribs at 18 inches as shown in Figure 4–46. The shear stress was extrapolated to the center of the element from the four reduced Gaussian integration points. All values were studied for each of the 28 models analyzed in the parametric study.

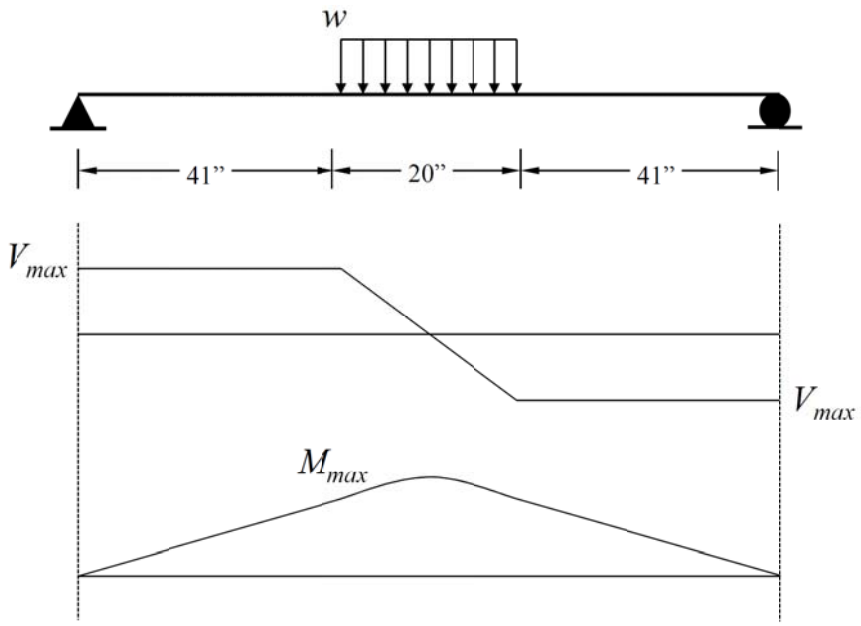

Figure 4–44: One Way System Assumption

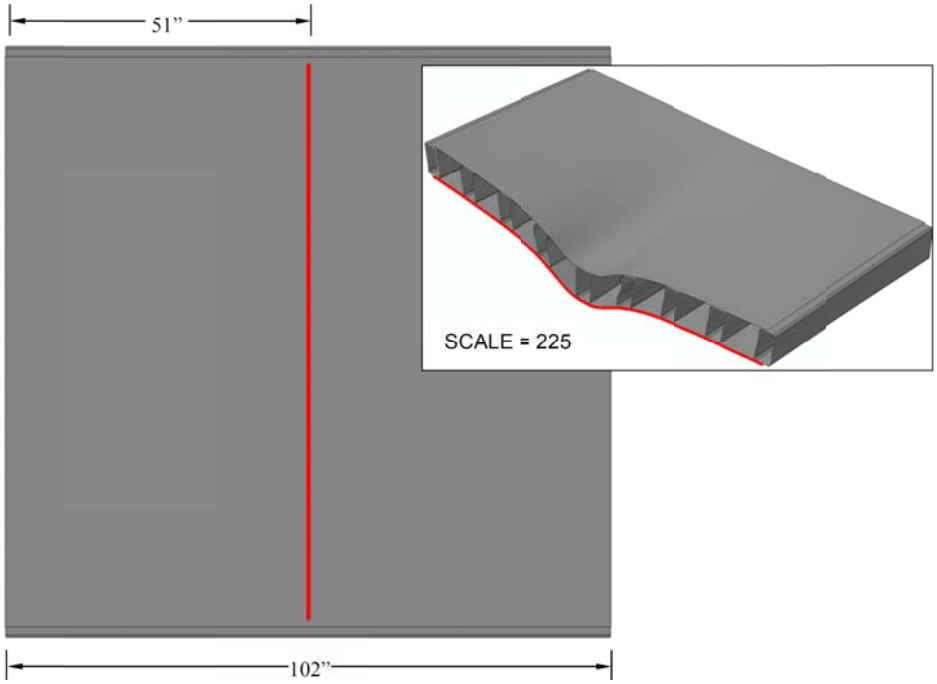

Figure 4–45: Sandwich Panel Bottom Plate Vertical Nodal Displacements at Mid Span

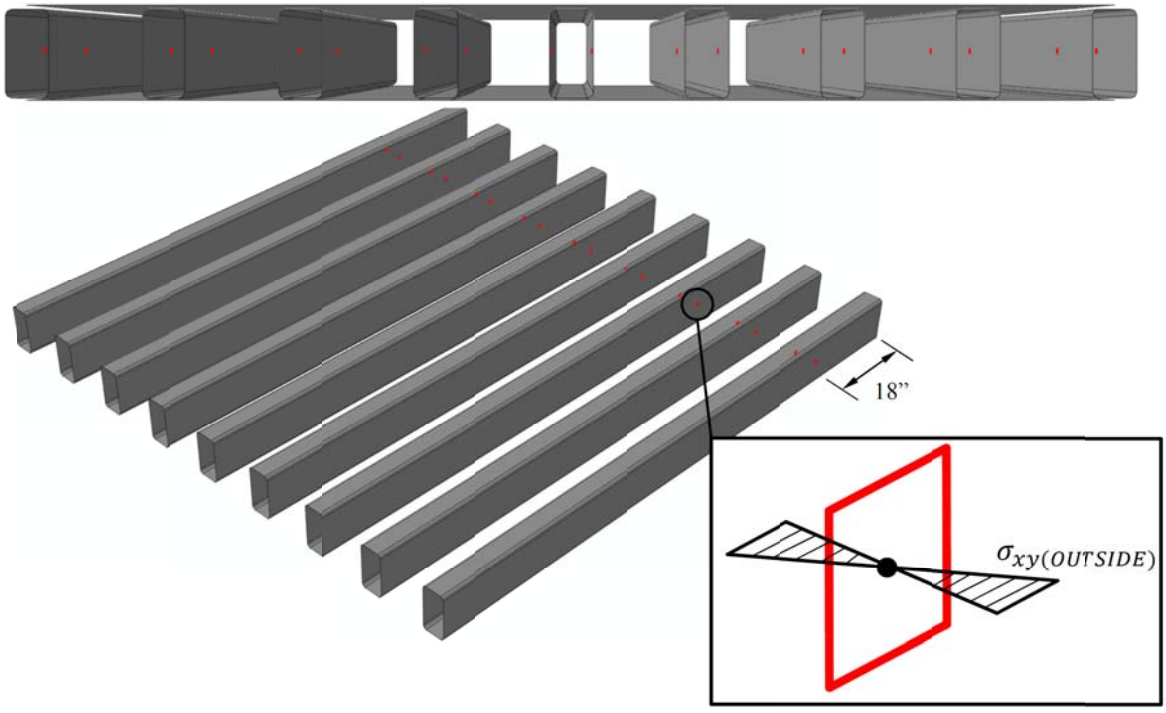

Figure 4–46: Shear Stress Study in HSS Webs along the Maximum Shear Region

4.2.2.2 Comparison Parameters to Generalized Fatigue Test Specimen Models

In order to provide a comparison to the individual fatigue tests, the same parameters discussed in section 4.1.2.4 were calculated for each of the 28 sandwich panel models analyzed in the parametric study. As shown in Figure 4–47 equivalent fatigue stresses, maximum vertical differential displacements, maximum slope, and distance between inflection points were computed at mid span, along the bottom plate, between center and adjacent internal HSS stiffening ribs. Stated previously, these values shall allow for a particular sandwich panel configuration to compare to the average of the values of the fatigue test specimens, thus being able to take advantage of the S-N curves generated. The equivalent fatigue stresses were calculated using the same method described in section 4.1.2.2. The other comparison values were calculated in nearly the identical manner described in section 4.1.2.4, in which the nodal displacements along the bottom refer to Figure 4–48.

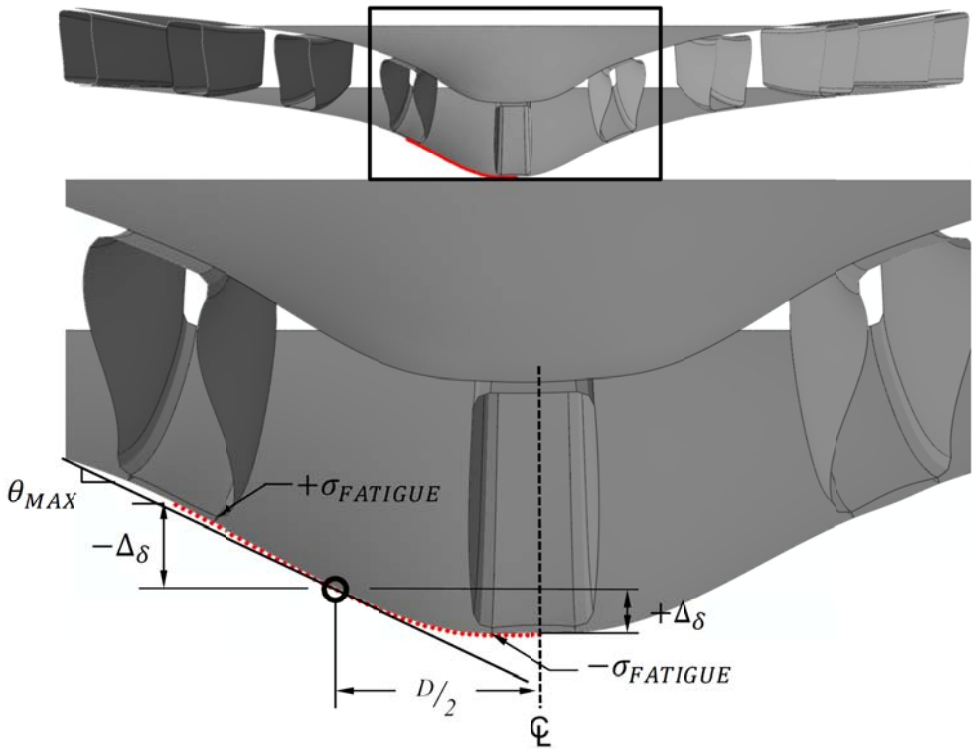

Figure 4–47: Comparison Parameters to the Generalized Fatigue Test Specimen Models

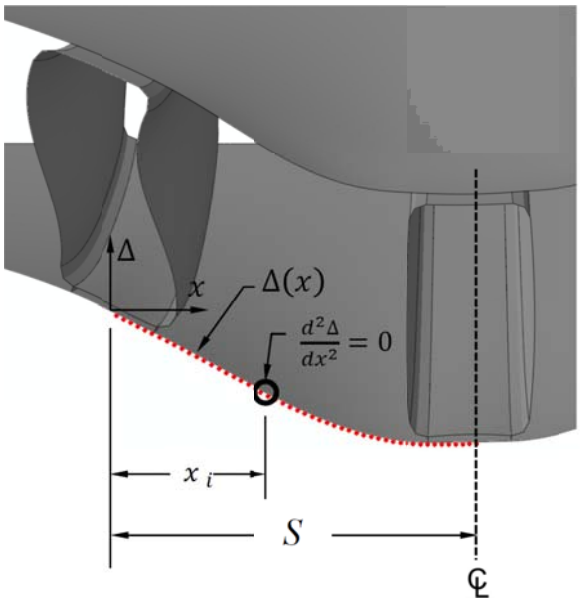

$$\Delta(x) = ax^3 + bx^2 + cx + d$$

$$\frac{d\Delta}{dx} = 3ax^2 + bx + c$$

$$\frac{d^2\Delta}{dx^2} = 6ax + b$$

$$\theta_{MAX} = 3a\left(\frac{-b}{6a}\right)^2 + b\left(\frac{-b}{6a}\right) + c$$

$$x_i = \frac{-b}{6a}$$

$$D = 2(S - x_i)$$

Figure 4–48: Determining Comparison Parameters from Finite Element Analysis Nodal Output

5.1 EXPERIMENTAL RESULTS

5.1.1 MATERIAL PROPERTIES

The values displayed in Table 5-1 are the mean values gathered from the tension tests described in section 3.3.1. The stress strain curve for the $^{3}/_{16}$ in. steel plate depicted that of mild steel, whereas the stress strain curve for the HSS coupons represented cold rolled steel. Therefore, the lower yield strength was taken for the plate yield stress and the 0.2 % offset method was utilized to determine the yield stress for the HSS steel. Refer to Appendix B for the stress strain curves of each rectangular coupon.

Table 5-1: ASTM E8 Tension Testing Summary

Specimen Component	F_y (ksi)	F_u (ksi)
$^{3}/_{16}$" Plate	60.3	72.1
HSS	53.5	71.0

5.1.2 FATIGUE TESTING

Table 5-2: Fatigue Testing Summary: Test Specimens Without a Fit-up Gap

Test Specimen	± P (lbs)	Cycles to Failure	Failure Location	Freq. (Hz)	Runtime (hrs)
FAT-LBW-02	250	2,507,172	*Plate Failure at Weld*	6	116.07
FAT-LBW-03	200	12,206,238	*Run-out*	6	378.50
FAT-LBW-04	400	450,761	*Weld Failure Along HSS/Plate Interface*	5	25.03
FAT-LBW-05	400	408,802	*Weld Failure Along HSS/Plate Interface*	5	22.71
FAT-LBW-06	300	322,501	*Plate Failure at Weld*	6	14.93
FAT-LBW-07	300	1,015,680	*Plate Failure at Weld*	6	47.02
FAT-LBW-08	300	1,032,013	*Plate Failure at Weld*	6	47.78
FAT-LBW-09	250	1,460,125	*Plate Failure at Weld*	6	67.60
FAT-HLAW-01	400	212,329	*Weld Failure Along HSS/Plate Interface*	6	48.00
FAT-HLAW-02	400	247,544	*Weld Failure Along HSS/Plate Interface*	6	55.52
FAT-HLAW-03	250	10,066,008	*Run-out*	5	28.29
FAT-HLAW-04	350	3,774,172	*Plate Failure at Weld*	6	40.49
FAT-HLAW-05	350	10,000,000	*Run-out*	7	43.75
FAT-HLAW-06	375	659,796	*Plate Failure at Weld*	5	36.58
FAT-HLAW-07	375	1,632,905	*Plate Failure at Weld*	6	50.94
FAT-HLAW-08	375	1,581,959	*Plate Failure at Weld*	6	47.73

Table 5-3: Fatigue Testing Summary: Fit-up Gap Test Specimens

Test Specimen	Fit-up Gap (inches)	± P (lbs)	Cycles to Failure	Failure Location	Freq. (Hz)	Runtime (hrs)
FAT-LBWG-01	0.000	400	201,083	*Plate Failure at Weld*	6	9.31
FAT-LBWG-02	0.000-0.003	350	573,339	*Plate Failure at Weld*	7	24.61
FAT-LBWG-03	0.003-0.006	400	545,449	*Plate Failure at Weld*	6	25.00
FAT-LBWG-04	0.006-0.010	350	1,468,607	*Plate Failure at Weld*	4	91.31
FAT-LBWG-05	0.010-0.012	400	264,622	*Plate Failure at Weld*	6	12.25
FAT-LBWG-06	0.012-0.016	350	350,162	*Plate Failure at Weld*	8	12.16
FAT-LBWG-07	0.016-0.018	400	239,294	*Plate Failure at Weld*	6	11.08
FAT-LBWG-08	0.018-0.022	350	367,890	*Plate Failure at Weld*	6	17.03
FAT-LBWG-09	0.022-0.032	400	203,824	*Plate Failure at Weld*	6	9.44
FAT-LBWG-10	0.032-0.035	350	262,871	*Plate Failure at Weld*	6	12.17
FAT-LBWG-11	0.035	400	90,387	*Plate Failure at Weld*	6	4.19
FAT-HLAWG-01	0.000	425	401,962	*Plate Failure at Weld*	6	18.61
FAT-HLAWG-02	0.000	400	679,049	*Plate Failure at Weld*	6	32.88
FAT-HLAWG-03	0.000-0.004	425	524,314	*Plate Failure at Weld*	6	24.28
FAT-HLAWG-04	0.004-0.006	400	583,248	*Weld Failure Along HSS/Plate Interface*	6	27.00
FAT-HLAWG-05	0.006-0.009	425	421,480	*Weld Failure Along HSS/Plate Interface*	6	19.50
FAT-HLAWG-06	0.009-0.010	400	845,279	*Plate Failure at Weld*	6	39.13
FAT-HLAWG-07	0.010-0.014	425	260,131	*Weld Failure Along HSS/Plate Interface*	6	12.04
FAT-HLAWG-08	0.014-0.019	400	367,231	*Weld Failure Along HSS/Plate Interface*	6	17.00
FAT-HLAWG-09	0.020-0.025	425	124,657	*Weld Failure Along HSS/Plate Interface*	6	5.77
FAT-HLAWG-10	0.025-0.035	400	326,943	*Weld Failure Along HSS/Plate Interface*	6	15.14
FAT-HLAWG-11	0.035	425	191,297	*Plate Failure at Weld*	6	8.86

5.1.2.1 Fractography

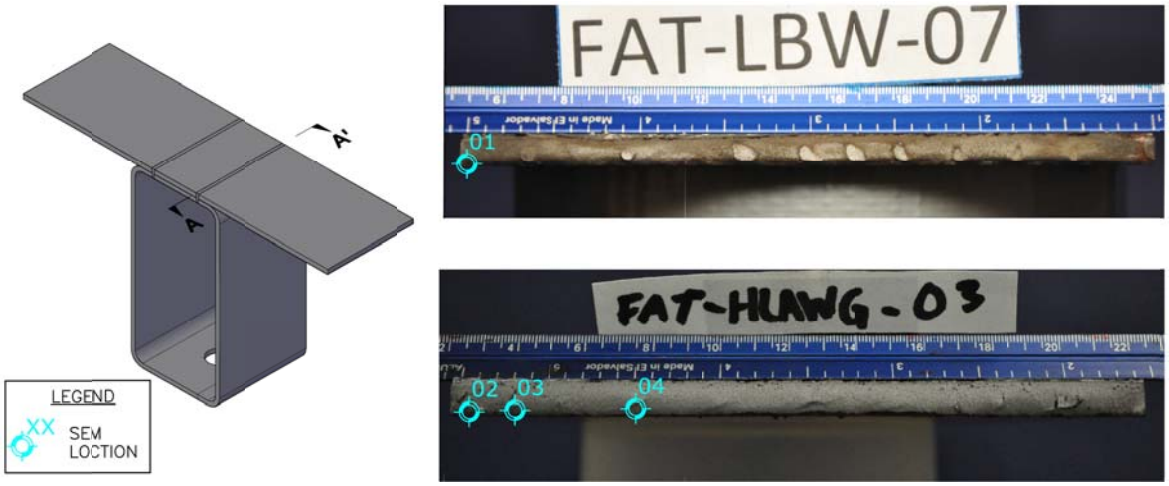

Figure 5–1: SEM Location Legend

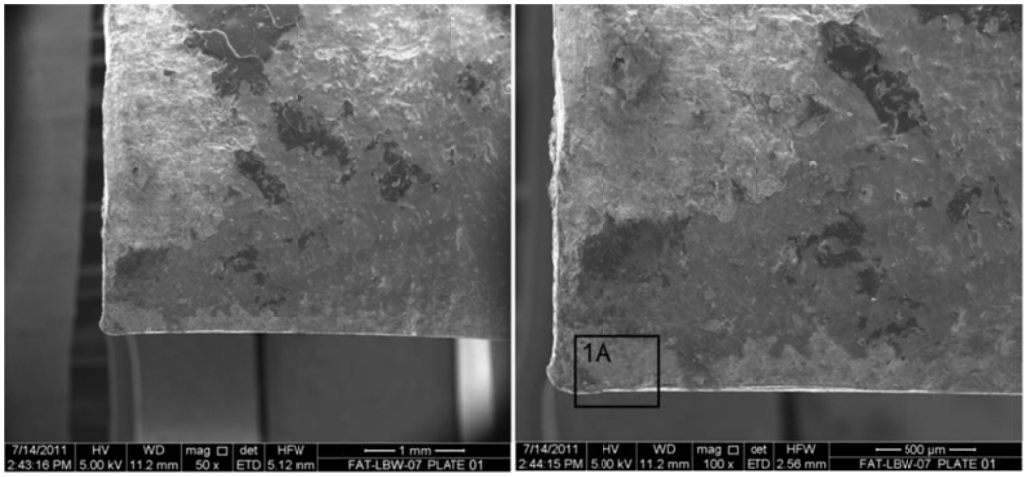

Figure 5–2: FAT-LBW-07 SEM Location 1 at 50x and 100x Magnification (Left to Right)

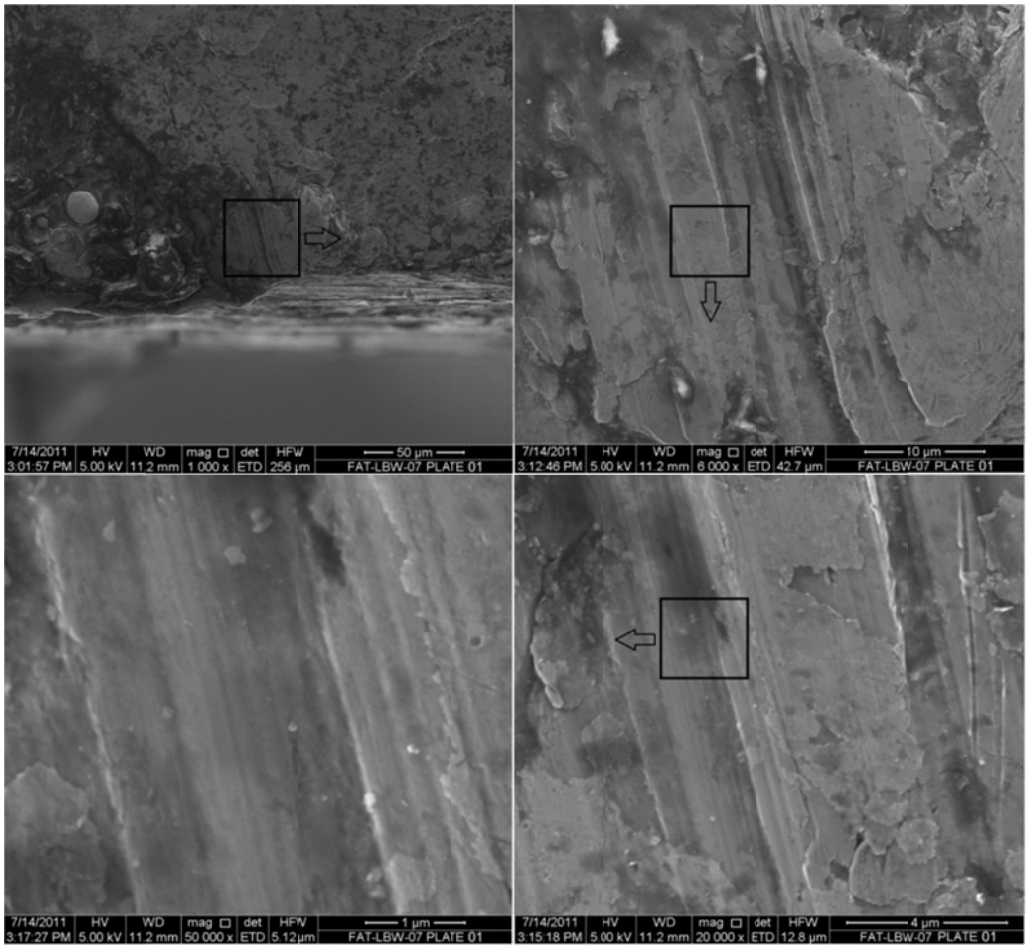

Figure 5–3: FAT-LBW-07 SEM Location 1A at 1000x, 6000x, 20000x, and 50000x (CW Start Upper Left)

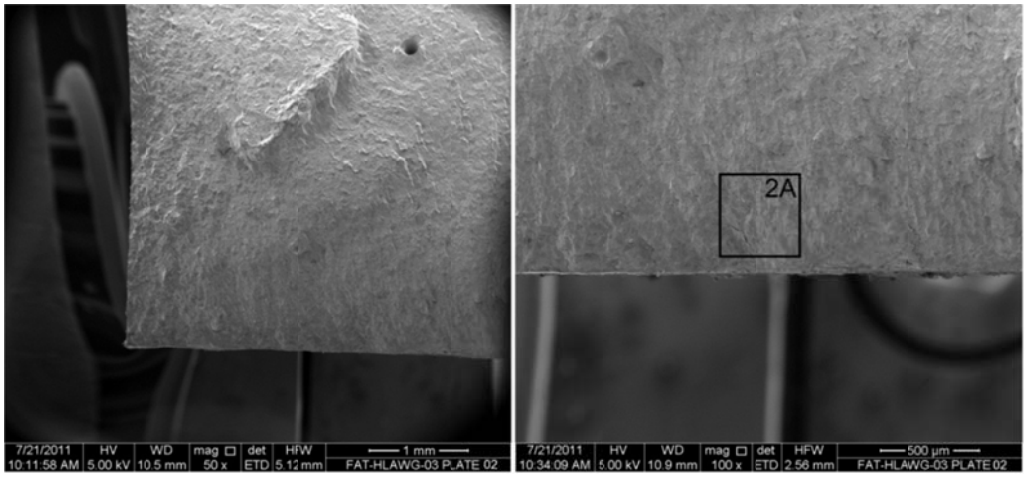

Figure 5–4: FAT-HLAW-03 SEM Location 2 at 50x and 100x (Left to Right)

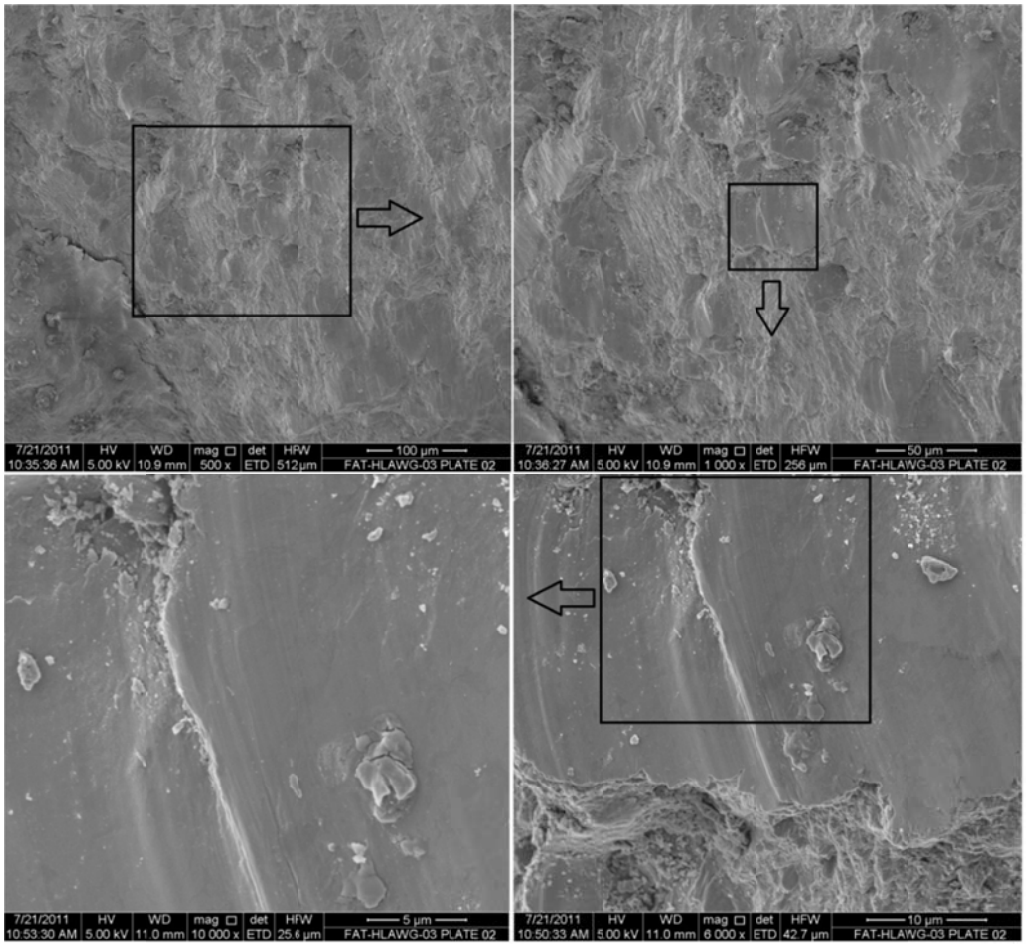

Figure 5–5: FAT-HLAW-03 SEM Location 2A at 500x, 1000x, 6000x, and 10000x (CW Start Upper Left)

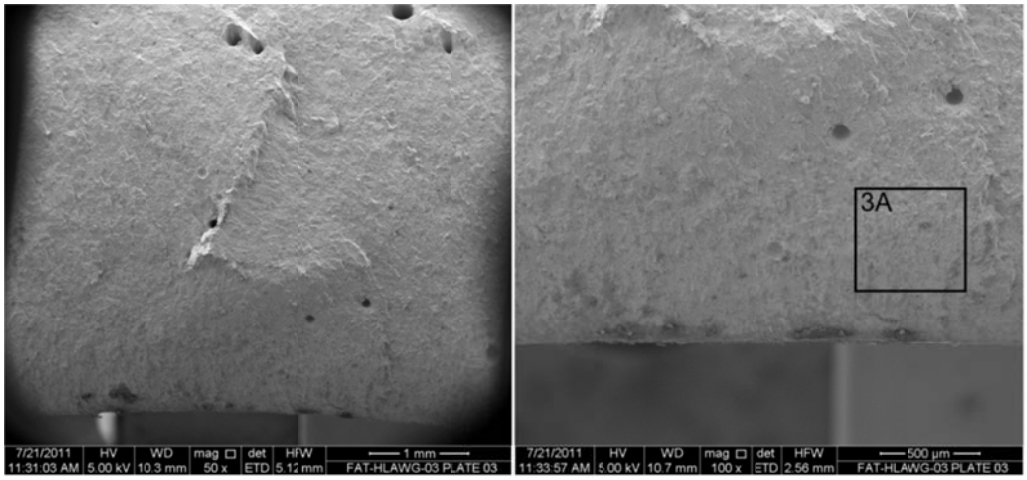

Figure 5–6: FAT-HLAW-03 SEM Location 3 at 50x and 100x (Left to Right)

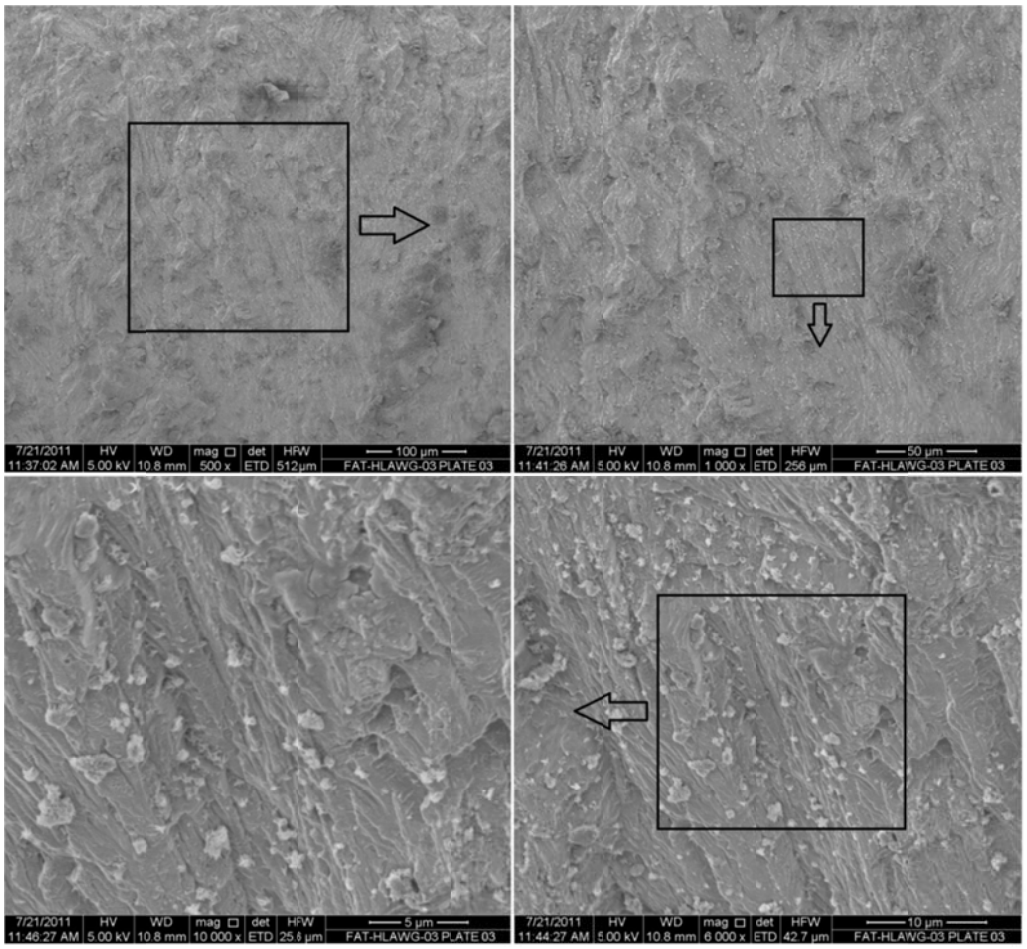

Figure 5–7: FAT-HLAW-03 SEM Location 3A at 500x, 1000x, 6000x, and 10000x (CW Start Upper Left)

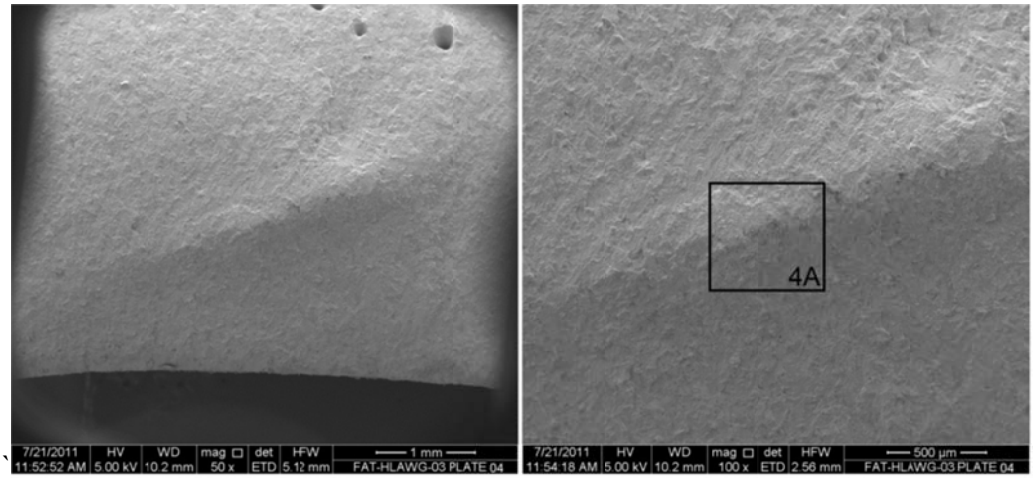

Figure 5–8: FAT-HLAW-03 SEM Location 4 at 50x and 100x (Left to Right)

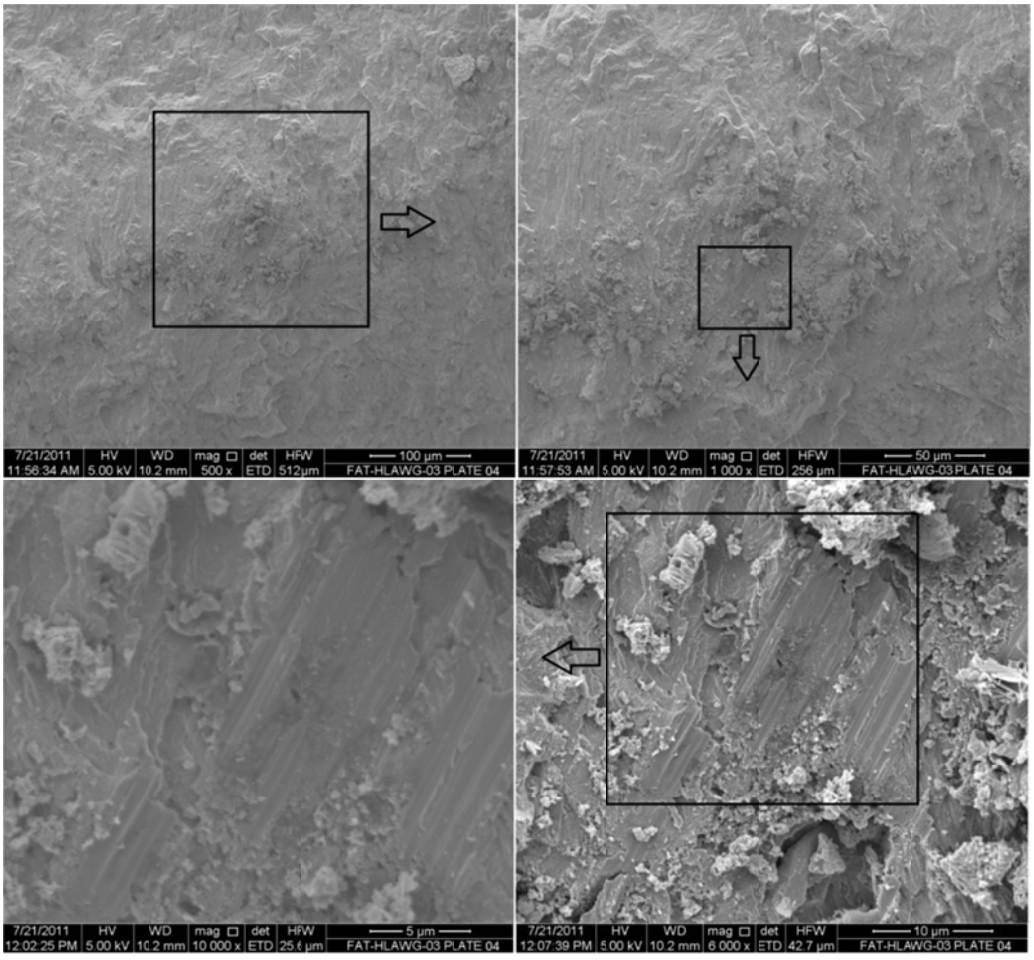

Figure 5–9: FAT-HLAW-03 SEM Location 4A at 500x, 1000x, 6000x, and 10000x (CW Start Upper Left)

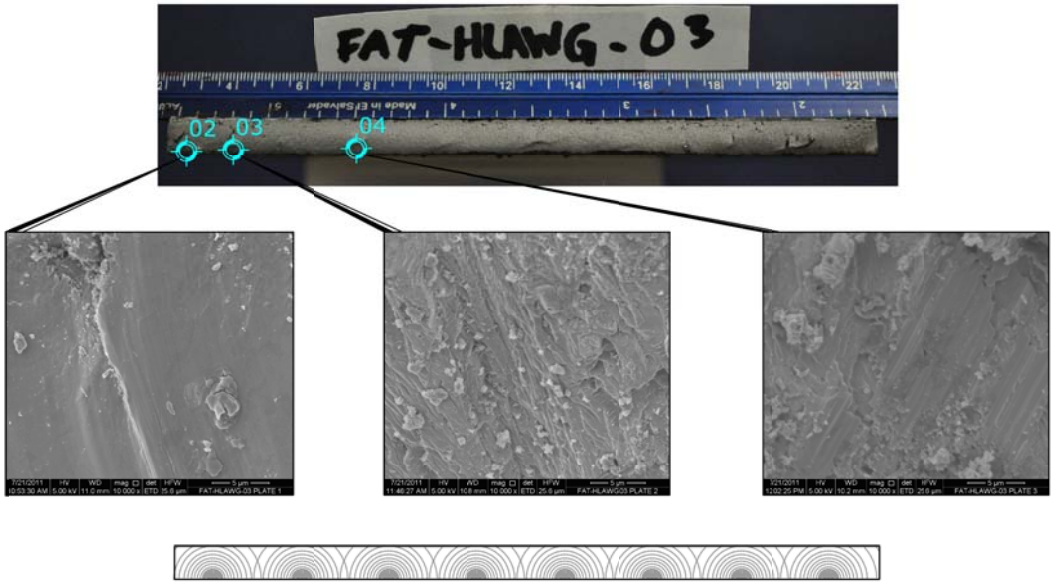

Figure 5–10: Fatigue Crack Initiation Pattern

5.1.3 ELASTIC LOAD TEST

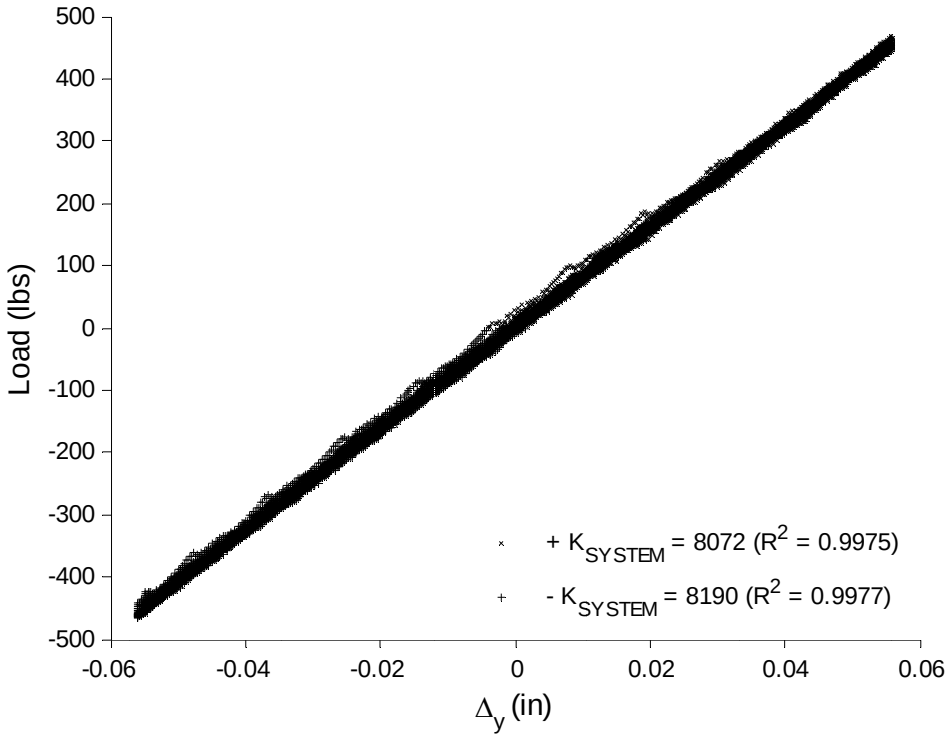

Figure 5–11: FAT-LBW-02 Load vs. Displacement Plot

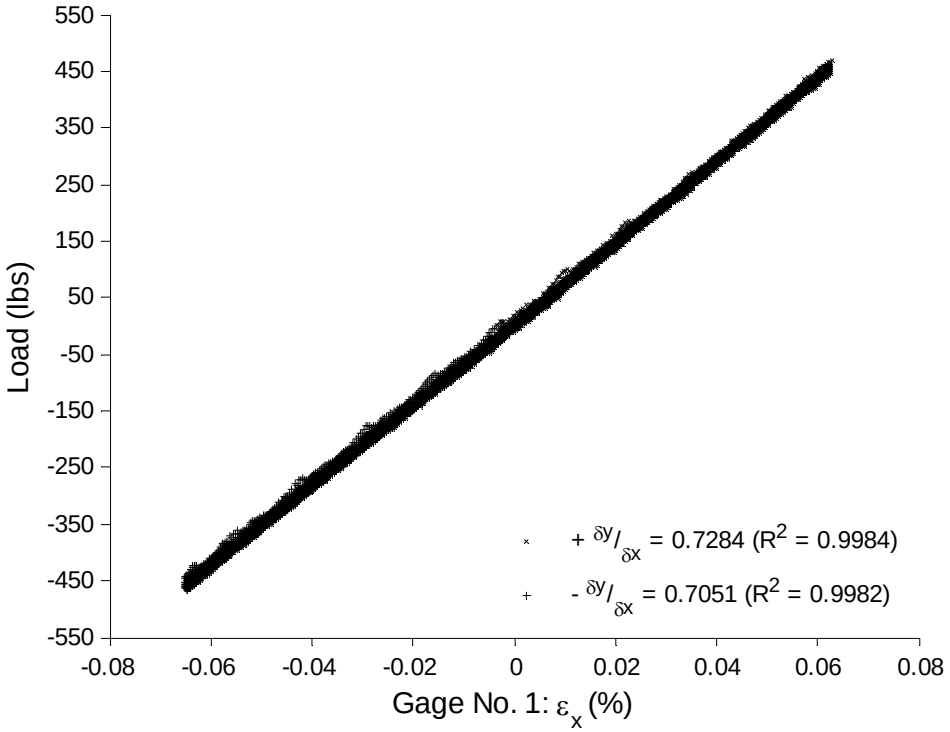

Figure 5–12: FAT-LBW-02 Gage No. 1 Load vs. Strain Plot

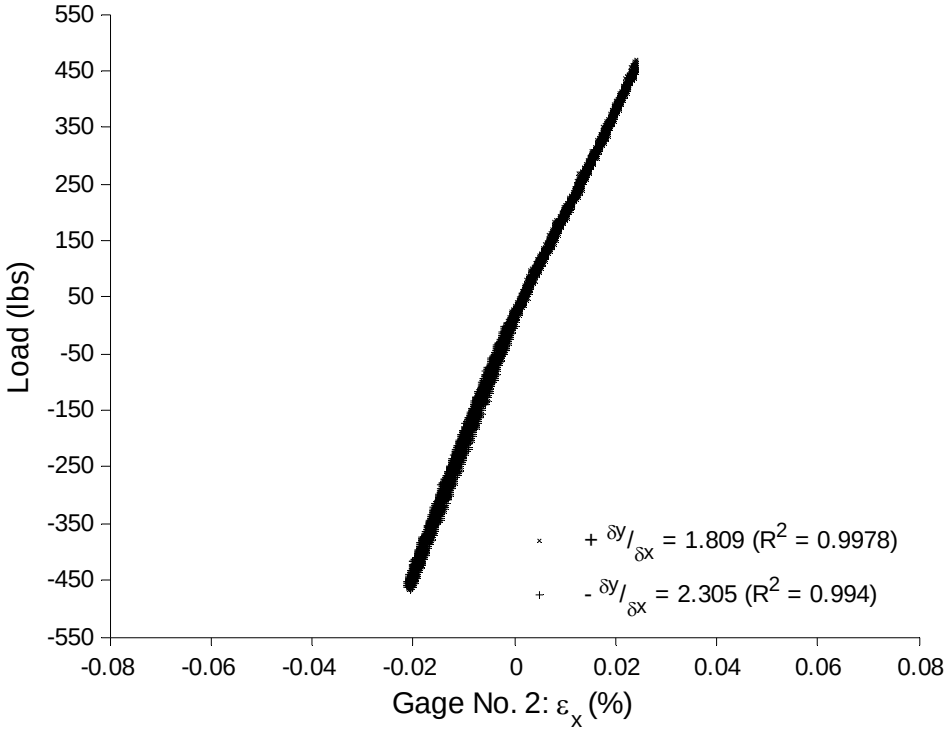

Figure 5–13: FAT-LBW-02 Gage No. 2 Load vs. Strain Plot

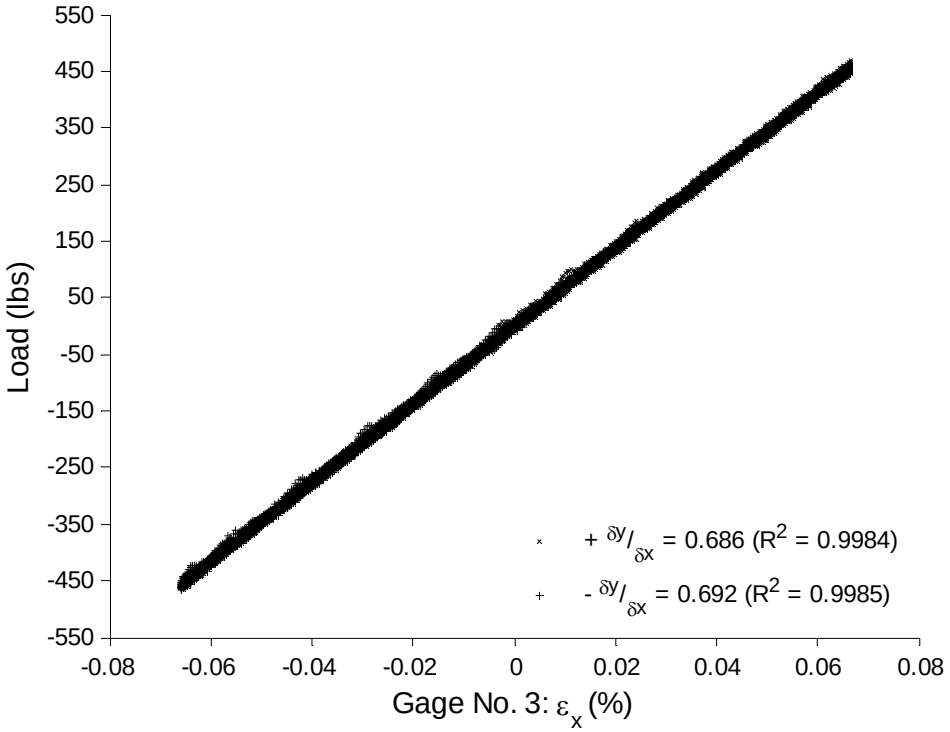

Figure 5–14: FAT-LBW-02 Gage No. 3 Load vs. Strain Plot

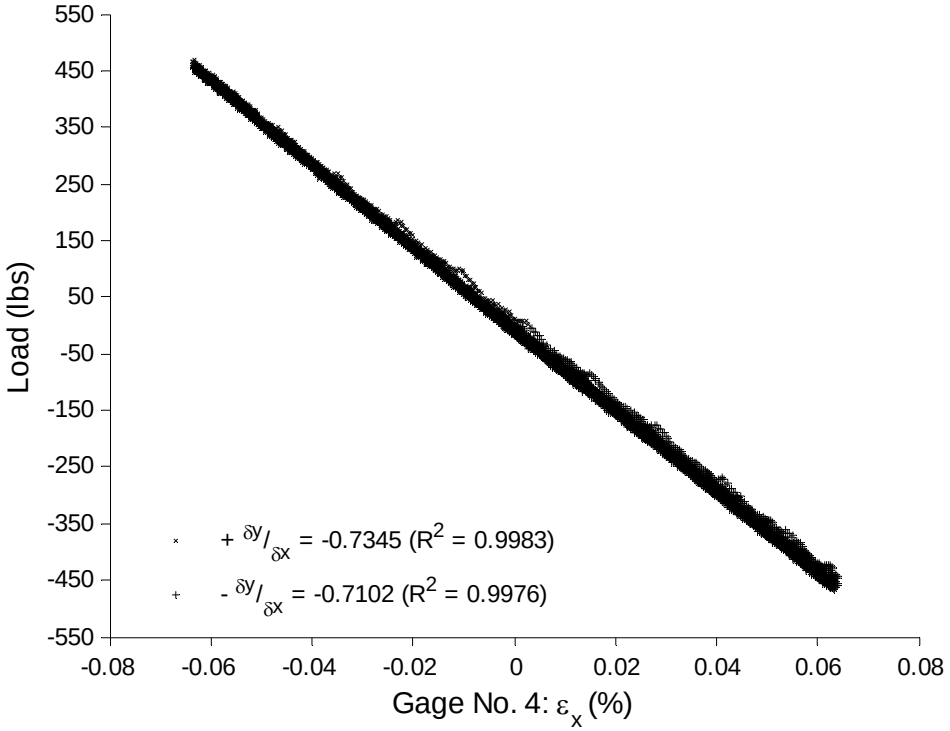

Figure 5–15: FAT-LBW-02 Gage No. 4 Load vs. Strain Plot

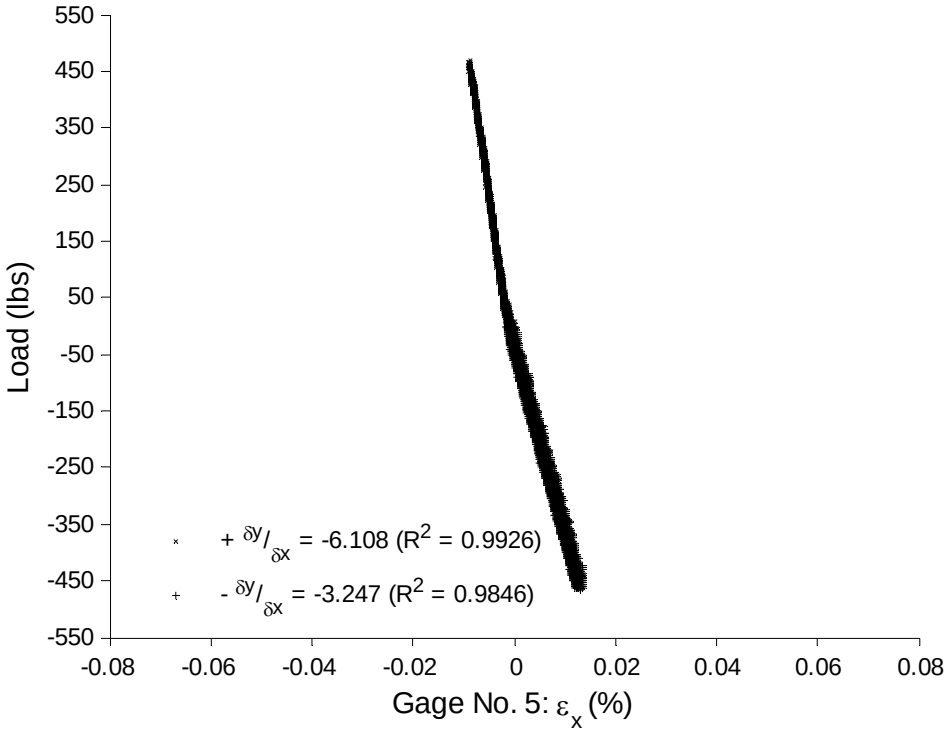

Figure 5–16: FAT-LBW-02 Gage No. 5 Load vs. Strain Plot

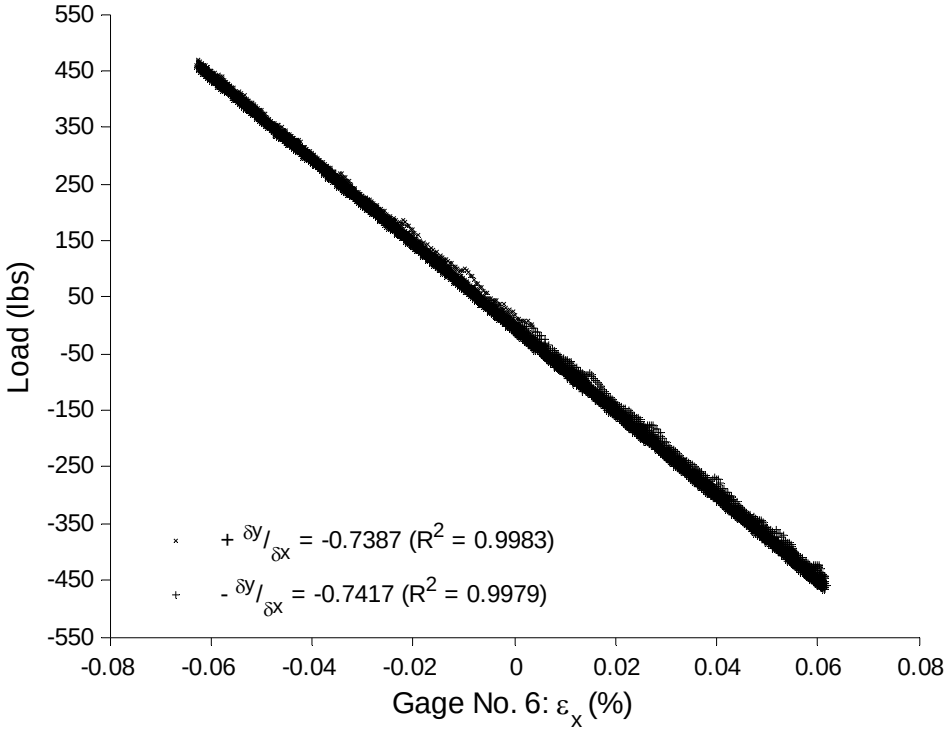

Figure 5–17: FAT-LBW-02 Gage No. 6 Load vs. Strain Plot

5.1.4 PARTIAL RESTRAINT VERIFICATION TESTING

The data displayed in following plots contains data recorded in the first load cycle of each test every 0.5 seconds, not the full three load cycles at 10 Hz in order to alleviate noise to distinguish between different clamping force data sets.

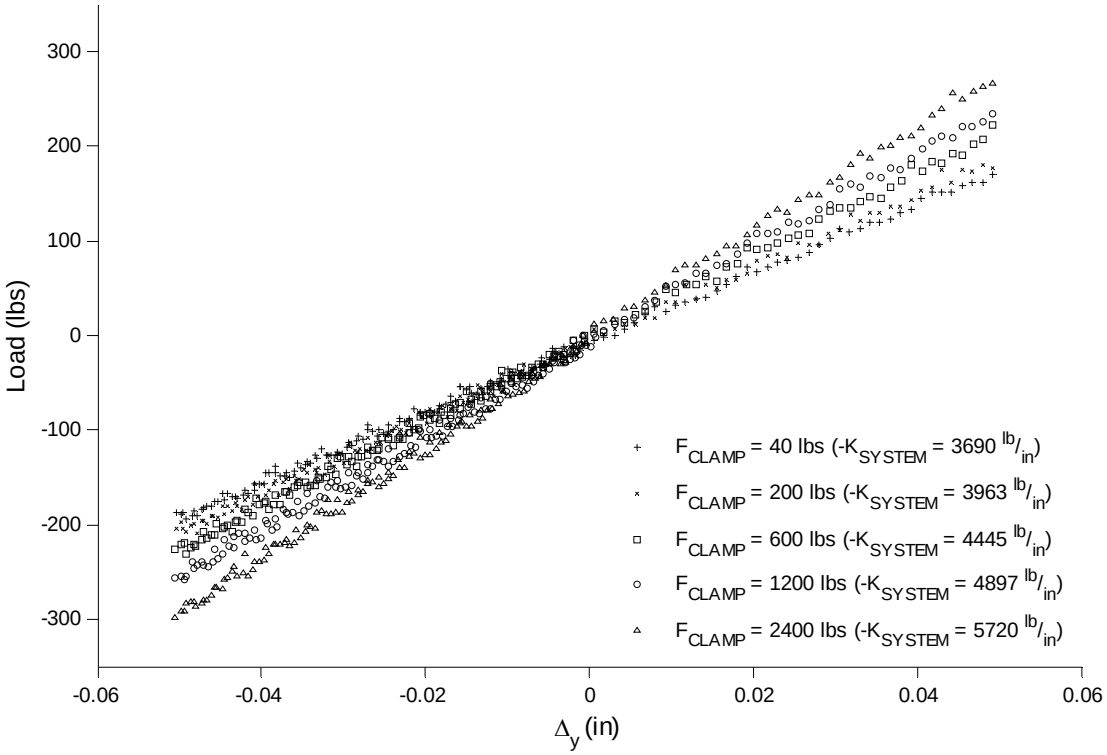

Figure 5–18: FAT-LBW-09 Load Displacement Plot at Varying Clamping Force

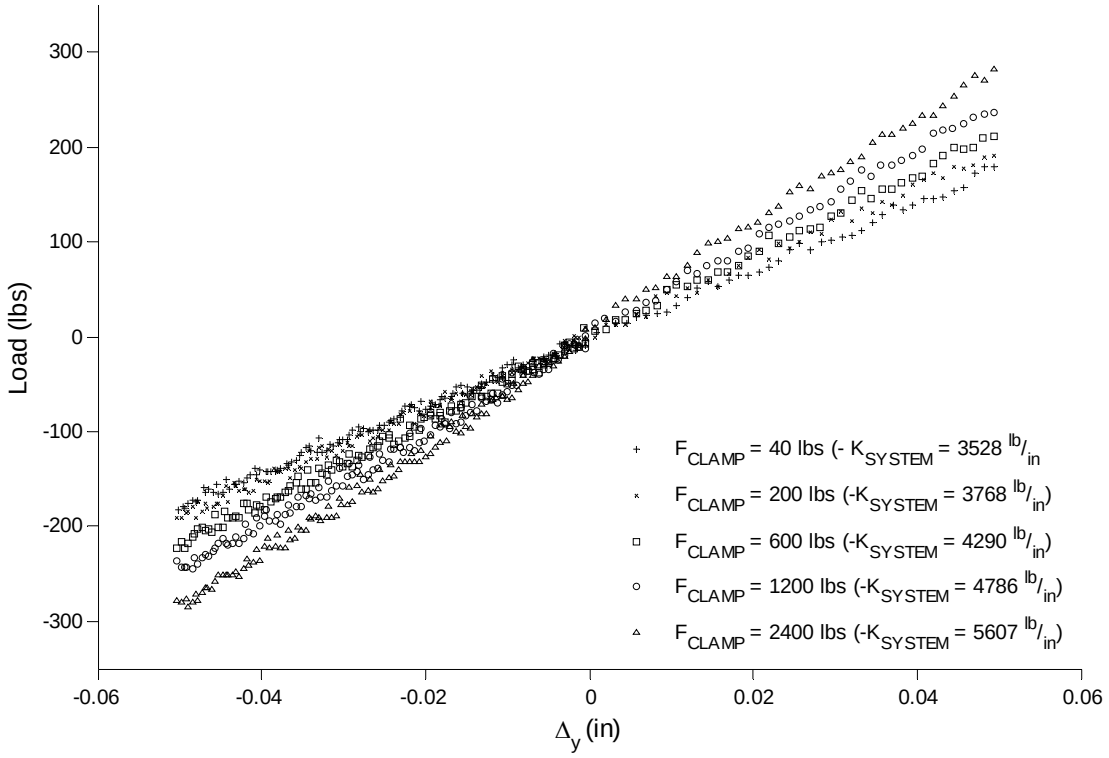

Figure 5–19: FAT-HLAW-06 Load Displacement Plot at Varying Clamping Force

5.1.5 FATIGUE CONFIRMATION TESTING

Table 5-4: Fatigue Confirmation Testing Summary

Test Specimen	Cycles to Failure	$\Delta\sigma_{NOMINAL}$ (ksi)	P (lbs)	t_{PL} (in.)	A (in^2)	Failure Location	Freq. (Hz)	Runtime (hrs)
FAT-LBW-01	251,995	35	26,460	0.1890	0.7560	*Plate Failure at Weld*	10	116.07
FAT-LBW-10	219,546	35	26,432	0.1888	0.7552	*Plate Failure at Weld*	15	378.50
FAT-LBW-11	279,510	35	26,474	0.1891	0.7564	*Plate Failure at Weld*	15	25.03
FAT-HLAW-09	845,725	30	22,575	0.1881	0.7524	*Plate Failure at Weld*	15	22.71
FAT-HLAW-10	885,957	30	22,500	0.1875	0.7500	*Plate Failure at Weld*	15	14.93

5.2 ANALYTICAL RESULTS

5.2.1 GENERALIZED FATIGUE TEST SPECIMENS

5.2.1.1 Elastic Load Test

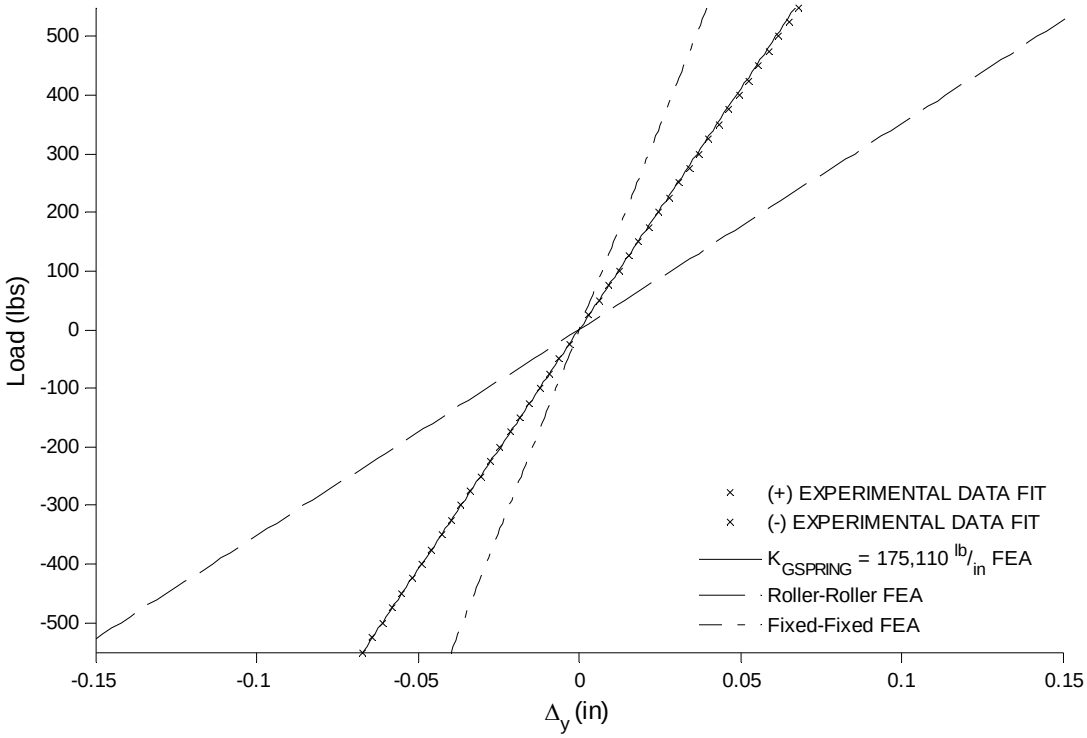

Figure 5–20: FAT-LBW-02 Analytical Load vs. Displacement Plot

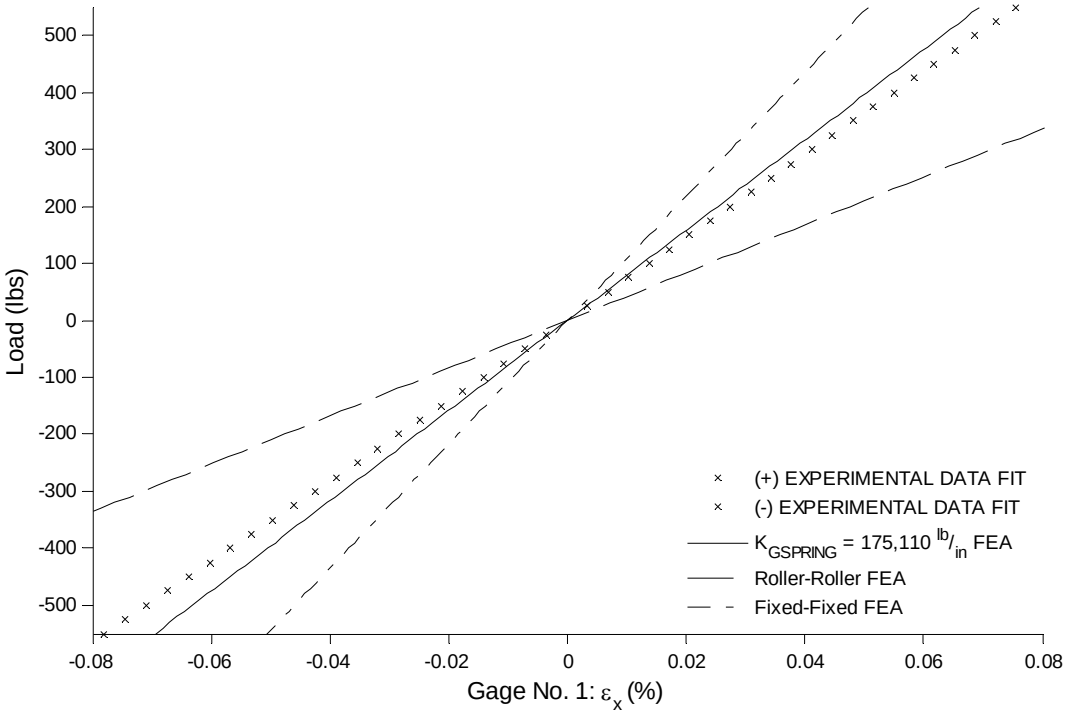

Figure 5–21: FAT-LBW-02 Analytical Gage No. 1 Load vs. Strain Plot

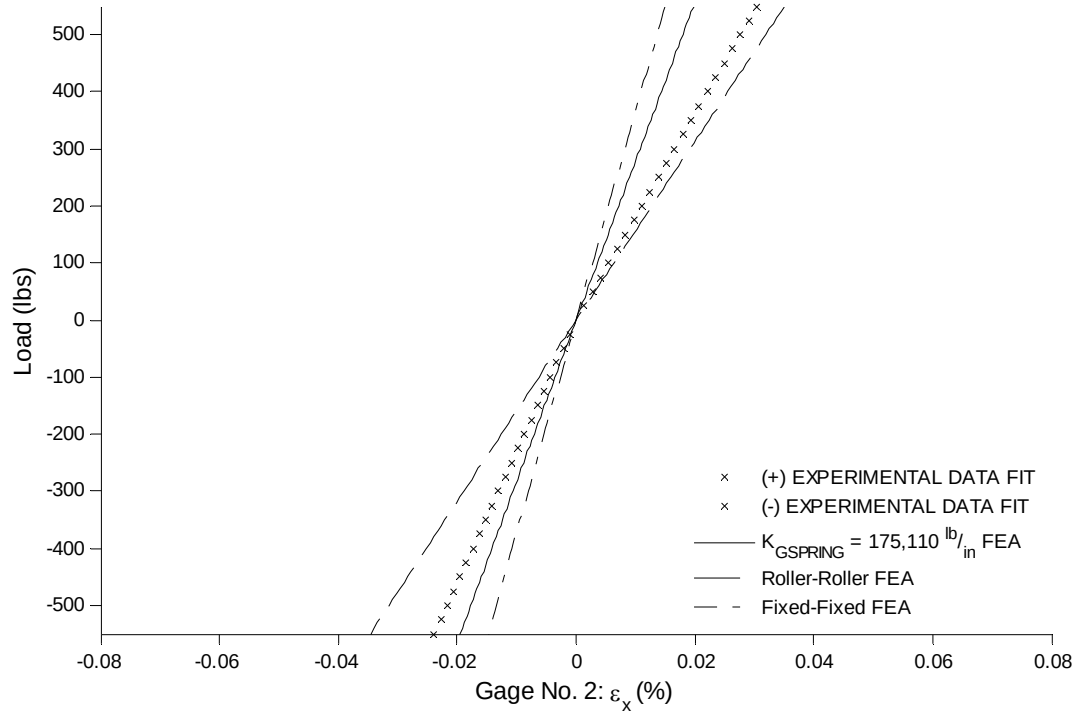

Figure 5–22: FAT-LBW-02 Analytical Gage No. 2 Load vs. Strain Plot

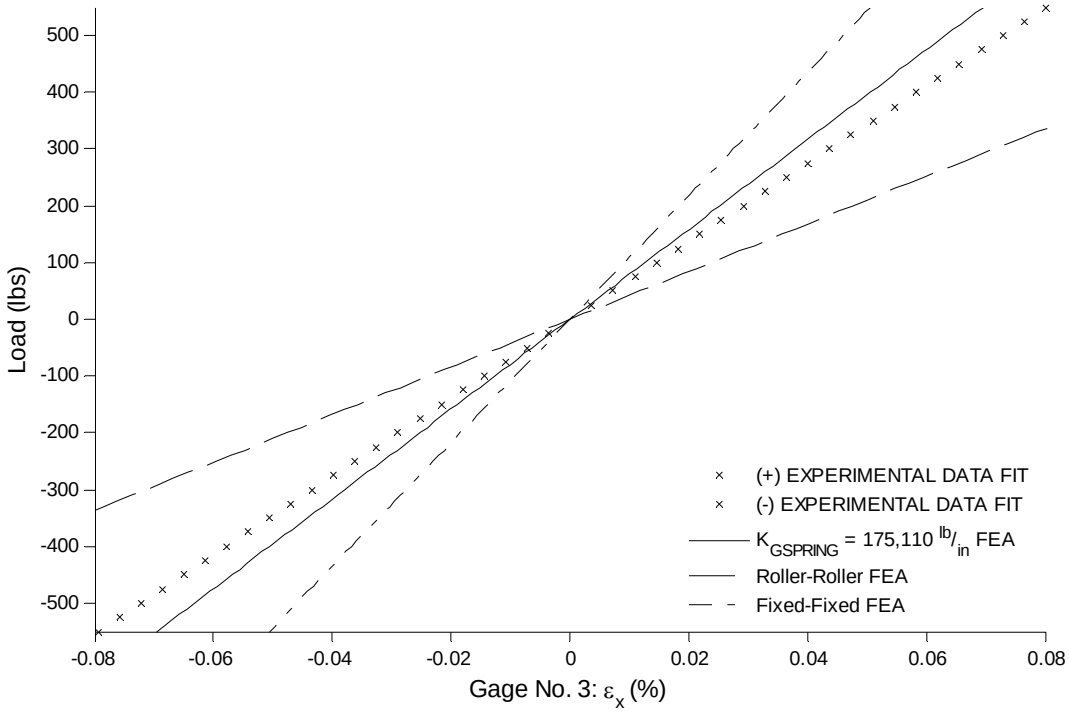

Figure 5–23:FAT-LBW-02 Analytical Gage No. 3 Load vs. Strain Plot

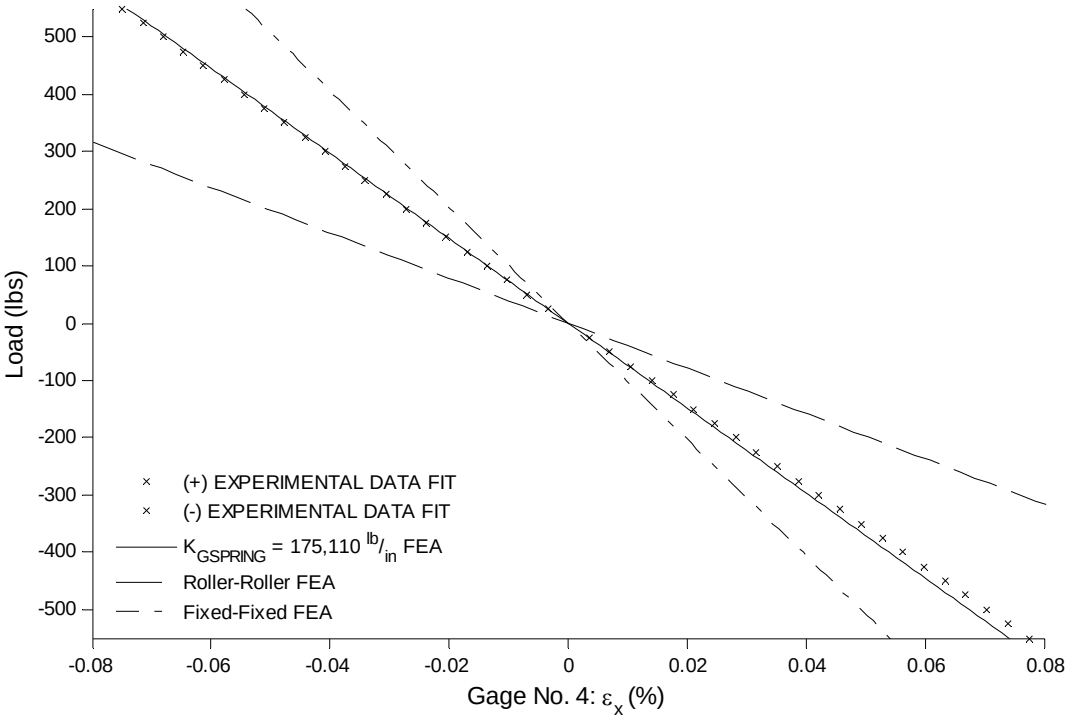

Figure 5–24: FAT-LBW-02 Analytical Gage No. 4 Load vs. Strain Plot

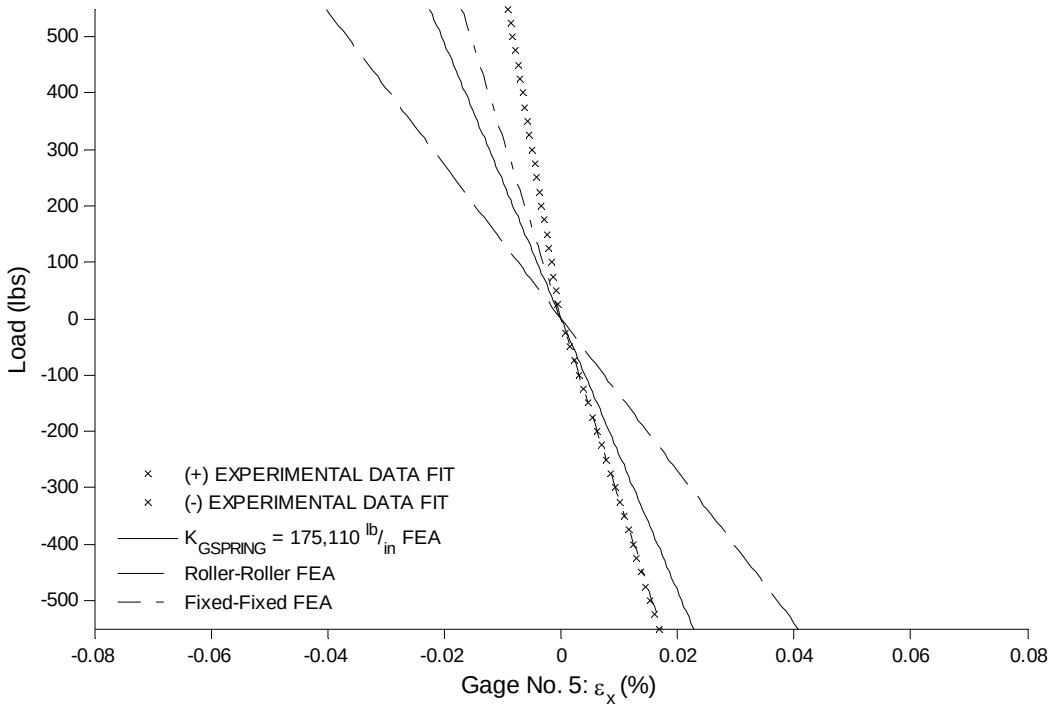

Figure 5–25: FAT-LBW-02 Analytical Gage No. 5 Load vs. Strain Plot

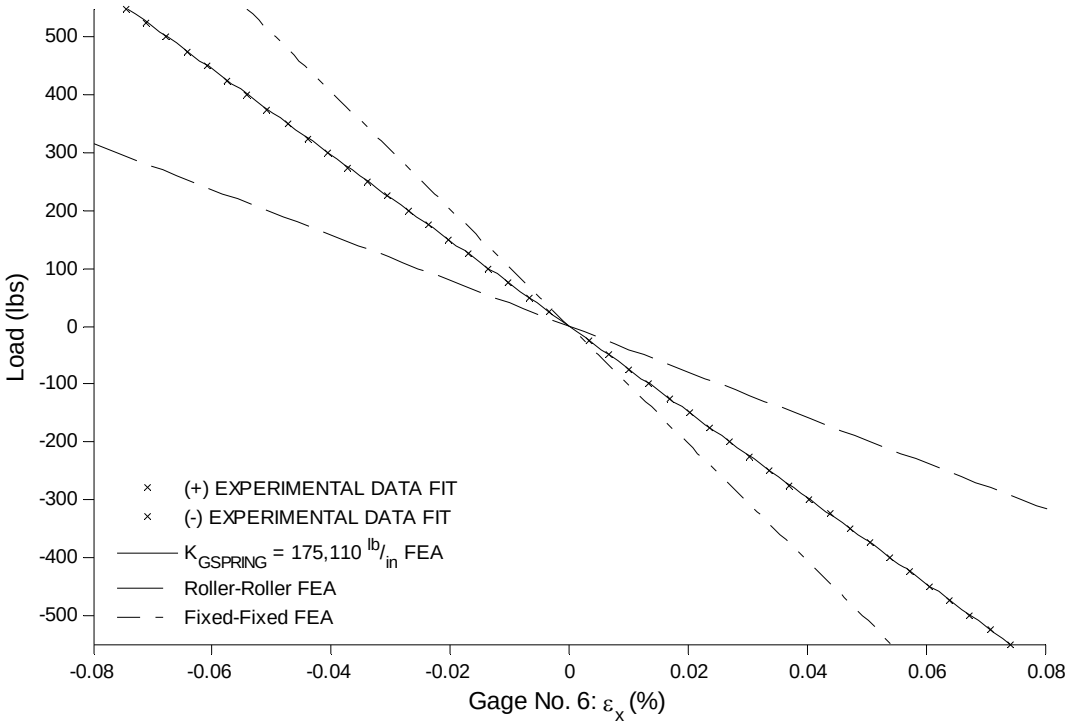

Figure 5–26: FAT-LBW-02 Analytical Gage No. 6 Load vs. Strain Plot

5.2.1.2 Reported Stress Ranges from Fatigue Testing Program

Table 5-5: Reported Stress Ranges

Test Specimen	K_{SYSTEM} *(lb/in)*	$K_{GSPRING}$ *(lb/in)*	$\Delta\sigma_{GSPRING}$ *(ksi)*	$\Delta\sigma_{ROLLER}$ *(ksi)*	$\Delta\sigma_{FIXED}$ *(ksi)*
FAT-LBW-02	7,184	116,289	31.96	50.61	23.40
FAT-LBW-03	8,715	214,954	23.06	40.48	18.72
FAT-LBW-04	7,143	114,260	51.31	80.97	37.44
FAT-LBW-05	8,237	178,350	47.48	80.97	37.44
FAT-LBW-06	5,881	62,155	43.16	60.73	28.08
FAT-LBW-07	7,753	147,173	43.16	60.73	28.08
FAT-LBW-08	8,506	198,175	35.02	60.73	28.08
FAT-LBW-09	5,388	46,045	38.00	50.61	23.40
FAT-HLAW-01	8,198	175,647	47.60	80.97	37.44
FAT-HLAW-02	6,316	78,133	55.11	80.97	37.44
FAT-HLAW-03	9,201	259,895	28.05	50.61	23.40
FAT-HLAW-04	8,802	222,370	40.15	70.85	32.76
FAT-HLAW-05	7,591	137,789	43.41	70.85	32.76
FAT-HLAW-06	5,086	37,053	59.18	75.91	35.10
FAT-HLAW-07	6,550	87,510	50.57	75.91	35.10
FAT-HLAW-08	7,347	124,560	47.35	75.91	35.10
FAT-LBWG-01	6,860	100,947	52.50	80.97	37.44
FAT-LBWG-02	6,182	73,031	48.84	70.85	32.76
FAT-LBWG-03	8,721	215,498	46.10	80.97	37.44
FAT-LBWG-04	9,009	241,034	39.68	70.85	32.76
FAT-LBWG-05	7,131	113,650	51.36	80.97	37.44
FAT-LBWG-06	6,388	80,972	47.90	70.85	32.76
FAT-LBWG-07	8,165	173,410	47.70	80.97	37.44
FAT-LBWG-08	7,067	110,566	45.17	70.85	32.76
FAT-LBWG-09	7,972	160,661	48.31	80.97	37.44
FAT-LBWG-10	7,880	154,845	42.54	70.85	32.76
FAT-LBWG-11	7,317	123,008	50.62	80.97	37.44
FAT-HLAWG-01	6,955	105,283	55.35	86.03	39.78
FAT-HLAWG-02	7,333	123,849	50.56	80.97	37.44
FAT-HLAWG-03	7,357	125,107	53.62	86.03	39.78
FAT-HLAWG-04	7,623	139,595	49.49	80.97	37.44
FAT-HLAWG-05	7,364	125,436	53.60	86.03	39.78
FAT-HLAWG-06	7,437	129,341	50.17	80.97	37.44
FAT-HLAWG-07	6,665	92,359	56.73	86.03	39.78
FAT-HLAWG-08	7,367	125,632	50.43	80.97	37.44
FAT-HLAWG-09	6,439	82,999	57.89	86.03	39.78
FAT-HLAWG-10	7,268	120,510	50.81	80.97	37.44
FAT-HLAWG-11	6,973	106,122	55.27	86.03	39.78

5.2.1.3 Comparison Parameters

Table 5-6: Generalized Fatigue Test Specimen Comparison Parameters

Test Specimen	D (In)	θ_{MAX} (in/in)	$-\Delta_{DIFF}$ (in)	$+\Delta_{DIFF}$ (in)	Δ_{DIFF} (in)	$+\sigma_x$ (ksi)	$-\sigma_x$ (ksi)	$\Delta\sigma$ (ksi)
FAT-LBW-02	9.23	0.0095	-0.02123	0.02122	0.04245	15.98	-15.98	31.96
FAT-LBW-03	8.66	0.0063	-0.01294	0.01293	0.02587	11.53	-11.53	23.06
FAT-LBW-04	9.24	0.0152	-0.03426	0.03425	0.06851	25.66	-25.65	51.31
FAT-LBW-05	8.81	0.0133	-0.02794	0.02792	0.05586	23.74	-23.74	47.48
FAT-LBW-06	9.94	0.0140	-0.03484	0.03483	0.06967	21.58	-21.58	43.16
FAT-LBW-07	9.94	0.0140	-0.03484	0.03483	0.06967	21.58	-21.58	43.16
FAT-LBW-08	8.72	0.0097	-0.02005	0.02004	0.04010	17.51	-17.51	35.02
FAT-LBW-09	10.31	0.0129	-0.03362	0.03361	0.06723	19.00	-19.00	38.00
FAT-HLAW-01	8.83	0.0133	-0.02812	0.02811	0.05623	23.80	-23.80	47.60
FAT-HLAW-02	9.67	0.0173	-0.04140	0.04138	0.08278	27.56	-27.56	55.11
FAT-HLAW-03	8.52	0.0075	-0.01506	0.01505	0.03012	14.03	-14.02	28.05
FAT-HLAW-04	8.63	0.0109	-0.02235	0.02234	0.04468	20.08	-20.08	40.15
FAT-HLAW-05	9.05	0.0125	-0.02743	0.02741	0.05484	21.70	-21.70	43.41
FAT-HLAW-06	10.57	0.0207	-0.05575	0.05574	0.11149	29.59	-29.59	59.18
FAT-HLAW-07	9.54	0.0156	-0.03666	0.03664	0.07330	25.28	-25.28	50.57
FAT-HLAW-08	9.15	0.0139	-0.03082	0.03080	0.06161	23.68	-23.68	47.35
FAT-LBWG-01	9.38	0.0159	-0.03641	0.03639	0.07280	26.25	-26.25	52.50
FAT-LBWG-02	9.75	0.0155	-0.03748	0.03747	0.07495	24.42	-24.42	48.84
FAT-LBWG-03	8.66	0.0126	-0.02585	0.02584	0.05170	23.05	-23.05	46.10
FAT-LBWG-04	8.57	0.0107	-0.02168	0.02166	0.04334	19.84	-19.84	39.68
FAT-LBWG-05	9.25	0.0153	-0.03435	0.03433	0.06869	25.68	-25.68	51.36
FAT-LBWG-06	9.63	0.0150	-0.03558	0.03556	0.07114	23.95	-23.95	47.90
FAT-LBWG-07	8.84	0.0134	-0.02828	0.02826	0.05654	23.85	-23.85	47.70
FAT-LBWG-08	9.28	0.0135	-0.03046	0.03045	0.06091	22.58	-22.58	45.17
FAT-LBWG-09	8.91	0.0137	-0.02923	0.02922	0.05845	24.16	-24.16	48.31
FAT-LBWG-10	8.94	0.0121	-0.02600	0.02599	0.05199	21.27	-21.27	42.54
FAT-LBWG-11	9.17	0.0149	-0.03307	0.03305	0.06612	25.31	-25.31	50.62
FAT-HLAWG-01	9.33	0.0166	-0.03789	0.03787	0.07576	27.67	-27.67	55.35
FAT-HLAWG-02	9.16	0.0148	-0.03296	0.03294	0.06590	25.28	-25.28	50.56
FAT-HLAWG-03	9.15	0.0157	-0.03485	0.03483	0.06968	26.81	-26.81	53.62
FAT-HLAWG-04	9.04	0.0143	-0.03116	0.03114	0.06230	24.75	-24.75	49.49
FAT-HLAWG-05	9.15	0.0157	-0.03481	0.03479	0.06960	26.80	-26.80	53.60
FAT-HLAWG-06	9.12	0.0146	-0.03229	0.03227	0.06456	25.08	-25.08	50.17
FAT-HLAWG-07	9.48	0.0174	-0.04044	0.04042	0.08085	28.36	-28.36	56.73
FAT-HLAWG-08	9.15	0.0148	-0.03273	0.03272	0.06545	25.22	-25.22	50.43
FAT-HLAWG-09	9.60	0.0180	-0.04267	0.04265	0.08532	28.94	-28.94	57.89
FAT-HLAWG-10	9.19	0.0150	-0.03339	0.03338	0.06677	25.41	-25.41	50.81
FAT-HLAWG-11	9.32	0.0166	-0.03774	0.03772	0.07547	27.63	-27.63	55.27

5.2.2 SANDWICH PANEL

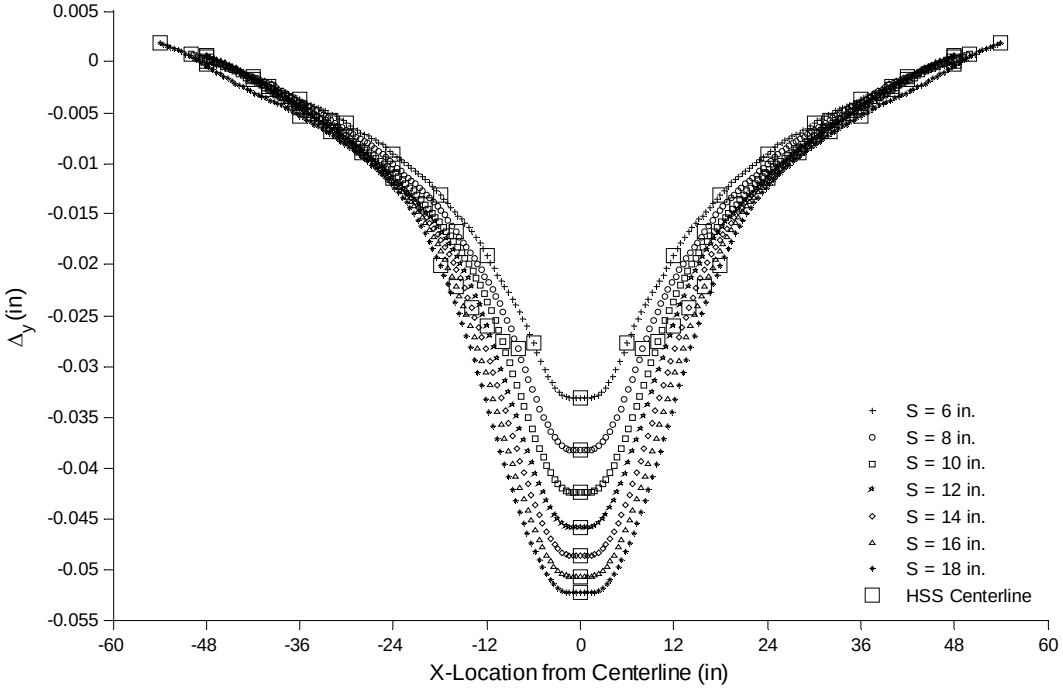

Figure 5–27: Bottom Plate Δ_y at Mid-Span with a $^9/_{16}$" Top Plate and Variable Rib Spacing

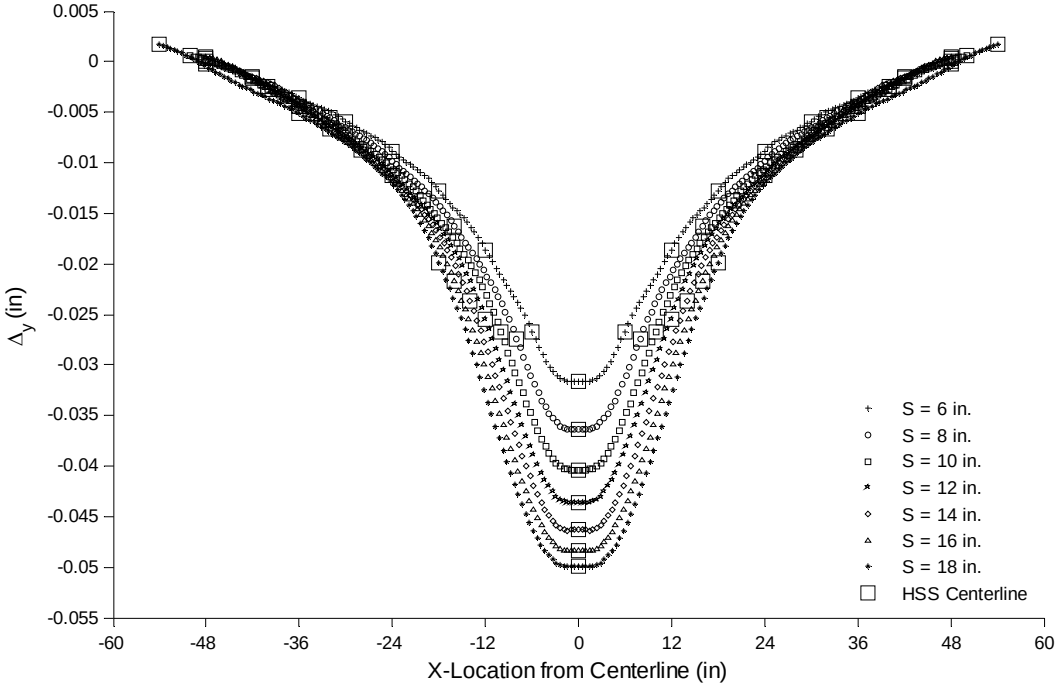

Figure 5–28: Bottom Plate Δ_y at Mid-Span with a $^5/_8$" Top Plate and Variable Rib Spacing

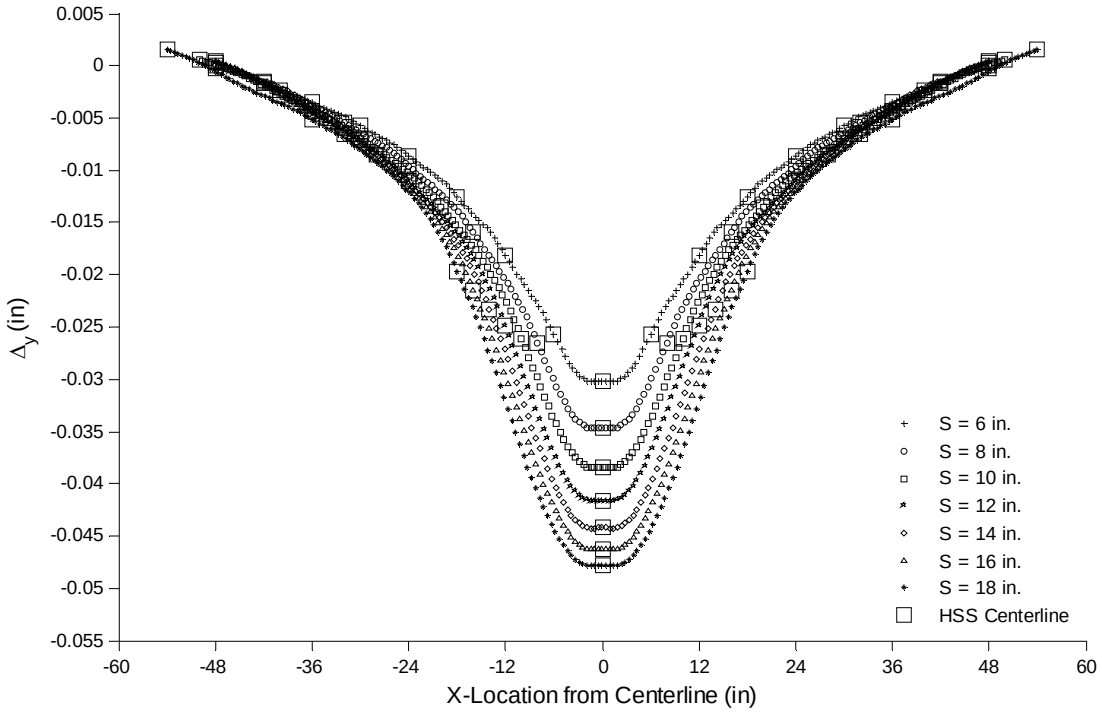

Figure 5–29: Bottom Plate Δy at Mid-Span with a $^{11}/_{16}$" Top Plate and Variable Rib Spacing

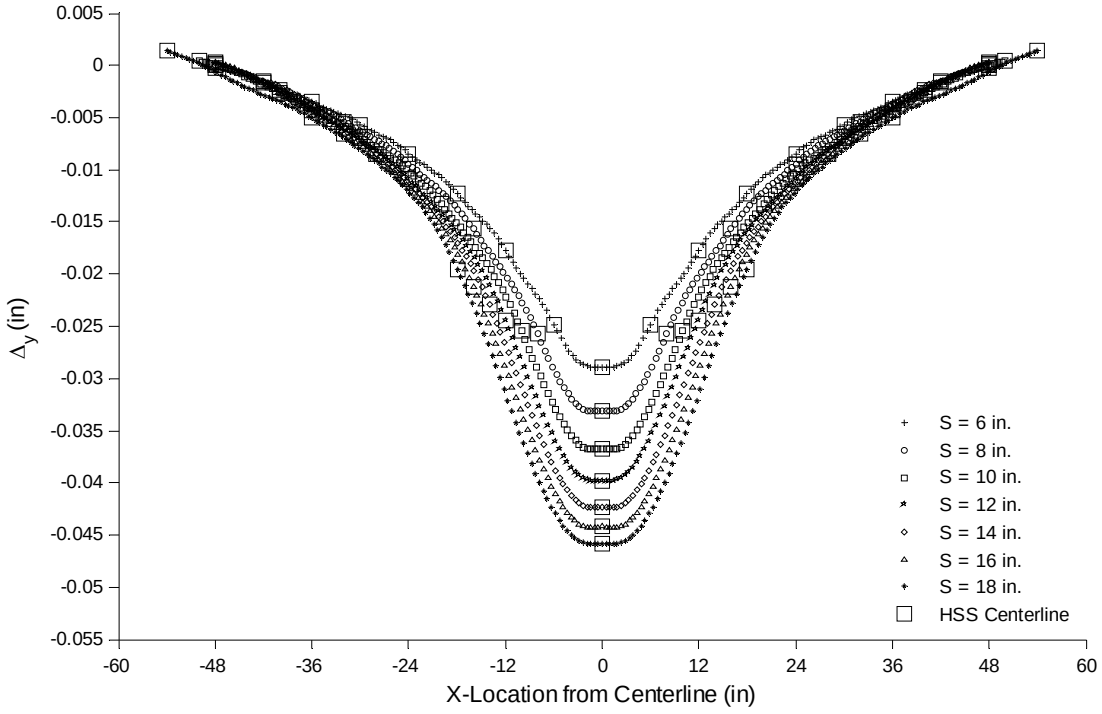

Figure 5–30: Bottom Plate Δy at Mid-Span with a $^{3}/_{4}$" Top Plate and Variable Rib Spacing

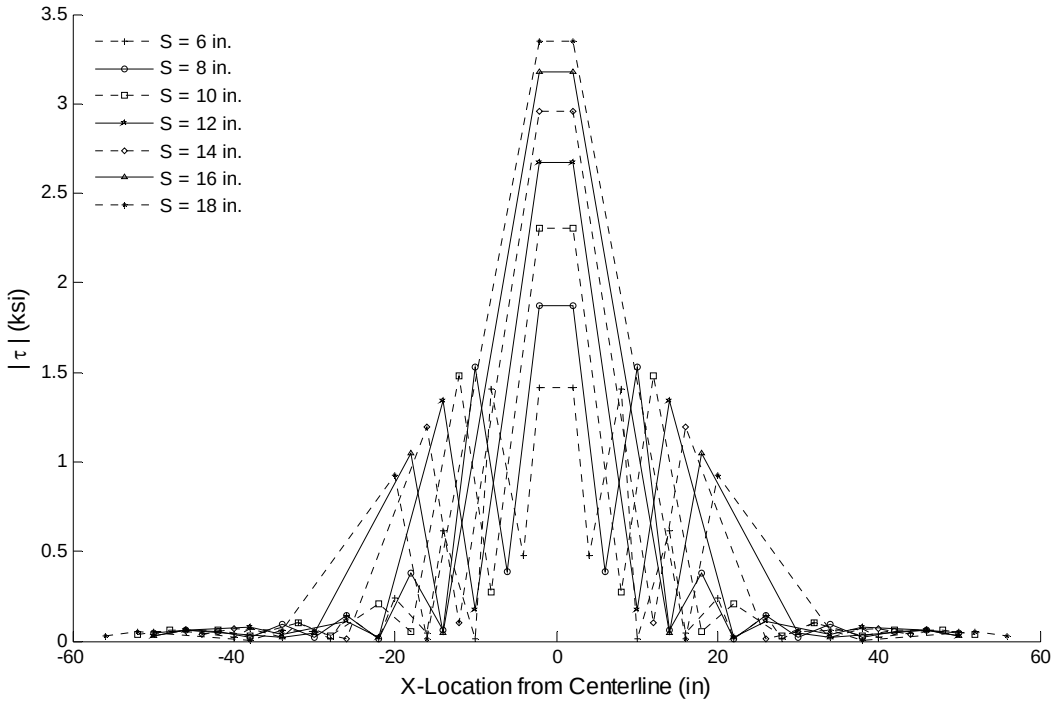

Figure 5–31: Shear Stress in HSS Webs at 18 inches with a $^{9}/_{16}$" Top Plate and Variable Rib Spacing

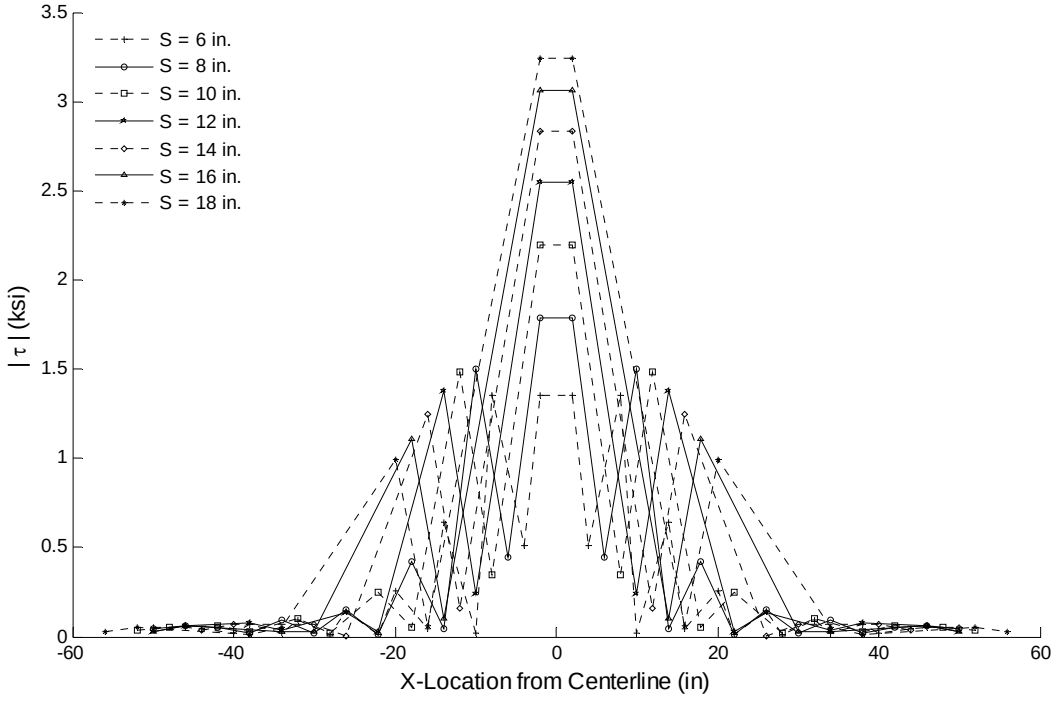

Figure 5–32: Shear Stress in HSS Webs at 18 inches with a $^{5}/_{8}$" Top Plate and Variable Rib Spacing

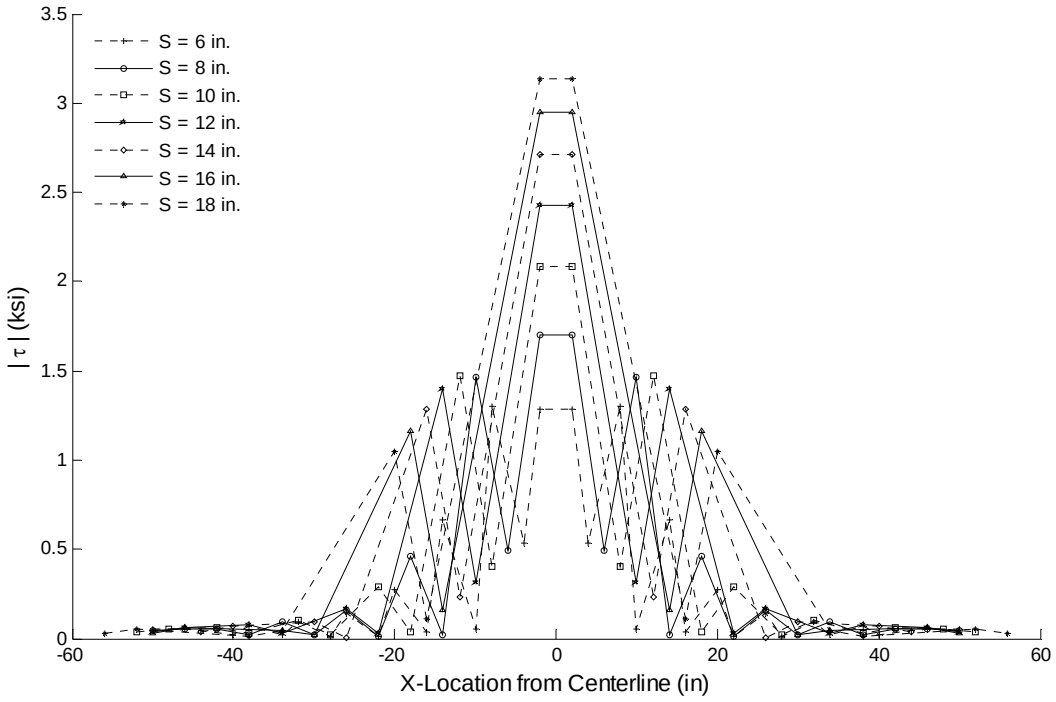

Figure 5–33: Shear Stress in HSS Webs at 18 inches with a $^{11}/_{16}$" Top Plate and Variable Rib Spacing

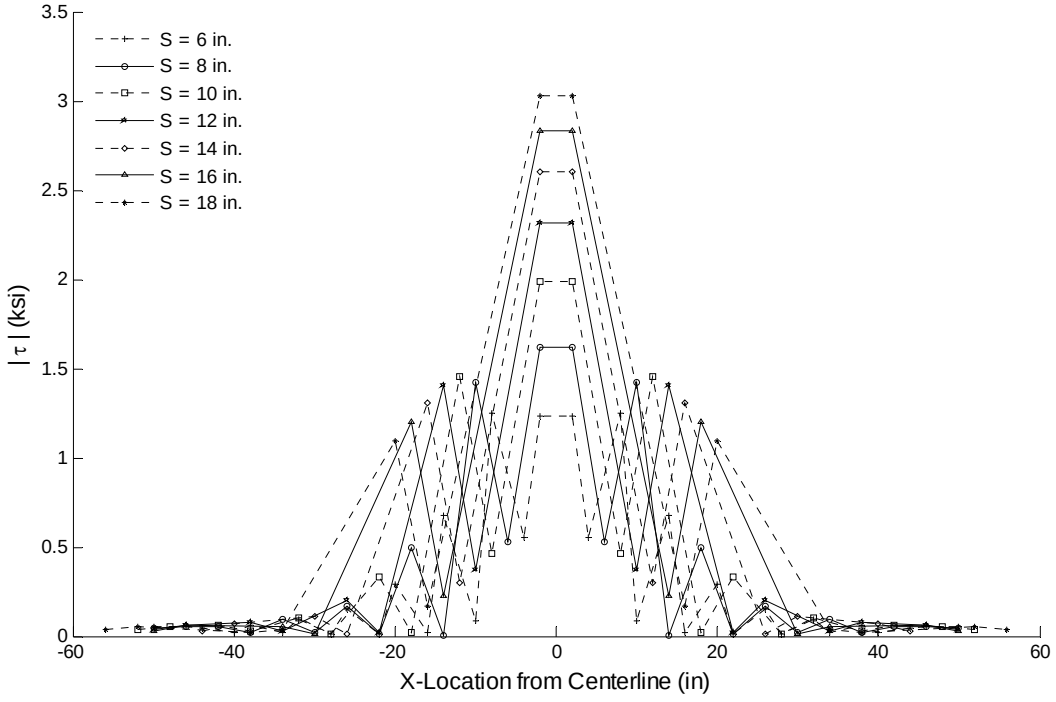

Figure 5–34: Shear Stress in HSS Webs at 18 inches with a $^{12}/_{16}$" Top Plate and Variable Rib Spacing

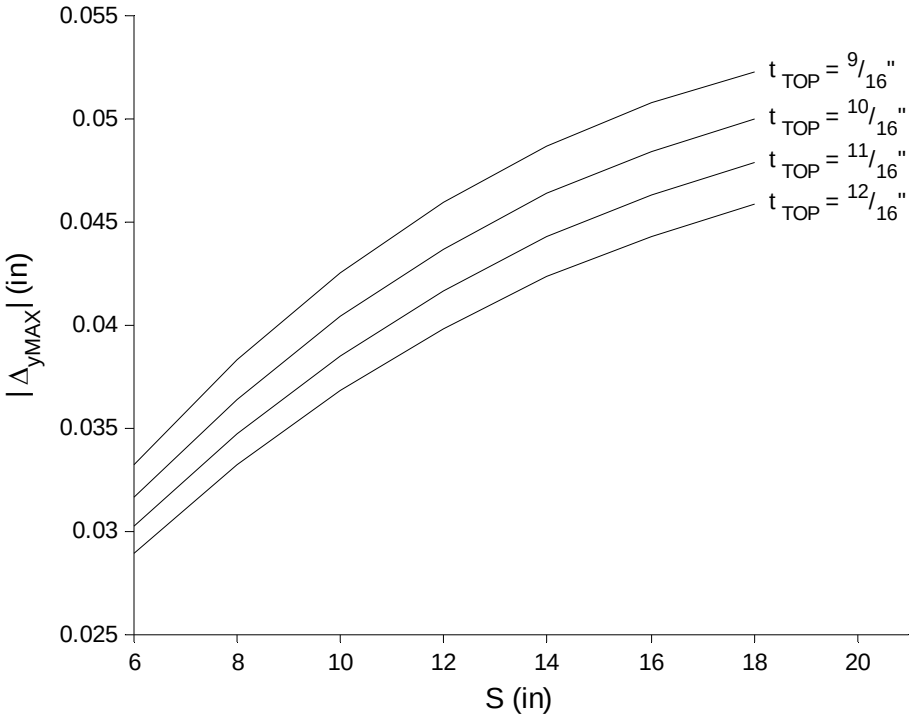

Figure 5–35: Internal Rib Spacing Influence on Maximum Vertical Deflection at Mid-span

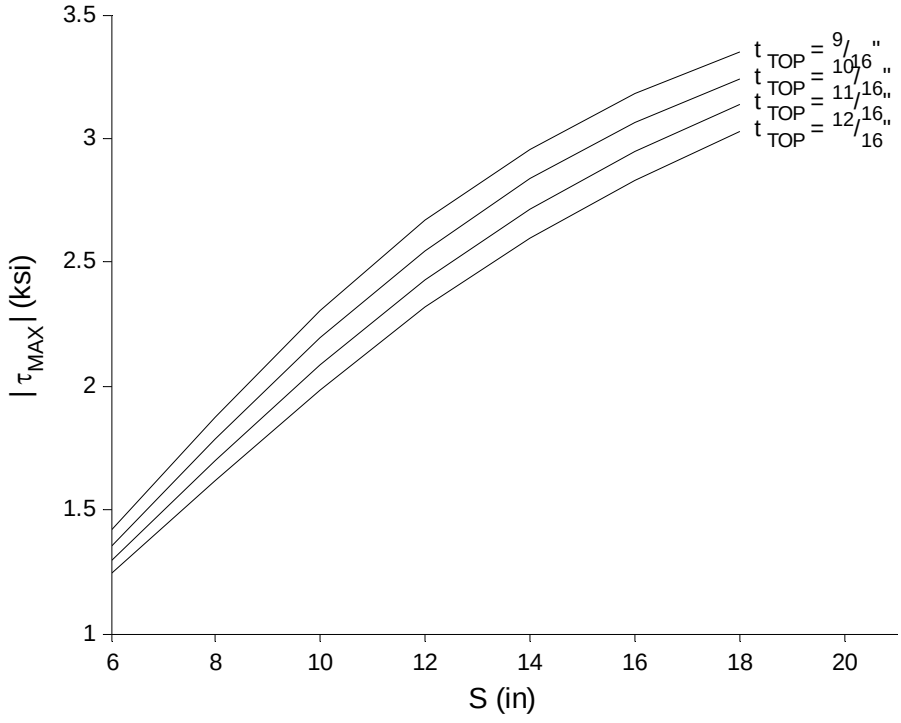

Figure 5–36: Internal Rib Spacing Influence on Maximum Shear Stress in the Central HSS Webs

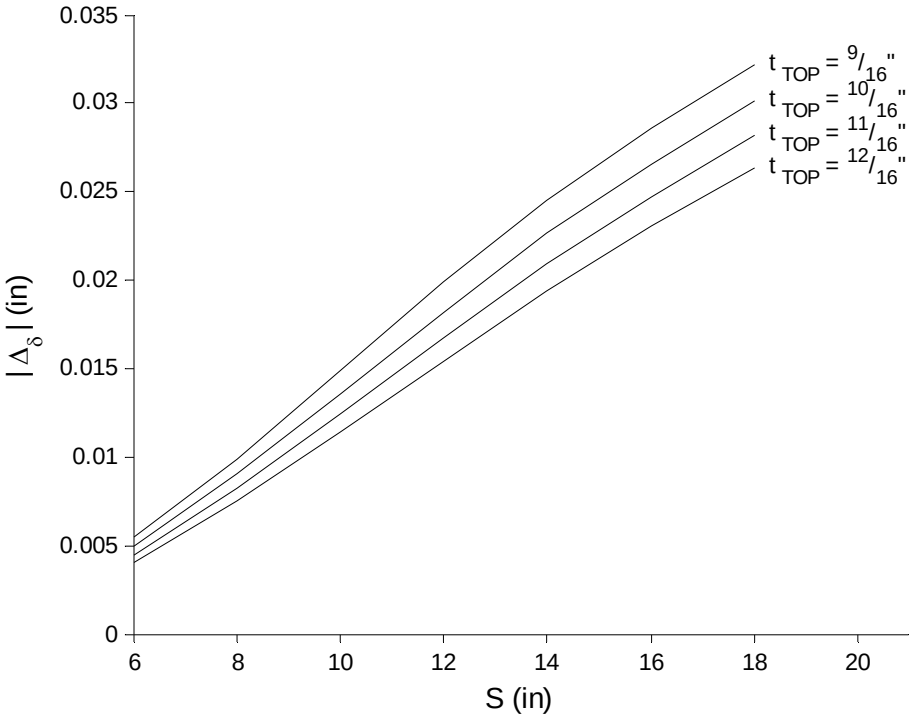

Figure 5–37: Internal Rib Spacing Influence on Maximum Differential Rib Deflection

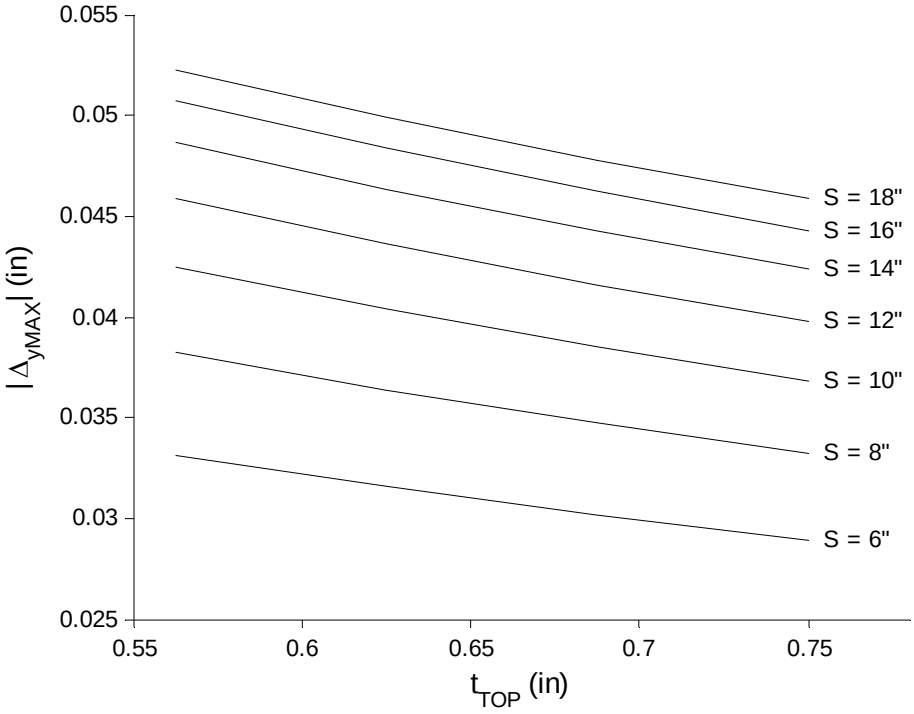

Figure 5–38: Top Plate Thickness Influence on Maximum Vertical Deflection at Mid-span

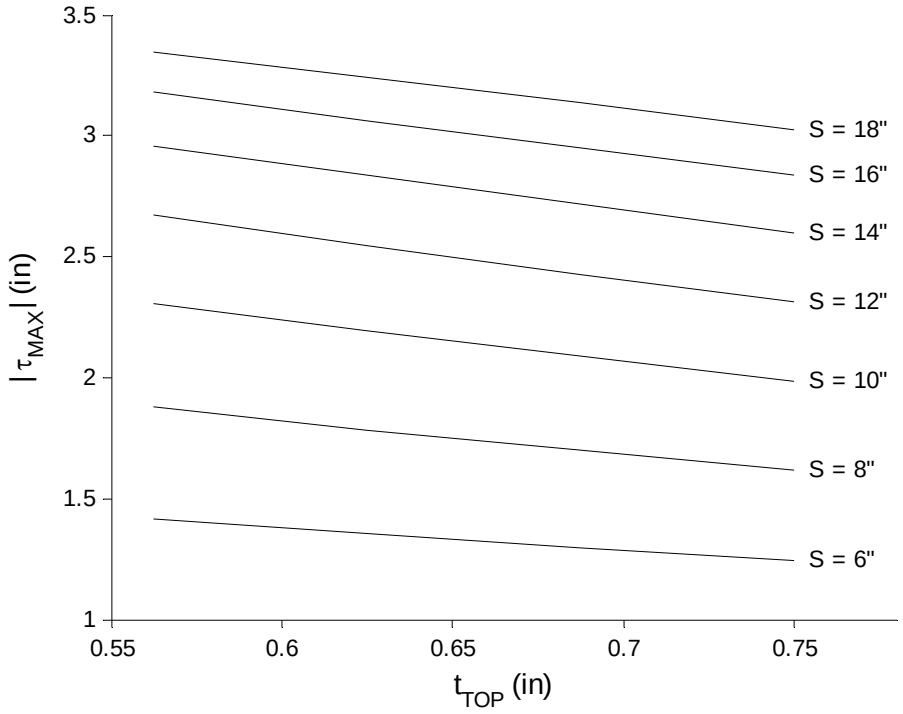

Figure 5–39: Top Plate Thickness Influence on Maximum Shear Stress in the Central HSS Webs

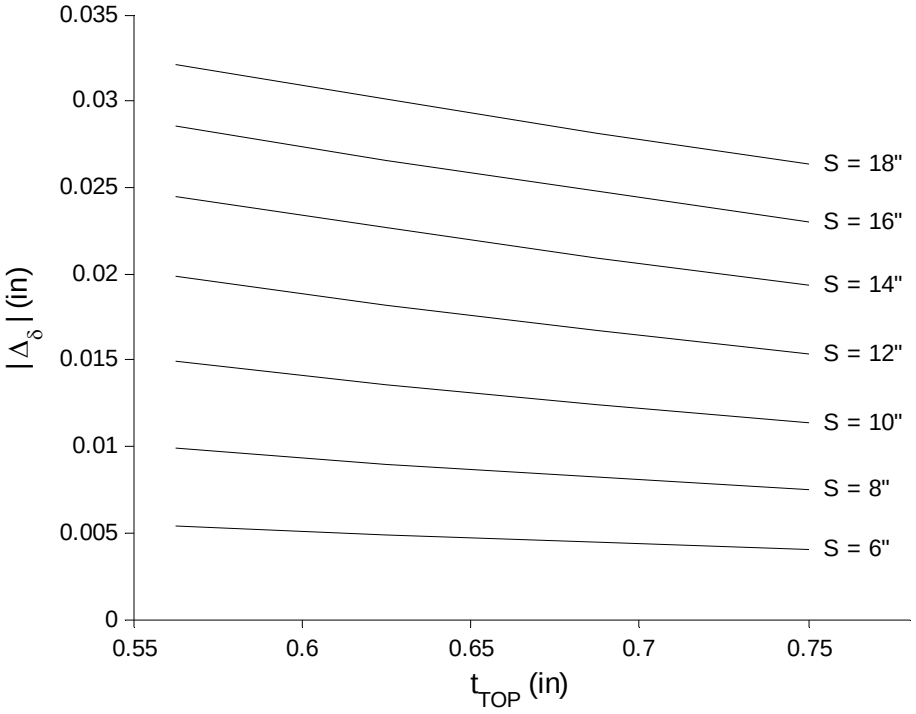

Figure 5–40: Top Plate Thickness Influence on Maximum Differential Rib Deflection

5.2.2.1 Comparison Parameters

Table 5-7: Sandwich Panel with a $^{9}/_{16}$" Top Plate Comparison Parameters

S (ln)	D (ln)	θ_{MAX} (in/in)	$+\Delta_{DIFF}$ (in)	$-\Delta_{DIFF}$ (in)	Δ_{DIFF} (in)	$+\sigma$ (ksi)	$+\sigma_{MISES}$ (ksi)	$-\sigma$ (ksi)	$-\sigma_{MISES}$ (ksi)	$\Delta\sigma$ (ksi)
6	16.62	0.0021	0.0045	0.0100	0.0079	-2.28	5.30	-2.57	5.98	2.57
8	16.91	0.0022	0.0009	0.0109	0.0128	-1.28	4.93	-2.92	6.89	2.92
10	17.14	0.0023	0.0033	0.0116	0.0179	-0.54	4.55	-3.11	7.54	3.11
12	18.24	0.0025	0.0067	0.0131	0.0228	-0.11	4.21	-3.21	8.03	3.21
14	19.87	0.0026	0.0096	0.0149	0.0273	0.12	3.90	-3.25	8.41	3.37
16	21.69	0.0026	0.0121	0.0165	0.0312	0.39	3.55	-3.11	8.59	3.49
18	23.66	0.0026	0.0141	0.0180	0.0346	0.61	3.21	-2.93	8.69	3.54

Table 5-8: Sandwich Panel with a $^{5}/_{8}$" Top Plate Comparison Parameters

S (ln)	D (ln)	θ_{MAX} (in/in)	$+\Delta_{DIFF}$ (in)	$-\Delta_{DIFF}$ (in)	Δ_{DIFF} (in)	$+\sigma$ (ksi)	$+\sigma_{MISES}$ (ksi)	$-\sigma$ (ksi)	$-\sigma_{MISES}$ (ksi)	$\Delta\sigma$ (ksi)
6	16.71	0.0019	0.0042	0.0092	0.0072	-2.18	5.18	-2.42	5.81	2.42
8	17.46	0.0021	0.0014	0.0104	0.0117	-1.31	4.89	-2.72	6.67	2.72
10	17.77	0.0022	0.0024	0.0112	0.0164	-0.65	4.55	-2.89	7.30	2.89
12	18.85	0.0023	0.0056	0.0126	0.0210	-0.24	4.23	-2.99	7.79	2.99
14	20.46	0.0024	0.0084	0.0142	0.0253	-0.02	3.92	-3.05	8.17	3.05
16	22.26	0.0024	0.0108	0.0158	0.0291	0.25	3.57	-2.93	8.36	3.18
18	24.22	0.0025	0.0129	0.0172	0.0325	0.49	3.23	-2.77	8.48	3.26

Table 5-9: Sandwich Panel with a $^{11}/_{16}$" Top Plate Comparison Parameters

S (ln)	D (ln)	θ_{MAX} (in/in)	$+\Delta_{DIFF}$ (in)	$-\Delta_{DIFF}$ (in)	Δ_{DIFF} (in)	$+\sigma$ (ksi)	$+\sigma_{MISES}$ (ksi)	$-\sigma$ (ksi)	$-\sigma_{MISES}$ (ksi)	$\Delta\sigma$ (ksi)
6	16.78	0.0018	0.0039	0.0084	0.0065	-2.09	5.07	-2.28	5.64	2.28
8	17.93	0.0019	0.0018	0.0100	0.0107	-1.32	4.84	-2.54	6.47	2.54
10	18.36	0.0020	0.0017	0.0108	0.0150	-0.72	4.54	-2.70	7.08	2.70
12	19.44	0.0021	0.0047	0.0120	0.0194	-0.34	4.24	-2.80	7.56	2.80
14	21.02	0.0022	0.0073	0.0136	0.0235	-0.13	3.94	-2.87	7.95	2.87
16	22.80	0.0023	0.0097	0.0150	0.0272	0.14	3.59	-2.77	8.15	2.91
18	24.75	0.0023	0.0117	0.0164	0.0305	0.38	3.26	-2.63	8.28	3.01

Table 5-10: Sandwich Panel with a $^{3}/_{4}$" Top Plate Comparison Parameters

S (ln)	D (ln)	θ_{MAX} (in/in)	$+\Delta_{DIFF}$ (in)	$-\Delta_{DIFF}$ (in)	Δ_{DIFF} (in)	$+\sigma$ (ksi)	$+\sigma_{MISES}$ (ksi)	$-\sigma$ (ksi)	$-\sigma_{MISES}$ (ksi)	$\Delta\sigma$ (ksi)
6	16.80	0.0016	0.0036	0.0077	0.0060	-2.00	4.96	-2.15	5.49	2.15
8	18.34	0.0018	0.0020	0.0095	0.0098	-1.31	4.79	-2.38	6.28	2.38
10	18.91	0.0019	0.0011	0.0103	0.0138	-0.77	4.52	-2.52	6.88	2.52
12	19.99	0.0020	0.0039	0.0115	0.0179	-0.42	4.24	-2.62	7.35	2.62
14	21.56	0.0021	0.0064	0.0130	0.0218	-0.22	3.96	-2.71	7.74	2.71
16	23.33	0.0021	0.0086	0.0144	0.0254	0.05	3.62	-2.62	7.95	2.67
18	25.26	0.0022	0.0106	0.0157	0.0286	0.29	3.28	-2.49	8.08	2.78

5.3 FATIGUE LIFE CYCLE PLOTS

5.3.1 STRESS RANGE CALCULATION SUMMARY FOR S-N CURVES

The following steps were conducted for each of the 38 test specimens in the fatigue testing program to calculate an appropriate stress range to correct for the partially restrained boundary conditions.

1) Obtain the load displacement data from the first 2,000 load cycles of the targeted test specimen and using a linear regression fit a curve to the negative data. Refer to Appendix E.
2) Take the slope from the regressed curve as the system stiffness in the negative direction, K_{SYSTEM} and plug it into equation (4.1) to obtain a grounded spring stiffness, $K_{GSPRING}$ to model the partially restrained condition as shown in Figure 4–12, as well as described in sections 4.1.1.4 and 4.1.1.6.4.
3) Create an ABAQUS input file using the modeling parameters discussed in section 4.1 and the grounded spring stiffness calculated in the previous step.
4) The ABAQUS input file was ran on the supercomputers through Virginia Tech, using two different static general load steps for both directions of the cyclic load magnitude, P.
5) The in-plane bending stress in the X-direction, σ_x perpendicular to laser weld, along the centerline on the underside of the $^3/_{16}$" plate, located at the integration point closest to the laser weld, shown in Figure 4–25 was extracted for both load directions from the two elastic load steps. The absolute values of both stresses were summed to form the stress range, $\Delta\sigma$ reported in the stress life cycle plots with the cycles to failure.

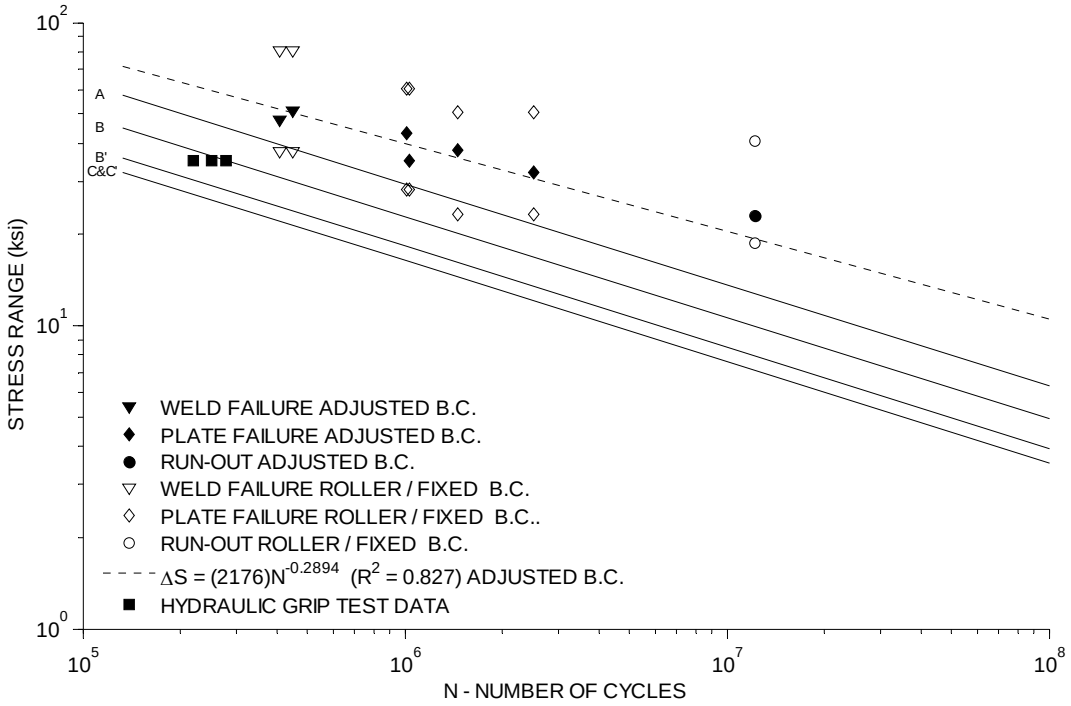

Figure 5–41: LBW Fatigue Test Specimens Data and Stress Life Cycle (S-N) Plot - Free Slope Regression

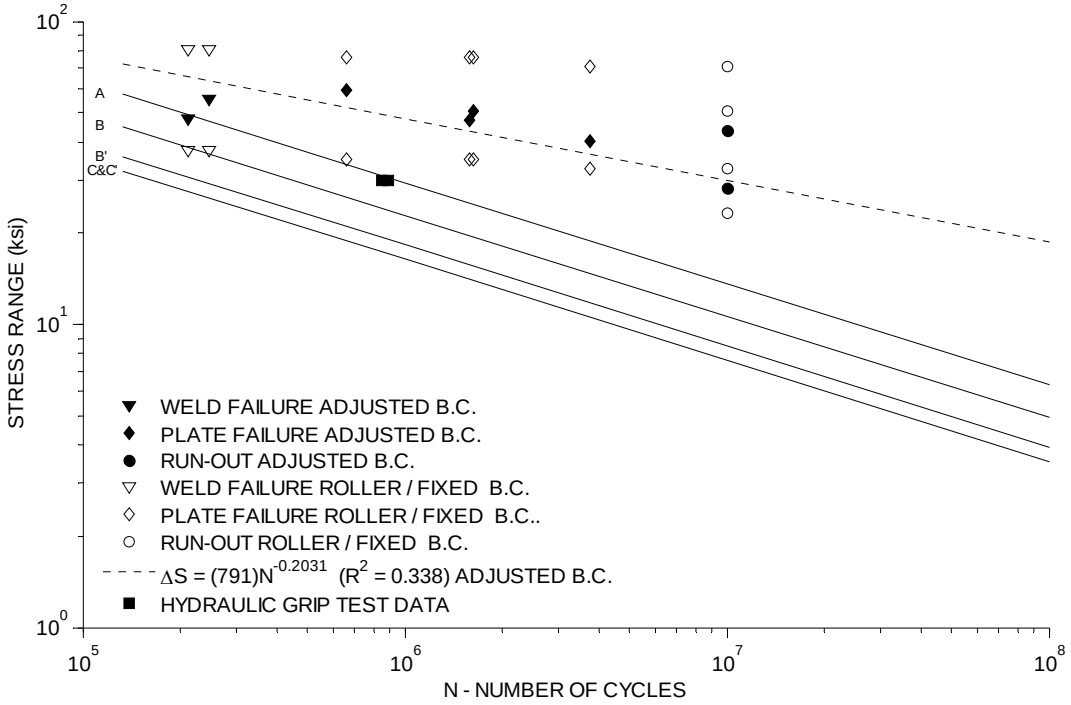

Figure 5–42: HLAW Fatigue Test Specimens Data and Stress Life Cycle (S-N) Plot - Free Slope Regression

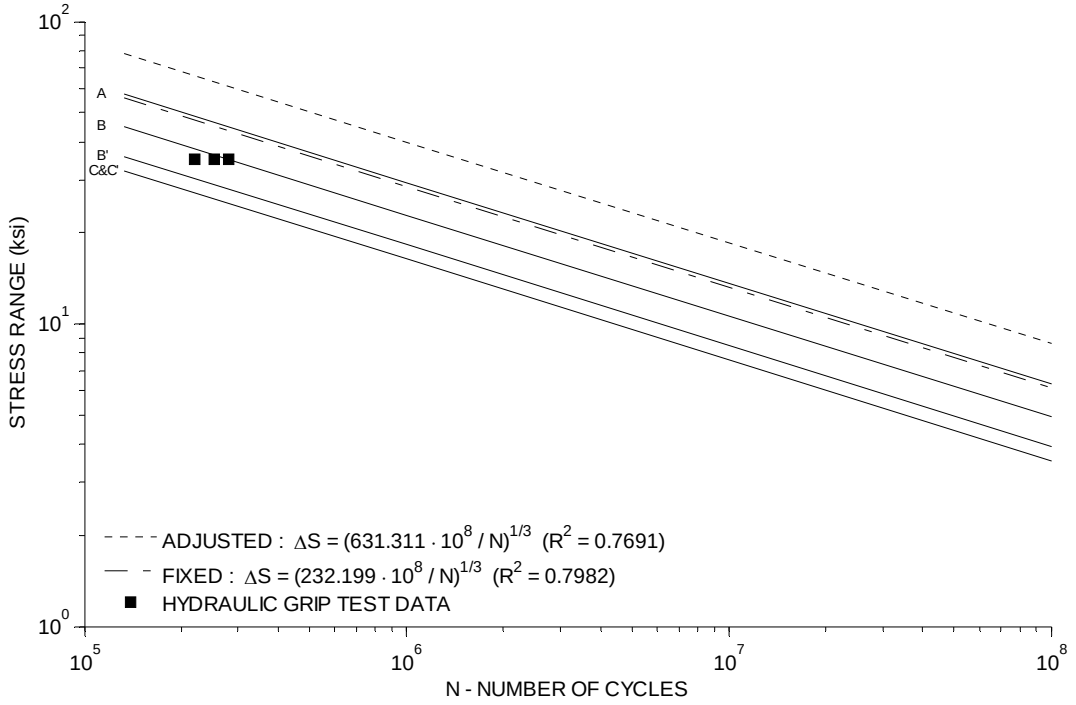

Figure 5–43: LBW Fatigue Test Specimens Stress Life Cycle (S-N) - Fixed Slope Regression

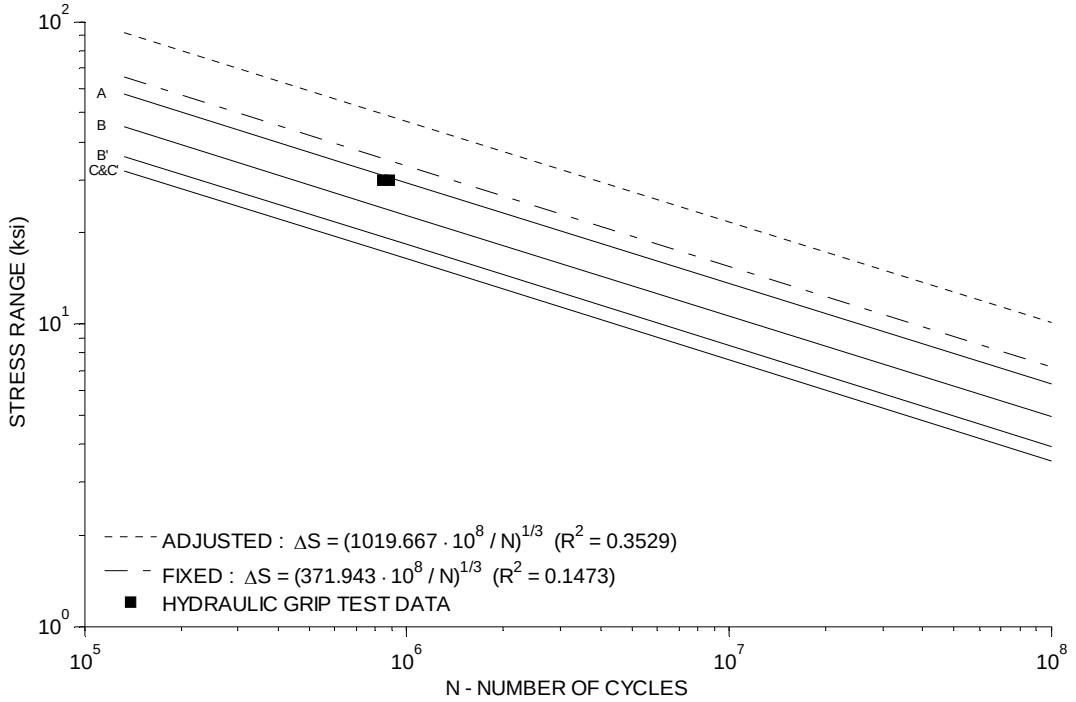

Figure 5–44: HLAW Fatigue Test Specimens Stress Life Cycle (S-N) - Fixed Slope Regression

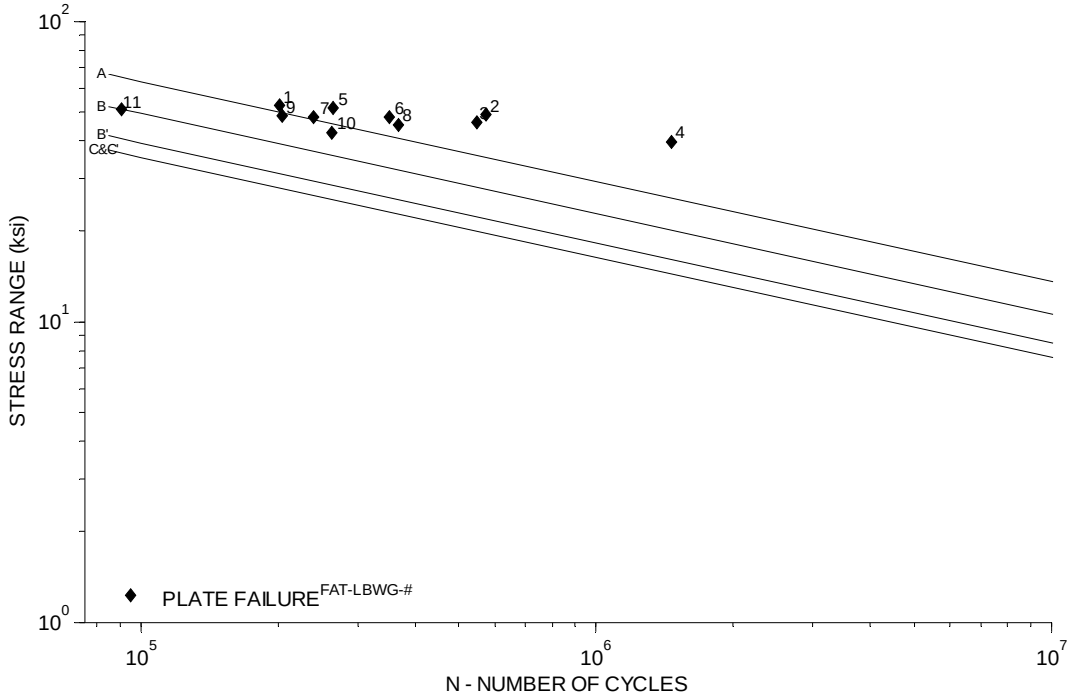

Figure 5–45: LBWG Fatigue Test Specimens Stress Life Cycle (S-N) Plot

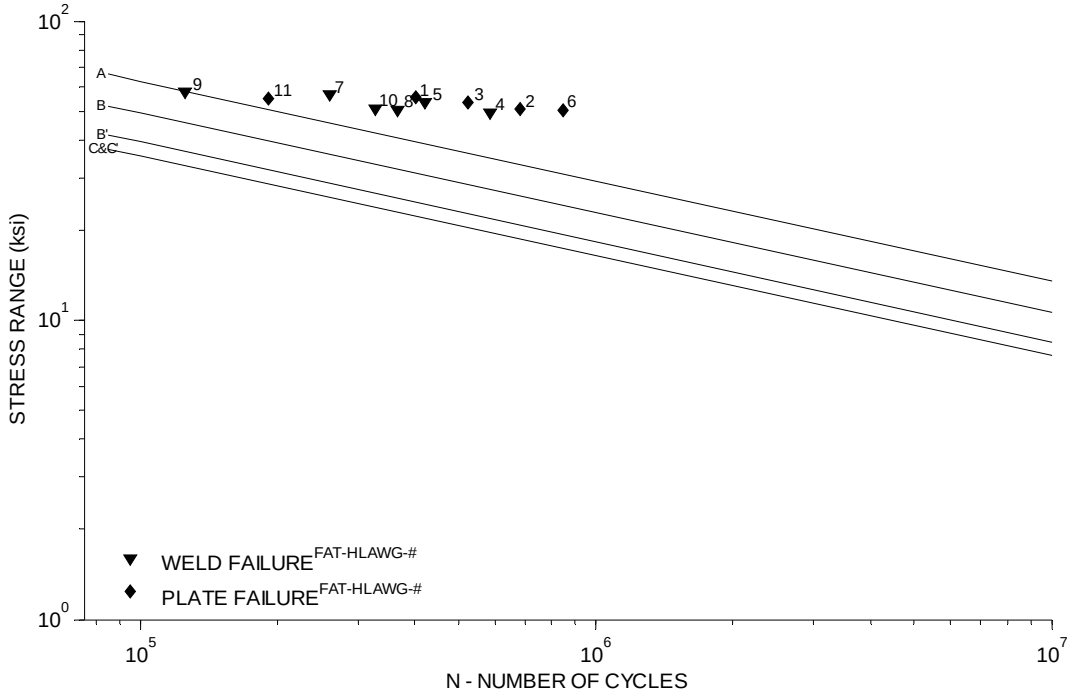

Figure 5–46: HLAWG Fatigue Test Specimens Stress Life Cycle (S-N) Plot

6.1 FATIGUE STRESS CALCULATION

There were many variables that impeded the evaluation of the reported stress ranges in the fatigue life cycle plots displayed in section 5.3. In addition to the problematic boundary conditions discussed throughout the report, residual stresses, the potential contact region between the $^{3}/_{16}$" plate and rounded corner of the HSS section, and an unknown stress across the laser weld interface due to modeling method, all could have potentially altered the reported stress range in some form.

The most time and effort was allocated to resolve the issue with the problematic boundary conditions, provided that they had largest impact on the reported stress magnitude. Though experimental strains were bounded by analytical models with different end conditions, there was no experimental evidence of variable boundary conditions. The partially restraint verification tests described in section 3.4.3, were therefore performed and yielded promising results. The load displacement plots shown in Figure 5–18 and Figure 5–19 clearly demonstrate a mutual relationship between clamping force and system stiffness, providing experimental evidence to support the presence of variable boundary conditions between each fatigue test. In addition the plots exhibit how at relatively low clamping forces, a small change can lead to a large change in system stiffness. This trend is also displayed in the theoretical relationship between grounded spring stiffness and system stiffness shown in Figure 4–19. Using this plot by thinking of clamping force simulated by grounded spring stiffness, the flatter region of the plot in Figure 4–19 demonstrates a large increase in system stiffness from small changes in grounded spring stiffness at relatively low values. The load strain plots that can be found in Appendix G also exhibit a mutual relationship between clamping force and slope,

furthering supporting this claim.

Though the experimental data from the elastic load test was bounded by "*Roller-Roller*" and "*Fixed-Fixed*" end conditions, as described in section 4.1.1.4, it was difficult to believe that the rollers from the load fixture supported fixed end moments. Fortunately, the load strain plots for strain gages 7 and 8 from both partial restraint verification tests experimentally reinforced these analytical bounds. Each of the plots for strain gages 7 and 8 found in Appendix G demonstrate that the average strain $^{5}/_{8}$" from the centerline of each roller in the $^{3}/_{16}$" plate, moves from zero strain with a nearly undefined slope at low clamping force, to substantial strains with increasing clamping force, thus proving the existence of a fixed end moment at the roller.

The application of clamping force was very difficult, as described previously, due to the rigidity of the load fixture in comparison to the specimen plate that resulted in erratic and excessive clamping force in each fatigue test. Even though the applied clamping forces in the partial restraint verification test were considerable high in comparison to the desired clamping force of 30 lbs per roller, all fatigue tests were performed with even larger clamping forces. During the setup in the partial restraint verification test, so much as $^{1}/_{16}$ of a turn of the $1^{5}/_{16}$" adjustment nuts resulted in approximately 100 lbs of clamping force that was not detected by the integrated 110 kip MTS force transducer. Observing this numerous times throughout the test setup and provided that average system stiffness was approximately 7,400 $^{lb}/_{in}$ during the first 2000 cycles of each fatigue test, lead to the conclusion that applied clamping force was well over 2,400 lbs per roller throughout each fatigue test. In many instances during the setup of fatigue tests, the $1^{5}/_{16}$" adjustment nuts became very tight and difficult to adjust, which never occurred during the application of clamping force in the partial restraint verification tests.

Provided that small adjustments were observed to result in large clamping forces, the over tightened adjustment nuts was an indication of a clamping force larger than 2,400 lbs per roller. Additionally, the system stiffness correlated to the 2,400 lbs clamping force was below the average system stiffness computed for the individual fatigue tests, also verifying a larger clamping force than 2,400 lbs per roller. Overall, the clamping force for each individual fatigue test was much larger than anticipated and unpredictable.

Fortunately, the analytical method discussed in section 4.1.2.1 resolved this issue and the primary theoretical relationship was proven experimentally, as displayed in the plots from the elastic load test in section 5.2.1.1. Using the relationship in equation (4.1) to calculate $K_{GSPRING,}$ where K_{SYSTEM} was the regressed slope computed from the load displacement data of the first 2000 load cycles in the negative direction for each fatigue test, proved to provide a very accurate measure of the partially restrained conditions. Figure 5–20 through Figure 5–26 include the regressed trends of the experimental data collected during the elastic load test of FAT-LBW-02 and finite element simulations using both analytical bounds, as well as the adjusted partially restrained condition. Given that the relationship used to model the partially restrained boundary conditions was derived based on the one dimensional system stiffness, the adjusted finite element analysis was anticipated to match load displacement data. Figure 5–20 clearly validates this hypothesis, as the regressed data and simulation with the adjusted end condition are nearly identical. Due to the complexity of laser stake welded connection, there was no preconceived notion on how well the adjusted finite element simulation would correlate to experimental strains recorded. Provided that the reported fatigue stress range was calculated from the dominant bending stress on the underside of the $^{3}/_{16}$" plate as shown in Figure 4–25 , the strain gages of primary concern were numbers 4 and 6 that were installed on the underside

of the $^{3}/_{16}$" plate, $4^{7}/_{8}$" from either end. The load strain plots for strain gages 4 and 6 are shown in Figure 5–24 and Figure 5–26 respectively, which together demonstrate how well the analytical method evaluates the strain in close proximity to reported fatigue stress. These plots provide an experimental validation of the method formulated to obtain the reported stress range in each fatigue test.

The load strain plots for strain gages 1 and 3, directly above gages 4 and 6 on the top of the $^{3}/_{16}$" plate, are shown in Figure 5–21 and Figure 5–23 respectively. These plots exhibit a slight underestimate of the experimental strain recorded, which results in a conservative estimate if reported in the S-N curves. Initially the difference between the analytical and experimental strains was unable to be explained, but after re-measuring the centerline locations of all strain gages, both gages 1 and 3 were approximately $^{1}/_{16}$" closer to the laser weld location. Since the strain gages measure the average strain over the bonded area, this small placement error can easily account for the larger experimental strains recorded. The load strain plots for strain gages 2 and 5 shown in Figure 5–22 and Figure 5–25 respectively, demonstrate the difficulty in modeling the contact between the $^{3}/_{16}$" plate and the top flange of the HSS. Together both plots exhibit how the analytical model falls apart in this contact region between the two linear laser stake welds. The method used to model contact with non-linear springs does not take into account the friction between plates. Additionally, un-measurable residual stresses in the form of a tensile stress gradient in the X-direction between the laser stake welds and clamping "*pre-stress*" between weld components can possibly alter behavior in this region. Figure 5–22 shows larger experimental strains than those computed from the finite element analysis. In addition to the problems discussed in modeling this region, the only plausible explanation for larger strains can be devised from the fictitious thickness assigned to the laser weld links as

described in section 4.1.1.6.2. Though it was necessary to assign a larger thickness to attain appropriate behavior, Figure 5–22 displays how the larger link thickness stiffened the region between the laser stake welds in the finite element simulation.

Since the dominant bending stress σ_x, was taken as the stress to initiate fatigue and formulate the reported stress range in the S-N curves, the major source of error stemmed from the effect of the potential contact region on the on the rounded corner of the HSS section shown in Figure 6–1. This possible contact region was neglected from the finite element analysis since it was unable to be measured even though it had the potential to alter behavior through a gap effect and/or prying action. Discussed in section 4.1.1.6.4, the system stiffness in the negative direction inducing positive curvature in the $^3/_{16}$" plate, as well engaging contact between the $^3/_{16}$" plate and top flange of the HSS section was selected in order to avoid error from the potential contact to formulate the correlation in order to model the partially restrained boundary conditions.

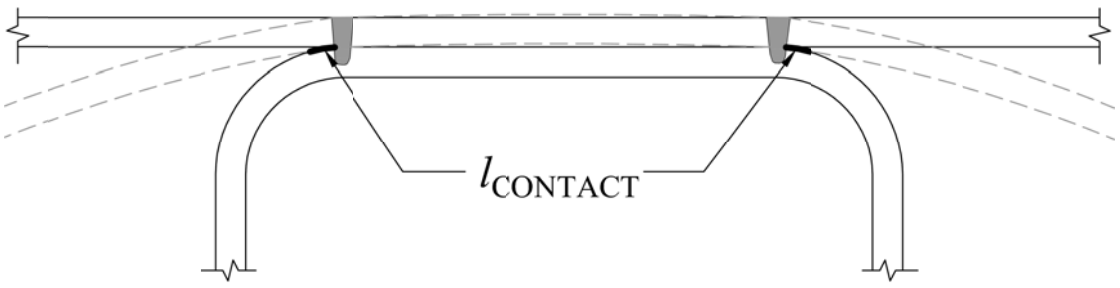

Figure 6–1: Potential Contact Region under Positive Loading

The gap effect from the potential contact region is displayed through moment diagrams in Figure 6–2. Assuming the contact region formulates a uniform distributed load, the bending moment in the $^3/_{16}$" plate would be reduced as shown in Figure 6–2(b). Figure 6–3 demonstrates prying action resulting from the potential contact region. The presence of prying

action induces tension into the stake weld that is compression, thus reducing the normal stress in the Y-direction. The effects from the potential contact region reduce the dominant bending stress in the $^{3}/_{16}$" plate at the laser weld interface and add pure tension into the laser weld that increases the likely hood of a different failure mode that occurs in the laser weld between the HSS and $^{3}/_{16}$" plate interface.

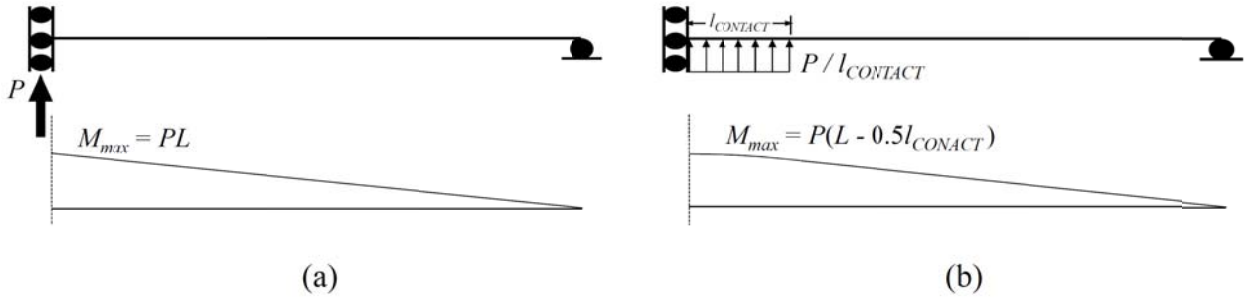

Figure 6–2: Gap Effect from Potential Contact Region. (a) No Contact (b) Contact Engaged

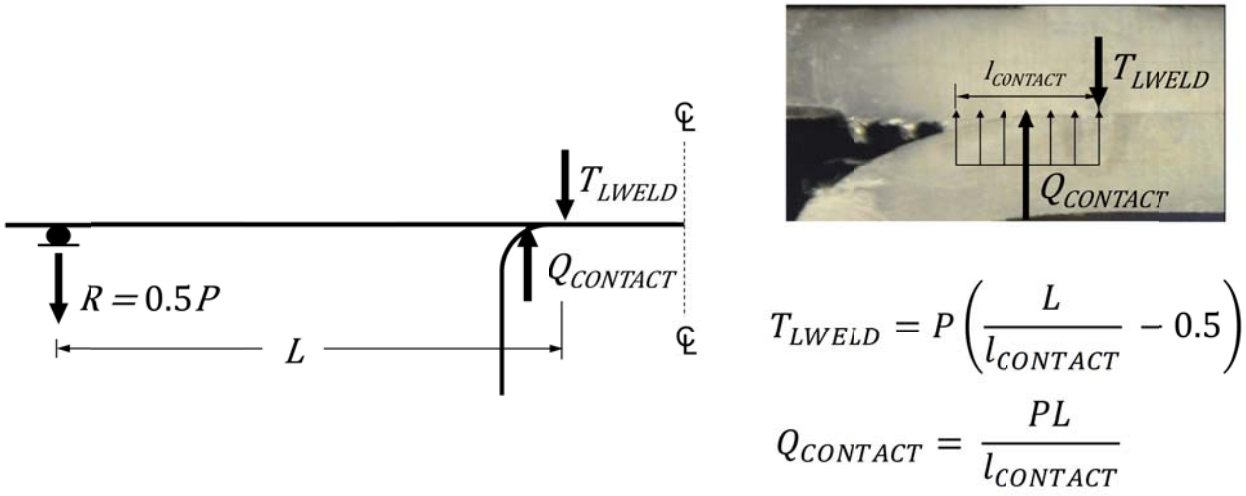

Figure 6–3: Prying Action form Potential Contact Region

Another noteworthy problem with analytical method formulated to compute the reported stress range is that it did not account for the other failure mode in the laser weld along the HSS and plate interface. As previously discussed the reported stress range was taken as the

dominant bending stress on the underside of the $^{3}/_{16}$" plate at the laser weld interface, perpendicular the crack initiation depicted in Figure 5–10. Plate failure at the laser weld interface accounted for 71.4% of failures, whereas the remaining 28.6% of failures occurred in the laser weld along the HSS and plate interface. Unfortunately, the method used to model the laser welds in the generalized fatigue test specimen model was unable to accurately calculate the stress concentration that caused this additional failure mode.

Though the laser weld is really an embedded element, when modeled as a separate element in a simple two dimensional beam model neglecting contact, the link transfers considerable moment relative to the maximum moment in the plate at the laser weld interface, as shown in Figure 6–4. Considering the small laser weld interface widths summarized in Table 3-4, in comparison to the plate thickness, substantial bending stresses are formed perpendicular to the HSS and plate interface shown in Figure 6–5. As a result of the change in load direction, this bending stress encounters a stress reversal when neglecting contact. Unfortunately, the fictitious shell thickness assigned to the laser weld link, altered the desired bending stress in the laser weld. Additionally, the modeling methodology neglected the fact that the laser weld was in reality an embedded within the $^{3}/_{16}$" plate and top flange of the HSS section. The actual laser weld behavior would therefore be constrained by the curvature of each of the welded components. Given that the HSS section experienced minimal strain according to the experimental data and finite element analysis, the laser weld was believed to behave similar to a cantilever beam. Conceptually, it was understood that the portion of the laser weld in the top flange of the HSS was fixed, where the extent of the laser weld in the $^{3}/_{16}$" plate would experience constrained bending based on the deformation of the plate, causing the maximum bending stress at the interface between the weld components. Furthermore, the neglected

potential contact region on the rounded corners of the HSS section would have a double-edged sword effect on the bending stress in the laser weld. The gap effect would reduce the bending moment in the $^{3}/_{16}$" plate at the laser weld interface, therefore decreasing the constrained bending of the embedded laser weld as discussed previously. However, the prying action would increase the maximum tensile stress in the laser weld bending stress profile.

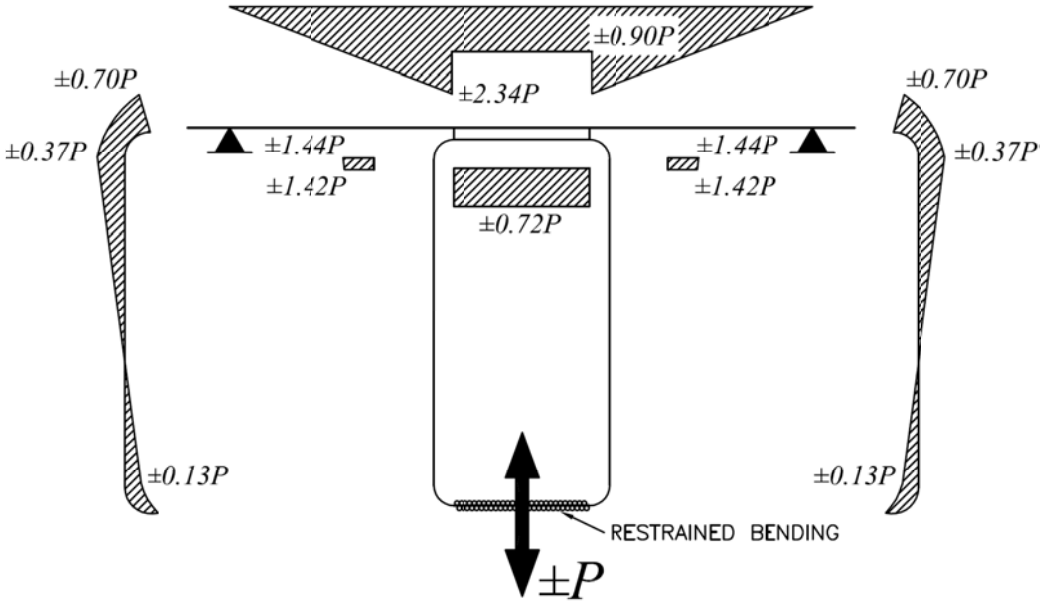

Figure 6–4: Moment Diagram Modeling the Laser Welds as Separate Elements

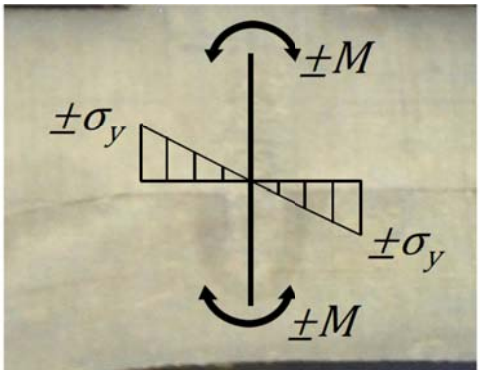

Figure 6–5: Laser Weld Bending Stress Profile Modeled with Beam Elements

Overall the stress at the laser welded connection between the $^{3}/_{16}$" plate and top flange of the HSS section was complex, requiring further finite element modeling using three dimensional continuum elements and contact formulations for the region on the rounded corners of the HSS section. Even with a complex modeling scheme, errors still persist with unknown residual stresses. The study conducted at the ARL at Penn State discussing the beneficial pre-stress from autogenous LBW acknowledges the presence of a thermally induced tension gradient, but concluded that better instrumentation was needed to measure the thermally induced strains during the welding process. Provided the complexity of the stress state at laser weld in question dealing with residual stresses, potential contact, and the unknown stress in the embedded laser weld, in addition to the variable boundary conditions, the overall method used to compute stress range was concluded to be appropriate for the problem at hand since the vast majority of failures occurred from the dominant bending stress in the $^{3}/_{16}$" plate.

6.2 FATIGUE PERFORMANCE

The fatigue testing program has proven both laser welding technologies to perform very well for the welded configuration investigated. The results have shown that the HLAW stake welds possess a higher resistance to fatigue than the LBW stake welds and are superior due to their ability to handle fit-up gaps between weld components through the addition of filler material.

The stress life cycle plots shown in Figure 5–41 and Figure 5–42 for the fatigue test specimens without fit-up gaps demonstrate the true mean of the regressed data for both processes to be above AASHTO detail category A. The AASHTO LRFD Bridge Design Specifications describe detail category A to be load induced fatigue in the base metal with a rolled or clean smooth ground surface.((AAHSTO), 2010) Provided that the predominant failure mode occurred in the $^{3}/_{16}$" plate at the laser weld and the analytical method utilized to calculate the stress range for this failure was verified experimentally, this outcome is justified. The other failure mode observed during the testing program occurred in the weld along the HSS and plate interface, which is depicted by the upside down triangles in Figure 5–41 and Figure 5–42. As discussed previously, the appropriate stress range for this failure mode was unattainable due to the modeling method. Fortunately, weld failure along the HSS and plate interface only accounted for 4 failures in the fatigue test specimens without fit-up gaps.

These failures occurred at the highest load range tested for these specimens at ±400 lbs. The study at Bristol University on the fatigue performance of laser welded bridge decks also observed signs of horizontal cracks across the joint interface at high load ranges of which did not lead to overall failure across the weld interface.(Bright and Smith, 2004) Discussed in the

previous section, the stress magnitude in the laser weld is governed by the deformation in $^{3}/_{16}$" plate and the interface width of the stake weld. Momentarily neglecting the variable boundary conditions, the largest load range simply causes the largest deformation, increasing bending moments in the laser welds, thus providing an explanation for the occurrence of weld failure along the joint interface at high load ranges.

The stress life cycle plot for HLAW test specimens in Figure 5–42 exhibits a larger disparity between the regressed curve and weld failure data points than stress life cycle plot for LBW test specimens in Figure 5–41. This is attributed to the nearly 39% difference in the measured laser weld interface width between the LBW and HLAW test specimens without fit-up gaps which were 0.0941" and 0.0679" respectively. The stresses present in HLAW stake welds were therefore presumed to be higher than those in an equivalent LBW specimen. Since the reported stress ranges were derived from the stresses present in $^{3}/_{16}$" plate and not the laser weld, the larger discrepancy observed in the HLAW stress life cycle plot is a result of a further underestimated stress range.

The fatigue confirmation testing program was initiated to alleviate all possible experimental errors and other unknown variables that altered the stress at the laser weld. The fatigue tests performed using the hydraulic grips induced pure tension into the $^{3}/_{16}$" plate and were utilized to provide experimental verification to the fatigue testing program. Prior to the commencement these fatigue tests, as discussed in section 3.4.1.1, the fatigue life of the laser welded connection tested in the configuration was considered to resemble either a welded cover plate connection, detail category E' or a full penetration groove welded butt splice, LBW detail category B and HLAW detail category C due to the presence of weld reinforcement. The hydraulic grip fatigue tests are represented by black square data points in Figure 5–41 through

Figure 5–44. Fortunately, the laser welded connection performed similar to a full penetration groove welded butt splice. The LBW specimens tested in pure tension are approximated between AASHTO detail categories B and B', though closer category B as shown in Figure 5–41 and Figure 5–43. The HLAW specimens tested in pure tension are approximated between categories A and B, though closer to category A as shown in Figure 5–42 and Figure 5–44. The AASHTO S-N curves for all detail categories are represented by the lower bound of the 95% confidence interval to ensure 95% survival, which correlates to a downward shift in the data by factor of 2 in life and 1.25 in stress.(Dowling, 2007) Therefore, detail categories B' and B for the LBW and HLAW specimens respectively would suffice as a conservative approximation for fatigue tests in pure tension. In comparison to the correlated conventional weld detail of the full penetration groove welded butt splice, the LBW specimens performed below the expected category, whereas the HLAW specimens performed above the expected category. The initial presumption for the AASHTO detail categories were based on a smooth ground surface for the LBW specimens and the presence of the weld reinforcement for the HLAW specimens. The LBW specimens were grounded down, but still possessed surface discontinuities from the laser weld. Certain locations in laser weld on the top surface of the $^{3}/_{16}$" plate in the LBW specimens possessed a reduced plate thickness from weld disruptions. Referring to the failure documentation for FAT-LBW-10 in Appendix F, the fatigue crack was observed to follow these surface defects, thus providing reason and evidence for the sub-par performance.

In order to better correlate the test data to the S-N curves for the AASHTO detail categories, a constrained linear regression was performed on both sets of test data for specimens without fit-up gaps using a fixed slope of 3 that is presented in Figure 5–43 and

Figure 5–44. The constrained linear regression was performed on the LBW and HLAW data using the stress ranges attained from both the adjusted and fixed boundary conditions to obtain S-N curves in the same form as AASHTO equation 6.6.1.2.5-2 shown below in **(6.1)**. Where, A represents a constant times 10^8 ksi^3, N is the number of cycles, ΔS is the stress range, and $(\Delta F)_n$ is the nominal fatigue resistance. ((AAHSTO), 2010)

$$\Delta S = (\Delta F)_n = \left(\frac{A}{N}\right)^{\frac{1}{3}} \quad \textbf{(6.1)}$$

Though, the analytical method used to approximate the partial restrained condition was verified experimentally, the fixed end condition was included in these plots to provide a conservative bound. The constrained linear least squares regression curve fit yielded the equations shown below. Equations (6.2) and (6.3) represent the adjusted and fixed end conditions respectively for the LBW fatigue tests. Whereas equations (6.4) and (6.5) represent the adjusted and fixed end conditions respectively for the HLAW fatigue tests.

$$\Delta S = \left(\frac{631.311}{N}\right)^{\frac{1}{3}} \quad \textbf{(6.2)}$$

$$\Delta S = \left(\frac{232.199}{N}\right)^{\frac{1}{3}} \quad \textbf{(6.3)}$$

$$\Delta S = \left(\frac{1019.667}{N}\right)^{\frac{1}{3}} \quad \textbf{(6.4)}$$

$$\Delta S = \left(\frac{371.943}{N}\right)^{\frac{1}{3}} \quad \textbf{(6.5)}$$

The constant *A*, for AASHTO detail category A is 250(10^8 ksi^3), which is less than both constants generated in the LBW and HLAW regressed equations using a fixed slope of 3 and the adjusted stress ranges. The regressed constants for the LBW and HLAW were approximately 2.5 and 4 times that of AASHTO detail category A respectively. Even though, this value represents the lower bound for 95% confidence, the generated constants are comparably high. On the other hand, even the curves generated using the stress ranges from the fixed condition yield constants that are considerable high for such conservative values. Overall, the stress life cycle plots shown in Figure 5–41 through Figure 5–44 demonstrate through the vertical locations of the S-N curves that the HLAW process generates stake welds with a higher fatigue resistance.

Prior to testing, literature suggested that one of the advantages to HLAW welding process was superior fatigue resistance.(Schwartz, 2011) Through further investigation, an explanation was founded to lie directly with the cooling rates of the different stake welds. As stated previously, the LBW welding process generates the stake weld geometry by liquefying the base metal of overlapped components using a high intensity laser beam. The high welding speed and low heat input results in a narrow stake weld with a limited HAZ due to rapid quenching caused by the cool surrounding base metal.((AWS), 1999) The HLAW welding process combines the LBW and conventional arc methods, introducing additional filler material that results in a larger molten pool during the formation of the stake weld geometry. The steel surrounding the laser beam stake weld is subsequently tempered due to the larger volume of liquefied metal and additional heat input from the arc. This effect creates a wider transition zone, thus potentially reducing hardness peaks.(Schwartz, 2011)

Though, metallurgic microstructures are highly dependent on the chemical composition

of structural steels, which in this study are unknown; the rapid solidification associated with the typical LBW process is known to promote hard and brittle microstructures at the fusion zone, leaving the stake welds susceptible to fatigue. A study performed by the American Welding Society (AWS) revealed that LBW stake welds exhibit weld metal regions with high hardness and strength due to the formation of martensite and bainite at the fusion zone, both of which are hard forms of steel crystalline structure. These grain structures observed at the narrow fusion line were confirmed with spikes in microhardness in the hardness profiles generated along the LBW stake weld.((AWS), 1999) Additionally, the rapid cooling rates associated with the LBW welding process leave the stake welds more susceptible to higher porosity levels. Micro pores are formed as result of dissolved gases arising from contaminated surfaces, trapped process gases, or evaporation of alloying elements. The rate of escape of bubbles formed in the fusion zone can be lower than the rate of solidification at excessive weld cooling rates, thus resulting in trapped micro pores increasing the porosity of the final weld.((AWS), 1999) Porosity in steels is especially apparent with the use of thin sheet material, in which the HSS tubes used in this study were most likely comprised of due to the shape of the associated stress strain curves in Appendix D.

The plots shown in Figure 5–45 and Figure 5–46 present the stress life cycle data gathered from the testing program on the fatigue test specimens with variable fit-up gaps. The LBWG test specimens were tested at load ranges of ±350 lbs and ±400 lbs, whereas the HLAWG test specimens were tested at load ranges of ±400 lbs and ±425 lbs. Referring to Table 3-2, the numbered data points in the stress life cycle plots for LBWG and HLAWG specimens, represent the test specimen number that increase mutually with gap magnitude. Additionally, the odd numbered data points shown in Figure 5–45 and Figure 5–46 represent

the larger of the two load ranges. Both plots in Figure 5–45 and Figure 5–46 demonstrate diminishing fatigue resistance with increased gap magnitude, as the larger test specimen numbers are shown to shift to the left in plots, exhibiting a smaller number of life cycles. The LBWG data scatter in Figure 5–45 is shown to fall below AASHTO detail category A, approaching category B with increased gap magnitude, represented by the data point for FAT-LBWG-11. The HLAWG data scatter in Figure 5–46 is shown to fall above AASHTO detail category A, approaching category A with increased gap magnitude, represented by data points for FAT-HLAWG-09 and FAT-HLAWG-11. The upward shift in the HLAWG data in comparison to the LBWG data tested at smaller load ranges, clearly demonstrates that the HLAW technology is more suitable to handle fit-up gaps. The difference in performance between both laser welding technologies lies directly with the presence of filler material. In the case of the LBW, the absence of filler material causes the stake weld to rely on the liquefied metal from the overlapped weld components. This results in a reduced plate thickness at the laser weld shown in Figure 6–6, since the stake weld essentially sinks due to the fit-up gap leaving a depression at weld surface. The reduced plate thickness causes a larger stress magnitude in the $^{3}/_{16}$" plate, increasing the likelihood of plate failure. This is reinforced by the results of the LBWG fatigue tests, as all failures occurred in the plate and not in the weld along the joint interface. On the other hand, the addition of filler material in the HLAW process eliminates the possibility of reducing the plate thickness as shown in Figure 6–6 . Unfortunately, the length of the embedded laser welds increases with larger fit-up gaps in both processes, increasing the probability of weld failure along the joint interface. Provided that the plate thickness is not reduced, weld failures are much more apparent with HLAW process and fit-up gaps. This is confirmed by the results of the HLAWG fatigue tests, as the majority of

failures occurred along the joint interface in the weld. Plate failure occurred in FAT-HLAWG-11, the HLAW test specimen with the largest fit-up gap as a result of laser burn damage from "run-off" that reduced the plate thickness, refer to Appendix C.

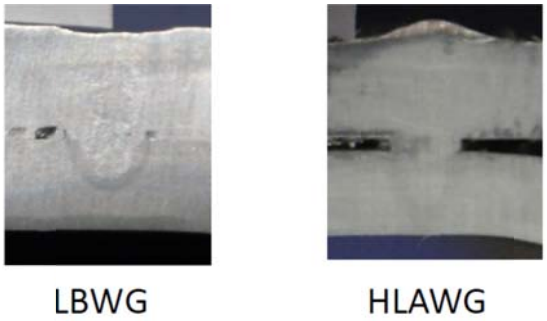

Figure 6–6: LBW and HLAW Stake Welds with a Fit-up Gap

The microscopic investigation on the failure surfaces of FAT-LBW-07 and FAT-HLAWG-03 using an SEM revealed diagonal striations, confirming that the failures were in fact fatigue driven. Diagonal striations were identified in four instances along the bottom of the $^{3}/_{16}$" plate cross section, as suspected that are shown in Figure 5–2 through Figure 5–9. These striations were identified through the comparison with known case studies involving fatigue Fractography from the (Esaklul and International, 1992). The change in direction of the diagonal striations identified along the bottom of the $^{3}/_{16}$" plate cross section of FAT-HLAW-03, lead to the conclusion there were multiple fatigue crack initiations along the bottom edge of the cross section as shown in Figure 5–10. It was believed that these thumbnail crack patterns eventually coalesced near mid-depth of the plate thickness, eventually resulting in fracture. The majority of the failure surfaces observed in Appendix F, resulting from plate failure exhibited a horizontal line approximately at mid-depth, thus reinforcing this explanation. The abnormal rounded protrusions and depressions that initiated this investigation, observed in the

failure surfaces of the LBW specimens went unidentified. Hydrogen damage and weld porosity were speculated to cause this peculiar failure geometry in the LBW specimens, provided that the rounded shapes depicted hydrogen fisheyes. Since there was no pre-heating of the base metals prior to laser welding during fabrication of the fatigue test specimens this assumption is plausible. Additionally, previous studies identified the LBW welding process to be susceptible to increased porosity at the weld fusion zone due to rapid solidification, adding credibility to the suggestion.

6.3 SANDWICH PANEL BEHAVIOR

The results from the parametric study summarized in section 5.2.2 demonstrate that the sandwich panel module, does not behave similar to a one way system, even with restraints to simulate a simply supported condition. The trends observed in Figure 5–27 through Figure 5–34, reveal that the panel's behavior is governed the by the deformation of the central rib directly centered beneath the applied load patch. Prior to the investigation, a thicker deck plate was believed to be a crucial to design parameter to limit differential rib deflection and prevent malfunctions observed in orthotropic bridge decks such as surface cracking and de-bonding. The parametric study uncovered that the internal rib spacing was just as crucial as the deck plate thickness. The results showed that decreasing internal rib spacing lead to significant reductions in differential rib deflection, as well as a decline in the overall maximum deflection in the bottom plate of the sandwich panel. In addition to reduced vertical deformations, decreased rib spacing promotes isotropic behavior by alleviating the spike in magnitude of the vertical deflection in the bottom plate and shear stress in the HSS webs observed at the central stiffening rib relative to the surrounding ribs. Additionally, the deflected shape of the bottom plate is unified from stepped cubic functions between the centerline of stiffening ribs, to a more evenly distributed deformed shape without inflection points between every pair of stiffening ribs.

As described in section 4.2.2.1, the shear stress on the outside walls of the HSS webs were analyzed 18 inches from the sandwich panel face, which was initially idealized as constant shear region depicted by Figure 4–44. The plots in Figure 5–27 through Figure 5–34 demonstrate that this location across the sandwich panel was not subjected to constant shear, reinforcing that the panel did behave similar to a one way system with simply supported

boundary conditions. A general understanding of the sandwich panel behavior can be conceptualized by imposing a vertical deflection on the centrally loaded rib according to the desired location and load scenario. The shear stress distribution observed in Figure 5–27 through Figure 5–34 attained from the walls of the HSS webs is explained through Figure 6–7 below. An imposed downward deflection at the central rib induces an upward reaction at each surrounding rib, as well as torsion in the rotational direction towards the central rib. The subsequent shear flows shown in Figure 6–7 throughout the HSS sections result in smaller magnitudes of shear stress in the HSS web closer to the central rib. This reasoning explains the peculiar distribution of shear stress observed in Figure 5–27 through Figure 5–34.

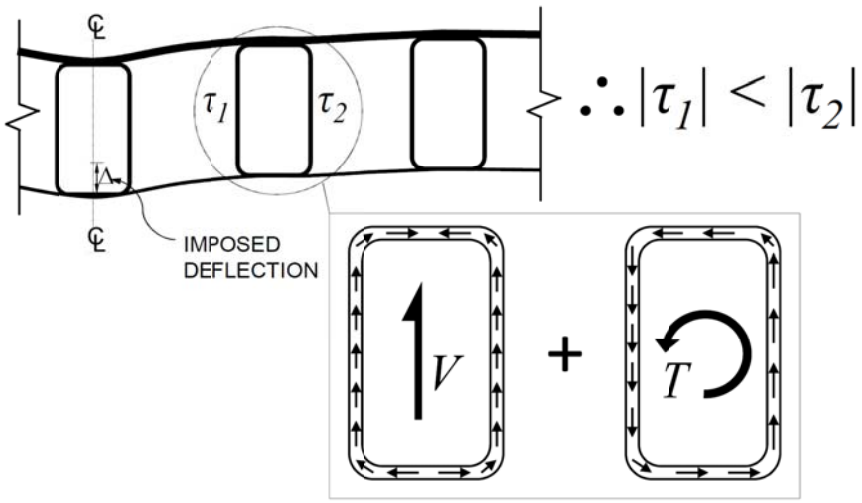

Figure 6–7: Shear Stress Distribution in Sandwich Panel HSS Stiffening Ribs

Figure 5–35 through Figure 5–40 visually depict the relationship between targeted values and the two sandwich panel variables analyzed in the parametric study, top plate thickness and internal rib spacing. The relationships displayed in the plots isolate each sandwich panel parameter not taking into account the influence from other variables. At a first glance, considering the top plate thickness in increments of $^1/_{16}$" and the rib spacing in increments of 1", all plots demonstrate that rib spacing is more influential to the global behavior of the

sandwich panel module than top plate thickness. Although this trend is clearly apparent, the problem at hand to optimize sandwich panel variables is much more complicated. The variables must be correlated to equivalent units that take into account weight and fabrication costs to understand the true impact of each design parameter. Though decreasing the internal rib spacing has shown promise as a result of the parametric study, promoting isotropic behavior, as well as reducing deflection and shear stress magnitudes, a thorough optimization analysis is warranted using all sandwich panel variables. Optimization parameters should include S, t_{TOP}, t_{BOTTOM}, t_{HSS}, B_{HSS}, and H_{HSS} equated to an equivalent unit combining weight and fabrication costs to minimize targeted design values.

6.4 FATIGUE TEST SPECIMEN AND SANDWICH PANEL COMPARISON

Initially, the comparison parameters were implemented to allow for the direct comparison between the sandwich panel modules and the generalized fatigue test specimens analyzed. It was believed that the partially restrained boundary conditions would cause the generalized fatigue test specimens to behave similarly to a sandwich panel configuration with closer internal rib spacing, due to increased stiffness. The comparison parameters computed for each individual fatigue test and sandwich panel configurations investigated in the parametric study are summarized in Table 5-5 and Table 5-6 through Table 5-10 respectively.

The evaluation of these parameters lead to the assessment that the localized Vierendeel load effect was not nearly as exaggerated as presumed. As a whole, the comparison parameters demonstrate that localized bending due to differential rib displacement in the sandwich panel modules is merely insignificant with regards to fatigue initiation. The stress ranges computed at the desired locations in the $^{3}/_{16}$" bottom plate as shown in Figure 4–48, resulting from localized bending between HSS ribs were very low in comparison to those calculated for the generalized fatigue test specimens. Comparing, the largest stress range of the sandwich panel modules to the smallest stress range of the fatigue test specimens emphasizes the insignificance of localized bending in the bottom plate of the sandwich panel configurations investigated. The largest stress range computed for the sandwich panels investigated was 3.54 ksi that occurred in the module with the largest rib spacing and thinnest top plate. The smallest stress range calculated in the fatigue test specimens was 23.06 ksi, occurring in run-out test specimen FAT-LBW-03. There is nearly six orders of magnitude difference between these values, demonstrating the substantial disparity between the localized bending in the bottom plate of sandwich panel modules and the fatigue test specimens.

Furthermore, the additional comparison parameters of the same sandwich panel configuration and fatigue test specimen exhibited the same inequality. The maximum slopes computed at the inflection points demonstrated roughly 2.5 orders of magnitude difference as they were computed to be 0.0026 $^{in}/_{in}$ and 0.0063 $^{in}/_{in}$ for the sandwich panel module and fatigue test specimen respectively. Even though, the differential displacement for the sandwich panel module was larger than that for the fatigue test specimen, it was irrelevant since the distances between the inflections are not the same. Fitting a simple circular curve to the largest directional displacement and distance between inflection points for the sandwich panel module and fatigue test specimen, the radiuses of curvature were founded at 3,887 inches and 724 inches respectively. Using elementary elastic beam theory, a simplified approach to moment curvature can be attained by inversing the radiuses of curvature resulting in the values of 0.0003 and 0.0014. These rough moment curvatures exhibit about 5 orders of magnitude difference, further supporting the discrepancy found between stresses to initiate fatigue.

Another noteworthy finding from the parametric study was the elevated von mises stress magnitudes at the locations in which the localized bending stresses were computed. With further investigation this was founded to be caused by the overall global bending of the sandwich panel as the dominant stress components were founded in the z-direction according to the coordinate system described in section 4.2. The elevated von mises stresses reported in Table 5-6 through Table 5-10 further accentuates how the sandwich panels studied were not susceptible to the Vierendeel load effect believed to govern fatigue. Though these values were relatively small, even in comparison to AASHTO detail category fatigue thresholds, they exhibit the necessity for full scale testing to investigate the fatigue performance of the true sandwich panel behavior.

Infinite life is evident when comparing the largest localized Vierendeel induced stress range of the sandwich panel configurations studied, 3.54 ksi, to experimental test run-outs and conservative approximations to AASHTO detail categories. Three fatigue specimens tested, FAT-LBW-03, FAT-HLAW-03, and FAT-HLAW-05 were identified as run-outs due to an exceedence of 10 million load cycles without failure. The stress ranges for these test specimens were calculated using the adjusted boundary conditions as 23.06 ksi, 28.05 ksi, and 43.41 ksi respectively, whereas the fixed end boundary conditions yielded stress ranges of 18.72 ksi, 23.40 ksi, and 32.76 ksi respectively. Additionally, as stated previously, the results from the tensile fatigue tests using the hydraulic grips conservatively approximated the LBW and HLAW specimens to AASHTO detail categories B' and B respectively. Table 6.6.1.2.5-3 in the AASHTO LRFD Bridge Design Specifications lists the constant amplitude fatigue thresholds as 12.0 ksi and 16.0 ksi for detail categories B' and B, which are approximately three and four times larger than the stress range observed in the bottom plate of the sandwich panel.((AAHSTO), 2010) All values, including conservative estimates derived from this study, point towards the obvious conclusion that the laser welded connection can be designed for infinite life.

CHAPTER 7: CONCLUSIONS AND RECOMMENDATIONS

The experimental and analytical investigations have shown that infinite fatigue life is achievable for the modular steel sandwich panel bridge deck system explored. The system exemplified excellent resistance to localized wheel loads, minimizing the Vierendeel load effect between adjacent stiffening ribs. The fatigue resistance data of the laser welded connection between the stiffening ribs and bottom plate exhibited superb performance. Although both laser welding technologies performed very well, the stake welds generated with the HLAW process were founded to possess superior fatigue resistance in comparison to those produced using the LBW process. Furthermore, the test data revealed that HLAW process is better suited to handle fit-up gaps between weld components during fabrication due to the addition of filler material.

This innovative modular bridge deck system shows much promise pushing forward as viable deck alternative. The panels possess excellent dead load reduction possibilities for the rehabilitation of structurally deficient bridges as those investigated weighed from 41 to 67 psf. In comparison to a typical 8" reinforced concrete deck weighing 97 psf and orthotropic bridge decks with weights ranging from 61 to 89 psf (Wolchuk, 1999), reductions up to 58% and 33% respectively are exhibited. Additionally, the full width modular system allows for rapid erection due to minimal field connections and promotes staged construction under short term closures. The panels are also well suited for mass production due to automated welding procedures. Overall, this technology holds the potential to revolutionize bridge infrastructure throughout the country.

Even though the fatigue resistance of the HLAW generated stake welds was outstanding, there lies the potential to enhance performance through focal adjustments of the laser beam.

The experimental testing program revealed that the HLAW stake welds were prone weld failure along the joint interface when subjected to higher load ranges. This was related to the relatively small stake weld interface width as discussed in section 6.2. Therefore it is presumed that altering the laser beam focus and focal location to increase the stake weld interface width can alleviate stake weld fatigue failures. The location of fatigue crack initiation has been verified through an SEM investigation to be underside of the bottom plate at the root of the laser stake weld, invisible during standard inspections. Therefore, it is even more crucial that the finalized deck system be designed with infinite fatigue life. In addition, it is highly recommended that non-destructive investigation methods and procedures are developed.

Based on the findings from the parametric study it is strongly suggested that panel parameters are optimized to minimize cost and weight. While, the localized Vierendeel load effect was deemed to be insignificant with regard to fatigue, it was clearly apparent analyzing the deflected shape of the panels at tremendous scales. Thus, it should still be taken into consideration during future optimization studies. The results also lead to the presumption that alternative configurations eliminating a thicker deck plate with conventional welds, moving towards a fully laser welded panel with equal face sheets near ¼" thicknesses and minimal rib spacing would be more ideal. The combination of equivalent face sheets and minimized rib spacing would increase isotropic behavior, as well as eliminate susceptibly localized loading to produce a more efficient panel.

In order for this system to be incorporated into America's infrastructure and be considered as a viable bridge deck alternative, further investigation is required. Based on the observations and knowledge gathered from this study, the following list provides future research topics to explore in descending order of significance:

1) Structural optimization investigating sandwich panel parameters S, t_{TOP}, t_{BOTTOM}, t_{HSS}, B_{HSS}, and H_{HSS} to minimize weight and cost, while maintaining superior performance.
2) Full Scale Experimental Testing
    a. A series of elastic load tests to verify the validity of the finite element model created.
    b. A series of fatigue tests with different load configurations to investigate the global fatigue resistance of the sandwich panels, localized fatigue integrity of structural connections to provide integration to support girders and deck continuity, as well as the reliability of an epoxy asphalt wearing surface.
    c. Strength tests to determine failure modes and ultimate capacity.
3) Design for the integration of a suitable crash barrier.
4) Additional fatigue testing programs targeted at optimizing the fatigue resistance of HLAW generated stake welds. Welding parameters that should be considered, but not limited to, include preheating, travel speed, beam focus, and beam focal location. Test specimens should be fabricated with both face sheets and three internal rib stiffeners at the desired spacing. A load fixture should be fabricated to fix the exterior stiffeners to provide symmetry and definitive boundary conditions.
5) A complete structural analysis of the laser welded connection utilizing continuum

elements in order to quantify the effects from the potential contact region between the bottom plate and the rounded corners of the HSS section, the laser weld interface width, and thermally induced residual stresses.

6) In-service testing to evaluate performance, as well as determine important design parameters for lateral load distribution and dynamic load allowance.
7) Develop an automated manufacturing method to minimize fabrication costs.
8) Cost-benefit analysis to provide a comparison to a typical reinforced concrete bridge deck.
9) Develop an economically efficient and effective non-destructive inspection method to allow for routine checks of fatigue crack initiation.
10) A metallurgic investigation to determine the chemical composition of the structural steel components to be welded influence on the crystalline steel structure at the fusion zone of the stake weld.

[1] Engineers, A. S. o. C. (2009). "Report Card for America's Infrastructure." *Transportation Bridges*, ASCE.
[2] (AAHSTO), A. A. o. S. H. a. T. O. (2010). "AASHTO LRFD Bridge Design Specifications." *Fifth Edition*.
[3] AWS, A. a. (2010). "Bridge Welding Code 6th Edition." *AASHTO/AWS D1.5:2010*.
[4] AISC (2005). "Steel Construction Manual 13th Edition."
[5] Reutzel, E. W., Rhoads, William G., Blomquist, Paul A. (2001). "LASCOR-The Development of Lightweight Laser Welded Corrugated Panels " *Technical Memorandum #01-011*, Pennsylvania State University, Applied Research Laboratory, State College, PA.
[6] Kortenoeven, J. (2008). "Application of sandwich panels in design and building of dredging ships." *Journal of ship production*, 24(4), 125-134.
[7] Dobmeier, J. M. (2001). "Failure study of an aluminum bridge deck panel." *Journal of performance of constructed facilities*, 15(2), 68-76.
[8] Harris, D. K., Cousins, T., Murray, T. M., and Sotelino, E. D. (2008). "Field Investigation of a Sandwich Plate System Bridge Deck." *Journal of Performance of Constructed Facilities*, 22(5), 305-315.
[9] Liu, Z. (2008). "Development and evaluation of an adhesively bonded panel-to-panel joint for a FRP bridge deck system." *Journal of composites for construction*, 12(2), 224-233.
[10] Hayes, M. D. (2000). "Performance of tube and plate fiberglass composite bridge deck." *Journal of composites for construction*, 4(2), 48-55.
[11] Cousins, T. E., Lesko, John J., Majumdar, Prasun K., Liu, Zihong (2009). "Rapid Replacement of Tangier Island Bridges Including Leightweight and Durable Fiber-Reinforced Polymer Deck Systems." Virginia Transportation Research Council (VTRC).
[12] M.S. Troitsky, D. S. (1994). *Planning and Design of Bridges* John Wiley & Sons, Inc., New York.
[13] Wolchuk, R. (1999). "Steel orthotropic decks: developments in the 1990s." *Transportation research record*(1688), 30-37.
[14] Wolchuk, R. (2001). "The use of orthotropic decks in redecking of bridges." *Engineering journal (New York, N.Y.)*, 38(1), 2-10.
[15] Tsakopoulos, P. A., Fisher, John W. (2005). "Fatigue Performance and Design Refinements of Steel Orthotropic Deck Panels Based on Full-Scale Laboratory Tests." *Journal of Korean Soceity of Steel Construction (KSSC)*, 5, 211-223.
[16] Olsen, F. O. (2009). *Hybrid laser-arc welding*, Woodhead Publishing ; CRC Press, Cambridge, U.K.; Boca Raton, Fla.
[17] Schwartz, M. M. (2011). "Innovations in materials manufacturing, fabrication, and environmental safety." <http://www.crcnetbase.com/isbn/978-1-4200-8215-9>.
[18] (DNV), D. N. V. (2006). "Qualification and Approval of Hybrid Laser-Arc Welding in Shipbuilding." *Rules for Classification of Ships*, Det Norske Veritas, Norway.
[19] Copley, S. (2006). "Beneficial pre-stress in laser fabricated, metallic, square cellular sandwich panels."
[20] Abbott, S. P., Caccese, V., Thompson, L., Blomquist, P.A., Hansen, E.E. "Automated Laser Welded High Performance Steel Sandwich Bridge Deck Development." *Proc., Transporation Research Boad*.
[21] Bright, S. R., and Smith, J. W. (2004). "Fatigue performance of laser-welded steel bridge

decks." *Structural Engineer*, 82(Compendex), 31-39.
[22] Bright, S. R. (2007). "A new design for steel bridge decks using laser fabrication." *Structural engineer (London, England : 1988)*, 85(21), 49-57.
[23] (ASTM), A. S. f. T. a. M. (2008). "Standard Test Methods for Tension Testing of Metallic Materials."
[24] Dowling, N. E. (2007). *Mechanical Behavior of Materials Engineering Methods for Deformation, Fracture, and Fatigue*, Pearson Prentice Hall, Upper Saddle River, New Jersey.
[25] Simulia (2010). "ABAQUS version 6.9 Documentation."
[26] Caccese, V. Y., Serdar (2009). "Laser Welded Steel Sandwich Panel Bridge Deck Development: Finite Element Analysis and Stake Weld Strength Tests." The University of Maine, Orono, Maine.
[27] (AWS), A. W. S. (1999). "Determination of Mechanical and Fracture Properties of Laser Beam Welded Steel Joints." *Welding Research Supplement to the Welding Journal*.
[28] Esaklul, K. A., and International, A. S. M. (1992). *Handbook of case histories in failure analysis*, ASM International, Materials Park, OH.

APPENDIX A: PRELIMINARY DESIGN CALCULATIONS

Sample Calculations for Preliminary Investigation of Sandwich Panel Components

DESIGN ASSUMPTIONS:

Strength I - Limit State Considered

Load Factors

$\gamma_{LL} := 1.75$

$\gamma_{DC} := 1.25$

$\gamma_{DW} := 1.5$

Dynamic Load Allowance

$IM := 33$

Dead Loads:

$DW_{wearingsurface} := 0.015 \cdot \left(\frac{1}{12}\right)$

Self Weight

$DC(Area) := 0.000284 \cdot Area$

Live Loads:

$LL_{lane} := 0.64 \cdot \left(\frac{1}{12}\right)$ *

Single HL-93 Design Truck

AASHTO Table A4-1

Bridge Deck Geometry

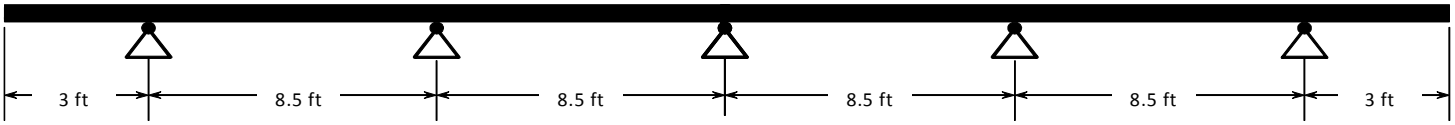

Sandwich Panel Geometry

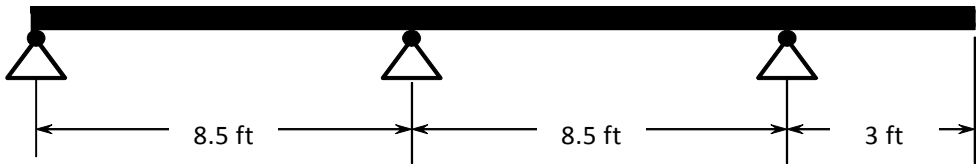

Unit Uniform Load Envelope

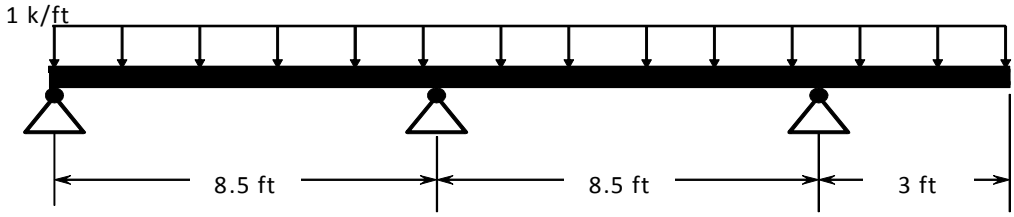

UNIT UNIFORM LOAD SHEAR ENVELOPE

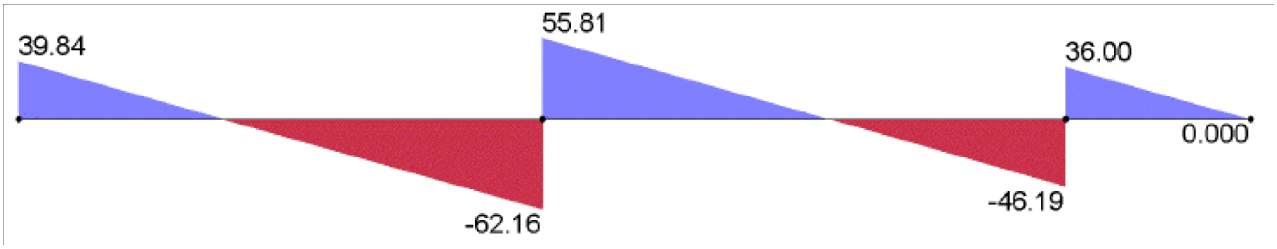

$V_{uniform1}(x) := (39.84 - x)$ $V_{uniform2}(x) := (157.81 - x)$ $V_{uniform3}(x) := (240. - x)$

UNIT UNIFORM LOAD MOMENT ENVELOPE

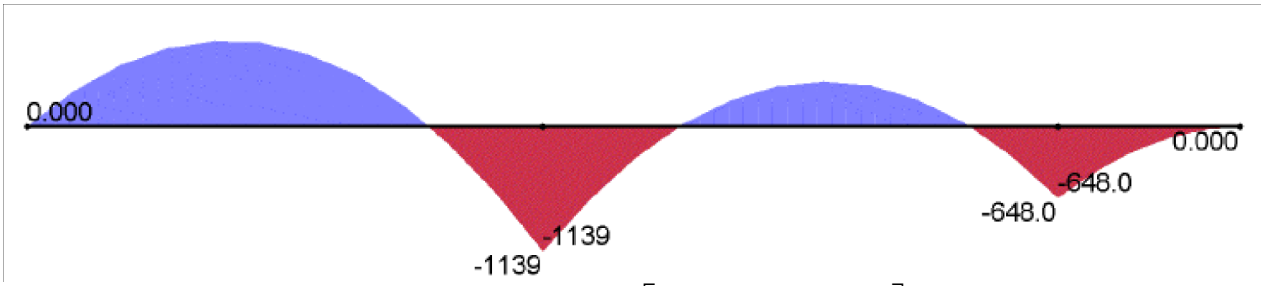

$M_{uniform1}(x) := \left[-\frac{(x - 157.81)^2}{2} + 12451.998\right]$ $Muniform2(x) := \left[-\frac{(x - 141.0)^2}{2} - 378.5\right]$ $Muniform3(x) := \left[-\frac{(x - 240.0)^2}{2}\right]$

Factored Uniform Load Design Shears and Moments

$$V_{uniform}(Area) := \left|V_{uniform1}(102)\right| \cdot \left(DC(Area) \cdot \gamma_{DC} + DW_{wearingsurface} \cdot \gamma_{DW} + LL_{lane} \cdot \gamma_{LL}\right) \rightarrow 0.022 \cdot Area + 5.91 \text{ kips}$$

$$M_{uniformpos}(Area) := M_{uniform1}(51) \cdot \left(DC(Area) \cdot \gamma_{DC} + DW_{wearingsurface} \cdot \gamma_{DW} + LL_{lane} \cdot \gamma_{LL}\right) \rightarrow 2.395 \cdot Area + 642.448 \text{ kip} \cdot \text{in}$$

$$M_{uniformneg}(Area) := M_{uniform1}(102) \cdot \left(DC(Area) \cdot \gamma_{DC} + DW_{wearingsurface} \cdot \gamma_{DW} + LL_{lane} \cdot \gamma_{LL}\right) \rightarrow 3.868 \cdot Area + 1037.25 \text{ kip} \cdot \text{in}$$

Design Truck Envelope

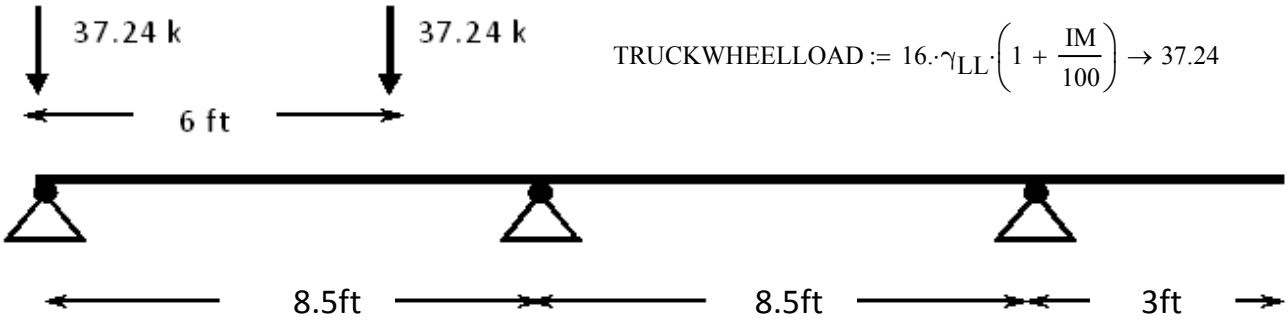

$$TRUCKWHEELLOAD := 16. \cdot \gamma_{LL} \cdot \left(1 + \frac{IM}{100}\right) \rightarrow 37.24$$

DESIGN TRUCK SHEAR ENVELOPE

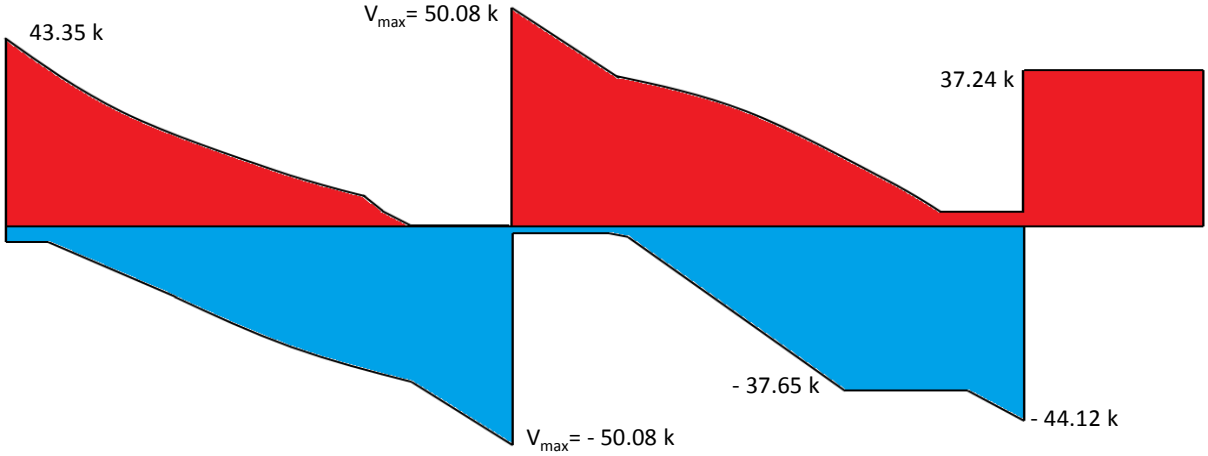

$$V_{truck} := 50.08 \text{ kips}$$

DESIGN TRUCK MOMENT ENVELOPE

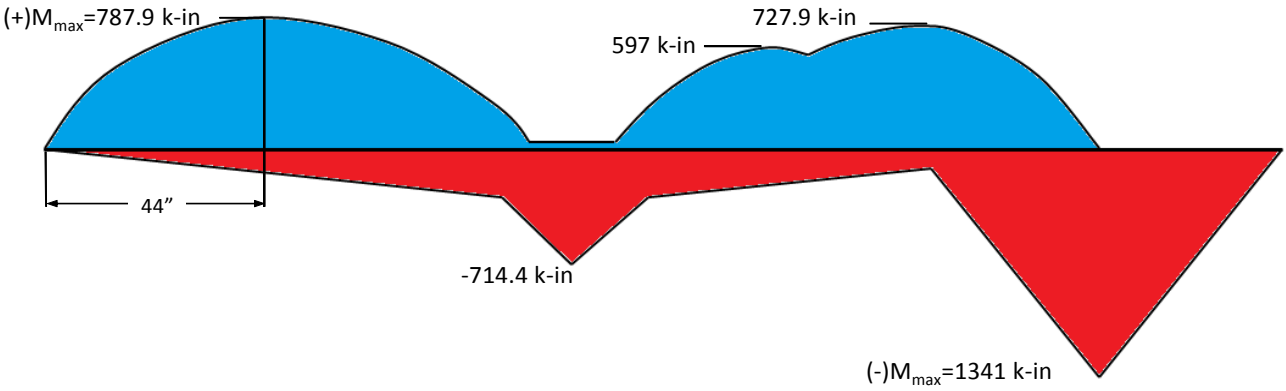

NOTE: The moment envelope shown above do not take into account wheel load distribution and two-way bending. The moment envelope shown above is an EXTREME load case that is impossible to attain, but was included to provide a comparison to the moments obtained from Table A4-1.

Table A4-1 Maximum Live Load Moments Per Unit Width, kip-ft./ft.

S	Positive Moment	NEGATIVE MOMENT						
		Distance from CL of Girder to Design Section for Negative Moment						
		0.0 in.	3 in.	6 in.	9 in.	12 in.	18 in.	24 in.
4' -0"	4.68	2.68	2.07	1.74	1.60	1.50	1.34	1.25
4' -3"	4.66	2.73	2.25	1.95	1.74	1.57	1.33	1.20
4' -6"	4.63	3.00	2.58	2.19	1.90	1.65	1.32	1.18
4' -9"	4.64	3.38	2.90	2.43	2.07	1.74	1.29	1.20
5' -0"	4.65	3.74	3.20	2.66	2.24	1.83	1.26	1.12
5' -3"	4.67	4.06	3.47	2.89	2.41	1.95	1.28	0.98
5' -6"	4.71	4.36	3.73	3.11	2.58	2.07	1.30	0.99
5' -9"	4.77	4.63	3.97	3.31	2.73	2.19	1.32	1.02
6' -0"	4.83	4.88	4.19	3.50	2.88	2.31	1.39	1.07
6' -3"	4.91	5.10	4.39	3.68	3.02	2.42	1.45	1.13
6' -6"	5.00	5.31	4.57	3.84	3.15	2.53	1.50	1.20
6' -9"	5.10	5.50	4.74	3.99	3.27	2.64	1.58	1.28
7' -0"	5.21	5.98	5.17	4.36	3.56	2.84	1.63	1.37
7' -3"	5.32	6.13	5.31	4.49	3.68	2.96	1.65	1.51
7' -6"	5.44	6.26	5.43	4.61	3.78	3.15	1.88	1.72
7' -9"	5.56	6.38	5.54	4.71	3.88	3.30	2.21	1.94
8' -0"	5.69	6.48	5.65	4.81	3.98	3.43	2.49	2.16
8' -3"	5.83	6.58	5.74	4.90	4.06	3.53	2.74	2.37
8' -6"	5.99	6.66	5.82	4.98	4.14	3.61	2.96	2.58
8' -9"	6.14	6.74	5.90	5.06	4.22	3.67	3.15	2.79
9' -0"	6.29	6.81	5.97	5.13	4.28	3.71	3.31	3.00
9' -3"	6.44	6.87	6.03	5.19	4.40	3.82	3.47	3.20
9' -6"	6.59	7.15	6.31	5.46	4.66	4.04	3.68	3.39

NOTE: Given that Table A4-1 from AASHTO is specified for concrete slabs, which are much more uniform than the proposed sandwich panel deck a factor of 2 will be multiplied in addition to the load factor and dynamic load allowance in order to provide an conservative strength calculation. The resulting design moments are much less in comparison to the moment envelope generated.

$$M_{truckpos} := 2 \cdot 5.99 \cdot 12 \cdot \gamma_{LL} \cdot \left(1 + \frac{IM}{100}\right) \rightarrow 334.6014 \ kip \cdot \frac{in}{ft}$$ At Mid-Span

$$M_{truckneg} := 2 \cdot 6.66 \cdot 12 \cdot \gamma_{LL} \cdot \left(1 + \frac{IM}{100}\right) \rightarrow 372.0276 \ kip \cdot \frac{in}{ft}$$ At Interior Support

DESIGN SHEAR AND MOMENTS

Since the truck design moments are in terms of strip width in ft, the spacing of internal stiffening ribs(S) is the tributary lengthof each strip being analyzed.

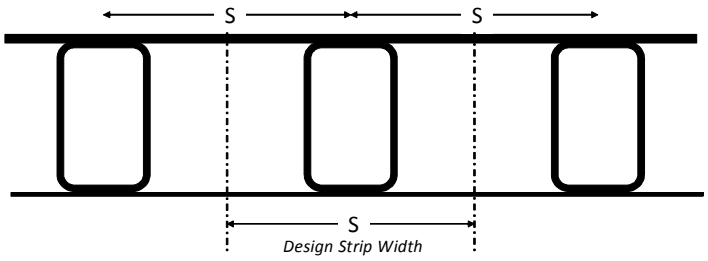

$$V_{max}(Area) := V_{truck} + V_{uniform}(Area) \rightarrow 0.022 \cdot Area + 55.998 \quad kips$$

$$M_{pos}(Area, S) := M_{truckpos} \cdot \left(\frac{S}{12}\right) + M_{uniformpos}(Area) \rightarrow 2.395 \cdot Area + 27.883 \cdot S + 642.448 \quad kip \cdot in$$

$$M_{neg}(Area, S) := M_{truckneg} \cdot \left(\frac{S}{12}\right) + M_{uniformneg}(Area) \rightarrow 3.868 \cdot Area + 31.002 \cdot S + 1037.259 \quad kip \cdot in$$

Variable Design Parameters

Top Plate Range: 9/16" to 1"

Bottom Plate Range: 3/16" to 5/16"

(37) AISC rectangular HSS sectons with an 8 inch dimension

Internal Rib Stiffener Spacing: 12",14",16"

} 2664 Sandwich Panel Configurations Studied

Sandwich Panel Configuration for Used for Sample Calculations

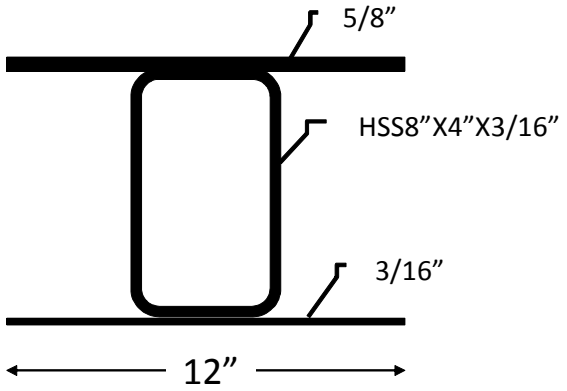

$S := 12 \ in$

$Area := 13.73 \ in^2$

$y_{bar} := 5.9692 \ in^2$

$I_x := 363.64 \ in^4$

$F_y := 50. \ ksi$

$E := 29000 \ ksi$

HSS LOCAL INSTABLITY

As a preliminary precaution, HSS sections were screened so that web local buckling was not an issue under flexural bending. The AISC manual was used to provide an local instablity check using table B4.1, case 13.

$h := 7.482 \ in$

$t_{des} := 0.174 \ in$ $\quad \frac{h}{t_{des}} \rightarrow 43.0$ $\quad \lambda_p := 2.42 \cdot \sqrt{\frac{E}{F_y}} \rightarrow 58.281$ $\quad 43 < 58.281$ **OK**

NOMINAL FLEXURAL CAPACITY

Since the stiffening rib is fully braced by both the deck plate and bottom plate and strength was the primary concern for the preliminary study, the yield moment was taken as the flexural capcity.

$\phi_b := 0.9$

$M_y := \frac{F_y \cdot I_x}{y_{bar}} \rightarrow 3045.969 \ kip \cdot in$ $\quad M_{upos} := M_{pos}(Area, S) \rightarrow 1009.939 \ kip \cdot in$

$M_n := M_y$

$\phi_b \cdot M_n \rightarrow 2741.372 \ kip \cdot in$ $\quad M_{uneg} := M_{neg}(Area, S) \rightarrow 1462.388 \ kip \cdot in$

$M_{upos} \le \phi_b \cdot M_n \rightarrow 1$

$M_{uneg} \le \phi_b \cdot M_n \rightarrow 1$ **OK**

NOMINAL SHEAR CAPACITY

The nominal shear capacity of the section analyzed in this study was calculated using Chapter G of the AISC manual. A conservative assumption was made by assuming that the shear was only supported by the webs of the HSS section.

AISC Chapter G Section 5: $A_w := 2 \cdot h \cdot t_{des} \rightarrow 2.603736$ $k_v := 5$ $\phi_v := 0.9$

$\frac{h}{t_{des}} \rightarrow 43.0$

$\frac{h}{t_{des}} \leq 1.10 \cdot \sqrt{\frac{k_v \cdot E}{F_y}} \rightarrow 1$ **OK** $C_v := 1$

$1.10 \cdot \sqrt{\frac{k_v \cdot E}{F_y}} \rightarrow 59.237$

$V_n := 0.6 \cdot F_y \cdot A_w \cdot C_v \rightarrow 78.11208$ kips

$V_u := V_{max}(Area) \rightarrow 56.301$ kips

$\phi_v \cdot V_n \rightarrow 70.300872$

$V_u \leq \phi_v \cdot V_n \rightarrow 1$ **OK**

HSS AND DECK PLATE WELD DESIGN

Since the weld detail required to join the deck plate to the HSS section is not listed in AASHTO as a prequalified weld, the AISC manual was used determine the minimum weld dimensions. The required weld for this joint is a flare-bevel groove weld, found in Table 8.2, pg 8-61 in the AISC manual sets minimum weld dimensions for a prequalified weld. Gas Metal Arc Weld (GMAW) will be chosen as the welding process

Table 8–2 (continued)
Prequalified Welded Joints
Flare-Bevel Groove Welds

Flare-bevel-groove weld (10)
Butt joint (B)
T-joint (T)
Corner joint (C)

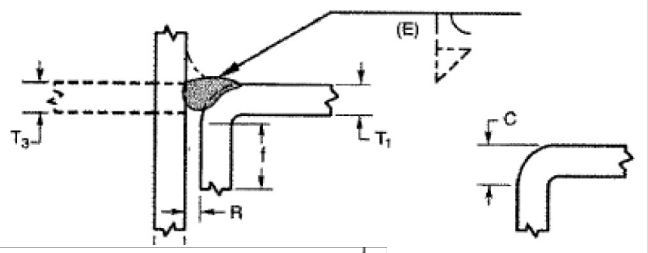

Welding Process	Joint Designation	Base Metal Thickness (U = unlimited) T_1	T_2	T_3	Groove Preparation: Root Opening, Root Face, Bend Radius*	Tolerances: As Detailed (see 3.12.3)	Tolerances: As Fit-Up (see 3.12.3)	Allowed Welding Positions	Total Weld Size (E)	Notes
SMAW	BTC-P10	3/16 min	U	T_1 min	R = 0 f = 3/16 min C = $\frac{3T_1}{2}$ min	+1/16, –0 +U, –0 +U, –0	+1/8, –1/16 +U, –1/16 +U, –0	All	$\frac{5T_1}{8}$	5, 7, 10, 12
GMAW FCAW	BTC-P10-GF	3/16 min	U	T_1 min	R = 0 f = 3/16 min C = $\frac{3T_1}{2}$ min	+1/16, –0 +U, –0 +U, –0	+1/8, –1/16 +U, –1/16 +U, –0	All	$\frac{5T_1}{8}$	1, 7, 10, 12
SAW	T-P10-S	1/2 min	1/2 min	N/A	R = 0 f = 1/2 min C = $\frac{3T_1}{2}$ min	±0 +U, –0 +U, –0	+1/16, –0° +U, –1/16 +U, –0	F	$\frac{5T_1}{8}$	7, 10, 12

* For cold formed (A500) rectangular tubes, C dimension is not limited. See the following:
Effective Weld Size of Flare-Bevel-Groove Welded Joints. Tests have been performed on cold formed ASTM A 500 material exhibiting a "C" dimension as small as T1 with a nominal radius of 2t. As the radius increases, the "C" dimension also increases. The corner curvature may not be a quadrant of a circle tangent to the sides. The corner dimension, "C," may be less than the radius of the corner.

$T_1 := 0.1875 \text{ in}$ $t_{deck} := 0.625 \text{ in}$ $F_{EXX} := 70 \text{ ksi}$

$T_2 := 0.625 \text{ in}$ $t_{bot} := 0.1875 \text{ in}$ $\phi_{weld} := 0.75$

$T_3 := 0.1875 \text{ in}$ $B_{HSS} := 4 \text{ in}$

$H_{HSS} := 8 \text{ in}$

TABLE J2.2
Effective Weld Sizes of Flare Groove Welds

Welding Process	Flare Bevel Groove[a]	Flare V Groove
GMAW and FCAW-G	$5/8\,R$	$3/4\,R$
SMAW and FCAW-S	$5/16\,R$	$5/8\,R$
SAW	$5/16\,R$	$1/2\,R$

[a] For Flare Bevel Groove with $R < 3/8$ in. (10 mm) use only reinforcing fillet weld on filled flush joint.
General Note: R = radius of joint surface (can be assumed to be $2t$ for HSS), in. (mm)

Effective Weld Size According to Table J2.2 pg 16.1-94 AISC

$$t_e := \frac{5}{8.}\cdot\left(2\cdot T_1\right) \rightarrow 0.234375 \text{ in}$$

$$Q := t_{deck}\cdot\left(\frac{S}{2} - \frac{B_{HSS}}{2}\right)\cdot\left(H_{HSS} + t_{deck} + t_{bot} - y_{bar}\right) \rightarrow 7.10825 \text{ in}^3$$

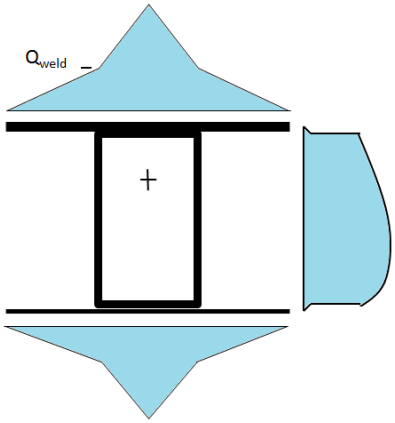

$$R_u := \frac{V_{max}(Area)\cdot Q}{I_x} \rightarrow 1.101 \frac{k}{in}$$

$$R_n := 0.6\cdot F_{EXX}\cdot t_e \rightarrow 9.844 \frac{k}{in}$$

$$\phi_{weld}\cdot R_n \rightarrow 7.383 \frac{k}{in}$$

$$R_u \le \phi_{weld}\cdot R_n \rightarrow 1 \quad \textbf{OK}$$

The following parameters were chosen resulting from the preliminary investigation:

Internal Rib Spacing = 12 in

Internal Rib Stiffener HSS8"X4"X3/16"

Deck Plate Thickness = 0.625" (5/8")

Bottom Plate Thickness = 0.625" (3/16")

LOCAL BUCKLING OF BOTTOM PLATE

There was concern for local buckling of the bottom plate under negative flexural. In order to investigate this issue, a CUFSM model was created to analyze the local buckling of the bottom plate. Givent that CUFSM only analyzes open cross sections, the HSS sections were divided in half as shown in the figure below. The eight nodes that border the model were pinned to simulate deck continuity. The nodes shown in green are constraints in 1,2,4 so that cross sections act together as if they were fully bonded, neglecting contact. The section was then subjected to negative flexure about the x axis and a constrained analysis for local buckling was performed.

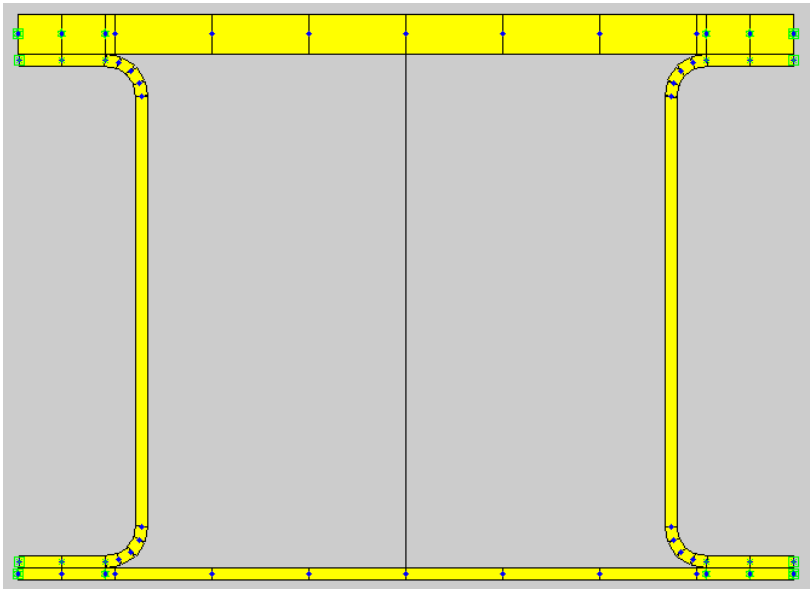

Sandwich Panel Member Input Geometry

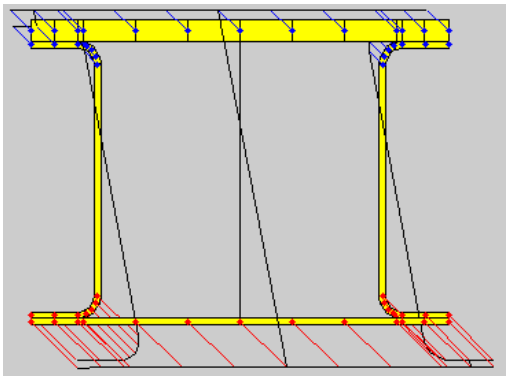

Negative Flexure Load Scheme

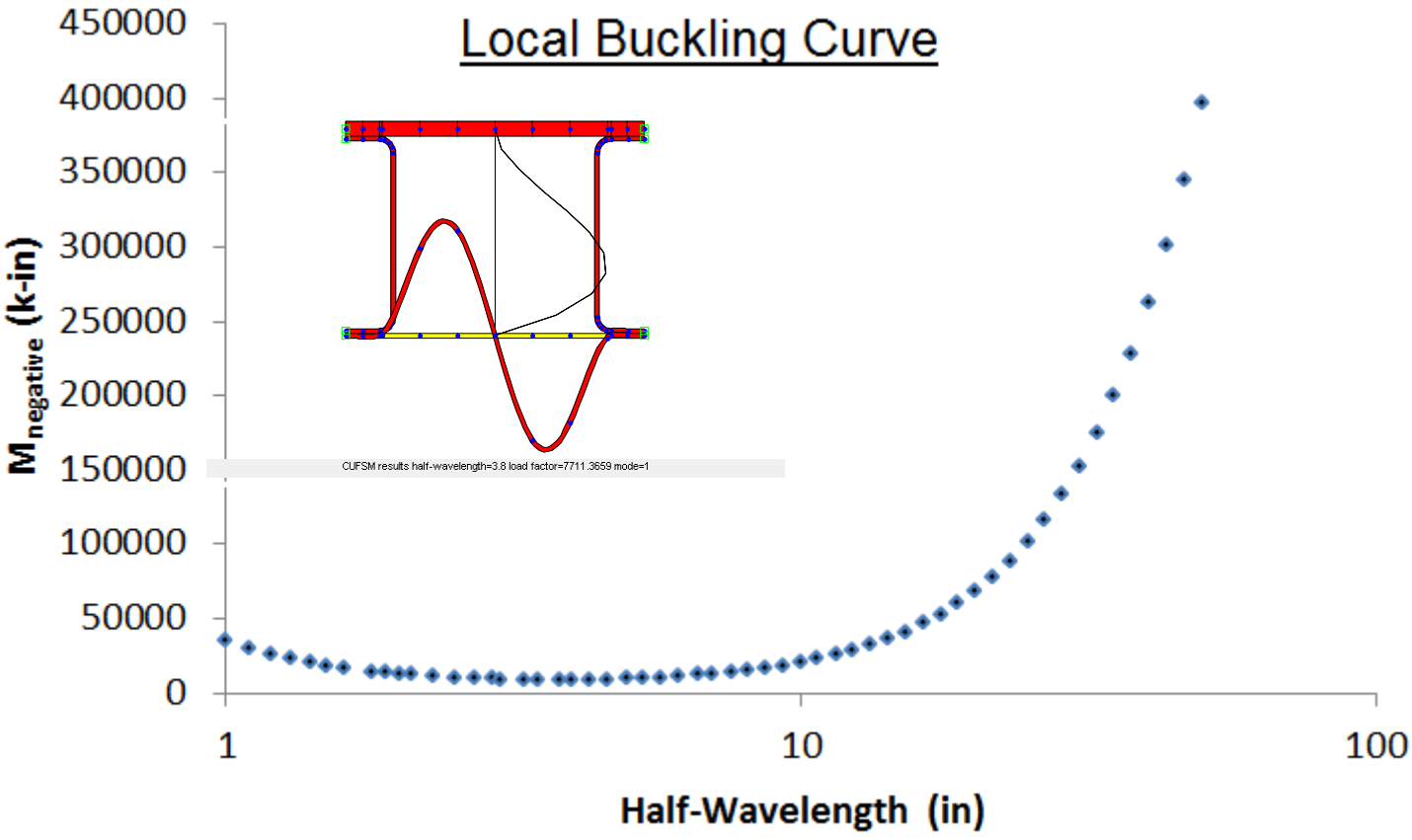

Lowest potential energy buckling mode was reported

$M_{localbuckling} := 7711.4 \quad k \cdot in$ Halfwavelentgh $:= 3.8 \quad in$

$\phi_b \cdot M_y \rightarrow 2741.372 \quad k \cdot in$

$\phi_b \cdot M_y \leq M_{localbuckling}$ **OK LOCAL BUCKLING IS NOT A PROBLEM**

APPENDIX B: FATIGUE TEST SPECIMEN DIMENSIONS

Table B-1: LBW Stake Welded Fatigue Test Specimen Dimensions

Spec. No.		FAT-LBW-02		FAT-LBW-09		FAT-LBWG-05		FAT-LBWG-11	
Dim		Side A	Side B	Side A	Side B	Side A	Side B	Side A	Side B
H_1	*(in)*	8.0010	8.0040	7.9995	8.0035	8.0055	7.9970	7.9995	7.9985
H_2	*(in)*	7.9615	7.9660	7.9685	7.9640	7.9645	7.9750	7.9580	7.9720
H_3	*(in)*	7.9595	7.9705	7.9634	7.9660	7.9630	7.9555	7.9610	7.9860
H_4	*(in)*	8.0030	7.9995	8.0050	8.0000	8.0050	8.0010	7.9990	8.0015
B_1	*(in)*	3.9910	3.9695	3.9905	3.9945	3.9960	4.0050	4.0075	4.0000
B_2	*(in)*	4.1450	4.1110	4.1240	4.0995	4.0990	4.1260	4.1300	4.1250
B_3	*(in)*	4.1355	4.1065	4.1105	4.0990	4.1025	4.1180	4.1125	4.1165
B_4	*(in)*	3.9920	3.9730	3.9920	3.9830	3.9840	3.9820	3.9820	3.9865
R_{o1}	*(in)*	0.7300	0.6590	0.7245	0.7370	0.6920	0.7135	0.7230	0.6445
R_{o2}	*(in)*	0.7005	0.6940	0.6760	0.7665	0.6605	0.7220	0.6680	0.6880
R_{o3}	*(in)*	0.7090	0.7070	0.6825	0.6900	0.6700	0.7200	0.6530	0.6915
R_{o4}	*(in)*	0.7275	0.7015	0.6730	0.7065	0.6635	0.6760	0.6470	0.7040
D_{w1}	*(in)*	5.6800	5.6705	5.7245	5.7340	5.7100	5.7200	5.7360	5.6680
D_{w2}	*(in)*	5.7100	5.6760	5.7060	5.6970	5.6990	5.7150	5.6340	5.7235
S_w	*(in)*	2.6060	2.5730	2.5930	2.5955	2.5880	2.5425	2.6025	2.6125
L_{PL}	*(in)*	13.9960	13.9195	14.0235	14.0265	13.9970	13.9775	13.9725	14.0040
t_{PL1}	*(in)*	0.1880	0.1890	0.1900	0.1895	0.1880	0.1850	0.1870	0.1865
t_{PL2}	*(in)*	0.1870	0.1890	0.1890	0.1890	0.1850	0.1890	0.1840	0.1865
t_{HSS1}	*(in)*	0.1830	0.1790	0.1780	0.1755	0.1785	0.1790	0.1785	0.1810
t_{HSS2}	*(in)*	0.1735	0.1730	0.1740	0.1730	0.1745	0.1750	0.1735	0.1730

Table B-2: HLAW Stake Welded Fatigue Test Specimen Dimensions

Spec. No.		FAT-HLAW-03		FAT-HLAW-06		FAT-HLAWG-03		FAT-HLAWG-10	
Dim		Side A	Side B	Side A	Side B	Side A	Side B	Side A	Side B
H_1	*(in)*	7.9885	8.0035	7.9995	8.0000	8.0045	7.9915	7.9955	8.0005
H_2	*(in)*	7.9620	7.9710	7.9655	7.9730	7.9745	7.9890	7.9620	7.9610
H_3	*(in)*	7.9670	7.9805	7.9565	7.9685	7.9650	7.9665	7.9650	7.9695
H_4	*(in)*	8.0035	8.0015	8.0035	8.0025	8.0035	7.9975	8.0010	7.9935
B_1	*(in)*	3.9800	3.9860	3.9880	3.9850	3.9870	4.0115	3.9805	3.9930
B_2	*(in)*	4.1210	4.1075	4.1205	4.1155	4.1075	4.1285	4.1015	4.1030
B_3	*(in)*	4.1280	4.1040	4.1190	4.1225	4.0950	4.1165	4.0930	4.0980
B_4	*(in)*	4.0075	3.9930	4.0020	3.9955	3.9815	3.9870	3.9700	3.9735
R_{o1}	*(in)*	0.6855	0.6850	0.6950	0.7175	0.6720	0.7340	0.6985	0.6915
R_{o2}	*(in)*	0.6940	0.6940	0.6945	0.6700	0.7155	0.6880	0.6870	0.6985
R_{o3}	*(in)*	0.6670	0.6205	0.6920	0.6765	0.6580	0.6505	0.6745	0.7020
R_{o4}	*(in)*	0.6655	0.6360	0.6760	0.7010	0.6450	0.6485	0.6645	0.6815
D_{w1}	*(in)*	5.7380	5.7120	5.6680	5.7545	5.7155	5.7170	5.6810	5.7670
D_{w2}	*(in)*	5.6890	5.7180	5.7665	5.6720	5.5635	5.7035	5.7425	5.6720
S_w	*(in)*	2.5980	2.6050	2.5680	2.5430	5.7125	2.5755	2.5690	2.5470
L_{PL}	*(in)*	14.0250	14.0350	14.0025	13.9695	16.9915	13.9960	13.9925	13.9860
t_{PL1}	*(in)*	0.1855	0.1895	0.1890	0.1895	0.1905	0.1960	0.1880	0.1910
t_{PL2}	*(in)*	0.1905	0.1895	0.1890	0.1900	0.1920	0.1925	0.1900	0.1910
t_{HSS1}	*(in)*	0.1750	0.1770	0.1800	0.1810	0.1765	0.1800	0.1865	0.1780
t_{HSS2}	*(in)*	0.1710	0.1710	0.1720	0.1735	0.1730	0.1735	0.1755	0.1750

APPENDIX C: FATIGUE TEST SPECIMEN LASER WELD DIMENSIONS

Table C-1: Laser Weld Dimensions for LBW Fatigue Test Specimens

TEST SPECIMEN	WELD TYPE	LASER STAKE WELD	LASER STAKE WELD AREA (in^2)	LASER STAKE WELD INTERFACE WIDTH (in)	LASER STAKE WELD HSS PENETRATION DEPTH (in)
FAT-LBW-01	LBW	A1	0.0236	0.0840	0.1277
FAT-LBW-01	LBW	A2	0.0280	0.0980	0.1305
FAT-LBW-01	LBW	B1	0.0296	0.1073	0.1141
FAT-LBW-01	LBW	B2	0.0185	0.0693	0.0732
FAT-LBW-02	LBW	A1	0.0261	0.0902	0.0898
FAT-LBW-02	LBW	A2	0.0274	0.0813	0.1289
FAT-LBW-02	LBW	B1	0.0289	0.0942	0.1134
FAT-LBW-02	LBW	B2	0.0298	0.1020	0.1033
FAT-LBW-03	LBW	A1	0.0360	0.1279	0.1038
FAT-LBW-03	LBW	A2	0.0241	0.0852	0.0900
FAT-LBW-03	LBW	B1	0.0276	0.0973	0.0957
FAT-LBW-03	LBW	B2	0.0275	0.0950	0.1006
FAT-LBW-04	LBW	A1	0.0256	0.0867	0.1048
FAT-LBW-04	LBW	A2	0.0232	0.0832	0.0837
FAT-LBW-04	LBW	B1	0.0216	0.0824	0.0718
FAT-LBW-04	LBW	B2	0.0331	0.1199	0.0943
FAT-LBW-05	LBW	A1	0.0517	0.1443	0.1685
FAT-LBW-05	LBW	A2	0.0322	0.1063	0.0953
FAT-LBW-05	LBW	B1	0.0318	0.1073	0.0932
FAT-LBW-05	LBW	B2	0.0366	0.1011	0.1665
FAT-LBW-06	LBW	A1	0.0238	0.0764	0.1147
FAT-LBW-06	LBW	A2	0.0272	0.0900	0.1104
FAT-LBW-06	LBW	B1	0.0249	0.0808	0.1035
FAT-LBW-06	LBW	B2	0.0315	0.1054	0.1188
FAT-LBW-08	LBW	A1	0.0276	0.0896	0.1174
FAT-LBW-08	LBW	A2	0.0240	0.0824	0.0831
FAT-LBW-08	LBW	B1	0.0271	0.0922	0.0893
FAT-LBW-08	LBW	B2	0.0268	0.0920	0.0815
FAT-LBW-09	LBW	A1	0.0229	0.0808	0.0748
FAT-LBW-09	LBW	A2	0.0285	0.1023	0.0875
FAT-LBW-09	LBW	B1	0.0346	0.1267	0.0955
FAT-LBW-09	LBW	B2	0.0225	0.0719	0.0987
FAT-LBW-10	LBW	A1	0.0241	0.0809	0.0848
FAT-LBW-10	LBW	A2	0.0293	0.0911	0.1064
FAT-LBW-10	LBW	B1	0.0303	0.0882	0.0970
FAT-LBW-10	LBW	B2	0.0297	0.0941	0.0929
FAT-LBW-11	LBW	A1	0.0262	0.0935	0.0741
FAT-LBW-11	LBW	A2	0.0243	0.0817	0.0876
FAT-LBW-11	LBW	B1	0.0262	0.0961	0.0803
FAT-LBW-11	LBW	B2	0.0236	0.0851	0.0784

Table C-2: Laser Weld Dimensions for HLAW Fatigue Test Specimens

TEST SPECIMEN	WELD TYPE	LASER STAKE WELD	LASER STAKE WELD AREA (in^2)	LASER STAKE WELD INTERFACE WIDTH (in)	LASER STAKE WELD HSS PENETRATION DEPTH (in)	LASER STAKE WELD HLAW SURPLUS HEIGHT (in)
FAT-HLAW-01	HLAW	A1	0.0225	0.0627	0.0834	0.0536
FAT-HLAW-01	HLAW	A2	0.0278	0.0788	0.1088	0.0592
FAT-HLAW-01	HLAW	B1	0.0266	0.0801	0.0971	0.0506
FAT-HLAW-01	HLAW	B2	0.0305	0.0928	0.0998	0.0507
FAT-HLAW-02	HLAW	A1	0.0204	0.0694	0.0655	0.0606
FAT-HLAW-02	HLAW	A2	0.0246	0.0777	0.0860	0.0619
FAT-HLAW-02	HLAW	B1	0.0235	0.0713	0.0791	0.0632
FAT-HLAW-02	HLAW	B2	0.0220	0.0969	0.0670	0.0609
FAT-HLAW-03	HLAW	A1	0.0204	0.0646	0.0902	0.0603
FAT-HLAW-03	HLAW	A2	0.0189	0.0596	0.0789	0.0642
FAT-HLAW-03	HLAW	B1	0.0193	0.0672	0.0749	0.0598
FAT-HLAW-03	HLAW	B2	0.0203	0.0640	0.0953	0.0654
FAT-HLAW-04	HLAW	A1	0.0197	0.0680	0.0766	0.0654
FAT-HLAW-04	HLAW	A2	0.0213	0.0672	0.0833	0.0706
FAT-HLAW-04	HLAW	B1	0.0210	0.0578	0.0841	0.0535
FAT-HLAW-04	HLAW	B2	0.0245	0.0680	0.0905	0.054
FAT-HLAW-05	HLAW	A1	0.0193	0.0567	0.0951	0.0549
FAT-HLAW-05	HLAW	A2	0.0152	0.0507	0.0677	0.0673
FAT-HLAW-05	HLAW	B1	0.0206	0.0674	0.0779	0.0571
FAT-HLAW-05	HLAW	B2	0.0210	0.0662	0.0943	0.0541
FAT-HLAW-06	HLAW	A1	0.0267	0.0889	0.0982	0.0518
FAT-HLAW-06	HLAW	A2	0.0274	0.0806	0.1352	0.0506
FAT-HLAW-06	HLAW	B1	0.0240	0.0669	0.1152	0.0509
FAT-HLAW-06	HLAW	B2	0.0218	0.0628	0.1083	0.0584
FAT-HLAW-07	HLAW	A1	0.0215	0.0672	0.1020	0.0646
FAT-HLAW-07	HLAW	A2	0.0209	0.0651	0.1071	0.0645
FAT-HLAW-07	HLAW	B1	0.0231	0.0656	0.1041	0.0523
FAT-HLAW-07	HLAW	B2	0.0202	0.0598	0.0731	0.0564
FAT-HLAW-08	HLAW	A1	0.0170	0.0549	0.0655	0.0691
FAT-HLAW-08	HLAW	A2	0.0215	0.0671	0.0963	0.0535
FAT-HLAW-08	HLAW	B1	0.0244	0.0705	0.0985	0.0481
FAT-HLAW-08	HLAW	B2	0.0213	0.0722	0.0592	0.0562
FAT-HLAW-09	HLAW	A1	0.0233	0.0686	0.1264	0.0711
FAT-HLAW-09	HLAW	A2	0.0208	0.0638	0.0899	0.0628
FAT-HLAW-09	HLAW	B1	0.0217	0.0626	0.0840	0.058
FAT-HLAW-09	HLAW	B2	0.0247	0.0689	0.1137	0.053
FAT-HLAW-10	HLAW	A1	0.0193	0.0613	0.0970	0.0522
FAT-HLAW-10	HLAW	A2	0.0152	0.0613	0.0622	0.0656
FAT-HLAW-10	HLAW	B1	0.0206	0.0561	0.0728	0.057
FAT-HLAW-10	HLAW	B2	0.0210	0.0647	0.0987	0.0614

Table C-3: Laser Weld Dimensions for LBWG Fatigue Test Specimens

TEST SPECIMEN	WELD TYPE	LASER STAKE WELD	LASER STAKE WELD AREA (in^2)	LASER STAKE WELD INTERFACE WIDTH (in)	LASER STAKE WELD HSS PENETRATION DEPTH (in)
FAT-LBWG-01	LBWG	A1	0.0292	0.0917	0.1124
FAT-LBWG-01	LBWG	A2	0.0250	0.0770	0.1085
FAT-LBWG-01	LBWG	B1	0.0313	0.0906	0.1456
FAT-LBWG-01	LBWG	B2	0.0239	0.0742	0.1152
FAT-LBWG-02	LBWG	A1	0.0252	0.0809	0.1070
FAT-LBWG-02	LBWG	A2	0.0274	0.0892	0.1071
FAT-LBWG-02	LBWG	B1	0.0294	0.0943	0.1071
FAT-LBWG-02	LBWG	B2	0.0242	0.0765	0.1034
FAT-LBWG-03	LBWG	A1	0.0252	0.0772	0.1085
FAT-LBWG-03	LBWG	A2	0.0264	0.0895	0.0830
FAT-LBWG-03	LBWG	B1	0.0285	0.0907	0.0956
FAT-LBWG-03	LBWG	B2	0.0245	0.0789	0.0931
FAT-LBWG-04	LBWG	A1	0.0276	0.0901	0.0882
FAT-LBWG-04	LBWG	A2	0.0227	0.0722	0.0686
FAT-LBWG-04	LBWG	B1	0.0219	0.0674	0.0836
FAT-LBWG-04	LBWG	B2	0.0249	0.0824	0.0870
FAT-LBWG-05	LBWG	A1	0.0273	0.0886	0.0853
FAT-LBWG-05	LBWG	A2	0.0280	0.0921	0.0774
FAT-LBWG-05	LBWG	B1	0.0324	0.1093	0.0773
FAT-LBWG-05	LBWG	B2	0.0279	0.0884	0.0970
FAT-LBWG-06	LBWG	A1	0.0279	0.0846	0.0963
FAT-LBWG-06	LBWG	A2	0.0343	0.1225	0.0777
FAT-LBWG-06	LBWG	B1	0.0267	0.0991	0.0782
FAT-LBWG-06	LBWG	B2	0.0258	0.0851	0.0802
FAT-LBWG-07	LBWG	A1	0.0264	0.0889	0.0738
FAT-LBWG-07	LBWG	A2	0.0302	0.1083	0.0569
FAT-LBWG-07	LBWG	B1	0.0358	0.1191	0.0785
FAT-LBWG-07	LBWG	B2	0.0293	0.0959	0.0838
FAT-LBWG-08	LBWG	A1	0.0240	0.0751	0.0741
FAT-LBWG-08	LBWG	A2	0.0341	0.1200	0.0848
FAT-LBWG-08	LBWG	B1	0.0366	0.1299	0.0706
FAT-LBWG-08	LBWG	B2	0.0261	0.0823	0.0862
FAT-LBWG-09	LBWG	A1	0.0297	0.1032	0.0558
FAT-LBWG-09	LBWG	A2	0.0298	0.1112	0.0457
FAT-LBWG-09	LBWG	B1	0.0298	0.0970	0.0731
FAT-LBWG-09	LBWG	B2	0.0265	0.0871	0.0715
FAT-LBWG-10	LBWG	A1	0.0315	0.1073	0.0831
FAT-LBWG-10	LBWG	A2	0.0343	0.1220	0.0803
FAT-LBWG-10	LBWG	B1	0.0375	0.1334	0.0709
FAT-LBWG-10	LBWG	B2	0.0349	0.1273	0.0701
FAT-LBWG-11	LBWG	A1	0.0367	0.1230	0.0589
FAT-LBWG-11	LBWG	A2	0.0375	0.1307	0.0510
FAT-LBWG-11	LBWG	B1	0.0325	0.1174	0.0465
FAT-LBWG-11	LBWG	B2	0.0319	0.1076	0.0768

Table C-4: Laser Weld Dimensions for HLAWG Fatigue Test Specimens

TEST SPECIMEN	WELD TYPE	LASER STAKE WELD	LASER STAKE WELD AREA (in^2)	LASER STAKE WELD INTERFACE WIDTH (in)	LASER STAKE WELD HSS PENETRATION DEPTH (in)	LASER STAKE WELD HLAW SURPLUS HEIGHT (in)
FAT-HLAWG-01	HLAWG	A1	0.0235	0.0817	0.0890	0.0533
FAT-HLAWG-01	HLAWG	A2	0.0270	0.0863	0.0826	0.0538
FAT-HLAWG-01	HLAWG	B1	0.0291	0.1095	0.0612	0.0736
FAT-HLAWG-01	HLAWG	B2	0.0245	0.0910	0.0544	0.0611
FAT-HLAWG-02	HLAWG	A1	0.0237	0.0722	0.0705	0.0599
FAT-HLAWG-02	HLAWG	A2	0.0251	0.0863	0.0755	0.0651
FAT-HLAWG-02	HLAWG	B1	0.0258	0.0887	0.0792	0.0560
FAT-HLAWG-02	HLAWG	B2	0.0249	0.0810	0.0757	0.0596
FAT-HLAWG-03	HLAWG	A1	0.0231	0.0801	0.0971	0.0709
FAT-HLAWG-03	HLAWG	A2	0.0272	0.0930	0.0907	0.0674
FAT-HLAWG-03	HLAWG	B1	0.0272	0.0890	0.0842	0.0660
FAT-HLAWG-03	HLAWG	B2	0.0249	0.0839	0.0827	0.0643
FAT-HLAWG-04	HLAWG	A1	0.0238	0.0762	0.0873	0.0679
FAT-HLAWG-04	HLAWG	A2	0.0261	0.0890	0.0925	0.0711
FAT-HLAWG-04	HLAWG	B1	0.0246	0.0814	0.0859	0.0659
FAT-HLAWG-04	HLAWG	B2	0.0235	0.0790	0.0739	0.0631
FAT-HLAWG-05	HLAWG	A1	0.0246	0.0801	0.0971	0.0506
FAT-HLAWG-05	HLAWG	A2	0.0307	0.1058	0.0893	0.0557
FAT-HLAWG-05	HLAWG	B1	0.0344	0.1144	0.0828	0.0518
FAT-HLAWG-05	HLAWG	B2	0.0243	0.0798	0.0711	0.0497
FAT-HLAWG-06	HLAWG	A1	0.0255	0.0817	0.0895	0.0527
FAT-HLAWG-06	HLAWG	A2	0.0339	0.1095	0.1041	0.0513
FAT-HLAWG-06	HLAWG	B1	0.0298	0.0958	0.0996	0.0559
FAT-HLAWG-06	HLAWG	B2	0.0247	0.0778	0.0929	0.0637
FAT-HLAWG-07	HLAWG	A1	0.0281	0.0813	0.1195	0.0478
FAT-HLAWG-07	HLAWG	A2	0.0274	0.0802	0.1054	0.0557
FAT-HLAWG-07	HLAWG	B1	0.0301	0.0860	0.0981	0.0546
FAT-HLAWG-07	HLAWG	B2	0.0273	0.0828	0.0979	0.0508
FAT-HLAWG-08	HLAWG	A1	0.0256	0.0731	0.1156	0.0537
FAT-HLAWG-08	HLAWG	A2	0.0281	0.0799	0.1278	0.0508
FAT-HLAWG-08	HLAWG	B1	0.0266	0.0760	0.1028	0.0496
FAT-HLAWG-08	HLAWG	B2	0.0241	0.0786	0.0869	0.0447
FAT-HLAWG-09	HLAWG	A1	0.0296	0.0833	0.1066	0.0426
FAT-HLAWG-09	HLAWG	A2	0.0290	0.0760	0.1641	0.0260
FAT-HLAWG-09	HLAWG	B1	0.0313	0.0821	0.1472	0.0473
FAT-HLAWG-09	HLAWG	B2	0.0228	0.0663	0.0991	0.0513
FAT-HLAWG-10	HLAWG	A1	0.0309	0.0789	0.1173	0.0396
FAT-HLAWG-10	HLAWG	A2	0.0336	0.0932	0.1357	0.0391
FAT-HLAWG-10	HLAWG	B1	0.0294	0.0690	0.1700	0.0336
FAT-HLAWG-10	HLAWG	B2	0.0291	0.0783	0.1095	0.0422
FAT-HLAWG-11	HLAWG	A1	0.0213	0.0715	0.1152	0.0000
FAT-HLAWG-11	HLAWG	A2	0.0343	0.0943	0.1211	0.0000
FAT-HLAWG-11	HLAWG	B1	0.0306	0.0823	0.1364	0.0373
FAT-HLAWG-11	HLAWG	B2	0.0288	0.0764	0.1163	0.0309

STAKE WELD	STAKE WELD AREA	STAKE WELD HSS/PLATE INTERFACE WIDTH	STAKE WELD HSS PENETRATION DEPTH
(UNITS)	(sqin)	(in.)	(in.)
A1	0.0236	0.0840	0.1277
A2	0.0280	0.0980	0.1305
B1	0.0296	0.1073	0.1141
B2	0.0185	0.0693	0.0732

LEGEND

INTERPOLATED LASER STAKE WELD AREA

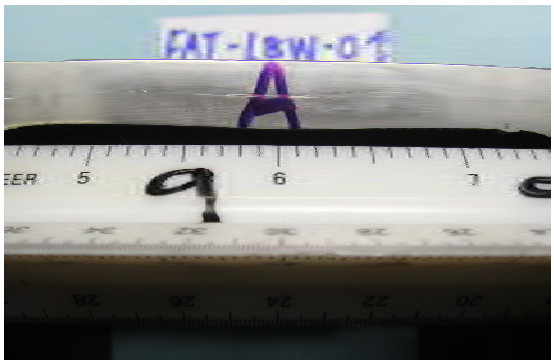

FAT–LBW–01 SIDE A STAKE WELD DETAIL

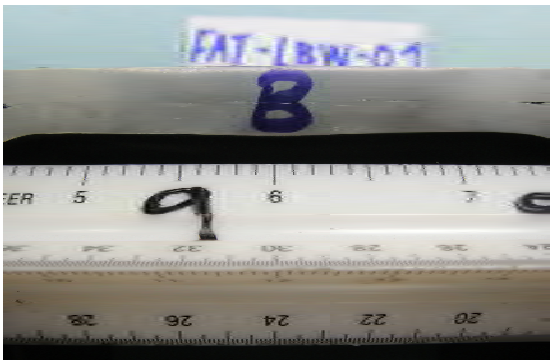

FAT–LBW–01 SIDE B STAKE WELD DETAIL

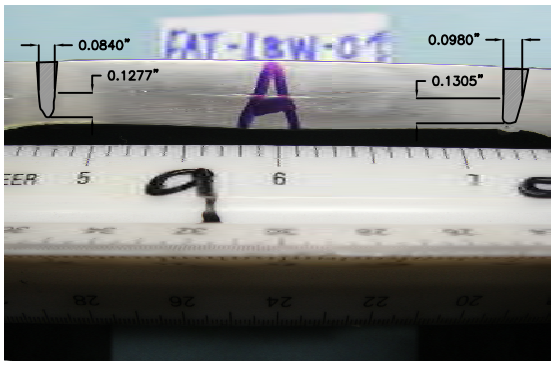

FAT–LBW–01 SIDE A STAKE WELD DETAIL INTERPOLATED DIMENSIONS

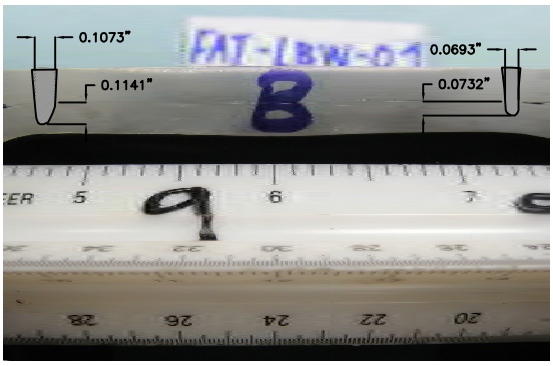

FAT–LBW–01 SIDE B STAKE WELD DETAIL INTERPOLATED DIMENSIONS

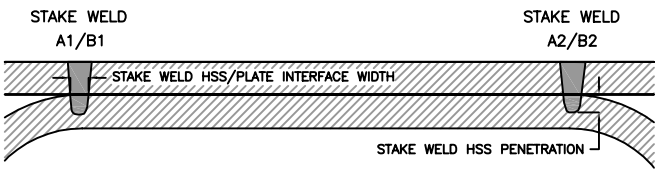

FIGURE REFERENCE

LOCATION	DRAWN BY		CHECKED BY		APPROVED BY		DRAWING NUMBER
BLACKSBURG, VA	G.PASSARELLI	3/31/2011	W.WRIGHT	3/31/2011	W.WRIGHT	3/31/2011	FAT-LBW-01

VIRGINIA POLYTECHNIC INSTITUTE AND STATE UNIVERSITY
BLACKSBURG, VIRGINIA

VirginiaTech VirginiaTech

FATIGUE SPECIMEN STAKE WELD DETAILS
LASER BEAM WELD TEST SPECIMEN: FAT-LBW-01
VIA DEPARTMENT OF CIVIL AND ENVIRONMENTAL ENGINEERING
BLACKSBURG, VIRGINIA

DESIGNED BY	G. Passarelli	3/31/2011	CHECKED BY	W.Wright	3/31/2011
DRAWN BY	G.Passarelli	3/31/2011	APPROVED BY	W.Wright	3/31/2011

SCALE:	DRAWING NO.	PROJECT NO.	SHEET NO.	REVISION NO.
1"=1"	FAT-LBW-01	SSP	---	--

PRODUCED BY AN AUTODESK EDUCATIONAL PRODUCT

PRODUCED BY AN AUTODESK EDUCATIONAL PRODUCT

STAKE WELD	STAKE WELD AREA	STAKE WELD HSS/PLATE INTERFACE WIDTH	STAKE WELD HSS PENETRATION DEPTH
(UNITS)	(sqin)	(in.)	(in.)
A1	0.0261	0.0902	0.0898
A2	0.0274	0.0813	0.1289
B1	0.0289	0.0942	0.1134
B2	0.0298	0.1020	0.1033

LEGEND

INTERPOLATED LASER STAKE WELD AREA

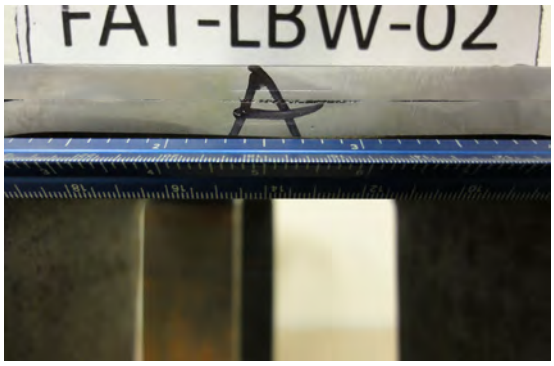

FAT–LBW–02 SIDE A STAKE WELD DETAIL

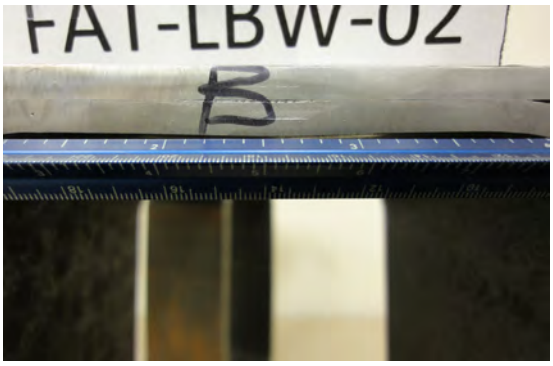

FAT–LBW–02 SIDE B STAKE WELD DETAIL

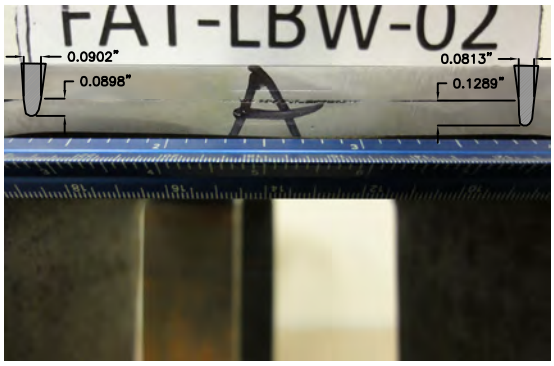

FAT–LBW–02 SIDE A STAKE WELD DETAIL INTERPOLATED DIMENSIONS

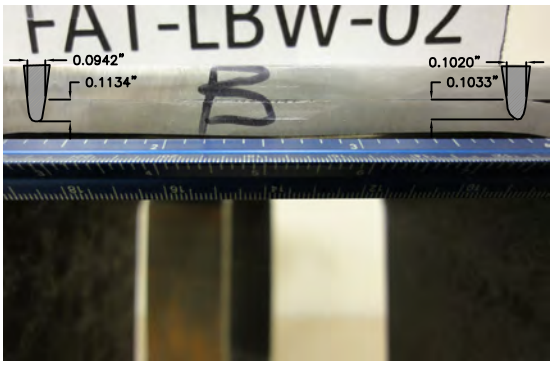

FAT–LBW–02 SIDE B STAKE WELD DETAIL INTERPOLATED DIMENSIONS

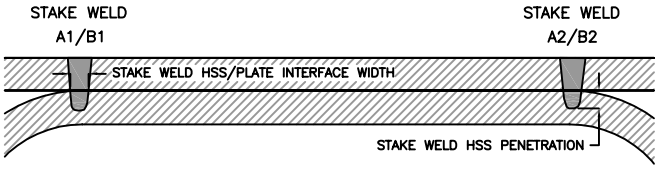

FIGURE REFERENCE

LOCATION	DRAWN BY	CHECKED BY	APPROVED BY	DRAWING NUMBER
BLACKSBURG, VA	G.PASSARELLI 3/31/2011	W.WRIGHT 3/31/2011	W.WRIGHT 3/31/2011	FAT-LBW-02

VIRGINIA POLYTECHNIC INSTITUTE AND STATE UNIVERSITY
BLACKSBURG, VIRGINIA

VirginiaTech VirginiaTech

FATIGUE SPECIMEN STAKE WELD DETAILS
LASER BEAM WELD TEST SPECIMEN: FAT-LBW-02
VIA DEPARTMENT OF CIVIL AND ENVIRONMENTAL ENGINEERING
BLACKSBURG, VIRGINIA

DESIGNED BY	G. Passarelli	3/31/2011	CHECKED BY	W.Wright	3/31/2011
DRAWN BY	G.Passarelli	3/31/2011	APPROVED BY	W.Wright	3/31/2011

SCALE:	DRAWING NO.	PROJECT NO.	SHEET NO.	REVISION NO.
1"=1"	FAT-LBW-02	SSP	---	--

PRODUCED BY AN AUTODESK EDUCATIONAL PRODUCT

PRODUCED BY AN AUTODESK EDUCATIONAL PRODUCT

STAKE WELD	STAKE WELD AREA	STAKE WELD HSS/PLATE INTERFACE WIDTH	STAKE WELD HSS PENETRATION DEPTH
(UNITS)	(sqin)	(in.)	(in.)
A1	0.0360	0.1279	0.1038
A2	0.0241	0.0852	0.0900
B1	0.0276	0.0973	0.0957
B2	0.0275	0.0950	0.1006

LEGEND

INTERPOLATED LASER STAKE WELD AREA

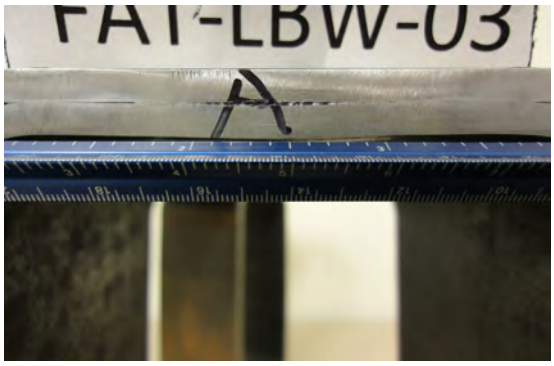

FAT–LBW–03 SIDE A STAKE WELD DETAIL

FAT–LBW–03 SIDE B STAKE WELD DETAIL

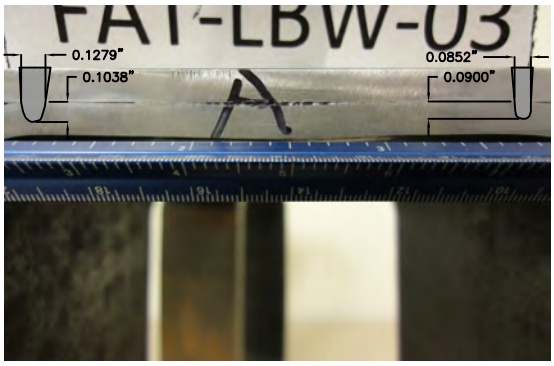

FAT–LBW–03 SIDE A STAKE WELD DETAIL INTERPOLATED DIMENSIONS

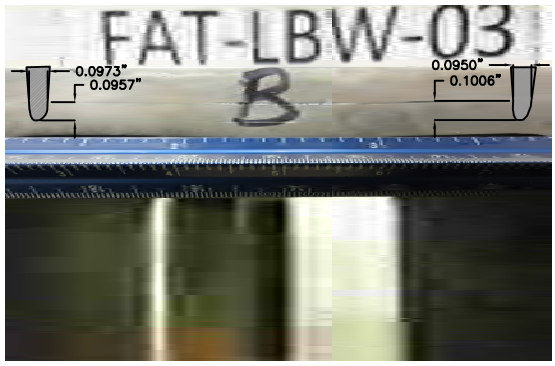

FAT–LBW–03 SIDE B STAKE WELD DETAIL INTERPOLATED DIMENSIONS

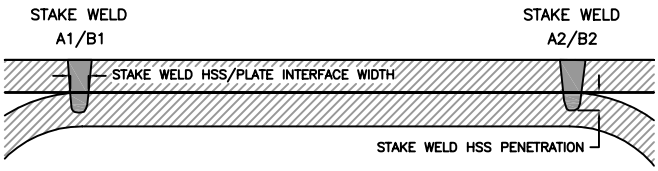

FIGURE REFERENCE

VIRGINIA POLYTECHNIC INSTITUTE AND STATE UNIVERSITY
BLACKSBURG, VIRGINIA

VirginiaTech VirginiaTech

FATIGUE SPECIMEN STAKE WELD DETAILS
LASER BEAM WELD TEST SPECIMEN: FAT-LBW-03
VIA DEPARTMENT OF CIVIL AND ENVIRONMENTAL ENGINEERING
BLACKSBURG, VIRGINIA

DESIGNED BY	G. Passarelli	3/31/2011	CHECKED BY	W.Wright	3/31/2011
DRAWN BY	G.Passarelli	3/31/2011	APPROVED BY	W.Wright	3/31/2011

SCALE:	DRAWING NO.	PROJECT NO.	SHEET NO.	REVISION NO.
1"=1"	FAT-LBW-03	SSP	---	--

LOCATION	DRAWN BY		CHECKED BY		APPROVED BY		DRAWING NUMBER
BLACKSBURG, VA	G.PASSARELLI	3/31/2011	W.WRIGHT	3/31/2011	W.WRIGHT	3/31/2011	FAT-LBW-03

PRODUCED BY AN AUTODESK EDUCATIONAL PRODUCT

PRODUCED BY AN AUTODESK EDUCATIONAL PRODUCT

STAKE WELD	STAKE WELD AREA	STAKE WELD HSS/PLATE INTERFACE WIDTH	STAKE WELD HSS PENETRATION DEPTH
(UNITS)	(sqin)	(in.)	(in.)
A1	0.0256	0.0867	0.1048
A2	0.0232	0.0832	0.0837
B1	0.0216	0.0824	0.0718
B2	0.0331	0.1199	0.0943

LEGEND

INTERPOLATED LASER STAKE WELD AREA

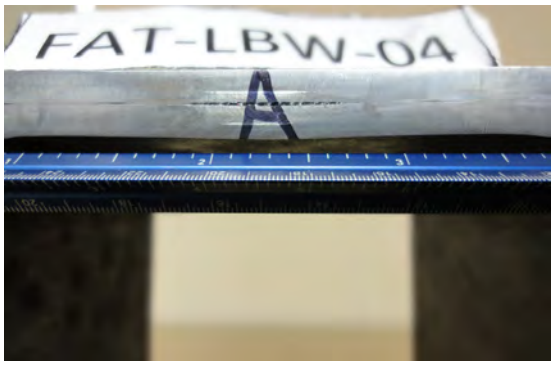

FAT–LBW–04 SIDE A STAKE WELD DETAIL

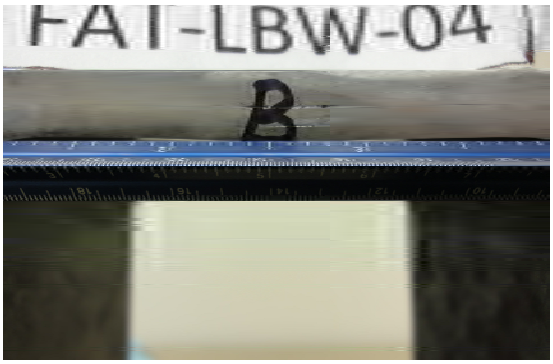

FAT–LBW–04 SIDE B STAKE WELD DETAIL

FAT–LBW–04 SIDE A STAKE WELD DETAIL INTERPOLATED DIMENSIONS

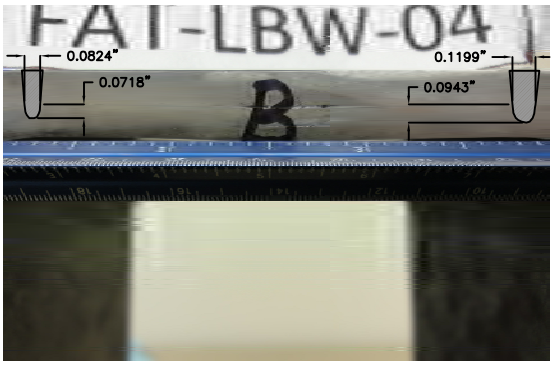

FAT–LBW–04 SIDE B STAKE WELD DETAIL INTERPOLATED DIMENSIONS

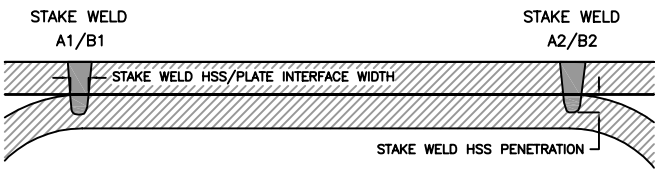

FIGURE REFERENCE

VIRGINIA POLYTECHNIC INSTITUTE AND STATE UNIVERSITY
BLACKSBURG, VIRGINIA

VirginiaTech VirginiaTech

FATIGUE SPECIMEN STAKE WELD DETAILS
LASER BEAM WELD TEST SPECIMEN: FAT-LBW-04
VIA DEPARTMENT OF CIVIL AND ENVIRONMENTAL ENGINEERING
BLACKSBURG, VIRGINIA

DESIGNED BY	G. Passarelli	3/31/2011	CHECKED BY	W.Wright	3/31/2011
DRAWN BY	G.Passarelli	3/31/2011	APPROVED BY	W.Wright	3/31/2011

SCALE:	DRAWING NO.	PROJECT NO.	SHEET NO.	REVISION NO.
1"=1"	FAT-LBW-04	SSP	---	--

LOCATION	DRAWN BY		CHECKED BY		APPROVED BY		DRAWING NUMBER
BLACKSBURG, VA	G.PASSARELLI	3/31/2011	W.WRIGHT	3/31/2011	W.WRIGHT	3/31/2011	FAT-LBW-04

PRODUCED BY AN AUTODESK EDUCATIONAL PRODUCT

PRODUCED BY AN AUTODESK EDUCATIONAL PRODUCT

STAKE WELD	STAKE WELD AREA	STAKE WELD HSS/PLATE INTERFACE WIDTH	STAKE WELD HSS PENETRATION DEPTH
(UNITS)	(sqin)	(in.)	(in.)
A1	0.0517	0.1443	0.1685/FULL
A2	0.0322	0.1063	0.0953
B1	0.0318	0.1073	0.0932
B2	0.0366	0.1011	0.1665/FULL

LEGEND

INTERPOLATED LASER STAKE WELD AREA

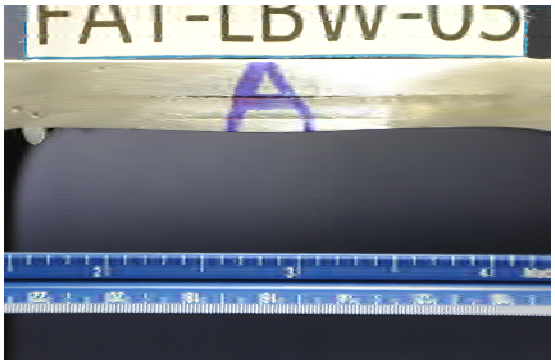

FAT-LBW-05 SIDE A STAKE WELD DETAIL

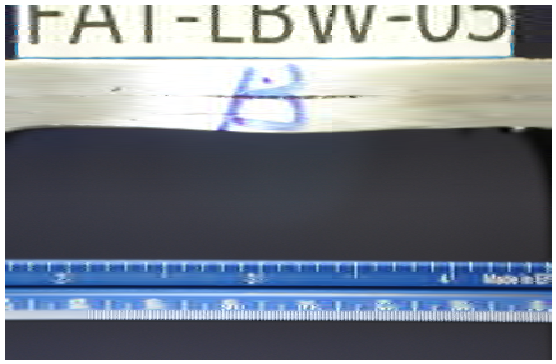

FAT-LBW-05 SIDE B STAKE WELD DETAIL

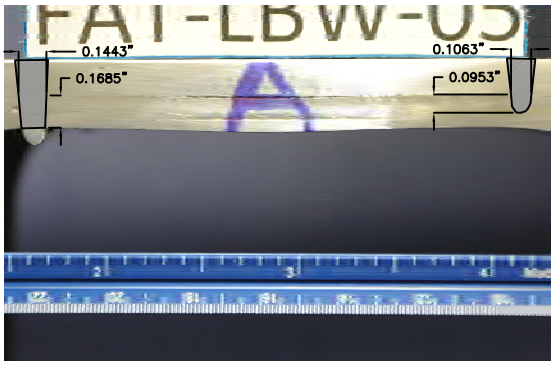

FAT-LBW-05 SIDE A STAKE WELD DETAIL INTERPOLATED DIMENSIONS

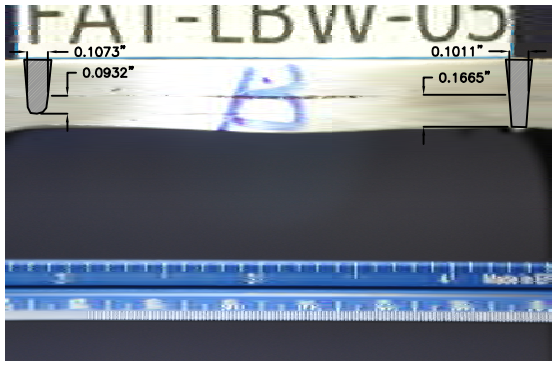

FAT-LBW-05 SIDE B STAKE WELD DETAIL INTERPOLATED DIMENSIONS

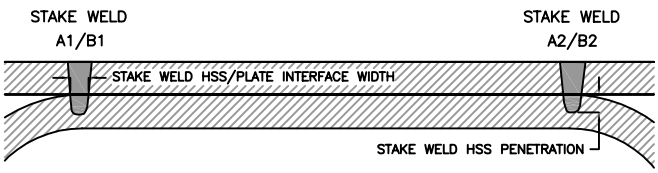

FIGURE REFERENCE

VIRGINIA POLYTECHNIC INSTITUTE AND STATE UNIVERSITY
BLACKSBURG, VIRGINIA

VirginiaTech VirginiaTech

FATIGUE SPECIMEN STAKE WELD DETAILS
LASER BEAM WELD TEST SPECIMEN: FAT-LBW-05
VIA DEPARTMENT OF CIVIL AND ENVIRONMENTAL ENGINEERING
BLACKSBURG, VIRGINIA

DESIGNED BY	G. Passarelli	3/31/2011	CHECKED BY	W.Wright	3/31/2011
DRAWN BY	G.Passarelli	3/31/2011	APPROVED BY	W.Wright	3/31/2011

SCALE:	DRAWING NO.	PROJECT NO.	SHEET NO.	REVISION NO.
1"=1"	FAT-LBW-05	SSP	---	--

LOCATION	DRAWN BY	CHECKED BY	APPROVED BY	DRAWING NUMBER
BLACKSBURG, VA	G.PASSARELLI 3/31/2011	W.WRIGHT 3/31/2011	W.WRIGHT 3/31/2011	FAT-LBW-05

PRODUCED BY AN AUTODESK EDUCATIONAL PRODUCT

STAKE WELD	STAKE WELD AREA	STAKE WELD HSS/PLATE INTERFACE WIDTH	STAKE WELD HSS PENETRATION DEPTH
(UNITS)	(sqin)	(in.)	(in.)
A1	0.0238	0.0764	0.1147
A2	0.0272	0.0900	0.1104
B1	0.0249	0.0808	0.1035
B2	0.0315	0.1054	0.1188

LEGEND

INTERPOLATED LASER STAKE WELD AREA

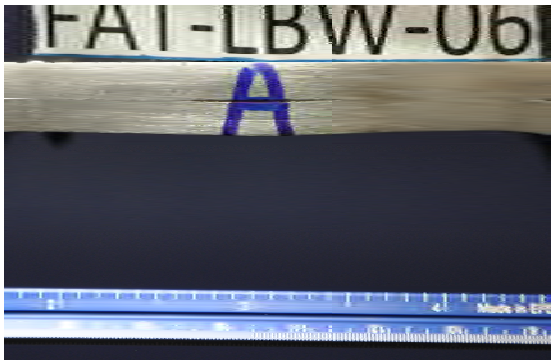

FAT–LBW–06 SIDE A STAKE WELD DETAIL

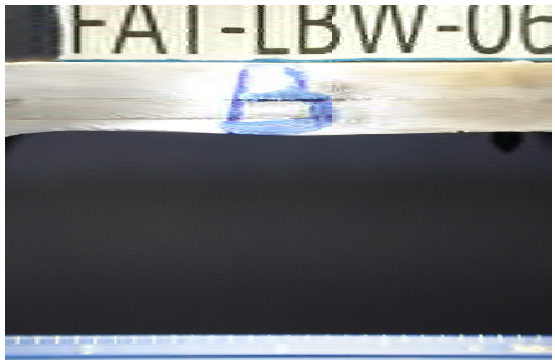

FAT–LBW–06 SIDE B STAKE WELD DETAIL

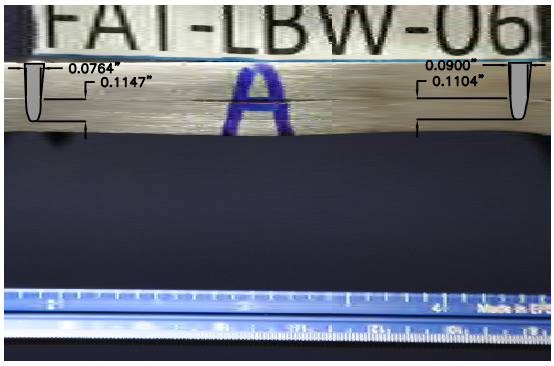

FAT–LBW–06 SIDE A STAKE WELD DETAIL INTERPOLATED DIMENSIONS

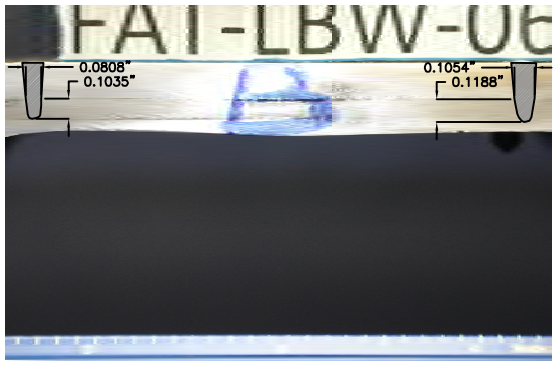

FAT–LBW–06 SIDE B STAKE WELD DETAIL INTERPOLATED DIMENSIONS

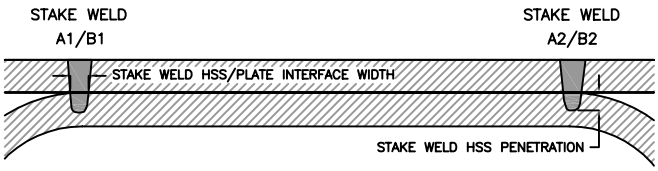

FIGURE REFERENCE

VIRGINIA POLYTECHNIC INSTITUTE AND STATE UNIVERSITY
BLACKSBURG, VIRGINIA

VirginiaTech VirginiaTech

FATIGUE SPECIMEN STAKE WELD DETAILS
LASER BEAM WELD TEST SPECIMEN: FAT-LBW-06
VIA DEPARTMENT OF CIVIL AND ENVIRONMENTAL ENGINEERING
BLACKSBURG, VIRGINIA

DESIGNED BY	G. Passarelli	3/31/2011	CHECKED BY	W.Wright	3/31/2011
DRAWN BY	G.Passarelli	3/31/2011	APPROVED BY	W.Wright	3/31/2011
SCALE: 1"=1"	DRAWING NO. FAT-LBW-06		PROJECT NO. SSP	SHEET NO. ---	REVISION NO. --

LOCATION	DRAWN BY		CHECKED BY		APPROVED BY		DRAWING NUMBER
BLACKSBURG, VA	G.PASSARELLI	3/31/2011	W.WRIGHT	3/31/2011	W.WRIGHT	3/31/2011	FAT-LBW-06

PRODUCED BY AN AUTODESK EDUCATIONAL PRODUCT

PRODUCED BY AN AUTODESK EDUCATIONAL PRODUCT

STAKE WELD	STAKE WELD AREA	STAKE WELD HSS/PLATE INTERFACE WIDTH	STAKE WELD HSS PENETRATION DEPTH
(UNITS)	(sqin)	(in.)	(in.)
A1	0.0276	0.0896	0.1174
A2	0.0240	0.0824	0.0831
B1	0.0271	0.0922	0.0893
B2	0.0268	0.0920	0.0815

LEGEND

INTERPOLATED LASER STAKE WELD AREA

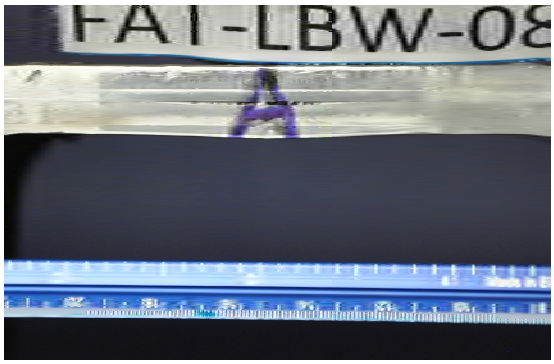

FAT–LBW–08 SIDE A STAKE WELD DETAIL

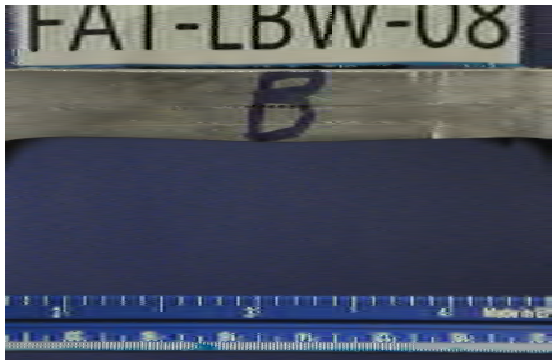

FAT–LBW–08 SIDE B STAKE WELD DETAIL

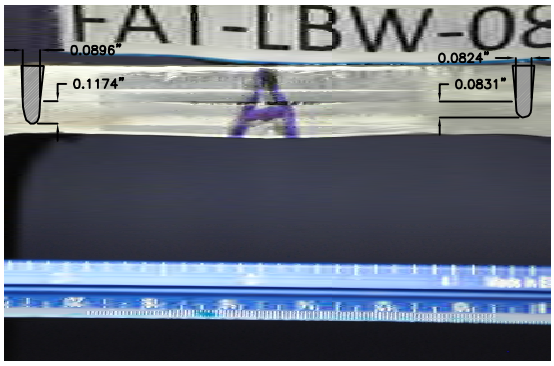

FAT–LBW–08 SIDE A STAKE WELD DETAIL INTERPOLATED DIMENSIONS

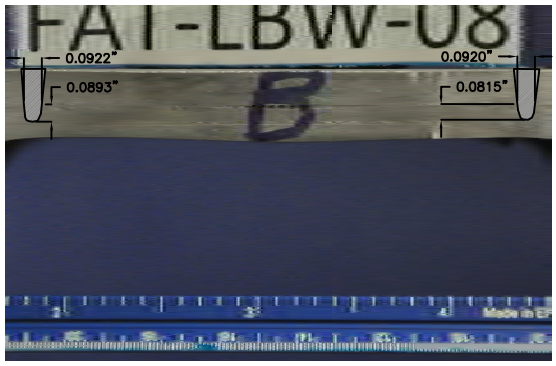

FAT–LBW–08 SIDE B STAKE WELD DETAIL INTERPOLATED DIMENSIONS

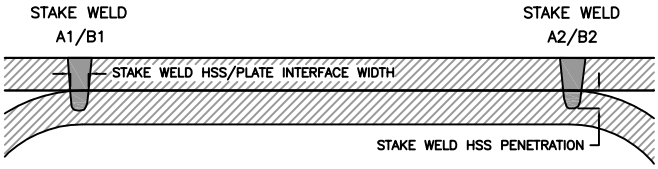

FIGURE REFERENCE

VIRGINIA POLYTECHNIC INSTITUTE AND STATE UNIVERSITY
BLACKSBURG, VIRGINIA

VirginiaTech VirginiaTech

FATIGUE SPECIMEN STAKE WELD DETAILS
LASER BEAM WELD TEST SPECIMEN: FAT-LBW-08
VIA DEPARTMENT OF CIVIL AND ENVIRONMENTAL ENGINEERING
BLACKSBURG, VIRGINIA

DESIGNED BY	G. Passarelli	3/31/2011	CHECKED BY	W.Wright	3/31/2011
DRAWN BY	G.Passarelli	3/31/2011	APPROVED BY	W.Wright	3/31/2011

SCALE:	DRAWING NO.	PROJECT NO.	SHEET NO.	REVISION NO.
1"=1"	FAT-LBW-08	SSP	---	--

LOCATION	DRAWN BY		CHECKED BY		APPROVED BY		DRAWING NUMBER
BLACKSBURG, VA	G.PASSARELLI	3/31/2011	W.WRIGHT	3/31/2011	W.WRIGHT	3/31/2011	FAT-LBW-08

PRODUCED BY AN AUTODESK EDUCATIONAL PRODUCT

PRODUCED BY AN AUTODESK EDUCATIONAL PRODUCT

STAKE WELD	STAKE WELD AREA	STAKE WELD HSS/PLATE INTERFACE WIDTH	STAKE WELD HSS PENETRATION DEPTH
(UNITS)	(sqin)	(in.)	(in.)
A1	0.0229	0.0808	0.0748
A2	0.0285	0.1023	0.0875
B1	0.0346	0.1267	0.0955
B2	0.0225	0.0719	0.0987

LEGEND

INTERPOLATED LASER STAKE WELD AREA

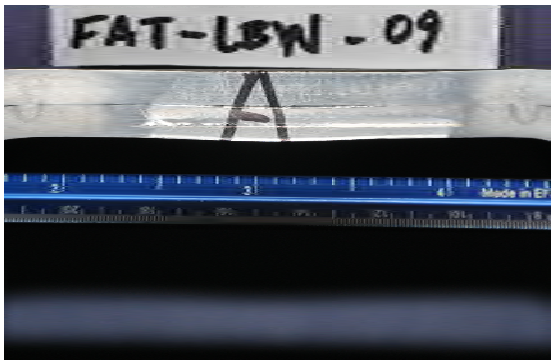

FAT–LBW–09 SIDE A STAKE WELD DETAIL

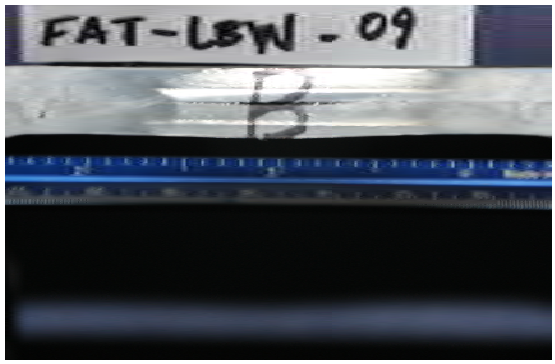

FAT–LBW–09 SIDE B STAKE WELD DETAIL

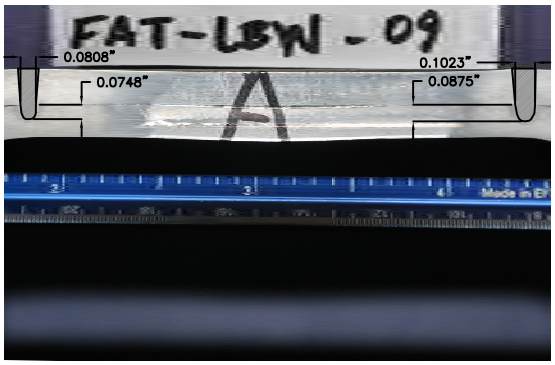

FAT–LBW–09 SIDE A STAKE WELD DETAIL INTERPOLATED DIMENSIONS

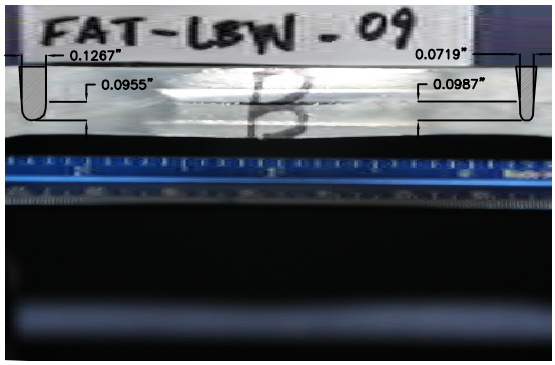

FAT–LBW–09 SIDE B STAKE WELD DETAIL INTERPOLATED DIMENSIONS

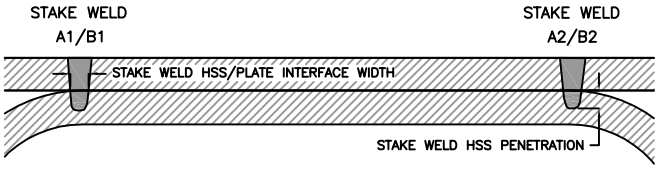

FIGURE REFERENCE

LOCATION	DRAWN BY		CHECKED BY		APPROVED BY		DRAWING NUMBER
BLACKSBURG, VA	G.PASSARELLI	4/9/2011	W.WRIGHT	4/9/2011	W.WRIGHT	4/9/2011	FAT-LBW-09

VIRGINIA POLYTECHNIC INSTITUTE AND STATE UNIVERSITY
BLACKSBURG, VIRGINIA

VirginiaTech VirginiaTech

FATIGUE SPECIMEN STAKE WELD DETAILS
LASER BEAM WELD TEST SPECIMEN: FAT-LBW-09
VIA DEPARTMENT OF CIVIL AND ENVIRONMENTAL ENGINEERING
BLACKSBURG, VIRGINIA

DESIGNED BY	G. Passarelli	4/9/2011	CHECKED BY	W.Wright	4/9/2011
DRAWN BY	G.Passarelli	4/9/2011	APPROVED BY	W.Wright	4/9/2011

SCALE:	DRAWING NO.	PROJECT NO.	SHEET NO.	REVISION NO.
1"=1"	FAT-LBW-09	SSP	---	--

PRODUCED BY AN AUTODESK EDUCATIONAL PRODUCT

PRODUCED BY AN AUTODESK EDUCATIONAL PRODUCT

STAKE WELD	STAKE WELD AREA	STAKE WELD HSS/PLATE INTERFACE WIDTH	STAKE WELD HSS PENETRATION DEPTH
(UNITS)	(sqin)	(in.)	(in.)
A1	0.0241	0.0809	0.0848
A2	0.0293	0.0911	0.1064
B1	0.0303	0.0882	0.0970
B2	0.0297	0.0941	0.0929

LEGEND

INTERPOLATED LASER STAKE WELD AREA

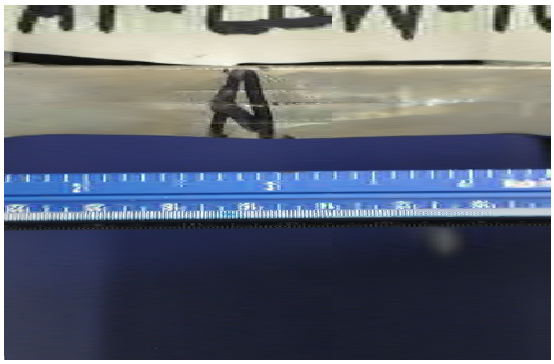

FAT–LBW–10 SIDE A STAKE WELD DETAIL

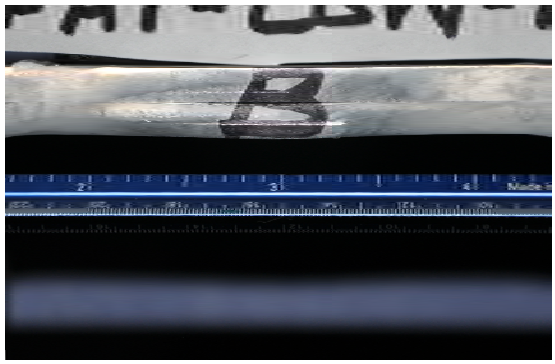

FAT–LBW–10 SIDE B STAKE WELD DETAIL

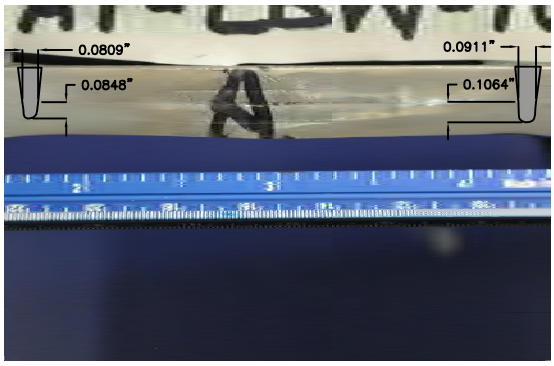

FAT–LBW–10 SIDE A STAKE WELD DETAIL INTERPOLATED DIMENSIONS

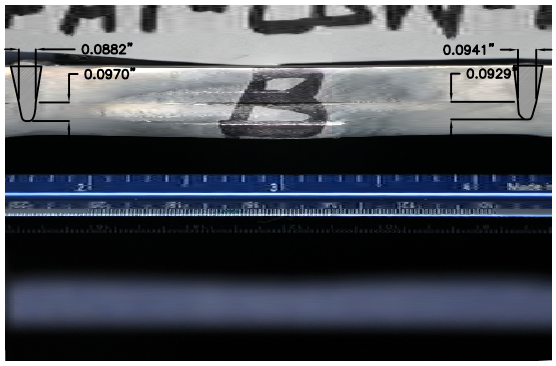

FAT–LBW–10 SIDE B STAKE WELD DETAIL INTERPOLATED DIMENSIONS

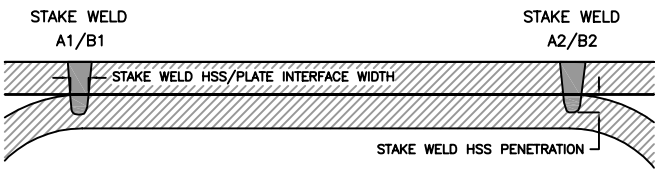

FIGURE REFERENCE

LOCATION	DRAWN BY		CHECKED BY		APPROVED BY		DRAWING NUMBER
BLACKSBURG, VA	G.PASSARELLI	3/31/2011	W.WRIGHT	3/31/2011	W.WRIGHT	3/31/2011	FAT-LBW-10

VIRGINIA POLYTECHNIC INSTITUTE AND STATE UNIVERSITY
BLACKSBURG, VIRGINIA

VirginiaTech VirginiaTech

FATIGUE SPECIMEN STAKE WELD DETAILS
LASER BEAM WELD TEST SPECIMEN: FAT-LBW-10
VIA DEPARTMENT OF CIVIL AND ENVIRONMENTAL ENGINEERING
BLACKSBURG, VIRGINIA

DESIGNED BY	G. Passarelli	3/31/2011	CHECKED BY	W.Wright	3/31/2011
DRAWN BY	G.Passarelli	3/31/2011	APPROVED BY	W.Wright	3/31/2011

SCALE:	DRAWING NO.	PROJECT NO.	SHEET NO.	REVISION NO.
1"=1"	FAT-LBW-10	SSP	---	--

PRODUCED BY AN AUTODESK EDUCATIONAL PRODUCT

PRODUCED BY AN AUTODESK EDUCATIONAL PRODUCT

STAKE WELD	STAKE WELD AREA	STAKE WELD HSS/PLATE INTERFACE WIDTH	STAKE WELD HSS PENETRATION DEPTH
(UNITS)	(sqin)	(in.)	(in.)
A1	0.0262	0.0935	0.0741
A2	0.0243	0.0817	0.0876
B1	0.0262	0.0961	0.0803
B2	0.0236	0.0851	0.0784

LEGEND

INTERPOLATED LASER STAKE WELD AREA

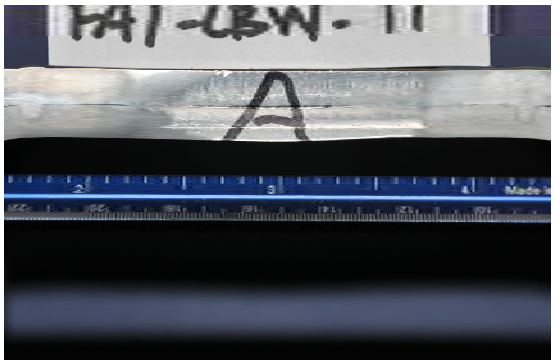

FAT–LBW–11 SIDE A STAKE WELD DETAIL

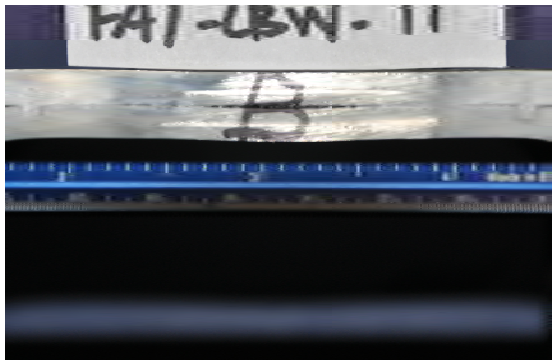

FAT–LBW–11 SIDE B STAKE WELD DETAIL

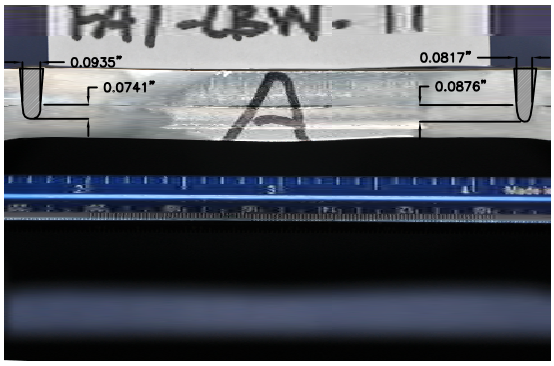

FAT–LBW–11 SIDE A STAKE WELD DETAIL INTERPOLATED DIMENSIONS

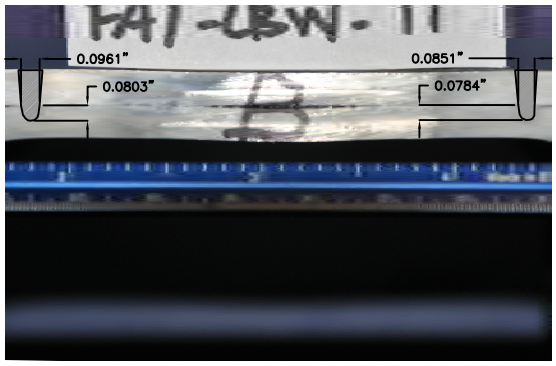

FAT–LBW–11 SIDE B STAKE WELD DETAIL INTERPOLATED DIMENSIONS

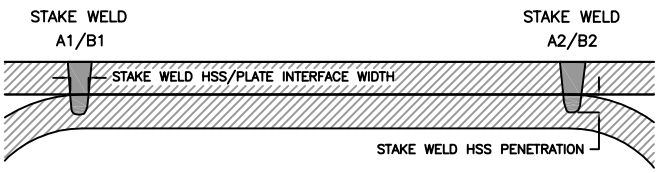

FIGURE REFERENCE

LOCATION	DRAWN BY	CHECKED BY	APPROVED BY	DRAWING NUMBER
BLACKSBURG, VA	G.PASSARELLI 4/9/2011	W.WRIGHT 4/9/2011	W.WRIGHT 4/9/2011	FAT-LBW-11

VIRGINIA POLYTECHNIC INSTITUTE AND STATE UNIVERSITY
BLACKSBURG, VIRGINIA

VirginiaTech VirginiaTech

FATIGUE SPECIMEN STAKE WELD DETAILS
LASER BEAM WELD TEST SPECIMEN: FAT-LBW-11
VIA DEPARTMENT OF CIVIL AND ENVIRONMENTAL ENGINEERING
BLACKSBURG, VIRGINIA

DESIGNED BY	G. Passarelli	4/9/2011	CHECKED BY	W.Wright	4/9/2011
DRAWN BY	G.Passarelli	4/9/2011	APPROVED BY	W.Wright	4/9/2011

SCALE:	DRAWING NO.	PROJECT NO.	SHEET NO.	REVISION NO.
1"=1"	FAT-LBW-11	SSP	---	--

PRODUCED BY AN AUTODESK EDUCATIONAL PRODUCT

PRODUCED BY AN AUTODESK EDUCATIONAL PRODUCT

STAKE WELD	STAKE WELD AREA	STAKE WELD HSS/PLATE INTERFACE WIDTH	STAKE WELD HSS PENETRATION DEPTH	STAKE WELD HLAW SURPLUS HEIGHT
(UNITS)	(sqin)	(in.)	(in.)	(in.)
A1	0.0225	0.0627	0.0834	0.0536
A2	0.0278	0.0788	0.1088	0.0592
B1	0.0266	0.0801	0.0971	0.0506
B2	0.0305	0.0928	0.0998	0.0507

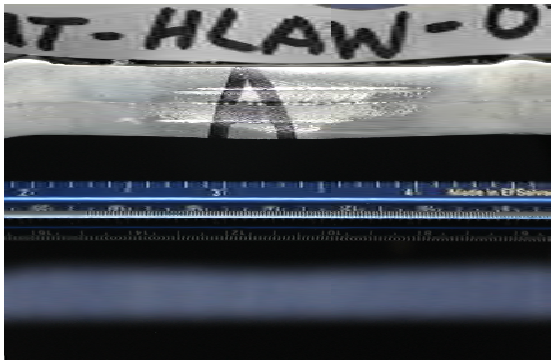

FAT–HLAW–01 SIDE A STAKE WELD DETAIL

FAT–HLAW–01 SIDE B STAKE WELD DETAIL

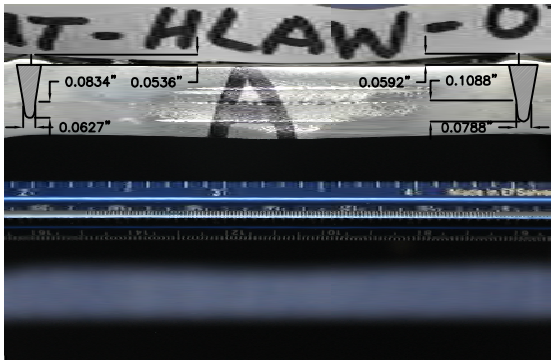

FAT–HLAW–01 SIDE A STAKE WELD DETAIL INTERPOLATED DIMENSIONS

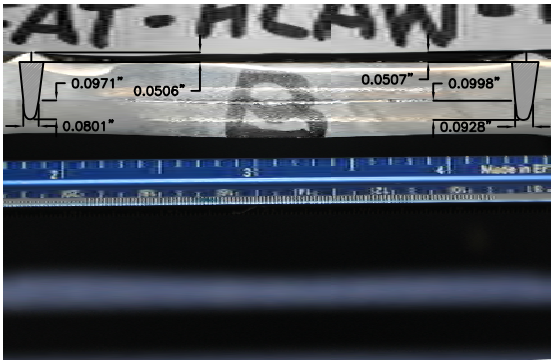

FAT–HLAW–01 SIDE B STAKE WELD DETAIL INTERPOLATED DIMENSIONS

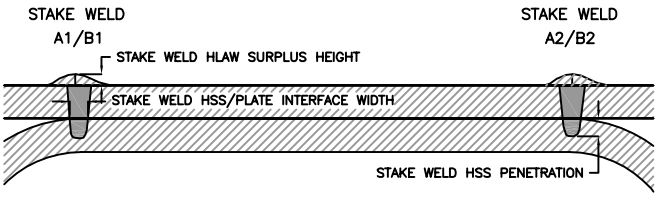

FIGURE REFERENCE

LEGEND

INTERPOLATED LASER STAKE WELD AREA

VIRGINIA POLYTECHNIC INSTITUTE AND STATE UNIVERSITY
BLACKSBURG, VIRGINIA

VirginiaTech VirginiaTech

FATIGUE SPECIMEN STAKE WELD DETAILS
HYBRID LASER ARC WELD TEST SPECIMEN: FAT-HLAW-01
VIA DEPARTMENT OF CIVIL AND ENVIRONMENTAL ENGINEERING
BLACKSBURG, VIRGINIA

DESIGNED BY	G.Passarelli	4/1/2011	CHECKED BY	W.Wright	4/1/2011
DRAWN BY	G.Passarelli	4/1/2011	APPROVED BY	W.Wright	4/1/2011
SCALE: 1"=1"	DRAWING NO. FAT-HLAW-01	PROJECT NO. SSP	SHEET NO. ---	REVISION NO. --	

LOCATION	DRAWN BY		CHECKED BY		APPROVED BY		DRAWING NUMBER
BLACKSBURG, VA	G.PASSARELLI	4/1/2011	W.WRIGHT	4/1/2011	W.WRIGHT	4/1/2011	FAT-HLAW-01

PRODUCED BY AN AUTODESK EDUCATIONAL PRODUCT

PRODUCED BY AN AUTODESK EDUCATIONAL PRODUCT

STAKE WELD	STAKE WELD AREA	STAKE WELD HSS/PLATE INTERFACE WIDTH	STAKE WELD HSS PENETRATION DEPTH	STAKE WELD HLAW SURPLUS HEIGHT
(UNITS)	(sqin)	(in.)	(in.)	(in.)
A1	0.0204	0.0694	0.0655	0.0606
A2	0.0246	0.0777	0.0860	0.0619
B1	0.0235	0.0713	0.0791	0.0632
B2	0.0220	0.0969	0.0670	0.0609

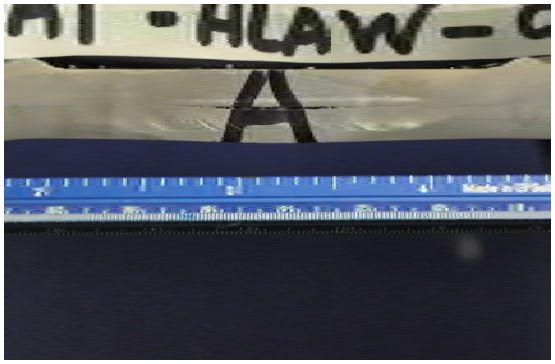

FAT-HLAW-02 SIDE A STAKE WELD DETAIL

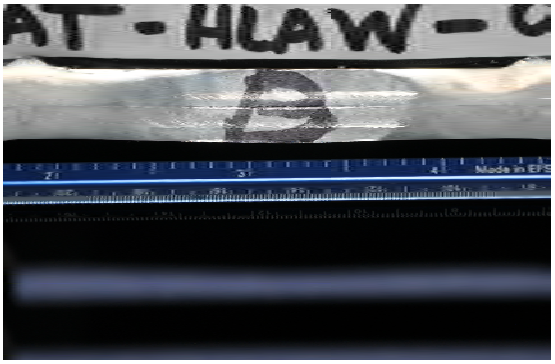

FAT-HLAW-02 SIDE B STAKE WELD DETAIL

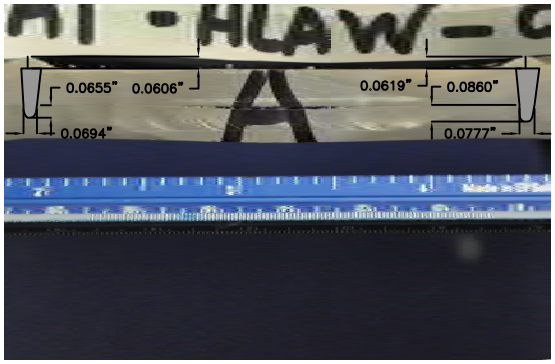

FAT-HLAW-02 SIDE A STAKE WELD DETAIL INTERPOLATED DIMENSIONS

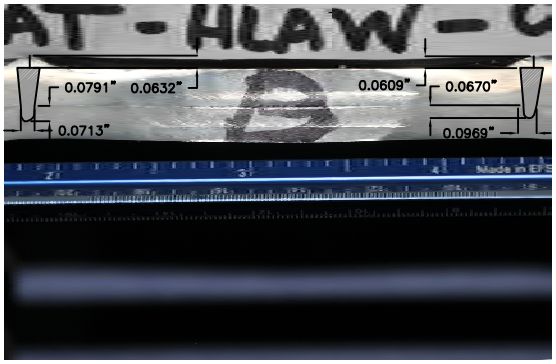

FAT-HLAW-02 SIDE B STAKE WELD DETAIL INTERPOLATED DIMENSIONS

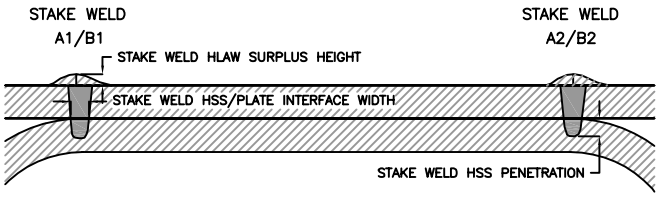

FIGURE REFERENCE

LEGEND

INTERPOLATED LASER STAKE WELD AREA

VIRGINIA POLYTECHNIC INSTITUTE AND STATE UNIVERSITY
BLACKSBURG, VIRGINIA

FATIGUE SPECIMEN STAKE WELD DETAILS
HYBRID LASER ARC WELD TEST SPECIMEN: FAT-HLAW-02
VIA DEPARTMENT OF CIVIL AND ENVIRONMENTAL ENGINEERING
BLACKSBURG, VIRGINIA

DESIGNED BY	G.Passarelli	4/1/2011	CHECKED BY	W.Wright	4/1/2011
DRAWN BY	G.Passarelli	4/1/2011	APPROVED BY	W.Wright	4/1/2011

SCALE:	DRAWING NO.	PROJECT NO.	SHEET NO.	REVISION NO.
1"=1"	FAT-HLAW-02	SSP	---	--

LOCATION	DRAWN BY		CHECKED BY		APPROVED BY		DRAWING NUMBER
BLACKSBURG, VA	G.PASSARELLI	4/1/2011	W.WRIGHT	4/1/2011	W.WRIGHT	4/1/2011	FAT-HLAW-02

PRODUCED BY AN AUTODESK EDUCATIONAL PRODUCT

STAKE WELD	STAKE WELD AREA	STAKE WELD HSS/PLATE INTERFACE WIDTH	STAKE WELD HSS PENETRATION DEPTH	STAKE WELD HLAW SURPLUS HEIGHT
(UNITS)	(sqin)	(in.)	(in.)	(in.)
A1	0.0204	0.0646	0.0902	0.0603
A2	0.0189	0.0596	0.0789	0.0642
B1	0.0193	0.0672	0.0749	0.0598
B2	0.0203	0.0640	0.0953	0.0654

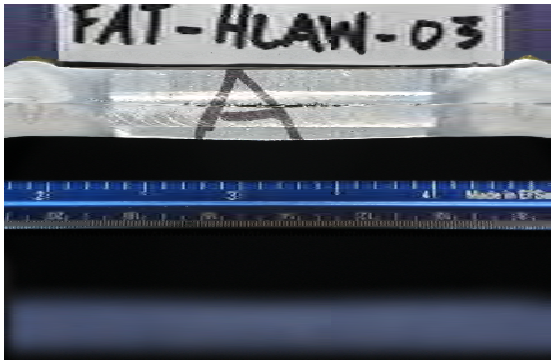

FAT–HLAW–03 SIDE A STAKE WELD DETAIL

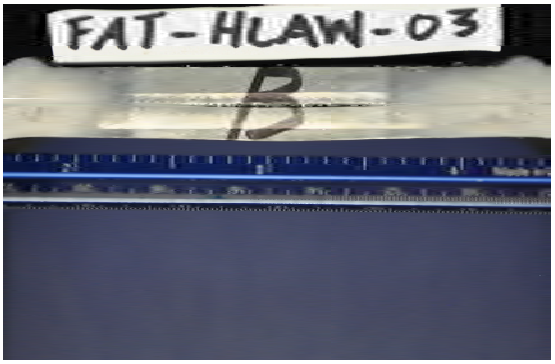

FAT–HLAW–03 SIDE B STAKE WELD DETAIL

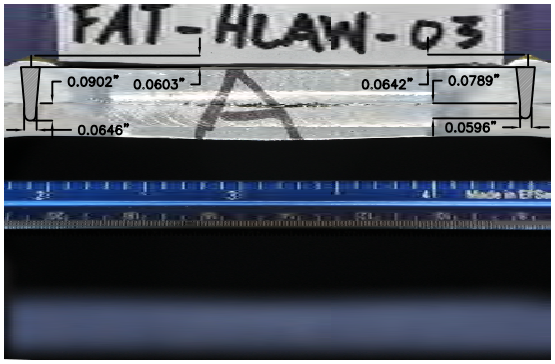

FAT–HLAW–03 SIDE A STAKE WELD DETAIL INTERPOLATED DIMENSIONS

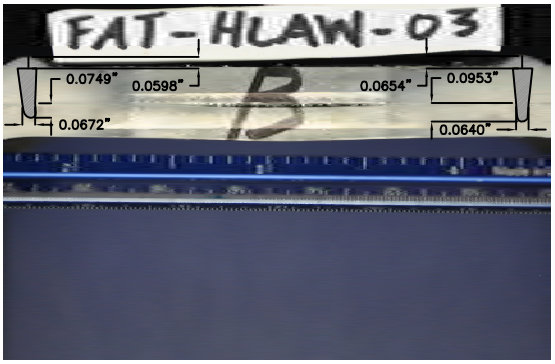

FAT–HLAW–03 SIDE B STAKE WELD DETAIL INTERPOLATED DIMENSIONS

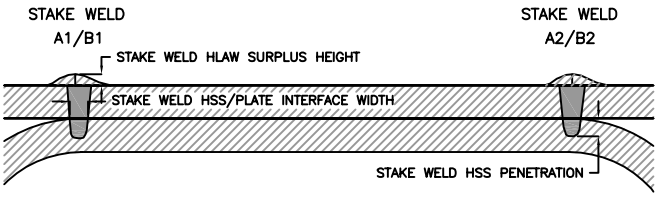

FIGURE REFERENCE

LEGEND

INTERPOLATED LASER STAKE WELD AREA

VIRGINIA POLYTECHNIC INSTITUTE AND STATE UNIVERSITY
BLACKSBURG, VIRGINIA

FATIGUE SPECIMEN STAKE WELD DETAILS
HYBRID LASER ARC WELD TEST SPECIMEN: FAT-HLAW-03
VIA DEPARTMENT OF CIVIL AND ENVIRONMENTAL ENGINEERING
BLACKSBURG, VIRGINIA

DESIGNED BY	G.Passarelli	4/9/2011	CHECKED BY	W.Wright	4/9/2011
DRAWN BY	G.Passarelli	4/9/2011	APPROVED BY	W.Wright	4/9/2011

SCALE:	DRAWING NO.	PROJECT NO.	SHEET NO.	REVISION NO.
1"=1"	FAT-HLAW-03	SSP	---	--

LOCATION	DRAWN BY		CHECKED BY		APPROVED BY		DRAWING NUMBER
BLACKSBURG, VA	G.PASSARELLI	4/9/2011	W.WRIGHT	4/9/2011	W.WRIGHT	4/9/2011	FAT-HLAW-03

PRODUCED BY AN AUTODESK EDUCATIONAL PRODUCT

STAKE WELD	STAKE WELD AREA	STAKE WELD HSS/PLATE INTERFACE WIDTH	STAKE WELD HSS PENETRATION DEPTH	STAKE WELD HLAW SURPLUS HEIGHT
(UNITS)	(sqin)	(in.)	(in.)	(in.)
A1	0.0197	0.0680	0.0766	0.0654
A2	0.0213	0.0672	0.0833	0.0706
B1	0.0210	0.0578	0.0841	0.0535
B2	0.0245	0.0680	0.0905	0.0540

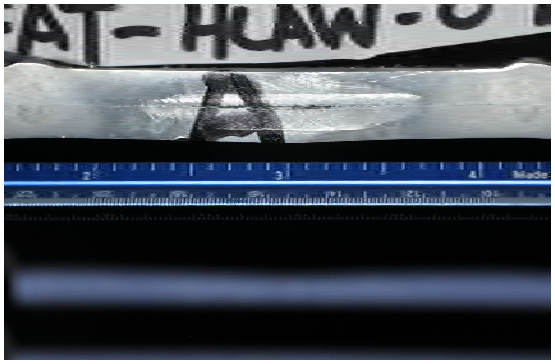

FAT-HLAW-04 SIDE A STAKE WELD DETAIL

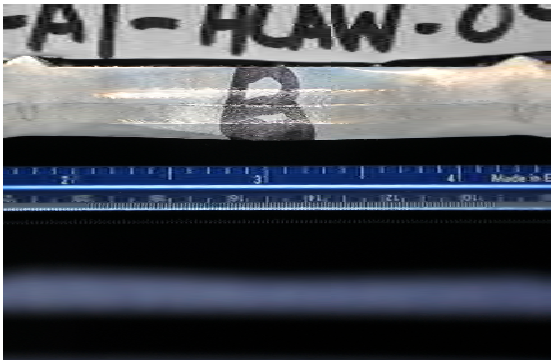

FAT-HLAW-04 SIDE B STAKE WELD DETAIL

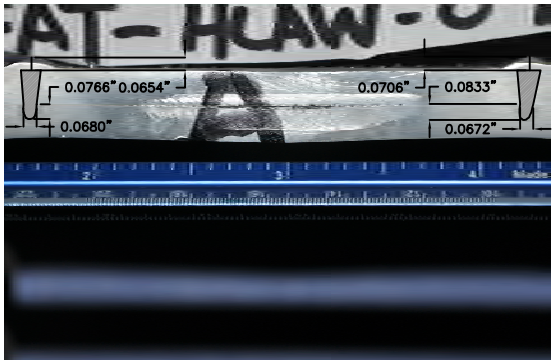

FAT-HLAW-04 SIDE A STAKE WELD DETAIL INTERPOLATED DIMENSIONS

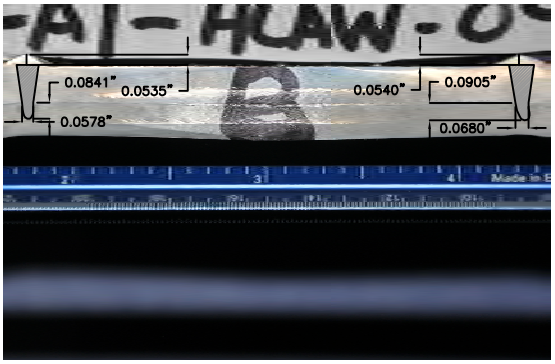

FAT-HLAW-04 SIDE B STAKE WELD DETAIL INTERPOLATED DIMENSIONS

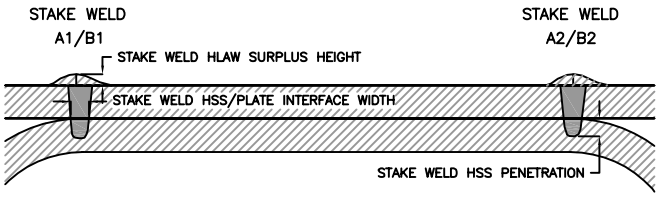

FIGURE REFERENCE

LEGEND

INTERPOLATED LASER STAKE WELD AREA

LOCATION	DRAWN BY		CHECKED BY		APPROVED BY		DRAWING NUMBER
BLACKSBURG, VA	G.PASSARELLI	4/1/2011	W.WRIGHT	4/1/2011	W.WRIGHT	4/1/2011	FAT-HLAW-04

VIRGINIA POLYTECHNIC INSTITUTE AND STATE UNIVERSITY
BLACKSBURG, VIRGINIA

VirginiaTech VirginiaTech

FATIGUE SPECIMEN STAKE WELD DETAILS
HYBRID LASER ARC WELD TEST SPECIMEN: FAT-HLAW-04
VIA DEPARTMENT OF CIVIL AND ENVIRONMENTAL ENGINEERING
BLACKSBURG, VIRGINIA

DESIGNED BY	G.Passarelli	4/1/2011	CHECKED BY	W.Wright	4/1/2011
DRAWN BY	G.Passarelli	4/1/2011	APPROVED BY	W.Wright	4/1/2011

SCALE:	DRAWING NO.	PROJECT NO.	SHEET NO.	REVISION NO.
1"=1"	FAT-HLAW-04	SSP	---	--

PRODUCED BY AN AUTODESK EDUCATIONAL PRODUCT

PRODUCED BY AN AUTODESK EDUCATIONAL PRODUCT

STAKE WELD	STAKE WELD AREA	STAKE WELD HSS/PLATE INTERFACE WIDTH	STAKE WELD HSS PENETRATION DEPTH	STAKE WELD HLAW SURPLUS HEIGHT
(UNITS)	(sqin)	(in.)	(in.)	(in.)
A1	0.0193	0.0567	0.0951	0.0549
A2	0.0152	0.0507	0.0677	0.0673
B1	0.0206	0.0674	0.0779	0.0571
B2	0.0210	0.0662	0.0943	0.0541

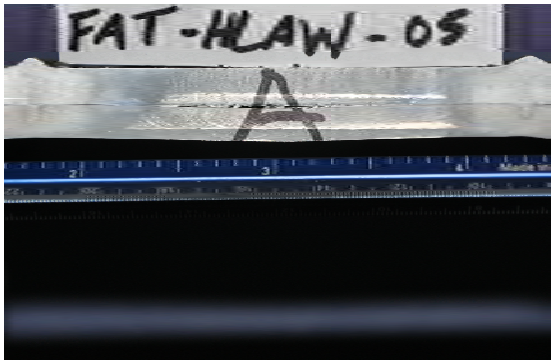

FAT–HLAW–05 SIDE A STAKE WELD DETAIL

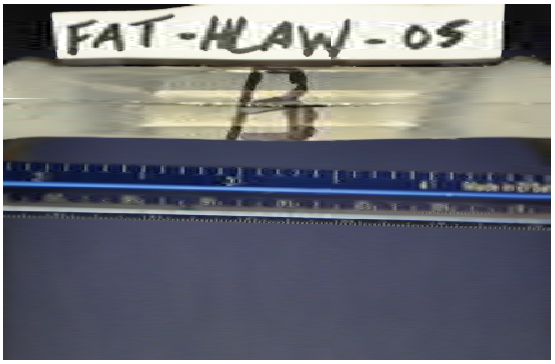

FAT–HLAW–05 SIDE B STAKE WELD DETAIL

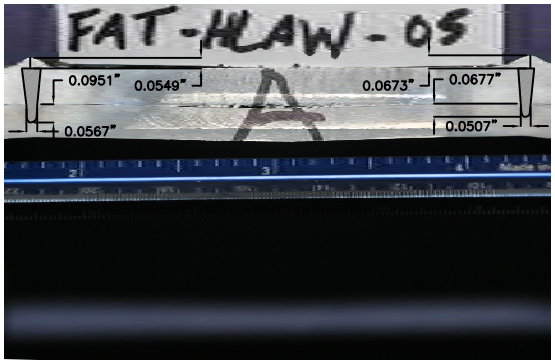

FAT–HLAW–05 SIDE A STAKE WELD DETAIL INTERPOLATED DIMENSIONS

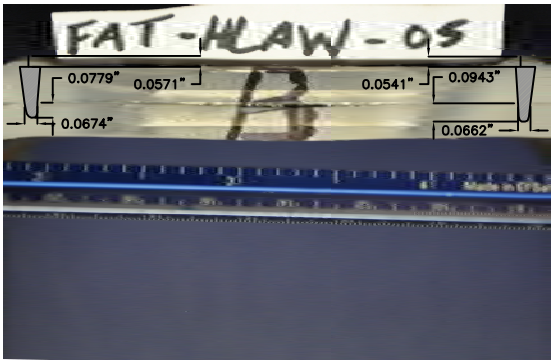

FAT–HLAW–05 SIDE B STAKE WELD DETAIL INTERPOLATED DIMENSIONS

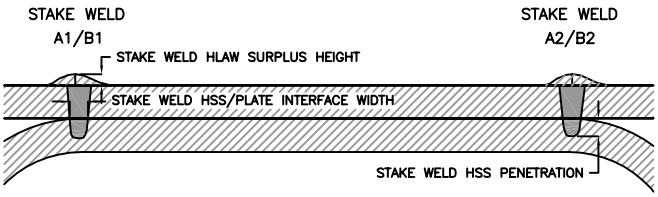

FIGURE REFERENCE

LEGEND

INTERPOLATED LASER STAKE WELD AREA

VIRGINIA POLYTECHNIC INSTITUTE AND STATE UNIVERSITY
BLACKSBURG, VIRGINIA

VirginiaTech VirginiaTech

FATIGUE SPECIMEN STAKE WELD DETAILS
HYBRID LASER ARC WELD TEST SPECIMEN: FAT-HLAW-05
VIA DEPARTMENT OF CIVIL AND ENVIRONMENTAL ENGINEERING
BLACKSBURG, VIRGINIA

DESIGNED BY	G.Passarelli	4/9/2011	CHECKED BY	W.Wright	4/9/2011
DRAWN BY	G.Passarelli	4/9/2011	APPROVED BY	W.Wright	4/9/2011
SCALE: 1"=1"	DRAWING NO. FAT-HLAW-05	PROJECT NO. SSP	SHEET NO. ---	REVISION NO. --	

LOCATION	DRAWN BY		CHECKED BY		APPROVED BY		DRAWING NUMBER
BLACKSBURG, VA	G.PASSARELLI	4/9/2011	W.WRIGHT	4/9/2011	W.WRIGHT	4/9/2011	FAT-HLAW-05

PRODUCED BY AN AUTODESK EDUCATIONAL PRODUCT

PRODUCED BY AN AUTODESK EDUCATIONAL PRODUCT

STAKE WELD	STAKE WELD AREA	STAKE WELD HSS/PLATE INTERFACE WIDTH	STAKE WELD HSS PENETRATION DEPTH	STAKE WELD HLAW SURPLUS HEIGHT
(UNITS)	(sqin)	(in.)	(in.)	(in.)
A1	0.0267	0.0889	0.0982	0.0518
A2	0.0274	0.0806	0.1352	0.0506
B1	0.0240	0.0669	0.1152	0.0509
B2	0.0218	0.0628	0.1083	0.0584

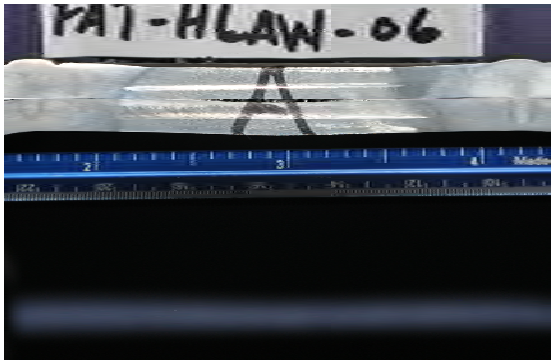

FAT–HLAW–06 SIDE A STAKE WELD DETAIL

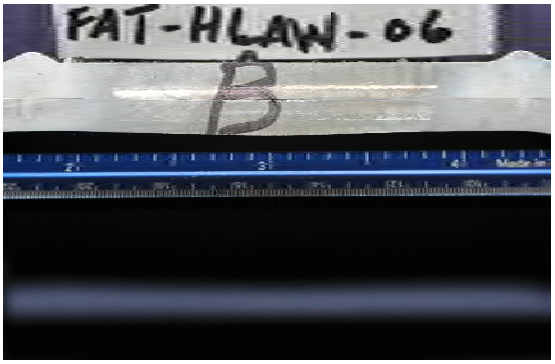

FAT–HLAW–06 SIDE B STAKE WELD DETAIL

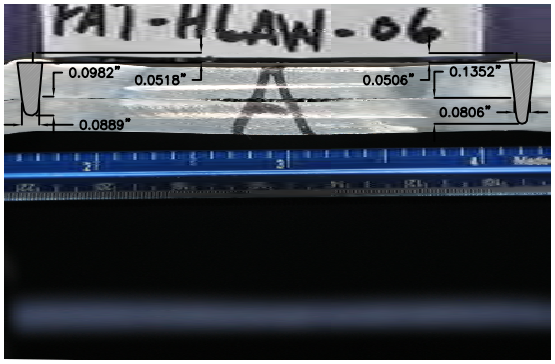

FAT–HLAW–06 SIDE A STAKE WELD DETAIL INTERPOLATED DIMENSIONS

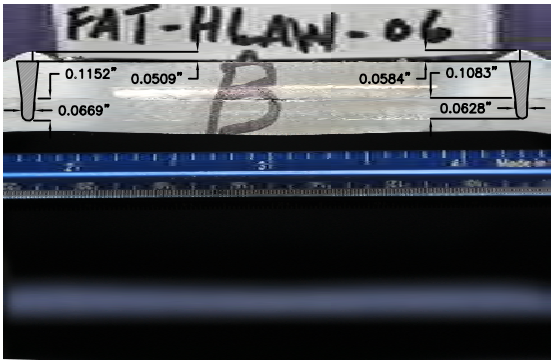

FAT–HLAW–06 SIDE B STAKE WELD DETAIL INTERPOLATED DIMENSIONS

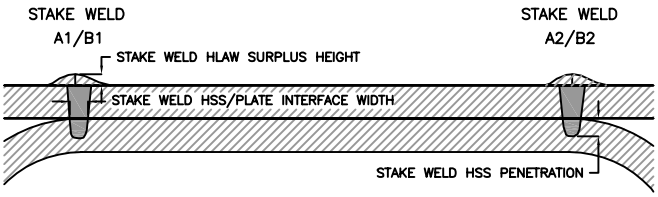

FIGURE REFERENCE

LEGEND

INTERPOLATED LASER STAKE WELD AREA

LOCATION	DRAWN BY		CHECKED BY		APPROVED BY		DRAWING NUMBER
BLACKSBURG, VA	G.PASSARELLI	4/9/2011	W.WRIGHT	4/9/2011	W.WRIGHT	4/9/2011	FAT-HLAW-06

VIRGINIA POLYTECHNIC INSTITUTE AND STATE UNIVERSITY
BLACKSBURG, VIRGINIA

VirginiaTech VirginiaTech

FATIGUE SPECIMEN STAKE WELD DETAILS
HYBRID LASER ARC WELD TEST SPECIMEN: FAT-HLAW-06
VIA DEPARTMENT OF CIVIL AND ENVIRONMENTAL ENGINEERING
BLACKSBURG, VIRGINIA

DESIGNED BY	G.Passarelli	4/9/2011	CHECKED BY	W.Wright	4/9/2011
DRAWN BY	G.Passarelli	4/9/2011	APPROVED BY	W.Wright	4/9/2011

SCALE:	DRAWING NO.	PROJECT NO.	SHEET NO.	REVISION NO.
1"=1"	FAT-HLAW-06	SSP	---	--

STAKE WELD	STAKE WELD AREA	STAKE WELD HSS/PLATE INTERFACE WIDTH	STAKE WELD HSS PENETRATION DEPTH	STAKE WELD HLAW SURPLUS HEIGHT
(UNITS)	(sqin)	(in.)	(in.)	(in.)
A1	0.0215	0.0672	0.1020	0.0646
A2	0.0209	0.0651	0.1071	0.0645
B1	0.0231	0.0656	0.1041	0.0523
B2	0.0202	0.0598	0.0731	0.0564

FAT-HLAW-07 SIDE A STAKE WELD DETAIL

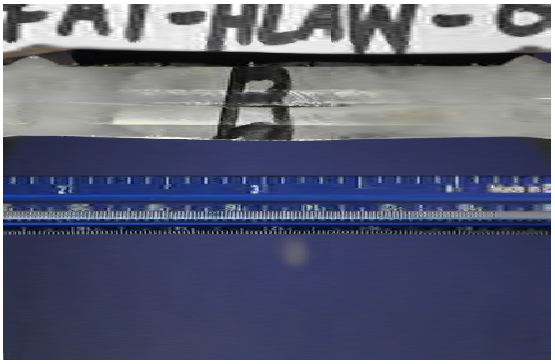

FAT-HLAW-07 SIDE B STAKE WELD DETAIL

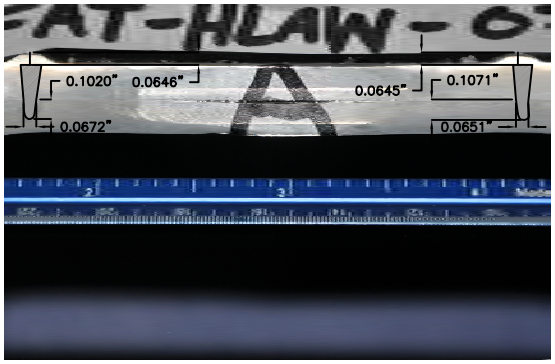

FAT-HLAW-07 SIDE A STAKE WELD DETAIL INTERPOLATED DIMENSIONS

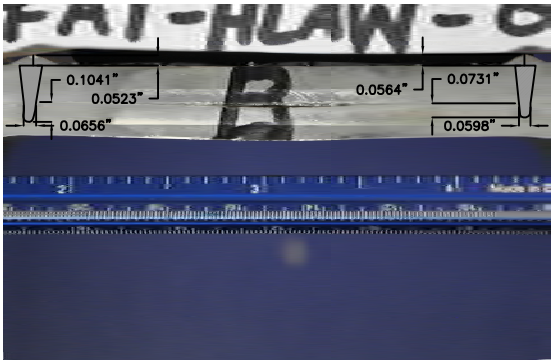

FAT-HLAW-07 SIDE B STAKE WELD DETAIL INTERPOLATED DIMENSIONS

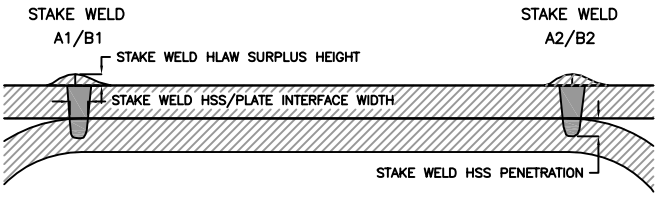

FIGURE REFERENCE

LEGEND

INTERPOLATED LASER STAKE WELD AREA

VIRGINIA POLYTECHNIC INSTITUTE AND STATE UNIVERSITY
BLACKSBURG, VIRGINIA

FATIGUE SPECIMEN STAKE WELD DETAILS
HYBRID LASER ARC WELD TEST SPECIMEN: FAT-HLAW-07
VIA DEPARTMENT OF CIVIL AND ENVIRONMENTAL ENGINEERING
BLACKSBURG, VIRGINIA

DESIGNED BY	G.Passarelli	4/3/2011	CHECKED BY	W.Wright	4/3/2011
DRAWN BY	G.Passarelli	4/3/2011	APPROVED BY	W.Wright	4/3/2011

SCALE:	DRAWING NO.	PROJECT NO.	SHEET NO.	REVISION NO.
1"=1"	FAT-HLAW-07	SSP	---	--

LOCATION	DRAWN BY		CHECKED BY		APPROVED BY		DRAWING NUMBER
BLACKSBURG, VA	G.PASSARELLI	4/3/2011	W.WRIGHT	4/3/2011	W.WRIGHT	4/3/2011	FAT-HLAW-07

PRODUCED BY AN AUTODESK EDUCATIONAL PRODUCT

STAKE WELD	STAKE WELD AREA	STAKE WELD HSS/PLATE INTERFACE WIDTH	STAKE WELD HSS PENETRATION DEPTH	STAKE WELD HLAW SURPLUS HEIGHT
(UNITS)	(sqin)	(in.)	(in.)	(in.)
A1	0.0170	0.0549	0.0655	0.0691
A2	0.0215	0.0671	0.0963	0.0535
B1	0.0244	0.0705	0.0985	0.0481
B2	0.0213	0.0722	0.0592	0.0562

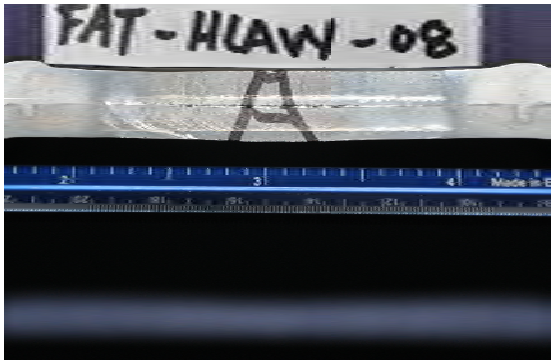

FAT–HLAW–08 SIDE A STAKE WELD DETAIL

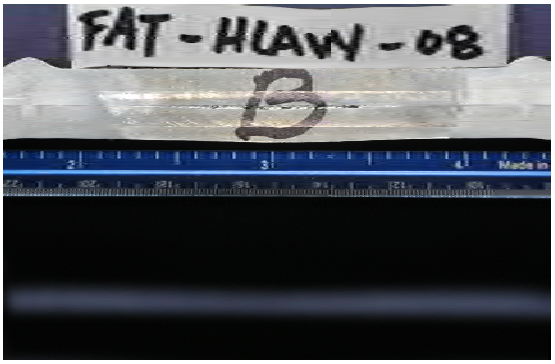

FAT–HLAW–08 SIDE B STAKE WELD DETAIL

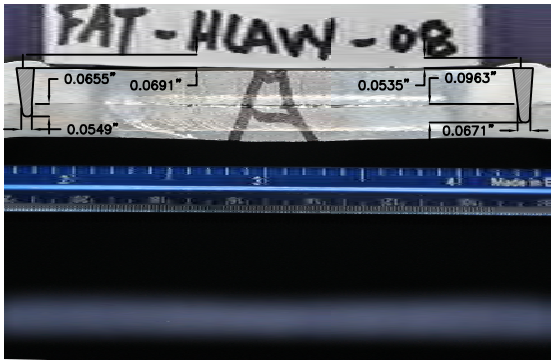

FAT–HLAW–08 SIDE A STAKE WELD DETAIL INTERPOLATED DIMENSIONS

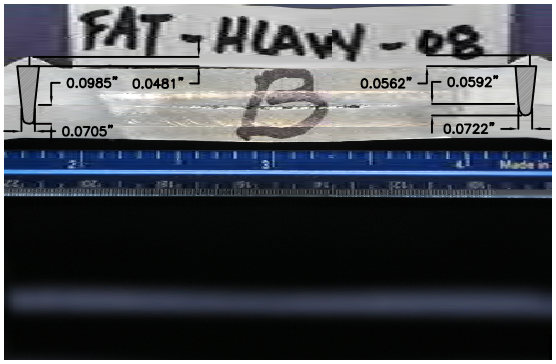

FAT–HLAW–08 SIDE B STAKE WELD DETAIL INTERPOLATED DIMENSIONS

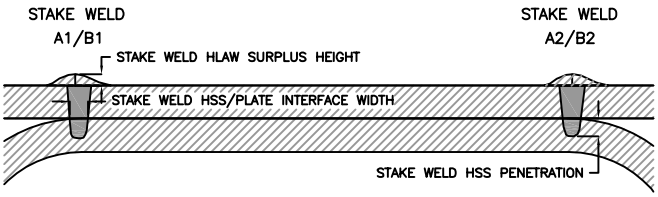

FIGURE REFERENCE

LEGEND

INTERPOLATED LASER STAKE WELD AREA

LOCATION	DRAWN BY		CHECKED BY		APPROVED BY	
BLACKSBURG, VA	G.PASSARELLI	4/9/2011	W.WRIGHT	4/9/2011	W.WRIGHT	4/9/2011

DRAWING NUMBER: FAT-HLAW-08

VIRGINIA POLYTECHNIC INSTITUTE AND STATE UNIVERSITY
BLACKSBURG, VIRGINIA

VirginiaTech VirginiaTech

FATIGUE SPECIMEN STAKE WELD DETAILS
HYBRID LASER ARC WELD TEST SPECIMEN: FAT-HLAW-08
VIA DEPARTMENT OF CIVIL AND ENVIRONMENTAL ENGINEERING
BLACKSBURG, VIRGINIA

DESIGNED BY	G.Passarelli	4/9/2011	CHECKED BY	W.Wright	4/9/2011
DRAWN BY	G.Passarelli	4/9/2011	APPROVED BY	W.Wright	4/9/2011

SCALE:	DRAWING NO.	PROJECT NO.	SHEET NO.	REVISION NO.
1"=1"	FAT-HLAW-08	SSP	---	--

PRODUCED BY AN AUTODESK EDUCATIONAL PRODUCT

PRODUCED BY AN AUTODESK EDUCATIONAL PRODUCT

STAKE WELD	STAKE WELD AREA	STAKE WELD HSS/PLATE INTERFACE WIDTH	STAKE WELD HSS PENETRATION DEPTH	STAKE WELD HLAW SURPLUS HEIGHT
(UNITS)	(sqin)	(in.)	(in.)	(in.)
A1	0.0233	0.0686	0.1264	0.0711
A2	0.0208	0.0638	0.0899	0.0628
B1	0.0217	0.0626	0.0840	0.0580
B2	0.0247	0.0689	0.1137	0.0530

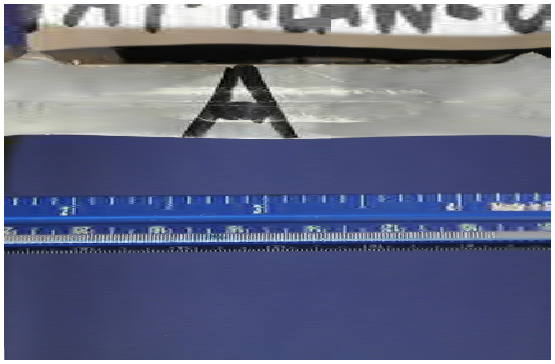

FAT-HLAW-09 SIDE A STAKE WELD DETAIL

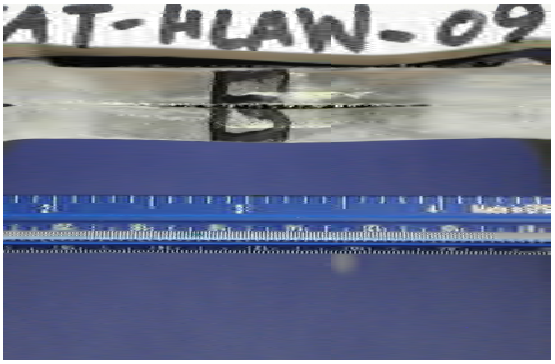

FAT-HLAW-09 SIDE B STAKE WELD DETAIL

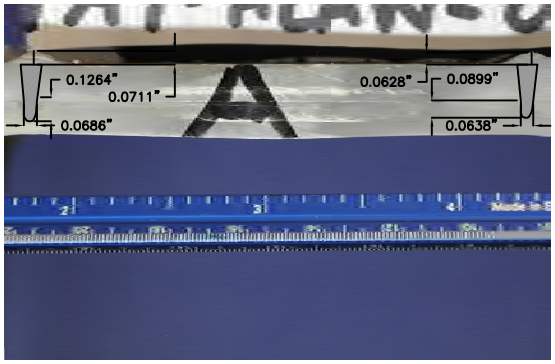

FAT-HLAW-09 SIDE A STAKE WELD DETAIL INTERPOLATED DIMENSIONS

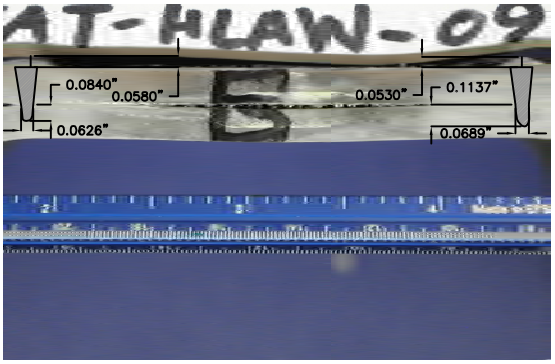

FAT-HLAW-09 SIDE B STAKE WELD DETAIL INTERPOLATED DIMENSIONS

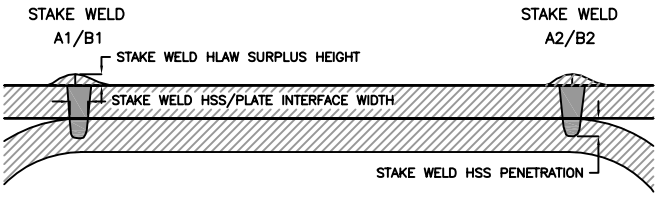

FIGURE REFERENCE

LEGEND

INTERPOLATED LASER STAKE WELD AREA

VIRGINIA POLYTECHNIC INSTITUTE AND STATE UNIVERSITY
BLACKSBURG, VIRGINIA

FATIGUE SPECIMEN STAKE WELD DETAILS
HYBRID LASER ARC WELD TEST SPECIMEN: FAT-HLAW-09
VIA DEPARTMENT OF CIVIL AND ENVIRONMENTAL ENGINEERING
BLACKSBURG, VIRGINIA

DESIGNED BY	G.Passarelli	4/3/2011	CHECKED BY	W.Wright	4/3/2011
DRAWN BY	G.Passarelli	4/3/2011	APPROVED BY	W.Wright	4/3/2011

SCALE:	DRAWING NO.	PROJECT NO.	SHEET NO.	REVISION NO.
1"=1"	FAT-HLAW-09	SSP	---	--

LOCATION	DRAWN BY		CHECKED BY		APPROVED BY		DRAWING NUMBER
BLACKSBURG, VA	G.PASSARELLI	4/3/2011	W.WRIGHT	4/3/2011	W.WRIGHT	4/3/2011	FAT-HLAW-09

PRODUCED BY AN AUTODESK EDUCATIONAL PRODUCT

STAKE WELD	STAKE WELD AREA	STAKE WELD HSS/PLATE INTERFACE WIDTH	STAKE WELD HSS PENETRATION DEPTH	STAKE WELD HLAW SURPLUS HEIGHT
(UNITS)	(sqin)	(in.)	(in.)	(in.)
A1	0.0193	0.0613	0.0970	0.0522
A2	0.0152	0.0613	0.0622	0.0656
B1	0.0206	0.0561	0.0728	0.0570
B2	0.0210	0.0647	0.0987	0.0614

FAT–HLAW–10 SIDE A STAKE WELD DETAIL

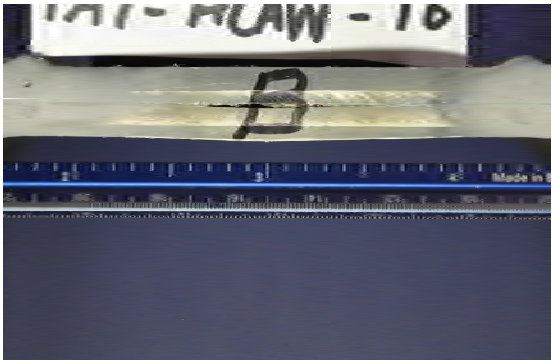

FAT–HLAW–10 SIDE B STAKE WELD DETAIL

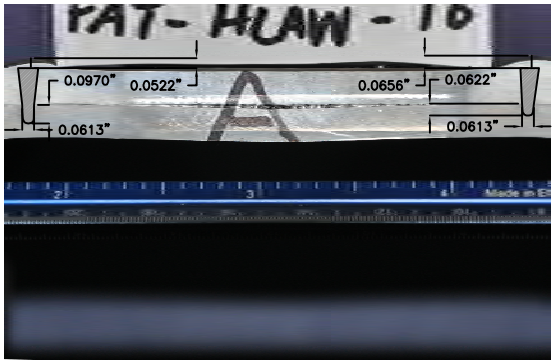

FAT–HLAW–10 SIDE A STAKE WELD DETAIL INTERPOLATED DIMENSIONS

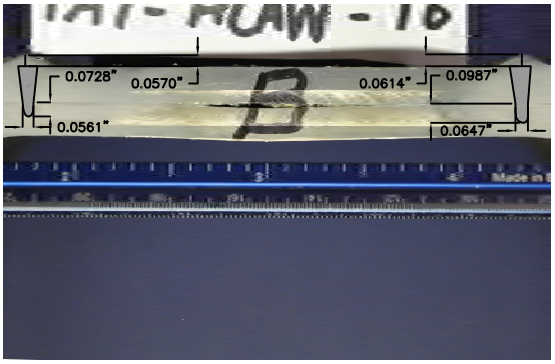

FAT–HLAW–10 SIDE B STAKE WELD DETAIL INTERPOLATED DIMENSIONS

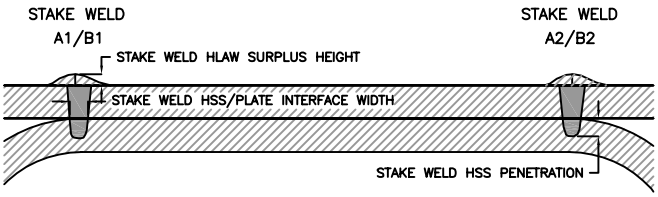

FIGURE REFERENCE

LEGEND

INTERPOLATED LASER STAKE WELD AREA

VIRGINIA POLYTECHNIC INSTITUTE AND STATE UNIVERSITY
BLACKSBURG, VIRGINIA

VirginiaTech VirginiaTech

FATIGUE SPECIMEN STAKE WELD DETAILS
HYBRID LASER ARC WELD TEST SPECIMEN: FAT-HLAW-10
VIA DEPARTMENT OF CIVIL AND ENVIRONMENTAL ENGINEERING
BLACKSBURG, VIRGINIA

DESIGNED BY	G.Passarelli	4/9/2011	CHECKED BY	W.Wright	4/9/2011
DRAWN BY	G.Passarelli	4/9/2011	APPROVED BY	W.Wright	4/9/2011
SCALE: 1"=1"	DRAWING NO. FAT-HLAW-10	PROJECT NO. SSP	SHEET NO. ---	REVISION NO. --	

LOCATION	DRAWN BY		CHECKED BY		APPROVED BY		DRAWING NUMBER
BLACKSBURG, VA	G.PASSARELLI	4/9/2011	W.WRIGHT	4/9/2011	W.WRIGHT	4/9/2011	FAT-HLAW-10

PRODUCED BY AN AUTODESK EDUCATIONAL PRODUCT

PRODUCED BY AN AUTODESK EDUCATIONAL PRODUCT

STAKE WELD	STAKE WELD AREA	STAKE WELD HSS/PLATE INTERFACE WIDTH	STAKE WELD HSS PENETRATION DEPTH
(UNITS)	(sqin)	(in.)	(in.)
A1	0.0292	0.0917	0.1124
A2	0.0250	0.0770	0.1085
B1	0.0313	0.0906	0.1456
B2	0.0239	0.0742	0.1152

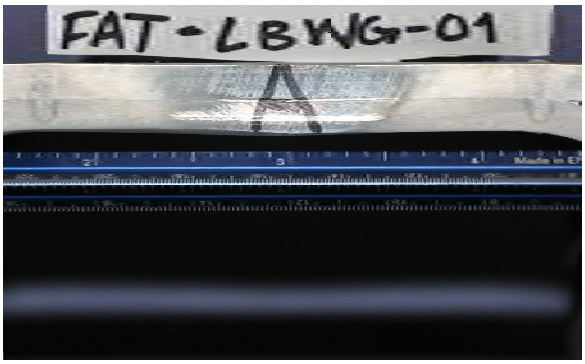

FAT–LBWG–01 SIDE A STAKE WELD DETAIL

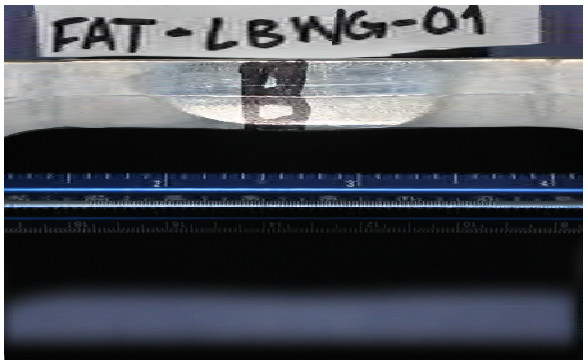

FAT–LBWG–01 SIDE B STAKE WELD DETAIL

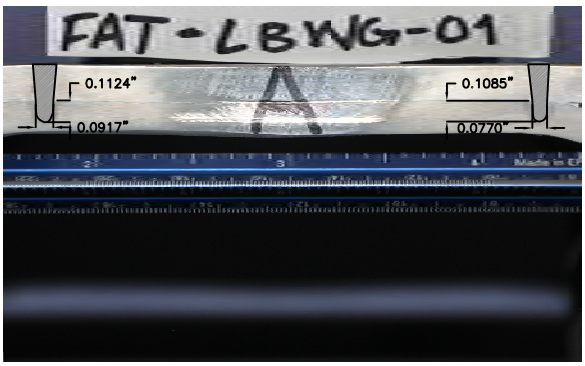

FAT–LBWG–01 SIDE A STAKE WELD DETAIL INTERPOLATED DIMENSIONS

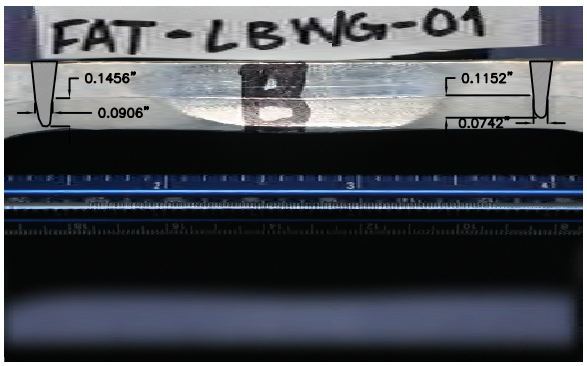

FAT–LBWG–01 SIDE B STAKE WELD DETAIL INTERPOLATED DIMENSIONS

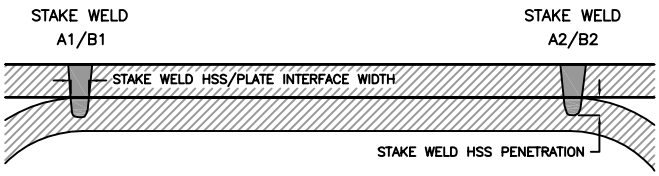

FIGURE REFERENCE

LEGEND

INTERPOLATED LASER STAKE WELD AREA

VIRGINIA POLYTECHNIC INSTITUTE AND STATE UNIVERSITY
BLACKSBURG, VIRGINIA

VirginiaTech VirginiaTech

FATIGUE SPECIMEN STAKE WELD DETAILS
LASER BEAM WELD WITH GAP TEST SPECIMEN: FAT-LBWG-01
VIA DEPARTMENT OF CIVIL AND ENVIRONMENTAL ENGINEERING
BLACKSBURG, VIRGINIA

DESIGNED BY	G.Passarelli	4/4/2011	CHECKED BY	W.Wright	4/4/2011
DRAWN BY	G.Passarelli	4/4/2011	APPROVED BY	W.Wright	4/4/2011

SCALE:	DRAWING NO.	PROJECT NO.	SHEET NO.	REVISION NO.
1"=1"	FAT-LBWG-01	SSP	---	--

LOCATION	DRAWN BY		CHECKED BY		APPROVED BY		DRAWING NUMBER
BLACKSBURG, VA	G.PASSARELLI	4/4/2011	W.WRIGHT	4/4/2011	W.WRIGHT	4/4/2011	FAT-LBWG-01

PRODUCED BY AN AUTODESK EDUCATIONAL PRODUCT

STAKE WELD	STAKE WELD AREA	STAKE WELD HSS/PLATE INTERFACE WIDTH	STAKE WELD HSS PENETRATION DEPTH
(UNITS)	(sqin)	(in.)	(in.)
A1	0.0252	0.0809	0.1070
A2	0.0274	0.0892	0.1071
B1	0.0294	0.0943	0.1071
B2	0.0242	0.0765	0.1034

FAT–LBWG–02 SIDE A STAKE WELD DETAIL

FAT–LBWG–02 SIDE B STAKE WELD DETAIL

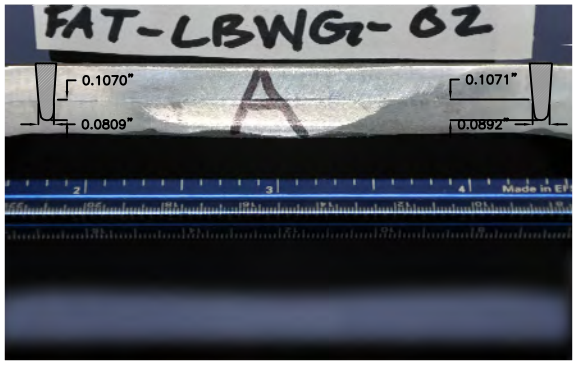

FAT–LBWG–02 SIDE A STAKE WELD DETAIL INTERPOLATED DIMENSIONS

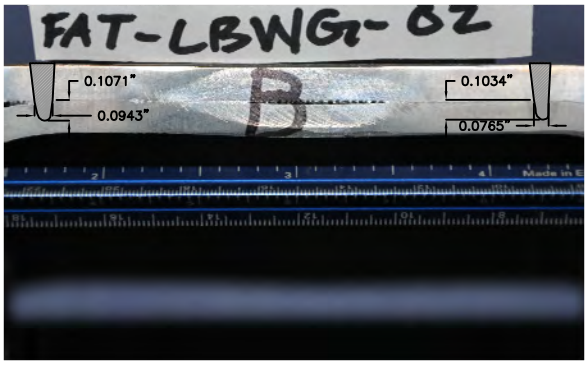

FAT–LBWG–02 SIDE B STAKE WELD DETAIL INTERPOLATED DIMENSIONS

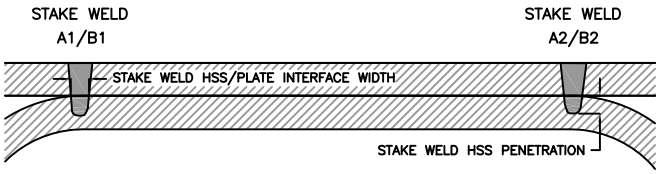

FIGURE REFERENCE

LEGEND

INTERPOLATED LASER STAKE WELD AREA

VIRGINIA POLYTECHNIC INSTITUTE AND STATE UNIVERSITY
BLACKSBURG, VIRGINIA

VirginiaTech VirginiaTech

FATIGUE SPECIMEN STAKE WELD DETAILS
LASER BEAM WELD WITH GAP TEST SPECIMEN: FAT-LBWG-02
VIA DEPARTMENT OF CIVIL AND ENVIRONMENTAL ENGINEERING
BLACKSBURG, VIRGINIA

DESIGNED BY	G.Passarelli	4/4/2011	CHECKED BY	W.Wright	4/4/2011
DRAWN BY	G.Passarelli	4/4/2011	APPROVED BY	W.Wright	4/4/2011

SCALE:	DRAWING NO.	PROJECT NO.	SHEET NO.	REVISION NO.
1"=1"	FAT-LBWG-02	SSP	—	—

LOCATION	DRAWN BY		CHECKED BY		APPROVED BY		DRAWING NUMBER
BLACKSBURG, VA	G.PASSARELLI	4/4/2011	W.WRIGHT	4/4/2011	W.WRIGHT	4/4/2011	FAT-LBWG-02

PRODUCED BY AN AUTODESK EDUCATIONAL PRODUCT

STAKE WELD	STAKE WELD AREA	STAKE WELD HSS/PLATE INTERFACE WIDTH	STAKE WELD HSS PENETRATION DEPTH
(UNITS)	(sqin)	(in.)	(in.)
A1	0.0252	0.0772	0.1085
A2	0.0264	0.0895	0.0830
B1	0.0285	0.0907	0.0956
B2	0.0245	0.0789	0.0931

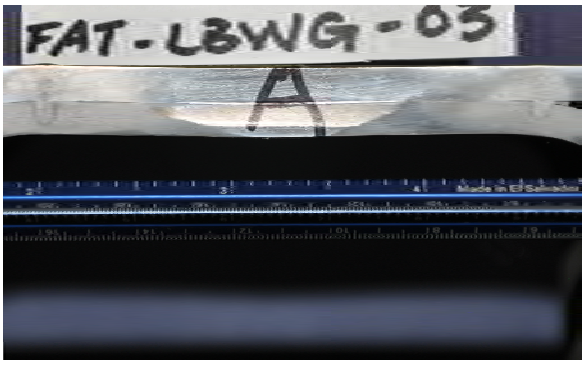

FAT–LBWG–03 SIDE A STAKE WELD DETAIL

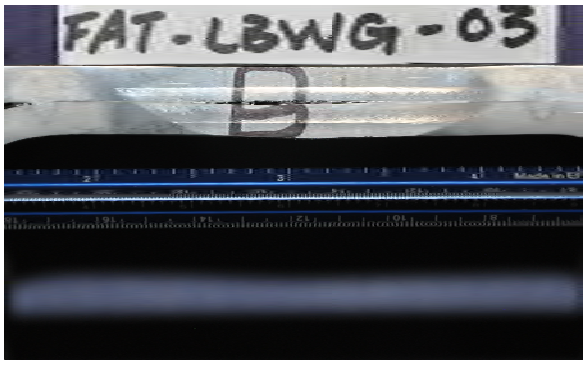

FAT–LBWG–03 SIDE B STAKE WELD DETAIL

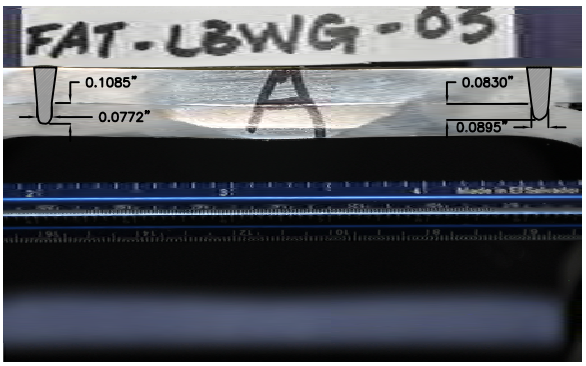

FAT–LBWG–03 SIDE A STAKE WELD DETAIL INTERPOLATED DIMENSIONS

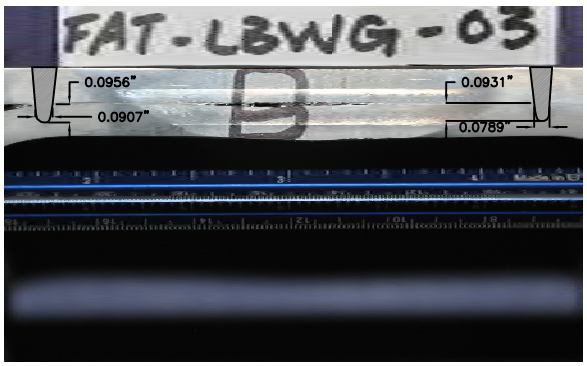

FAT–LBWG–03 SIDE B STAKE WELD DETAIL INTERPOLATED DIMENSIONS

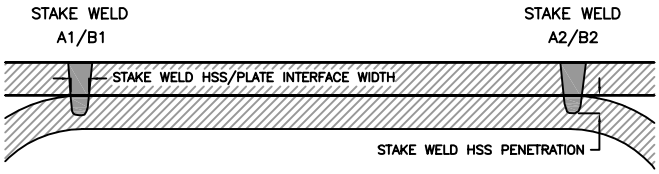

FIGURE REFERENCE

LEGEND

INTERPOLATED LASER STAKE WELD AREA

VIRGINIA POLYTECHNIC INSTITUTE AND STATE UNIVERSITY
BLACKSBURG, VIRGINIA

FATIGUE SPECIMEN STAKE WELD DETAILS
LASER BEAM WELD WITH GAP TEST SPECIMEN: FAT-LBWG-03
VIA DEPARTMENT OF CIVIL AND ENVIRONMENTAL ENGINEERING
BLACKSBURG, VIRGINIA

DESIGNED BY	G.Passarelli	4/4/2011	CHECKED BY	W.Wright	4/4/2011
DRAWN BY	G.Passarelli	4/4/2011	APPROVED BY	W.Wright	4/4/2011
SCALE: 1"=1"	DRAWING NO. FAT-LBWG-03	PROJECT NO. SSP	SHEET NO. ---		REVISION NO. --

LOCATION	DRAWN BY		CHECKED BY		APPROVED BY		DRAWING NUMBER
BLACKSBURG, VA	G.PASSARELLI	4/4/2011	W.WRIGHT	4/4/2011	W.WRIGHT	4/4/2011	FAT-LBWG-03

PRODUCED BY AN AUTODESK EDUCATIONAL PRODUCT

PRODUCED BY AN AUTODESK EDUCATIONAL PRODUCT

STAKE WELD	STAKE WELD AREA	STAKE WELD HSS/PLATE INTERFACE WIDTH	STAKE WELD HSS PENETRATION DEPTH
(UNITS)	(sqin)	(in.)	(in.)
A1	0.0276	0.0901	0.0882
A2	0.0227	0.0722	0.0686
B1	0.0219	0.0674	0.0836
B2	0.0249	0.0824	0.0870

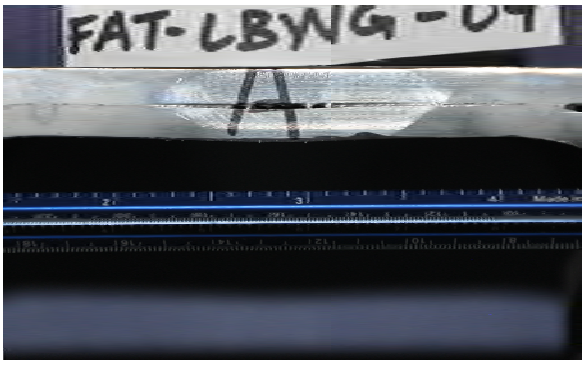

FAT–LBWG–04 SIDE A STAKE WELD DETAIL

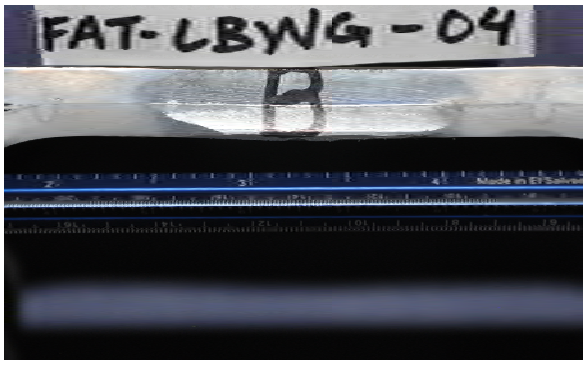

FAT–LBWG–04 SIDE B STAKE WELD DETAIL

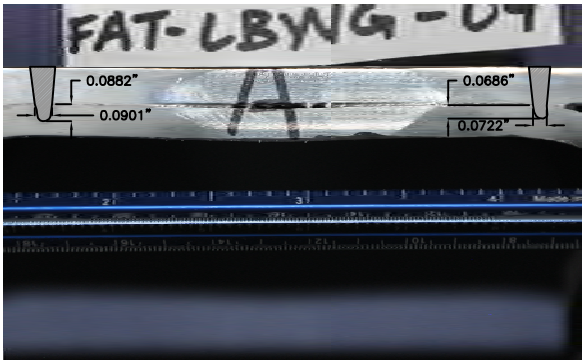

FAT–LBWG–04 SIDE A STAKE WELD DETAIL INTERPOLATED DIMENSIONS

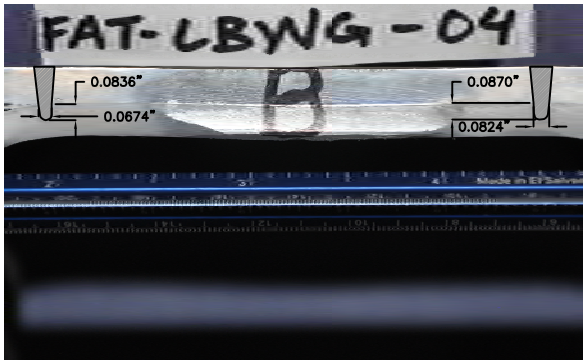

FAT–LBWG–04 SIDE B STAKE WELD DETAIL INTERPOLATED DIMENSIONS

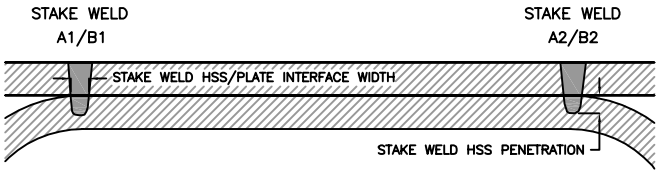

FIGURE REFERENCE

LEGEND

INTERPOLATED LASER STAKE WELD AREA

VIRGINIA POLYTECHNIC INSTITUTE AND STATE UNIVERSITY
BLACKSBURG, VIRGINIA

VirginiaTech VirginiaTech

FATIGUE SPECIMEN STAKE WELD DETAILS
LASER BEAM WELD WITH GAP TEST SPECIMEN: FAT-LBWG-04
VIA DEPARTMENT OF CIVIL AND ENVIRONMENTAL ENGINEERING
BLACKSBURG, VIRGINIA

DESIGNED BY	G.Passarelli	4/4/2011	CHECKED BY	W.Wright	4/4/2011
DRAWN BY	G.Passarelli	4/4/2011	APPROVED BY	W.Wright	4/4/2011
SCALE: 1"=1"	DRAWING NO. FAT-LBWG-04		PROJECT NO. SSP	SHEET NO. ---	REVISION NO. --

LOCATION	DRAWN BY		CHECKED BY		APPROVED BY		DRAWING NUMBER
BLACKSBURG, VA	G.PASSARELLI	4/4/2011	W.WRIGHT	4/4/2011	W.WRIGHT	4/4/2011	FAT-LBWG-04

PRODUCED BY AN AUTODESK EDUCATIONAL PRODUCT

STAKE WELD	STAKE WELD AREA	STAKE WELD HSS/PLATE INTERFACE WIDTH	STAKE WELD HSS PENETRATION DEPTH
(UNITS)	(sqin)	(in.)	(in.)
A1	0.0273	0.0886	0.0853
A2	0.0280	0.0921	0.0774
B1	0.0324	0.1093	0.0773
B2	0.0279	0.0884	0.0970

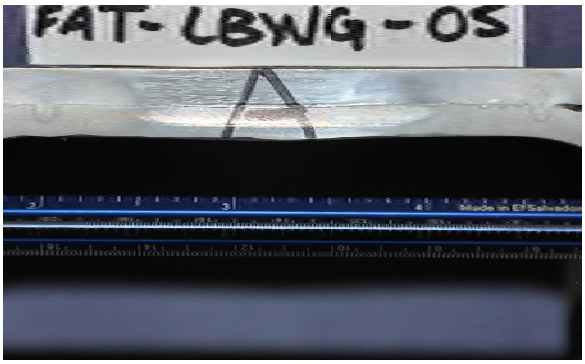

FAT–LBWG–05 SIDE A STAKE WELD DETAIL

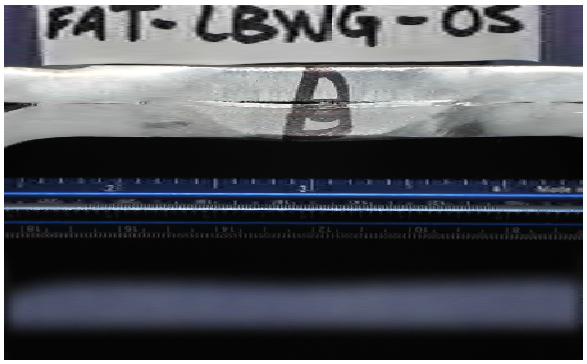

FAT–LBWG–05 SIDE B STAKE WELD DETAIL

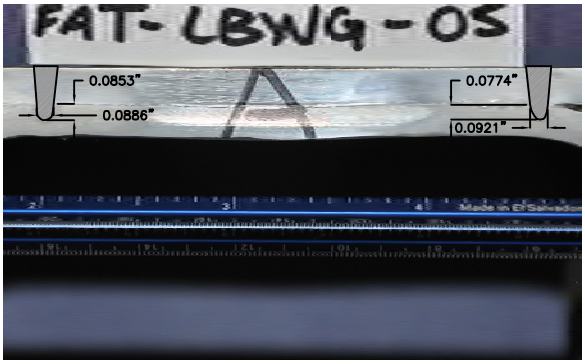

FAT–LBWG–05 SIDE A STAKE WELD DETAIL INTERPOLATED DIMENSIONS

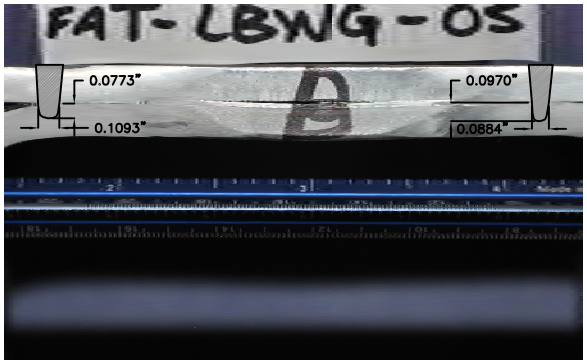

FAT–LBWG–05 SIDE B STAKE WELD DETAIL INTERPOLATED DIMENSIONS

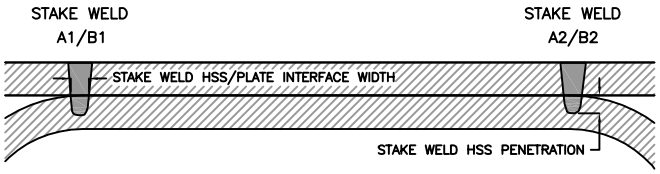

FIGURE REFERENCE

LEGEND

INTERPOLATED LASER STAKE WELD AREA

VIRGINIA POLYTECHNIC INSTITUTE AND STATE UNIVERSITY
BLACKSBURG, VIRGINIA

FATIGUE SPECIMEN STAKE WELD DETAILS
LASER BEAM WELD WITH GAP TEST SPECIMEN: FAT-LBWG-05
VIA DEPARTMENT OF CIVIL AND ENVIRONMENTAL ENGINEERING
BLACKSBURG, VIRGINIA

DESIGNED BY	G.Passarelli	4/4/2011	CHECKED BY	W.Wright	4/4/2011
DRAWN BY	G.Passarelli	4/4/2011	APPROVED BY	W.Wright	4/4/2011
SCALE: 1"=1"	DRAWING NO. FAT-LBWG-05	PROJECT NO. SSP	SHEET NO. ---	REVISION NO. --	

LOCATION	DRAWN BY		CHECKED BY		APPROVED BY		DRAWING NUMBER
BLACKSBURG, VA	G.PASSARELLI	4/4/2011	W.WRIGHT	4/4/2011	W.WRIGHT	4/4/2011	FAT-LBWG-05

PRODUCED BY AN AUTODESK EDUCATIONAL PRODUCT

PRODUCED BY AN AUTODESK EDUCATIONAL PRODUCT

STAKE WELD	STAKE WELD AREA	STAKE WELD HSS/PLATE INTERFACE WIDTH	STAKE WELD HSS PENETRATION DEPTH
(UNITS)	(sqin)	(in.)	(in.)
A1	0.0279	0.0846	0.0963
A2	0.0343	0.1225	0.0777
B1	0.0267	0.0991	0.0782
B2	0.0258	0.0851	0.0802

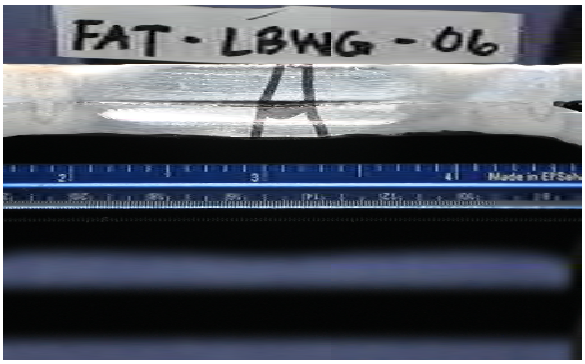

FAT–LBWG–06 SIDE A STAKE WELD DETAIL

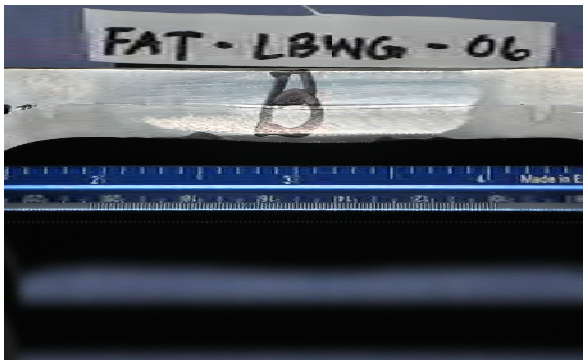

FAT–LBWG–06 SIDE B STAKE WELD DETAIL

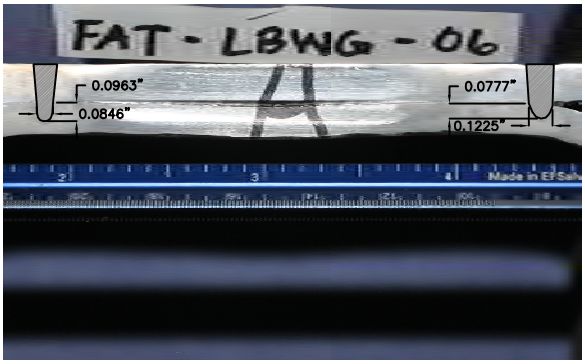

FAT–LBWG–06 SIDE A STAKE WELD DETAIL INTERPOLATED DIMENSIONS

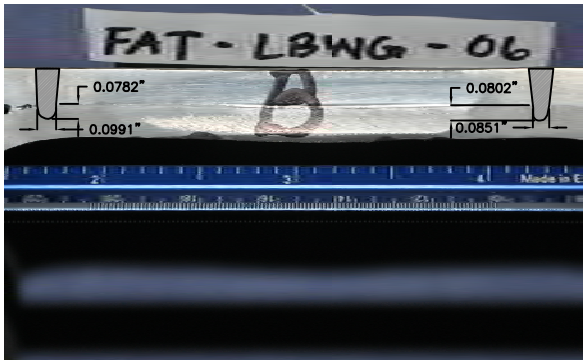

FAT–LBWG–06 SIDE B STAKE WELD DETAIL INTERPOLATED DIMENSIONS

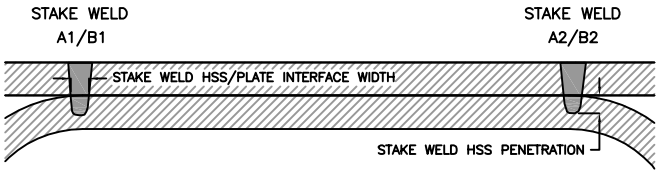

FIGURE REFERENCE

LEGEND

INTERPOLATED LASER STAKE WELD AREA

VIRGINIA POLYTECHNIC INSTITUTE AND STATE UNIVERSITY
BLACKSBURG, VIRGINIA

FATIGUE SPECIMEN STAKE WELD DETAILS
LASER BEAM WELD WITH GAP TEST SPECIMEN: FAT-LBWG-06
VIA DEPARTMENT OF CIVIL AND ENVIRONMENTAL ENGINEERING
BLACKSBURG, VIRGINIA

DESIGNED BY	G.Passarelli	4/4/2011	CHECKED BY	W.Wright	4/4/2011
DRAWN BY	G.Passarelli	4/4/2011	APPROVED BY	W.Wright	4/4/2011

SCALE:	DRAWING NO.	PROJECT NO.	SHEET NO.	REVISION NO.
1"=1"	FAT-LBWG-06	SSP	---	--

LOCATION	DRAWN BY		CHECKED BY		APPROVED BY		DRAWING NUMBER
BLACKSBURG, VA	G.PASSARELLI	4/4/2011	W.WRIGHT	4/4/2011	W.WRIGHT	4/4/2011	FAT-LBWG-06

PRODUCED BY AN AUTODESK EDUCATIONAL PRODUCT

PRODUCED BY AN AUTODESK EDUCATIONAL PRODUCT

STAKE WELD	STAKE WELD AREA	STAKE WELD HSS/PLATE INTERFACE WIDTH	STAKE WELD HSS PENETRATION DEPTH
(UNITS)	(sqin)	(in.)	(in.)
A1	0.0264	0.0889	0.0738
A2	0.0302	0.1083	0.0569
B1	0.0358	0.1191	0.0785
B2	0.0293	0.0959	0.0838

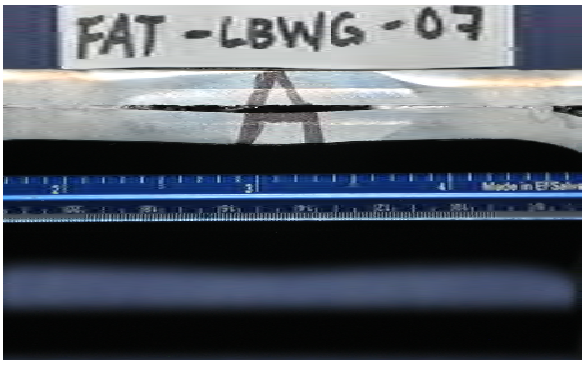

FAT–LBWG–07 SIDE A STAKE WELD DETAIL

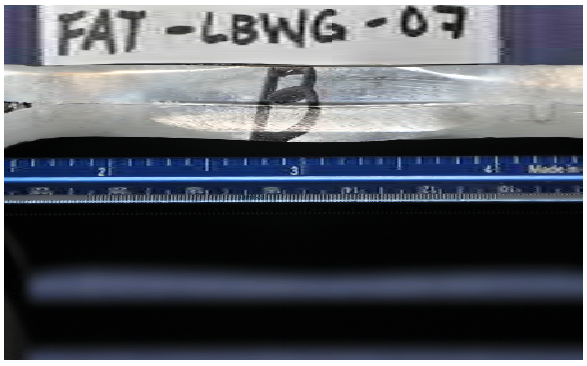

FAT–LBWG–07 SIDE B STAKE WELD DETAIL

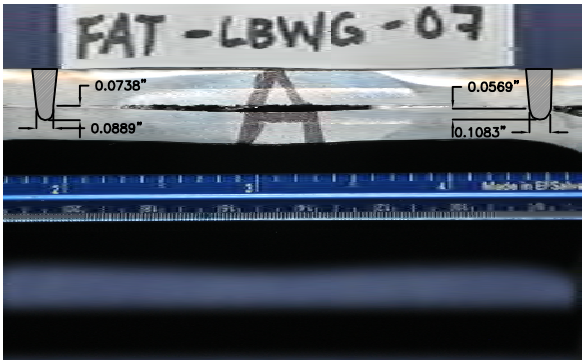

FAT–LBWG–07 SIDE A STAKE WELD DETAIL INTERPOLATED DIMENSIONS

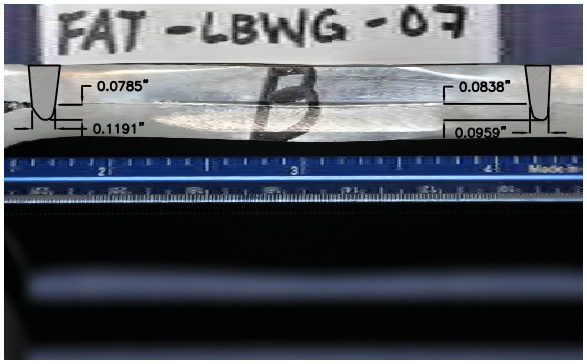

FAT–LBWG–07 SIDE B STAKE WELD DETAIL INTERPOLATED DIMENSIONS

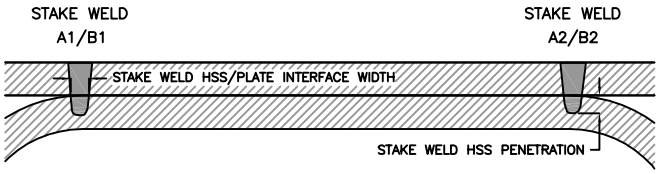

FIGURE REFERENCE

LEGEND

INTERPOLATED LASER STAKE WELD AREA

VIRGINIA POLYTECHNIC INSTITUTE AND STATE UNIVERSITY
BLACKSBURG, VIRGINIA

VirginiaTech VirginiaTech

FATIGUE SPECIMEN STAKE WELD DETAILS
LASER BEAM WELD WITH GAP TEST SPECIMEN: FAT-LBWG-07
VIA DEPARTMENT OF CIVIL AND ENVIRONMENTAL ENGINEERING
BLACKSBURG, VIRGINIA

DESIGNED BY	G.Passarelli	4/4/2011	CHECKED BY	W.Wright	4/4/2011
DRAWN BY	G.Passarelli	4/4/2011	APPROVED BY	W.Wright	4/4/2011

SCALE:	DRAWING NO.	PROJECT NO.	SHEET NO.	REVISION NO.
1"=1"	FAT-LBWG-07	SSP	---	--

LOCATION	DRAWN BY		CHECKED BY		APPROVED BY		DRAWING NUMBER
BLACKSBURG, VA	G.PASSARELLI	4/4/2011	W.WRIGHT	4/4/2011	W.WRIGHT	4/4/2011	FAT-LBWG-07

PRODUCED BY AN AUTODESK EDUCATIONAL PRODUCT

PRODUCED BY AN AUTODESK EDUCATIONAL PRODUCT

STAKE WELD	STAKE WELD AREA	STAKE WELD HSS/PLATE INTERFACE WIDTH	STAKE WELD HSS PENETRATION DEPTH
(UNITS)	(sqin)	(in.)	(in.)
A1	0.0240	0.0751	0.0741
A2	0.0341	0.1200	0.0848
B1	0.0366	0.1299	0.0706
B2	0.0261	0.0823	0.0862

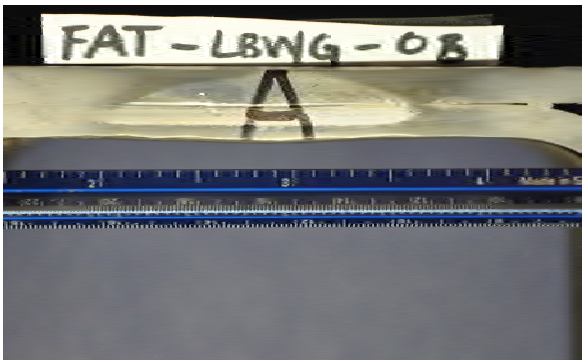

FAT–LBWG–08 SIDE A STAKE WELD DETAIL

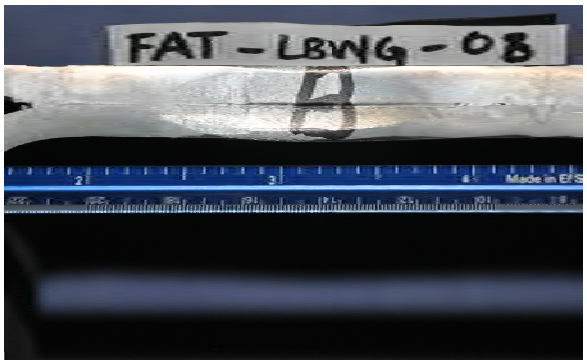

FAT–LBWG–08 SIDE B STAKE WELD DETAIL

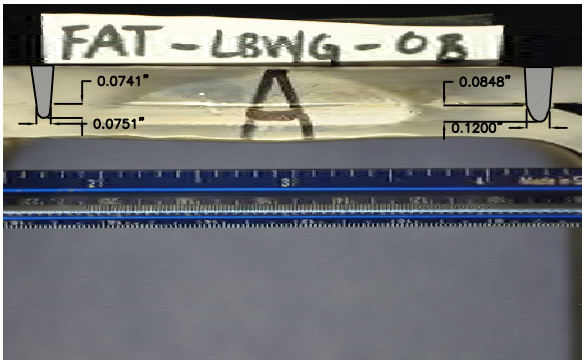

FAT–LBWG–08 SIDE A STAKE WELD DETAIL INTERPOLATED DIMENSIONS

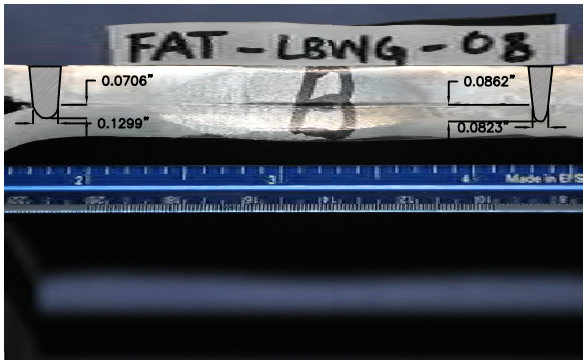

FAT–LBWG–08 SIDE B STAKE WELD DETAIL INTERPOLATED DIMENSIONS

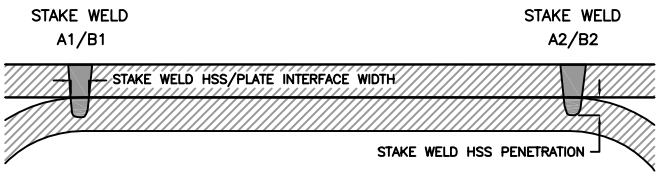

FIGURE REFERENCE

LEGEND

INTERPOLATED LASER STAKE WELD AREA

VIRGINIA POLYTECHNIC INSTITUTE AND STATE UNIVERSITY
BLACKSBURG, VIRGINIA

VirginiaTech VirginiaTech

FATIGUE SPECIMEN STAKE WELD DETAILS
LASER BEAM WELD WITH GAP TEST SPECIMEN: FAT-LBWG-08
VIA DEPARTMENT OF CIVIL AND ENVIRONMENTAL ENGINEERING
BLACKSBURG, VIRGINIA

DESIGNED BY	G.Passarelli	4/4/2011	CHECKED BY	W.Wright	4/4/2011
DRAWN BY	G.Passarelli	4/4/2011	APPROVED BY	W.Wright	4/4/2011

SCALE:	DRAWING NO.	PROJECT NO.	SHEET NO.	REVISION NO.
1"=1"	FAT-LBWG-08	SSP	---	--

LOCATION	DRAWN BY		CHECKED BY		APPROVED BY		DRAWING NUMBER
BLACKSBURG, VA	G.PASSARELLI	4/4/2011	W.WRIGHT	4/4/2011	W.WRIGHT	4/4/2011	FAT-LBWG-08

PRODUCED BY AN AUTODESK EDUCATIONAL PRODUCT

STAKE WELD	STAKE WELD AREA	STAKE WELD HSS/PLATE INTERFACE WIDTH	STAKE WELD HSS PENETRATION DEPTH
(UNITS)	(sqin)	(in.)	(in.)
A1	0.0297	0.1032	0.0558
A2	0.0298	0.1112	0.0457
B1	0.0298	0.0970	0.0731
B2	0.0265	0.0871	0.0715

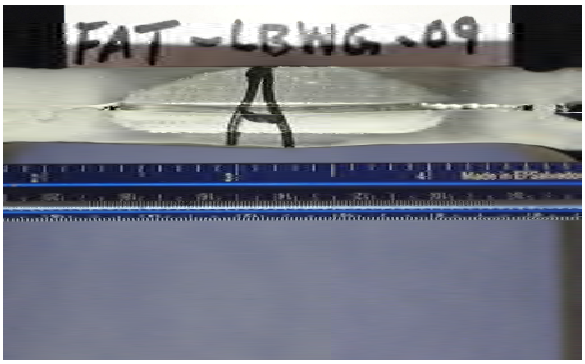

FAT–LBWG–09 SIDE A STAKE WELD DETAIL

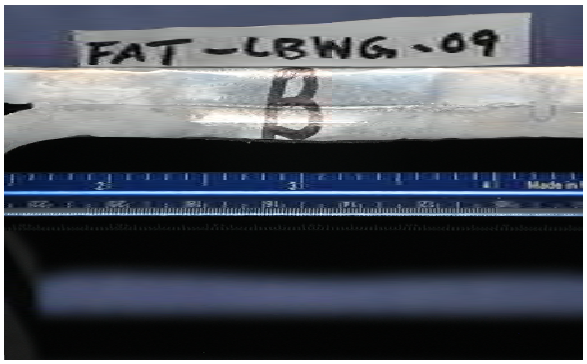

FAT–LBWG–09 SIDE B STAKE WELD DETAIL

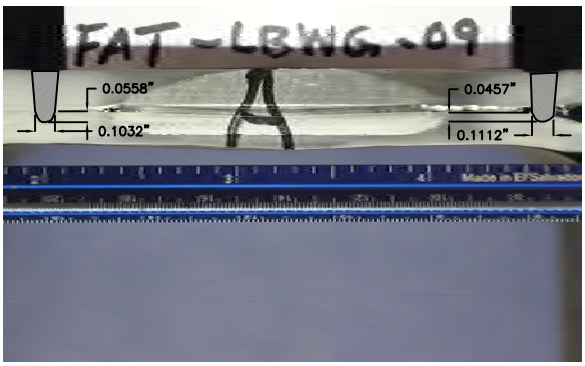

FAT–LBWG–09 SIDE A STAKE WELD DETAIL INTERPOLATED DIMENSIONS

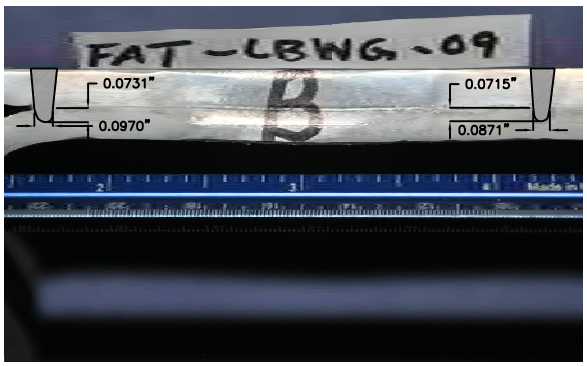

FAT–LBWG–09 SIDE B STAKE WELD DETAIL INTERPOLATED DIMENSIONS

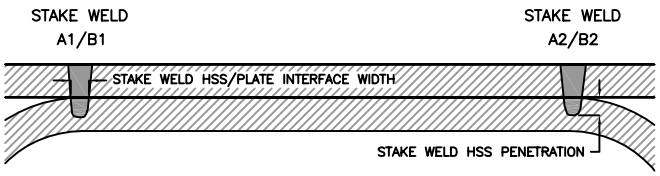

FIGURE REFERENCE

LEGEND

INTERPOLATED LASER STAKE WELD AREA

LOCATION	DRAWN BY		CHECKED BY		APPROVED BY		DRAWING NUMBER
BLACKSBURG, VA	G.PASSARELLI	4/5/2011	W.WRIGHT	4/5/2011	W.WRIGHT	4/5/2011	FAT-LBWG-09

VIRGINIA POLYTECHNIC INSTITUTE AND STATE UNIVERSITY
BLACKSBURG, VIRGINIA

VirginiaTech VirginiaTech

FATIGUE SPECIMEN STAKE WELD DETAILS
LASER BEAM WELD WITH GAP TEST SPECIMEN: FAT-LBWG-09
VIA DEPARTMENT OF CIVIL AND ENVIRONMENTAL ENGINEERING
BLACKSBURG, VIRGINIA

DESIGNED BY	G.Passarelli	4/5/2011	CHECKED BY	W.Wright	4/5/2011
DRAWN BY	G.Passarelli	4/5/2011	APPROVED BY	W.Wright	4/5/2011

SCALE:	DRAWING NO.	PROJECT NO.	SHEET NO.	REVISION NO.
1"=1"	FAT-LBWG-09	SSP	---	--

PRODUCED BY AN AUTODESK EDUCATIONAL PRODUCT

PRODUCED BY AN AUTODESK EDUCATIONAL PRODUCT

STAKE WELD	STAKE WELD AREA	STAKE WELD HSS/PLATE INTERFACE WIDTH	STAKE WELD HSS PENETRATION DEPTH
(UNITS)	(sqin)	(in.)	(in.)
A1	0.0315	0.1073	0.0831
A2	0.0343	0.1220	0.0803
B1	0.0375	0.1334	0.0709
B2	0.0349	0.1273	0.0701

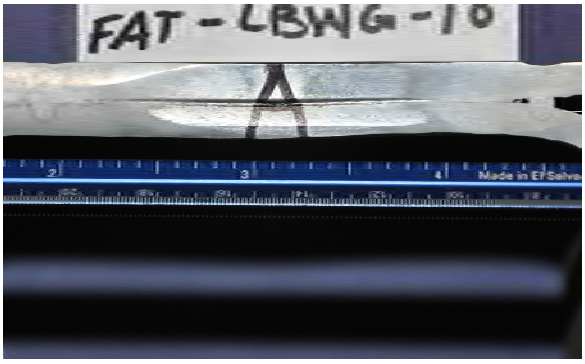

FAT–LBWG–10 SIDE A STAKE WELD DETAIL

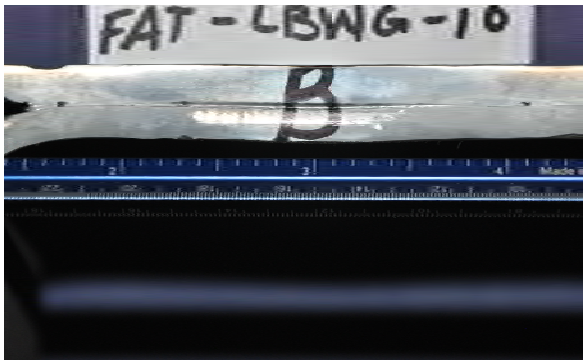

FAT–LBWG–10 SIDE B STAKE WELD DETAIL

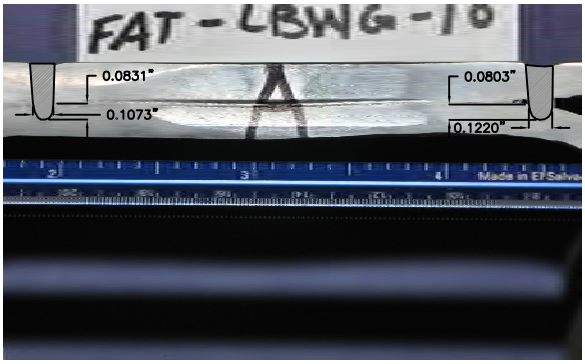

FAT–LBWG–10 SIDE A STAKE WELD DETAIL INTERPOLATED DIMENSIONS

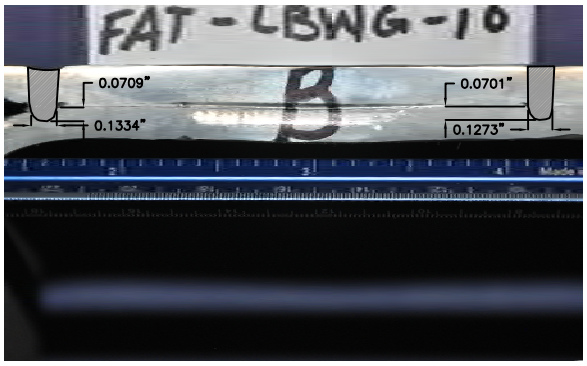

FAT–LBWG–10 SIDE B STAKE WELD DETAIL INTERPOLATED DIMENSIONS

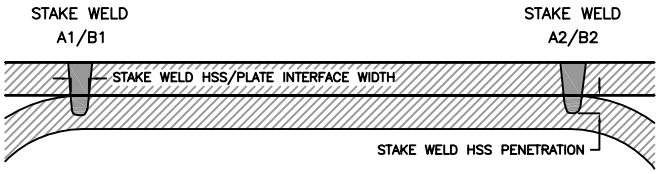

FIGURE REFERENCE

LEGEND

INTERPOLATED LASER STAKE WELD AREA

VIRGINIA POLYTECHNIC INSTITUTE AND STATE UNIVERSITY
BLACKSBURG, VIRGINIA

VirginiaTech VirginiaTech

FATIGUE SPECIMEN STAKE WELD DETAILS
LASER BEAM WELD WITH GAP TEST SPECIMEN: FAT-LBWG-10
VIA DEPARTMENT OF CIVIL AND ENVIRONMENTAL ENGINEERING
BLACKSBURG, VIRGINIA

DESIGNED BY	G.Passarelli	4/5/2011	CHECKED BY	W.Wright	4/5/2011
DRAWN BY	G.Passarelli	4/5/2011	APPROVED BY	W.Wright	4/5/2011
SCALE: 1"=1"	DRAWING NO. FAT-LBWG-10	PROJECT NO. SSP	SHEET NO. ---	REVISION NO. --	

LOCATION	DRAWN BY		CHECKED BY		APPROVED BY		DRAWING NUMBER
BLACKSBURG, VA	G.PASSARELLI	4/5/2011	W.WRIGHT	4/5/2011	W.WRIGHT	4/5/2011	FAT-LBWG-10

PRODUCED BY AN AUTODESK EDUCATIONAL PRODUCT

PRODUCED BY AN AUTODESK EDUCATIONAL PRODUCT

STAKE WELD	STAKE WELD AREA	STAKE WELD HSS/PLATE INTERFACE WIDTH	STAKE WELD HSS PENETRATION DEPTH
(UNITS)	(sqin)	(in.)	(in.)
A1	0.0367	0.1230	0.0589
A2	0.0375	0.1307	0.0510
B1	0.0325	0.1174	0.0465
B2	0.0319	0.1076	0.0768

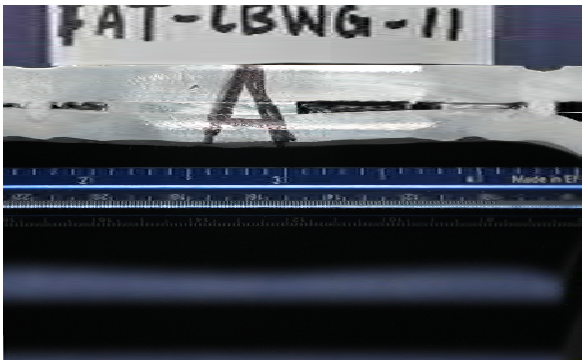

FAT–LBWG–11 SIDE A STAKE WELD DETAIL

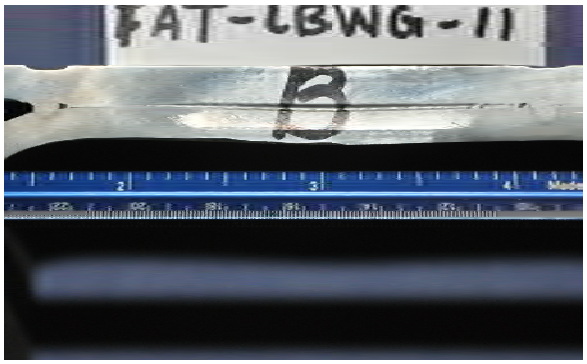

FAT–LBWG–11 SIDE B STAKE WELD DETAIL

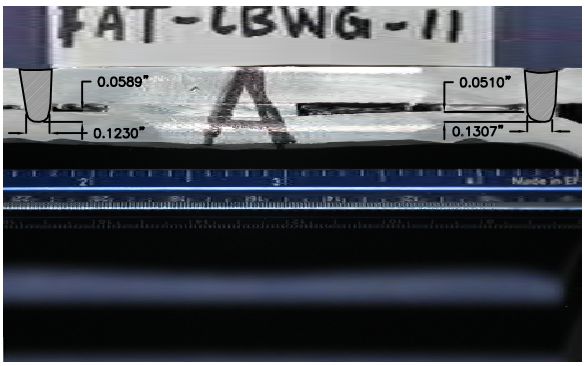

FAT–LBWG–11 SIDE A STAKE WELD DETAIL INTERPOLATED DIMENSIONS

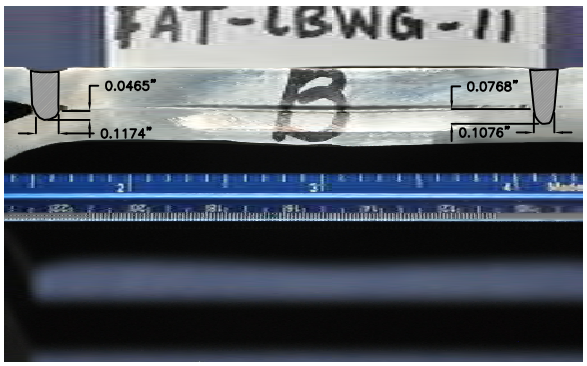

FAT–LBWG–11 SIDE B STAKE WELD DETAIL INTERPOLATED DIMENSIONS

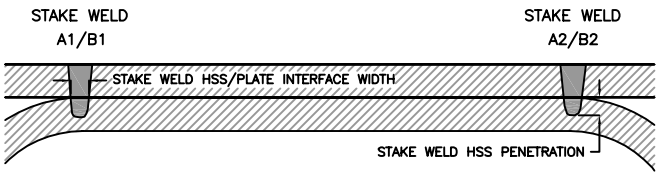

FIGURE REFERENCE

LEGEND

INTERPOLATED LASER STAKE WELD AREA

VIRGINIA POLYTECHNIC INSTITUTE AND STATE UNIVERSITY
BLACKSBURG, VIRGINIA

FATIGUE SPECIMEN STAKE WELD DETAILS
LASER BEAM WELD WITH GAP TEST SPECIMEN: FAT-LBWG-11
VIA DEPARTMENT OF CIVIL AND ENVIRONMENTAL ENGINEERING
BLACKSBURG, VIRGINIA

DESIGNED BY	G.Passarelli	4/5/2011	CHECKED BY	W.Wright	4/5/2011
DRAWN BY	G.Passarelli	4/5/2011	APPROVED BY	W.Wright	4/5/2011
SCALE: 1"=1"	DRAWING NO. FAT-LBWG-11	PROJECT NO. SSP	SHEET NO. ---	REVISION NO. --	

LOCATION	DRAWN BY		CHECKED BY		APPROVED BY		DRAWING NUMBER
BLACKSBURG, VA	G.PASSARELLI	4/5/2011	W.WRIGHT	4/5/2011	W.WRIGHT	4/5/2011	FAT-LBWG-11

PRODUCED BY AN AUTODESK EDUCATIONAL PRODUCT

PRODUCED BY AN AUTODESK EDUCATIONAL PRODUCT

STAKE WELD	STAKE WELD AREA	STAKE WELD HSS/PLATE INTERFACE WIDTH	STAKE WELD HSS PENETRATION DEPTH	STAKE WELD HLAW SURPLUS HEIGHT
(UNITS)	(sqin)	(in.)	(in.)	(in.)
A1	0.0235	0.0817	0.0890	0.0533
A2	0.0270	0.0863	0.0826	0.0538
B1	0.0291	0.1095	0.0612	0.0736
B2	0.0245	0.0910	0.0544	0.0611

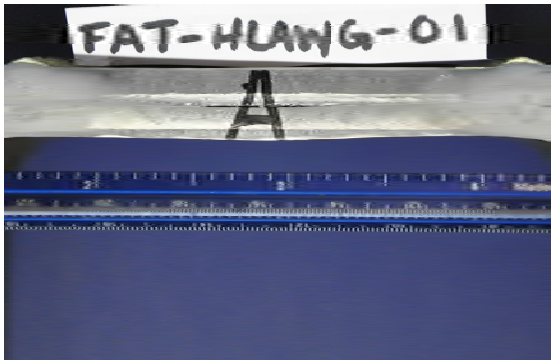

FAT–HLAWG–01 SIDE A STAKE WELD DETAIL

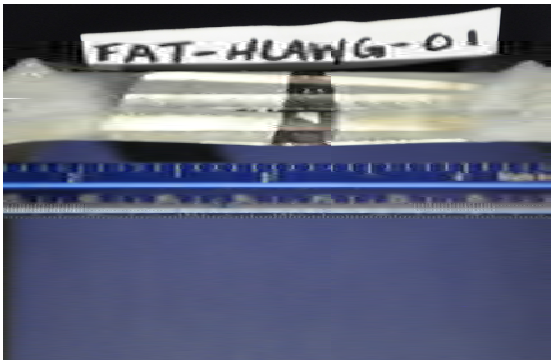

FAT–HLAWG–01 SIDE B STAKE WELD DETAIL

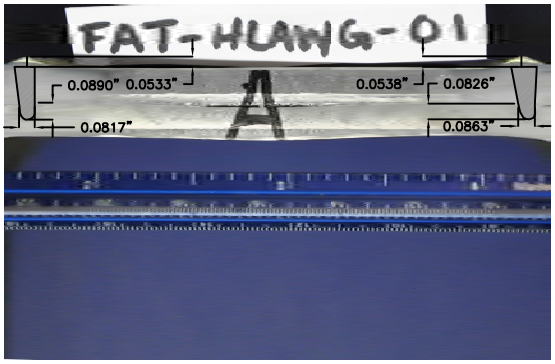

FAT–HLAWG–01 SIDE A STAKE WELD DETAIL INTERPOLATED DIMENSIONS

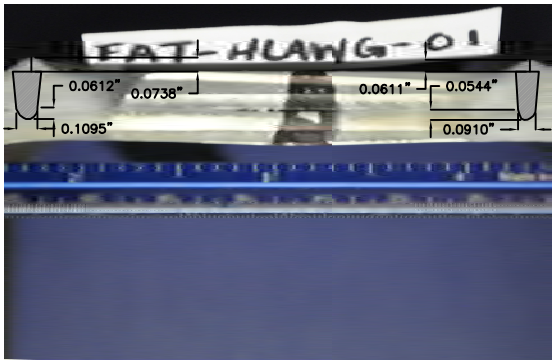

FAT–HLAWG–01 SIDE B STAKE WELD DETAIL INTERPOLATED DIMENSIONS

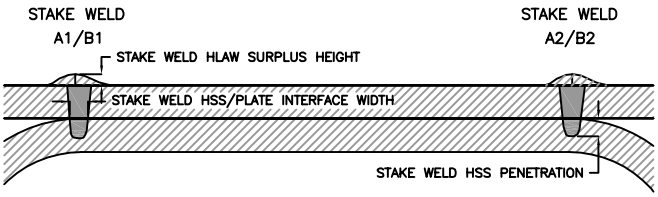

FIGURE REFERENCE

LEGEND

INTERPOLATED LASER STAKE WELD AREA

VIRGINIA POLYTECHNIC INSTITUTE AND STATE UNIVERSITY
BLACKSBURG, VIRGINIA

FATIGUE SPECIMEN STAKE WELD DETAILS
HYBRID LASER ARC WELD TEST SPECIMEN: FAT-HLAWG-01
VIA DEPARTMENT OF CIVIL AND ENVIRONMENTAL ENGINEERING
BLACKSBURG, VIRGINIA

DESIGNED BY	G.Passarelli	4/12/2011	CHECKED BY	W.Wright	4/12/2011
DRAWN BY	G.Passarelli	4/12/2011	APPROVED BY	W.Wright	4/12/2011
SCALE: 1"=1"	DRAWING NO. FAT-HLAWG-01	PROJECT NO. SSP	SHEET NO. ---	REVISION NO. --	

LOCATION	DRAWN BY		CHECKED BY		APPROVED BY		DRAWING NUMBER
BLACKSBURG, VA	G.PASSARELLI	4/12/2011	W.WRIGHT	4/12/2011	W.WRIGHT	4/12/2011	FAT-HLAWG-01

PRODUCED BY AN AUTODESK EDUCATIONAL PRODUCT

STAKE WELD	STAKE WELD AREA	STAKE WELD HSS/PLATE INTERFACE WIDTH	STAKE WELD HSS PENETRATION DEPTH	STAKE WELD HLAW SURPLUS HEIGHT
(UNITS)	(sqin)	(in.)	(in.)	(in.)
A1	0.0237	0.0722	0.0705	0.0599
A2	0.0251	0.0863	0.0755	0.0651
B1	0.0258	0.0887	0.0792	0.0560
B2	0.0249	0.0810	0.0757	0.0596

FAT–HLAWG–02 SIDE A STAKE WELD DETAIL

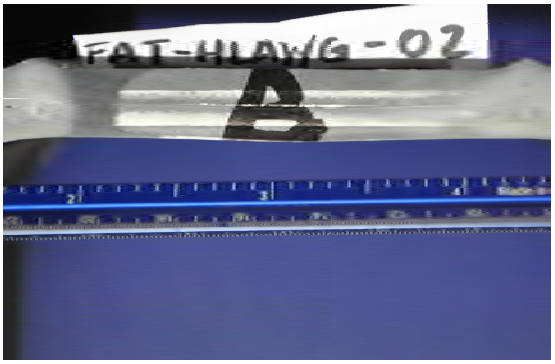

FAT–HLAWG–02 SIDE B STAKE WELD DETAIL

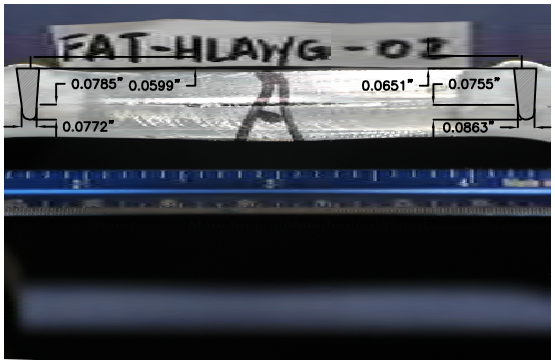

FAT–HLAWG–02 SIDE A STAKE WELD DETAIL INTERPOLATED DIMENSIONS

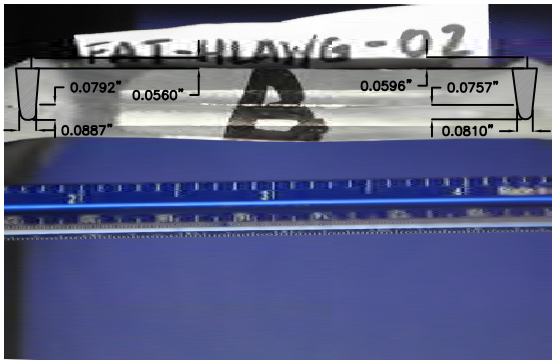

FAT–HLAWG–02 SIDE B STAKE WELD DETAIL INTERPOLATED DIMENSIONS

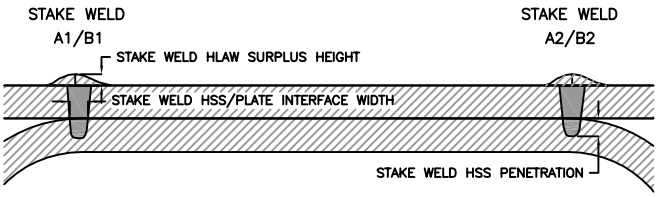

FIGURE REFERENCE

LEGEND

INTERPOLATED LASER STAKE WELD AREA

LOCATION	DRAWN BY	CHECKED BY	APPROVED BY	DRAWING NUMBER
BLACKSBURG, VA	G.PASSARELLI 4/12/2011	W.WRIGHT 4/12/2011	W.WRIGHT 4/12/2011	FAT-HLAWG-02

VIRGINIA POLYTECHNIC INSTITUTE AND STATE UNIVERSITY
BLACKSBURG, VIRGINIA

VirginiaTech VirginiaTech

FATIGUE SPECIMEN STAKE WELD DETAILS
HYBRID LASER ARC WELD TEST SPECIMEN: FAT-HLAWG-02
VIA DEPARTMENT OF CIVIL AND ENVIRONMENTAL ENGINEERING
BLACKSBURG, VIRGINIA

DESIGNED BY	G.Passarelli	4/12/2011	CHECKED BY	W.Wright	4/12/2011
DRAWN BY	G.Passarelli	4/12/2011	APPROVED BY	W.Wright	4/12/2011

SCALE:	DRAWING NO.	PROJECT NO.	SHEET NO.	REVISION NO.
1"=1"	FAT-HLAWG-02	SSP	---	--

PRODUCED BY AN AUTODESK EDUCATIONAL PRODUCT

PRODUCED BY AN AUTODESK EDUCATIONAL PRODUCT

STAKE WELD	STAKE WELD AREA	STAKE WELD HSS/PLATE INTERFACE WIDTH	STAKE WELD HSS PENETRATION DEPTH	STAKE WELD HLAW SURPLUS HEIGHT
(UNITS)	(sqin)	(in.)	(in.)	(in.)
A1	0.0231	0.0801	0.0971	0.0709
A2	0.0272	0.0930	0.0907	0.0674
B1	0.0272	0.0890	0.0842	0.0660
B2	0.0249	0.0839	0.0827	0.0643

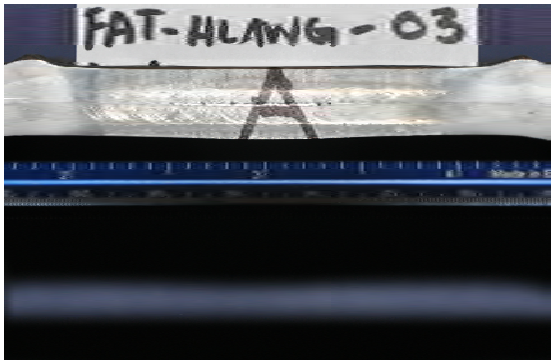

FAT–HLAWG–03 SIDE A STAKE WELD DETAIL

FAT–HLAWG–03 SIDE B STAKE WELD DETAIL

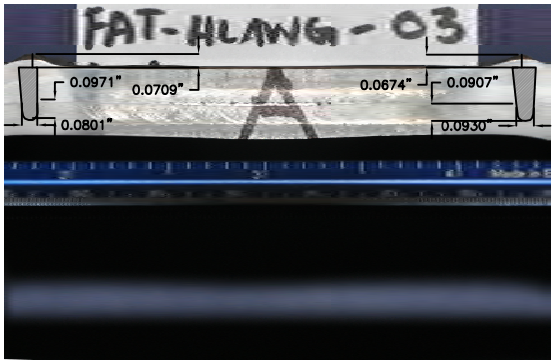

FAT–HLAWG–03 SIDE A STAKE WELD DETAIL INTERPOLATED DIMENSIONS

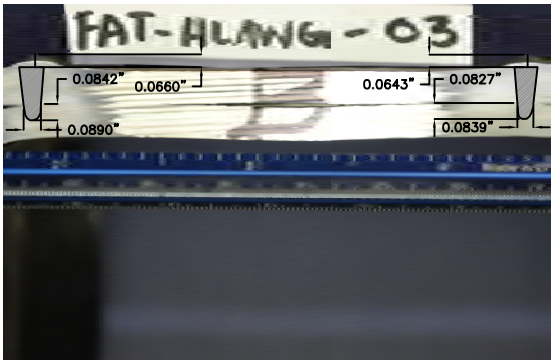

FAT–HLAWG–03 SIDE B STAKE WELD DETAIL INTERPOLATED DIMENSIONS

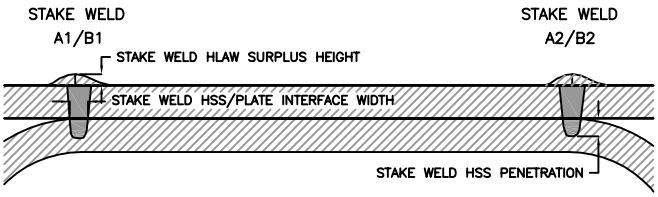

FIGURE REFERENCE

LEGEND

INTERPOLATED LASER STAKE WELD AREA

VIRGINIA POLYTECHNIC INSTITUTE AND STATE UNIVERSITY
BLACKSBURG, VIRGINIA

VirginiaTech VirginiaTech

FATIGUE SPECIMEN STAKE WELD DETAILS
HYBRID LASER ARC WELD TEST SPECIMEN: FAT-HLAWG-03
VIA DEPARTMENT OF CIVIL AND ENVIRONMENTAL ENGINEERING
BLACKSBURG, VIRGINIA

DESIGNED BY	G.Passarelli	4/12/2011	CHECKED BY	W.Wright	4/12/2011
DRAWN BY	G.Passarelli	4/12/2011	APPROVED BY	W.Wright	4/12/2011

SCALE:	DRAWING NO.	PROJECT NO.	SHEET NO.	REVISION NO.
1"=1"	FAT-HLAWG-03	SSP	---	--

LOCATION	DRAWN BY		CHECKED BY		APPROVED BY		DRAWING NUMBER
BLACKSBURG, VA	G.PASSARELLI	4/12/2011	W.WRIGHT	4/12/2011	W.WRIGHT	4/12/2011	FAT-HLAWG-03

PRODUCED BY AN AUTODESK EDUCATIONAL PRODUCT

STAKE WELD	STAKE WELD AREA	STAKE WELD HSS/PLATE INTERFACE WIDTH	STAKE WELD HSS PENETRATION DEPTH	STAKE WELD HLAW SURPLUS HEIGHT
(UNITS)	(sqin)	(in.)	(in.)	(in.)
A1	0.0238	0.0762	0.0873	0.0679
A2	0.0261	0.0890	0.0925	0.0711
B1	0.0246	0.0814	0.0859	0.0659
B2	0.0235	0.0790	0.0739	0.0631

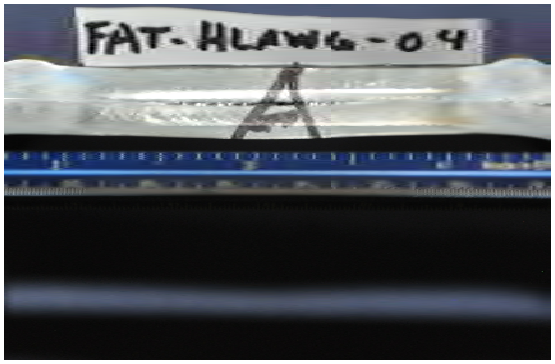

FAT–HLAWG–04 SIDE A STAKE WELD DETAIL

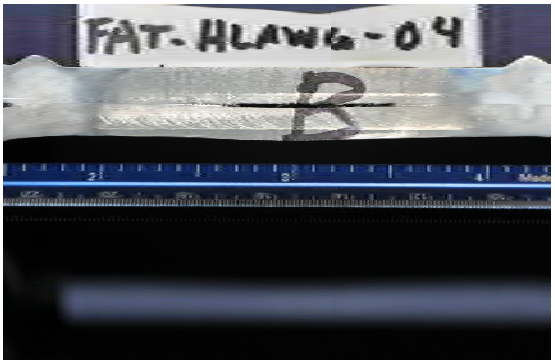

FAT–HLAWG–04 SIDE B STAKE WELD DETAIL

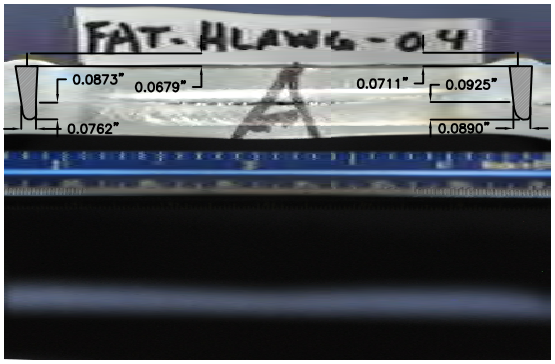

FAT–HLAWG–04 SIDE A STAKE WELD DETAIL INTERPOLATED DIMENSIONS

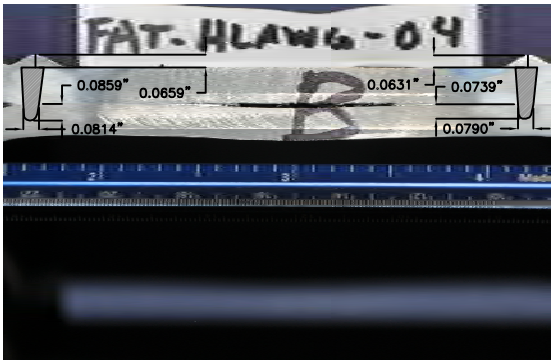

FAT–HLAWG–04 SIDE B STAKE WELD DETAIL INTERPOLATED DIMENSIONS

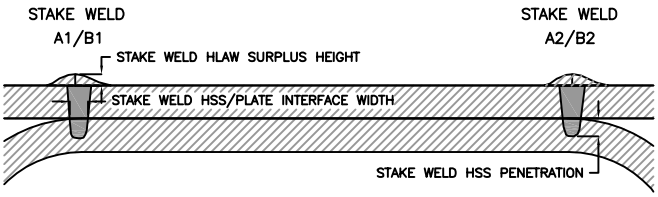

FIGURE REFERENCE

LEGEND

INTERPOLATED LASER STAKE WELD AREA

VIRGINIA POLYTECHNIC INSTITUTE AND STATE UNIVERSITY
BLACKSBURG, VIRGINIA

FATIGUE SPECIMEN STAKE WELD DETAILS
HYBRID LASER ARC WELD TEST SPECIMEN: FAT-HLAWG-04
VIA DEPARTMENT OF CIVIL AND ENVIRONMENTAL ENGINEERING
BLACKSBURG, VIRGINIA

DESIGNED BY	G.Passarelli	4/12/2011	CHECKED BY	W.Wright	4/12/2011
DRAWN BY	G.Passarelli	4/12/2011	APPROVED BY	W.Wright	4/12/2011
SCALE: 1"=1"	DRAWING NO. FAT-HLAWG-04	PROJECT NO. SSP	SHEET NO. ---	REVISION NO. --	

LOCATION	DRAWN BY		CHECKED BY		APPROVED BY		DRAWING NUMBER
BLACKSBURG, VA	G.PASSARELLI	4/12/2011	W.WRIGHT	4/12/2011	W.WRIGHT	4/12/2011	FAT-HLAWG-04

PRODUCED BY AN AUTODESK EDUCATIONAL PRODUCT

PRODUCED BY AN AUTODESK EDUCATIONAL PRODUCT

STAKE WELD	STAKE WELD AREA	STAKE WELD HSS/PLATE INTERFACE WIDTH	STAKE WELD HSS PENETRATION DEPTH	STAKE WELD HLAW SURPLUS HEIGHT
(UNITS)	(sqin)	(in.)	(in.)	(in.)
A1	0.0246	0.0801	0.0971	0.0506
A2	0.0307	0.1058	0.0893	0.0557
B1	0.0344	0.1144	0.0828	0.0518
B2	0.0243	0.0798	0.0711	0.0497

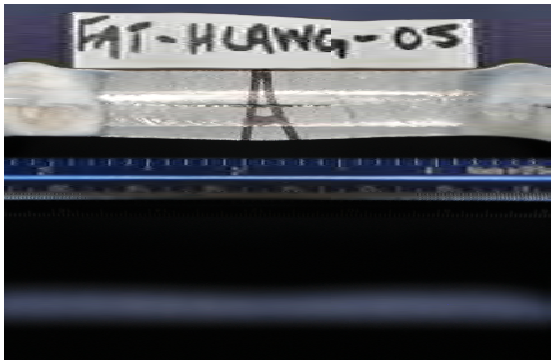

FAT–HLAWG–05 SIDE A STAKE WELD DETAIL

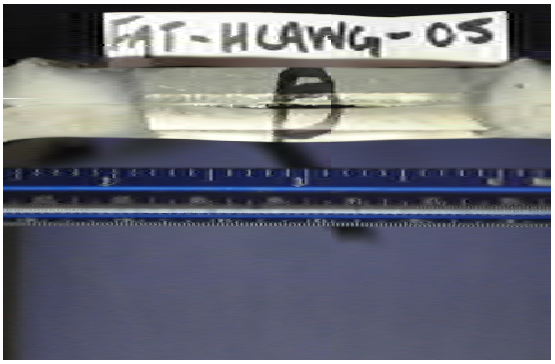

FAT–HLAWG–05 SIDE B STAKE WELD DETAIL

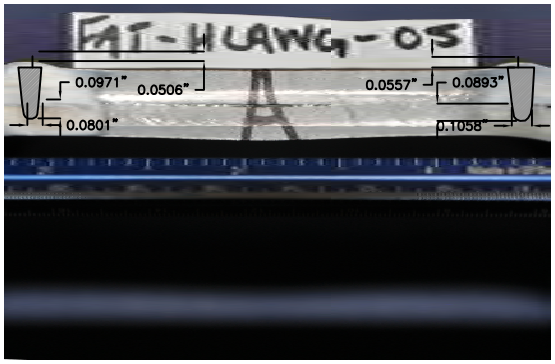

FAT–HLAWG–05 SIDE A STAKE WELD DETAIL INTERPOLATED DIMENSIONS

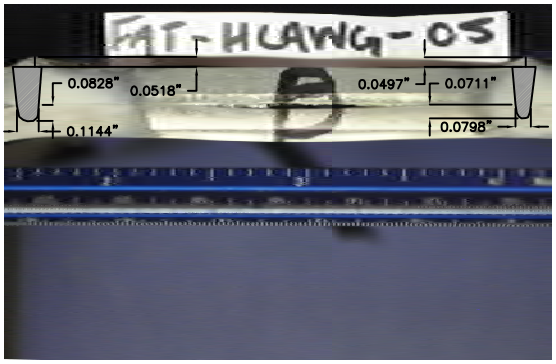

FAT–HLAWG–05 SIDE B STAKE WELD DETAIL INTERPOLATED DIMENSIONS

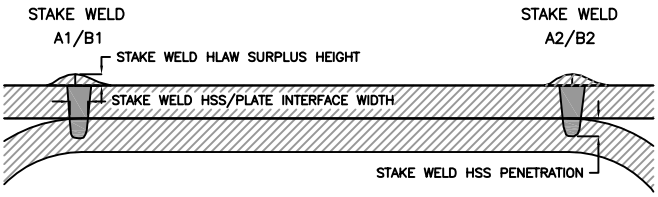

FIGURE REFERENCE

LEGEND

INTERPOLATED LASER STAKE WELD AREA

LOCATION	DRAWN BY		CHECKED BY		APPROVED BY		DRAWING NUMBER
BLACKSBURG, VA	G.PASSARELLI	4/12/2011	W.WRIGHT	4/12/2011	W.WRIGHT	4/12/2011	FAT-HLAWG-05

VIRGINIA POLYTECHNIC INSTITUTE AND STATE UNIVERSITY
BLACKSBURG, VIRGINIA

VirginiaTech VirginiaTech

FATIGUE SPECIMEN STAKE WELD DETAILS
HYBRID LASER ARC WELD TEST SPECIMEN: FAT-HLAWG-05
VIA DEPARTMENT OF CIVIL AND ENVIRONMENTAL ENGINEERING
BLACKSBURG, VIRGINIA

DESIGNED BY	G.Passarelli	4/12/2011	CHECKED BY	W.Wright	4/12/2011
DRAWN BY	G.Passarelli	4/12/2011	APPROVED BY	W.Wright	4/12/2011

SCALE:	DRAWING NO.	PROJECT NO.	SHEET NO.	REVISION NO.
1"=1"	FAT-HLAWG-05	SSP	---	--

PRODUCED BY AN AUTODESK EDUCATIONAL PRODUCT

STAKE WELD	STAKE WELD AREA	STAKE WELD HSS/PLATE INTERFACE WIDTH	STAKE WELD HSS PENETRATION DEPTH	STAKE WELD HLAW SURPLUS HEIGHT
(UNITS)	(sqin)	(in.)	(in.)	(in.)
A1	0.0255	0.0817	0.0895	0.0527
A2	0.0339	0.1095	0.1041	0.0513
B1	0.0298	0.0958	0.0996	0.0559
B2	0.0247	0.0778	0.0929	0.0637

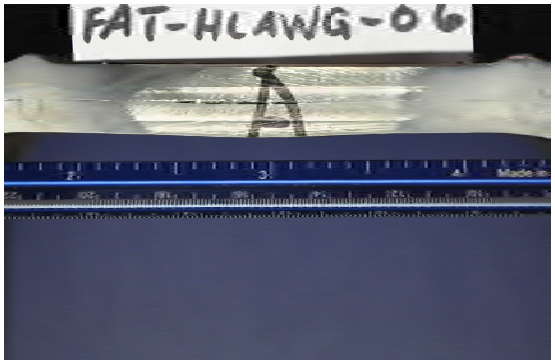

FAT–HLAWG–06 SIDE A STAKE WELD DETAIL

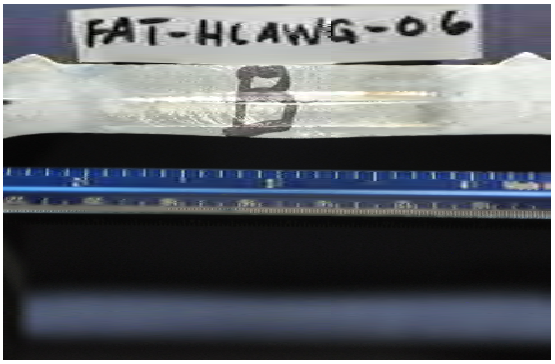

FAT–HLAWG–06 SIDE B STAKE WELD DETAIL

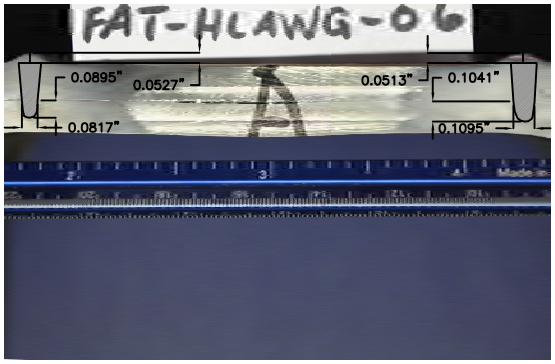

FAT–HLAWG–06 SIDE A STAKE WELD DETAIL INTERPOLATED DIMENSIONS

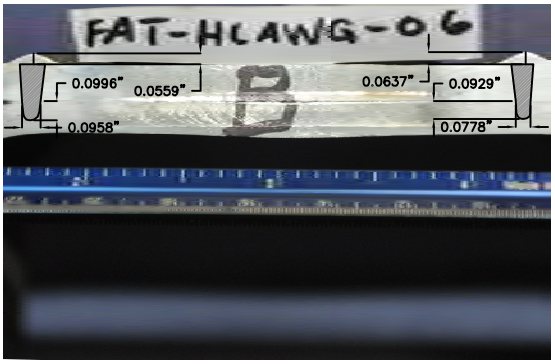

FAT–HLAWG–06 SIDE B STAKE WELD DETAIL INTERPOLATED DIMENSIONS

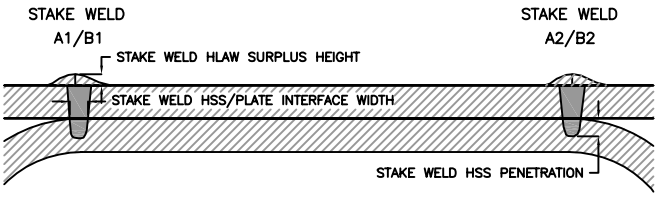

FIGURE REFERENCE

LEGEND

INTERPOLATED LASER STAKE WELD AREA

VIRGINIA POLYTECHNIC INSTITUTE AND STATE UNIVERSITY
BLACKSBURG, VIRGINIA

VirginiaTech VirginiaTech

FATIGUE SPECIMEN STAKE WELD DETAILS
HYBRID LASER ARC WELD TEST SPECIMEN: FAT-HLAWG-06
VIA DEPARTMENT OF CIVIL AND ENVIRONMENTAL ENGINEERING
BLACKSBURG, VIRGINIA

DESIGNED BY	G.Passarelli	4/12/2011	CHECKED BY	W.Wright	4/12/2011
DRAWN BY	G.Passarelli	4/12/2011	APPROVED BY	W.Wright	4/12/2011
SCALE: 1"=1"	DRAWING NO. FAT-HLAWG-06	PROJECT NO. SSP	SHEET NO. ---	REVISION NO. --	

LOCATION	DRAWN BY		CHECKED BY		APPROVED BY		DRAWING NUMBER
BLACKSBURG, VA	G.PASSARELLI	4/12/2011	W.WRIGHT	4/12/2011	W.WRIGHT	4/12/2011	FAT-HLAWG-06

PRODUCED BY AN AUTODESK EDUCATIONAL PRODUCT

STAKE WELD	STAKE WELD AREA	STAKE WELD HSS/PLATE INTERFACE WIDTH	STAKE WELD HSS PENETRATION DEPTH	STAKE WELD HLAW SURPLUS HEIGHT
(UNITS)	(sqin)	(in.)	(in.)	(in.)
A1	0.0281	0.0813	0.1195	0.0478
A2	0.0274	0.0802	0.1054	0.0557
B1	0.0301	0.0860	0.0981	0.0546
B2	0.0273	0.0828	0.0979	0.0508

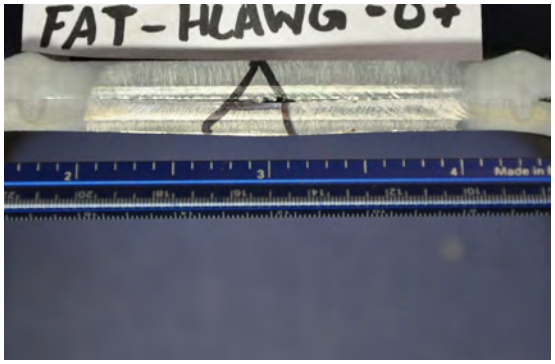

FAT–HLAWG–07 SIDE A STAKE WELD DETAIL

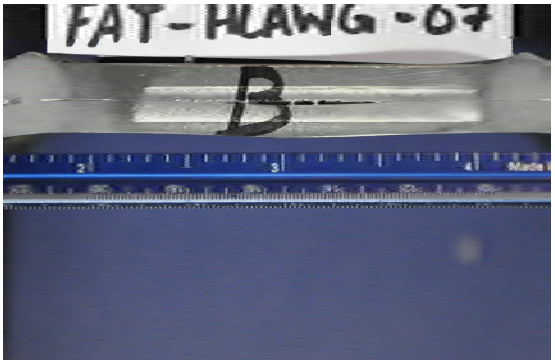

FAT–HLAWG–07 SIDE B STAKE WELD DETAIL

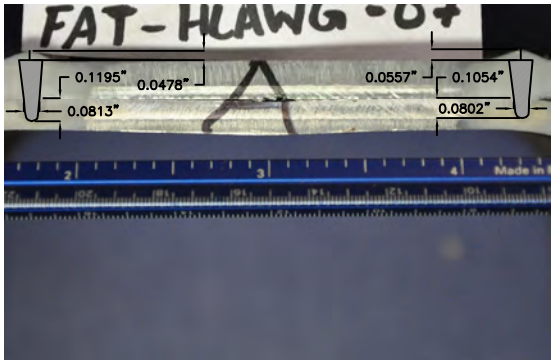

FAT–HLAWG–07 SIDE A STAKE WELD DETAIL INTERPOLATED DIMENSIONS

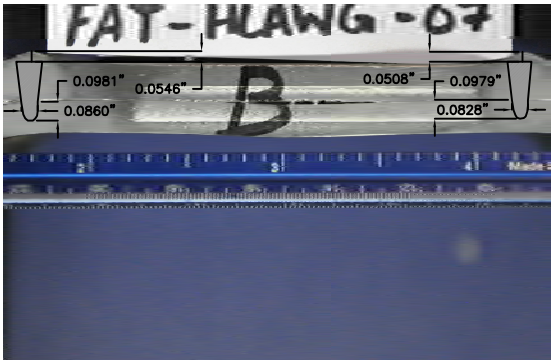

FAT–HLAWG–07 SIDE B STAKE WELD DETAIL INTERPOLATED DIMENSIONS

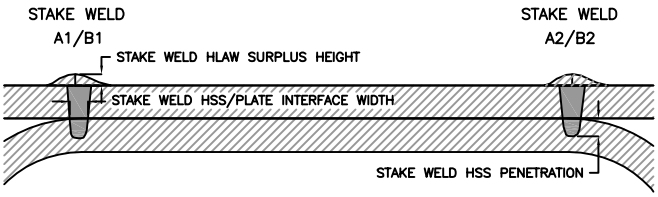

FIGURE REFERENCE

LEGEND

INTERPOLATED LASER STAKE WELD AREA

LOCATION	DRAWN BY		CHECKED BY		APPROVED BY		DRAWING NUMBER
BLACKSBURG, VA	G.PASSARELLI	4/12/2011	W.WRIGHT	4/12/2011	W.WRIGHT	4/12/2011	FAT-HLAWG-07

VIRGINIA POLYTECHNIC INSTITUTE AND STATE UNIVERSITY
BLACKSBURG, VIRGINIA

VirginiaTech VirginiaTech

FATIGUE SPECIMEN STAKE WELD DETAILS
HYBRID LASER ARC WELD TEST SPECIMEN: FAT-HLAWG-07
VIA DEPARTMENT OF CIVIL AND ENVIRONMENTAL ENGINEERING
BLACKSBURG, VIRGINIA

DESIGNED BY	G.Passarelli	4/12/2011	CHECKED BY	W.Wright	4/12/2011
DRAWN BY	G.Passarelli	4/12/2011	APPROVED BY	W.Wright	4/12/2011

SCALE:	DRAWING NO.	PROJECT NO.	SHEET NO.	REVISION NO.
1"=1"	FAT-HLAWG-07	SSP	---	--

PRODUCED BY AN AUTODESK EDUCATIONAL PRODUCT

STAKE WELD	STAKE WELD AREA	STAKE WELD HSS/PLATE INTERFACE WIDTH	STAKE WELD HSS PENETRATION DEPTH	STAKE WELD HLAW SURPLUS HEIGHT
(UNITS)	(sqin)	(in.)	(in.)	(in.)
A1	0.0256	0.0731	0.1156	0.0537
A2	0.0281	0.0799	0.1278	0.0508
B1	0.0266	0.0760	0.1028	0.0496
B2	0.0241	0.0786	0.0869	0.0447

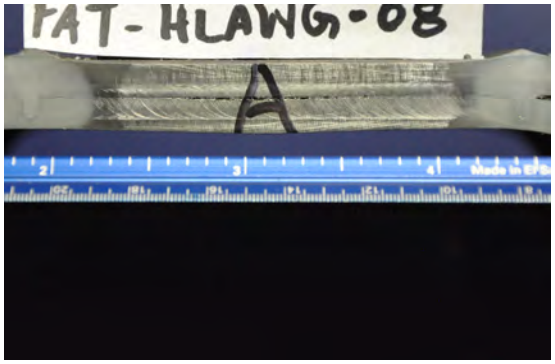

FAT–HLAWG–08 SIDE A STAKE WELD DETAIL

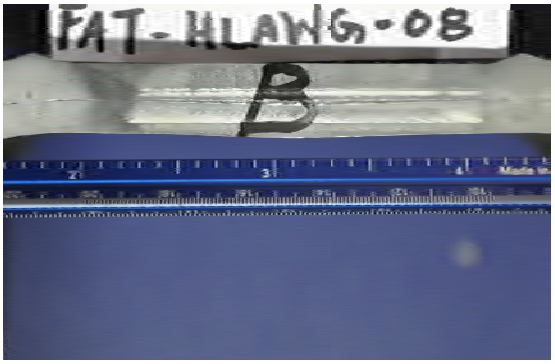

FAT–HLAWG–08 SIDE B STAKE WELD DETAIL

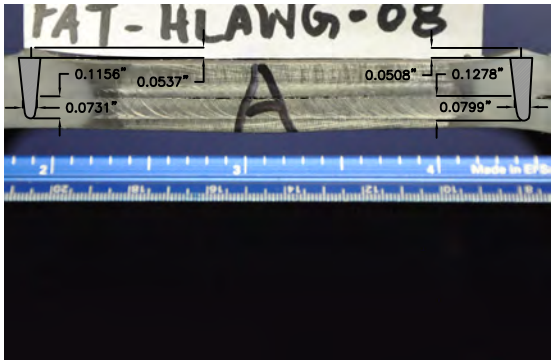

FAT–HLAWG–08 SIDE A STAKE WELD DETAIL INTERPOLATED DIMENSIONS

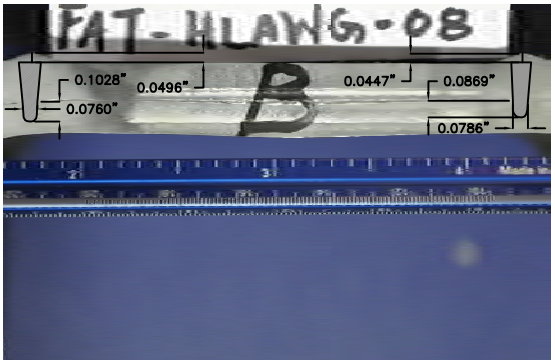

FAT–HLAWG–08 SIDE B STAKE WELD DETAIL INTERPOLATED DIMENSIONS

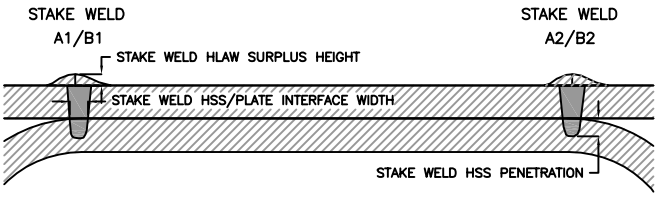

FIGURE REFERENCE

LEGEND

INTERPOLATED LASER STAKE WELD AREA

LOCATION	DRAWN BY		CHECKED BY		APPROVED BY		DRAWING NUMBER
BLACKSBURG, VA	G.PASSARELLI	4/12/2011	W.WRIGHT	4/12/2011	W.WRIGHT	4/12/2011	FAT-HLAWG-08

VIRGINIA POLYTECHNIC INSTITUTE AND STATE UNIVERSITY
BLACKSBURG, VIRGINIA

VirginiaTech VirginiaTech

FATIGUE SPECIMEN STAKE WELD DETAILS
HYBRID LASER ARC WELD TEST SPECIMEN: FAT-HLAWG-08
VIA DEPARTMENT OF CIVIL AND ENVIRONMENTAL ENGINEERING
BLACKSBURG, VIRGINIA

DESIGNED BY	G.Passarelli	4/12/2011	CHECKED BY	W.Wright	4/12/2011
DRAWN BY	G.Passarelli	4/12/2011	APPROVED BY	W.Wright	4/12/2011

SCALE:	DRAWING NO.	PROJECT NO.	SHEET NO.	REVISION NO.
1"=1"	FAT-HLAWG-08	SSP	---	--

PRODUCED BY AN AUTODESK EDUCATIONAL PRODUCT

PRODUCED BY AN AUTODESK EDUCATIONAL PRODUCT

STAKE WELD	STAKE WELD AREA	STAKE WELD HSS/PLATE INTERFACE WIDTH	STAKE WELD HSS PENETRATION DEPTH	STAKE WELD HLAW SURPLUS HEIGHT
(UNITS)	(sqin)	(in.)	(in.)	(in.)
A1	0.0296	0.0833	0.1066	0.0426
A2	0.0290	0.0760	0.1641/FULL	0.0260
B1	0.0313	0.0821	0.1472	0.0473
B2	0.0228	0.0663	0.0991	0.0513

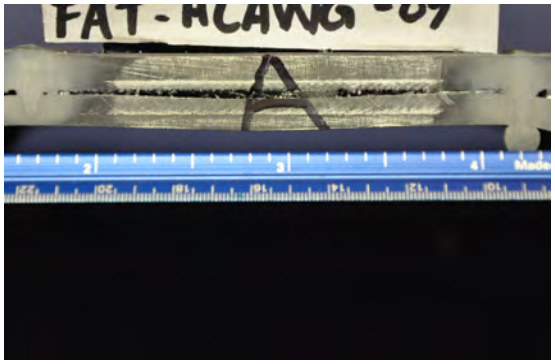

FAT-HLAWG-09 SIDE A STAKE WELD DETAIL

FAT-HLAWG-09 SIDE B STAKE WELD DETAIL

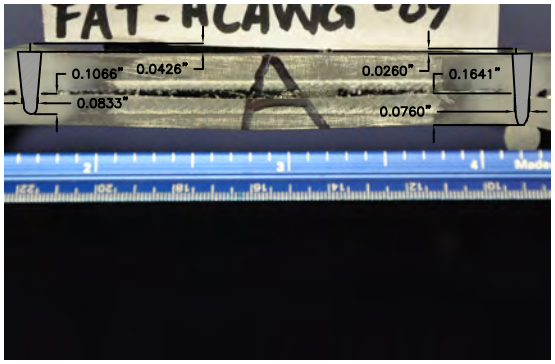

FAT-HLAWG-09 SIDE A STAKE WELD DETAIL INTERPOLATED DIMENSIONS

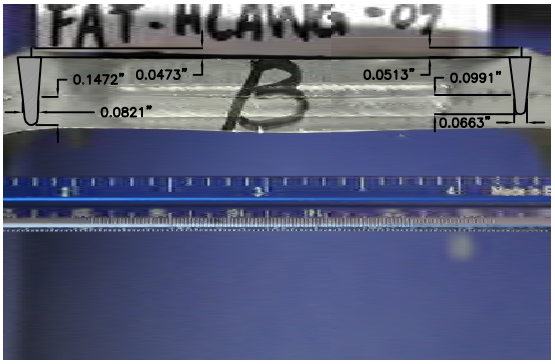

FAT-HLAWG-09 SIDE B STAKE WELD DETAIL INTERPOLATED DIMENSIONS

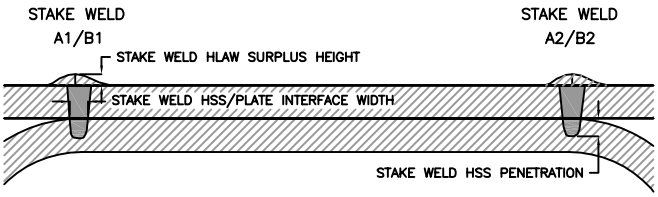

FIGURE REFERENCE

LEGEND

INTERPOLATED LASER STAKE WELD AREA

LOCATION	DRAWN BY	CHECKED BY	APPROVED BY	DRAWING NUMBER
BLACKSBURG, VA	G.PASSARELLI 4/12/2011	W.WRIGHT 4/12/2011	W.WRIGHT 4/12/2011	FAT-HLAWG-09

VIRGINIA POLYTECHNIC INSTITUTE AND STATE UNIVERSITY
BLACKSBURG, VIRGINIA

VirginiaTech VirginiaTech

FATIGUE SPECIMEN STAKE WELD DETAILS
HYBRID LASER ARC WELD TEST SPECIMEN: FAT-HLAWG-09
VIA DEPARTMENT OF CIVIL AND ENVIRONMENTAL ENGINEERING
BLACKSBURG, VIRGINIA

DESIGNED BY	G.Passarelli	4/12/2011	CHECKED BY	W.Wright	4/12/2011
DRAWN BY	G.Passarelli	4/12/2011	APPROVED BY	W.Wright	4/12/2011

SCALE:	DRAWING NO.	PROJECT NO.	SHEET NO.	REVISION NO.
1"=1"	FAT-HLAWG-09	SSP	---	--

PRODUCED BY AN AUTODESK EDUCATIONAL PRODUCT

PRODUCED BY AN AUTODESK EDUCATIONAL PRODUCT

STAKE WELD	STAKE WELD AREA	STAKE WELD HSS/PLATE INTERFACE WIDTH	STAKE WELD HSS PENETRATION DEPTH	STAKE WELD HLAW SURPLUS HEIGHT
(UNITS)	(sqin)	(in.)	(in.)	(in.)
A1	0.0309	0.0789	0.1173	0.0396
A2	0.0336	0.0932	0.1357	0.0391
B1	0.0294	0.0690	0.1700/FULL	0.0336
B2	0.0291	0.0783	0.1095	0.0422

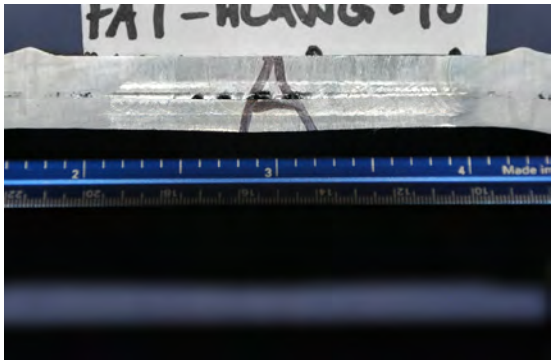

FAT–HLAWG–10 SIDE A STAKE WELD DETAIL

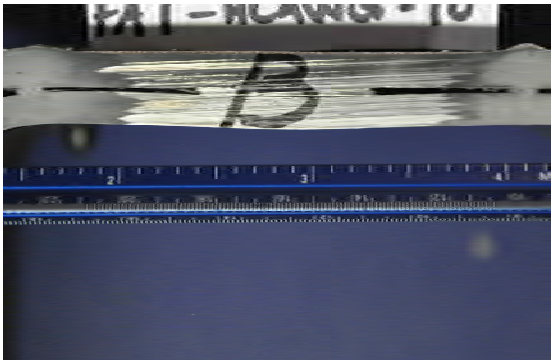

FAT–HLAWG–10 SIDE B STAKE WELD DETAIL

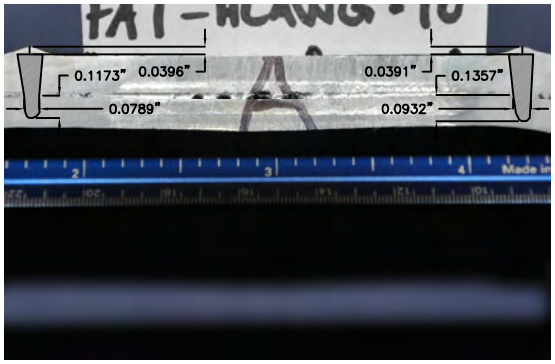

FAT–HLAWG–10 SIDE A STAKE WELD DETAIL INTERPOLATED DIMENSIONS

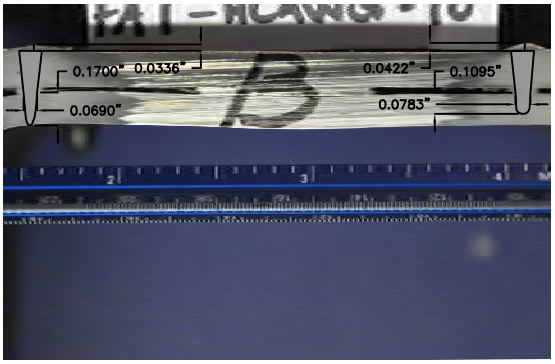

FAT–HLAWG–10 SIDE B STAKE WELD DETAIL INTERPOLATED DIMENSIONS

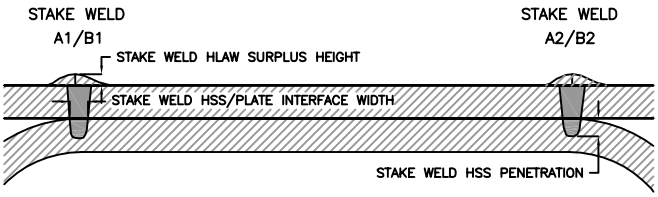

FIGURE REFERENCE

LEGEND

INTERPOLATED LASER STAKE WELD AREA

LOCATION	DRAWN BY		CHECKED BY		APPROVED BY		DRAWING NUMBER
BLACKSBURG, VA	G.PASSARELLI	4/12/2011	W.WRIGHT	4/12/2011	W.WRIGHT	4/12/2011	FAT-HLAWG-10

VIRGINIA POLYTECHNIC INSTITUTE AND STATE UNIVERSITY
BLACKSBURG, VIRGINIA

VirginiaTech VirginiaTech

FATIGUE SPECIMEN STAKE WELD DETAILS
HYBRID LASER ARC WELD TEST SPECIMEN: FAT-HLAWG-10
VIA DEPARTMENT OF CIVIL AND ENVIRONMENTAL ENGINEERING
BLACKSBURG, VIRGINIA

DESIGNED BY	G.Passarelli	4/12/2011	CHECKED BY	W.Wright	4/12/2011
DRAWN BY	G.Passarelli	4/12/2011	APPROVED BY	W.Wright	4/12/2011

SCALE:	DRAWING NO.	PROJECT NO.	SHEET NO.	REVISION NO.
1"=1"	FAT-HLAWG-10	SSP	---	--

PRODUCED BY AN AUTODESK EDUCATIONAL PRODUCT

STAKE WELD	STAKE WELD AREA	STAKE WELD HSS/PLATE INTERFACE WIDTH	STAKE WELD HSS PENETRATION DEPTH	STAKE WELD HLAW SURPLUS HEIGHT
(UNITS)	(sqin)	(in.)	(in.)	(in.)
A1	0.0213	0.0715	0.1152	0.0000
A2	0.0343	0.0943	0.1211	0.0000
B1	0.0306	0.0823	0.1364	0.0373
B2	0.0288	0.0764	0.1163	0.0309

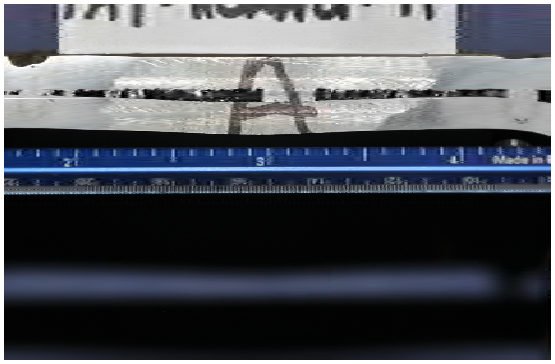

FAT-HLAWG-11 SIDE A STAKE WELD DETAIL

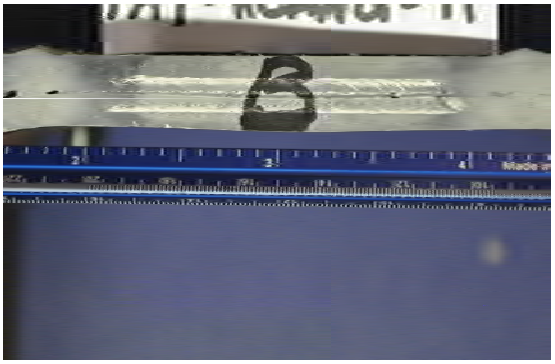

FAT-HLAWG-11 SIDE B STAKE WELD DETAIL

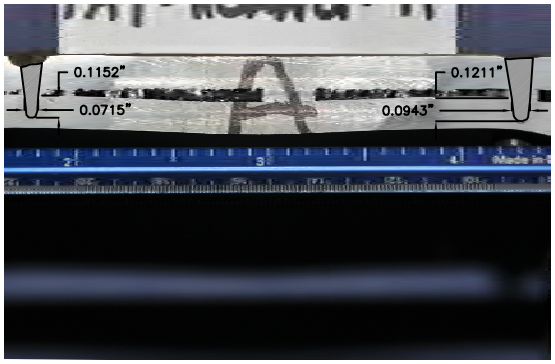

FAT-HLAWG-11 SIDE A STAKE WELD DETAIL INTERPOLATED DIMENSIONS

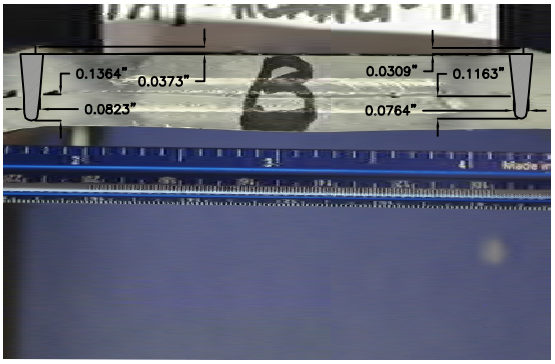

FAT-HLAWG-11 SIDE B STAKE WELD DETAIL INTERPOLATED DIMENSIONS

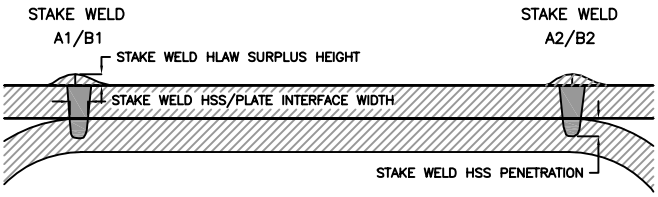

FIGURE REFERENCE

LEGEND

INTERPOLATED LASER STAKE WELD AREA

LOCATION	DRAWN BY		CHECKED BY		APPROVED BY		DRAWING NUMBER
BLACKSBURG, VA	G.PASSARELLI	4/12/2011	W.WRIGHT	4/12/2011	W.WRIGHT	4/12/2011	FAT-HLAWG-11

VIRGINIA POLYTECHNIC INSTITUTE AND STATE UNIVERSITY
BLACKSBURG, VIRGINIA

VirginiaTech VirginiaTech

FATIGUE SPECIMEN STAKE WELD DETAILS
HYBRID LASER ARC WELD TEST SPECIMEN: FAT-HLAWG-11
VIA DEPARTMENT OF CIVIL AND ENVIRONMENTAL ENGINEERING
BLACKSBURG, VIRGINIA

DESIGNED BY	G.Passarelli	4/12/2011	CHECKED BY	W.Wright	4/12/2011
DRAWN BY	G.Passarelli	4/12/2011	APPROVED BY	W.Wright	4/12/2011

SCALE:	DRAWING NO.	PROJECT NO.	SHEET NO.	REVISION NO.
1"=1"	FAT-HLAWG-11	SSP	---	--

PRODUCED BY AN AUTODESK EDUCATIONAL PRODUCT